EXPERIMENTAL INVESTIGATION OF INELASTIC SDOF STEEL STRUCTURES USING ENERGY-BASED PRINCIPALS

by

Hümeyra Börekçi

B.S., Civil Engineering, Yeditepe University, 2011

Submitted to the Institute for Graduate Studies in
Science and Engineering in partial fulfillment of
the requirements for the degree of
Master of Science

Graduate Program in Civil Engineering

Boğaziçi University

2019

ACKNOWLEDGEMENTS

I would like to express my sincere gratitude to Assoc. Prof. Cem Yalçın for his invaluable guidance and continuous support during my Master's study and research. His guidance helped me throughout my research and writing of this thesis.

I would also like to thank Prof. Ercan Yüksel due to his guidance and effort especially during experimental part of this study.

Additionally, I would like to thank Dr. Ahmet Güllü and Ph.D. students Burak Horoz, Seyhan Okuyan and Ferit Yardımcı for their help and sharing their own experiences in the progress of this research.

Moreover, I would like to thank Istanbul Technical University's Structural and Earthquake Engineering laboratory staff for their cooperation.

Also, I would like to thank Boğazici University Research Fund (Project Code: 11164, Project BOUN Code: 17A04P2) for the financial support of this project.

Finally, I must express my deepest gratitude to my parents for providing me with unfailing support and continuous encouragement throughout my years of education from the very first day and through the process of research and writing this thesis. This accomplishment would not have been possible without them.

ABSTRACT

EXPERIMENTAL INVESTIGATION OF INELASTIC SDOF STEEL STRUCTURES USING ENERGY-BASED PRINCIPALS

In this research, twenty-eight experimental tests were performed with 0.75-meter-high single degree of freedom system (SDOF) steel models on a shaking table. Actual scaled 1986 San Salvador earthquake ground motion data was used to excite the SDOF models beyond their elastic displacement limits. The main goal was to verify the existing energy demand spectra, especially within the inelastic range. Elasto-plastic material behavior was considered and responses that were obtained from the experiments were used to calculate the energy quantities for varying natural period of the SDOF system. The damping ratios of the specimens were determined experimentally by means of free vibration after the excitation was completed, and analytically determined through Logarithmic Decrement method. Also, the damping ratios of the specimens were calculated during the earthquake excitation through Chopra's (Chopra, 1995) method. Lastly, an energy spectrum with mass-normalized energy versus natural period of the SDOF system was determined experimentally with respect to varying damping ratios. As a result, experimental data had good agreement with the existing (Güllü, 2019) Energy Spectrum, when data were compared.

ÖZET

TEK SERBESTLİK DERECELİ ELASTİK OLMAYAN ÇELİK YAPILARIN ENERJİ ESASLI TASARIM PRENSİPLERİ KULLANILARAK DENEYSEL OLARAK ARAŞTIRILMASI

Bu çalışma, 0.75 metre yüksekliğinde tek serbestlik dereceli çelik numuneler üzerinde gerçekleştirilmiş yirmi sekiz ayrı sarsma masası deneyinden oluşmaktadır. 1986 San Salvador depremi gerçek ölçekli olarak uygulanarak numunelerin elastik limitler dışına geçirilmesi sağlanmıştır. Bu çalışmanın temel amacı elastik ve özellikle elastik olmayan kısımda mevcut enerji spektrumlarının deneysel olarak doğrulanmasıdır. Çalışma boyunca elasto-plastik malzeme modeli kullanılmıştır. Bu çalışmada; enerjiler deneysel olarak elde edilen verilerden hesaplanmıştır. Sönüm oranları deneysel veriler kullanılarak logaritmik azalım ve Chopra metotlarıyla hesaplanmıştır. Logaritmik azalım metodu için deprem sonrası kayıt, Chopra metodu içinse deprem süresi kaydı kullanılmıştır. Son olarak, değişen sönüm oranlarına karşılık giren enerjiler spektrumları çizilmiştir. Veriler (Güllü, 2019) enerji spektrumuyla kıyaslandığında çoğu deneyde yakın sonuç alınmıştır .

TABLE OF CONTENTS

LIST OF FIGURES

LIST OF TABLES

LIST OF SYMBOLS

c	Damping coefficient
Ea	Absorbed energy
Ed	Damping energy
Ek	Kinetic energy
El	Input energy
Ep	Plastic energy
Es	Strain energy
F	Force
fs	Restoring force
fy	Yielding stress
k	Stiffness
m	Mass
M	Moment
Td	Natural Period of Damped Vibration
Tn	Natural Period
wd	Natural Frequency of Damped Vibration
wn	Natural Frequency
ζ	Damping Ratio

LIST OF ACRONYMS/ABBREVIATIONS

EQ	Earthquake
PEER	The Pacific Earthquake Engineering Research Center
SDOF	Single Degree of Freedom

1. INTRODUCTION

1.1. General

Throughout the years, earthquake-resistant design is in constant development. In the 1960s and 1970s, the importance of inelastic structural behavior under severe earthquakes were realized. Thus, researchers mainly focused on the inelastic deformation capacity of the structural members (Priestley, 2000). The main challenge for proper earthquake-resistant design is to capture the balance between seismic demand and seismic capacity, where seismic demand corresponds to the effects of ground motion on the structure whereas the capacity is the capability of the structure to resist and yield without any catastrophic failure (Gioncu *et al.*, 2010).

While development of alternative methods still underway, current available methods are revised and earthquake behavior of structures are better understood. Displacement, velocity and acceleration are the dynamic responses of structures under earthquake excitation. They depend on the characteristics of the structural material and the nature of the earthquake, as well as, dynamic properties of the system and the soil-structure interaction. Unlike most commonly-used design methods, i.e. force and displacement-based methods, Energy-Based approach takes into account the hysteretic behavior of the structure in terms of energy dissipation capacity, as well as duration of the ground motion and its frequency content. Thus, energy-based design approach could be a useful tool to analyze seismic actions.

This study aims to utilize the Energy-Based approach to calculate experimentally the damping ratios of Single Degree of Freedom Systems (SDOF) made up of steel columns. Experiments were performed on shake table with representative earthquake ground motion of the 1986 San Salvador earthquake. Its intensity was adjusted so that different excitations could yield elastic and inelastic behavior of the test specimens. Furthermore, resulting energy components were calculated and compared with experimental results in order to verify the damping ratios. Finally, experimental results

were verified with inelastic energy spectrum (Güllü, 2019).

1.2. Current Design Methods

For earthquake-resistant design, various design approaches are currently being used by practicing structural engineers. They are described in the following subsections.

1.2.1. Force-Based Method

In the seismic design process, Force-Based method (Figure 1.1) is the most commonly used design procedure by practicing engineers to calculate the dynamic forces imposed to the structures. Force-Based seismic design primarily focuses on seismic forces acting on the system. As it determines the forces at the end of the analysis, this method neglects the performance of the building and cannot truly provide seismic demand of the system. In this method, individual members of the structure are proportioned for strength in earthquake-resistant analysis using initial stiffness and period of the structure.

It has been utilized for many years to evaluate the dynamic responses and soil-structure interactions. However, it does not accurately reflect the dynamic problems and could potentially yield towards more conservative results. Force-Based seismic design lacks many attributes as mentioned below, which results in need for a better design approach.

First of all, this method uses initial stiffness, which is unknown in the beginning of the design process. Thus, if the reinforcement content is increased or decreased to satisfy the results of the design, final stiffness would not be the same. Likewise, if the flange thickness of steel member is changed for satisfying a strength requirement, the member stiffness would ultimately change. So, there is a need for updating the stiffness information every time section properties change, and carry out calculations accordingly.

Moreover, elastic estimates of stiffness are irrational and cause concentrated strength in structural members. Since the force reduction factor is the function of the ductility and period of the system in the inelastic range, it reduces the elastic forces for inelastic design purposes. Here, the force reduction factor is not precisely known, and given for specific type of structures in design codes (Dindar, 2009). Furthermore, this method does not take into account the hysteretic behavior of the system during inelastic range.

Also, period of the structure is unknown. Therefore, it should be estimated by empirical formulations according the seismic design codes. Moreover, Force-Based seismic design does not consider the cumulative damage effect of the earthquake's duration and frequency content, and it takes into account only the maximum response of the structure.

Additionally, ductility capacity depends on structural geometry, not just structural type. So, it is not practical to define same displacement ductility factor for all structures of the same type (Priestley, 1993-2003).

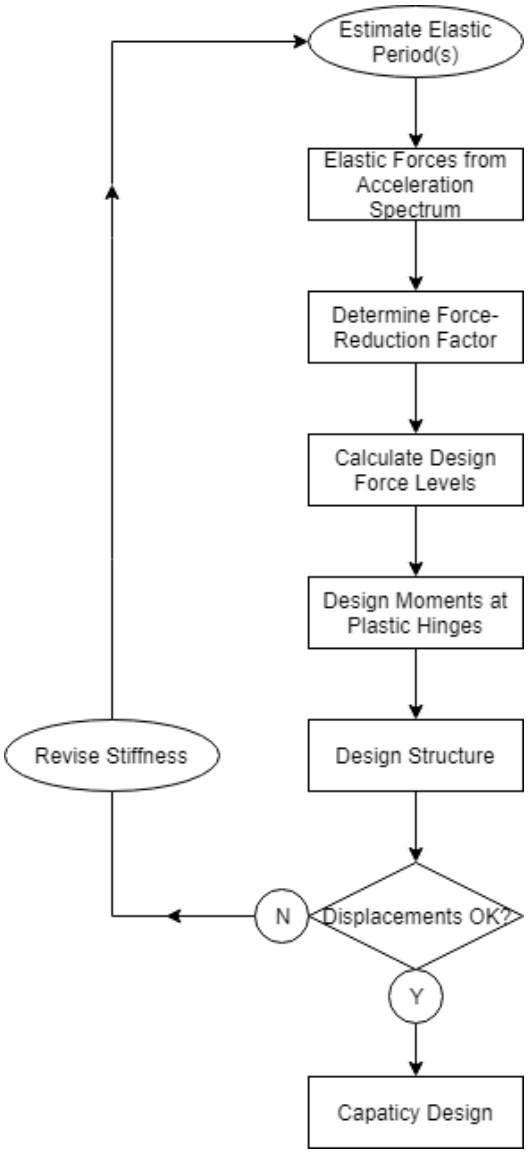

Figure 1.1. Force-Based Design Process (Priestley, 2002).

1.2.2. Displacement-Based Method

Displacement-Based design method (Figure 1.2) focuses on a specified target displacement of the structure. The performance of the structure is defined according to the deformation capacity of the structural members during earthquake.

First of all, Displacement-Based design process starts with the estimation of the dimensions of the structural elements and the stiffness of the structure. The period of the structural system could be calculated knowing the stiffness, and thus, the strength

of the structure could be readily calculated. Therefore, obtained seismic forces are used to analyze the system and the displacement of the structural system is evaluated. When the displacement satisfies the specified target displacement, the design process is completed. If it does not satisfy the specified target displacement, the dimension of the structure is changed and then design process is repeated from the start.

The advantage of using Displacement-Based design method is that it considers the nonlinear behavior of the system while force-based design considers only pseudo nonlinear behavior using force reduction factors, as described in the preceding section. Also, selection of performance level of the system provides logical results rather than force reduction factor obtained from design codes.

However, displacement-based design method has some drawbacks since it does not include the duration and the frequency content of the earthquake event, which are the main reasons of the accumulated damage in the structural members (Dindar, 2009). Therefore, capacity curve that is plotted for the top displacement versus base shear, does not provide the same damage occurrence in the members. Moreover, like Force-Based method, this method obtains seismic demand from elastic response spectrum.

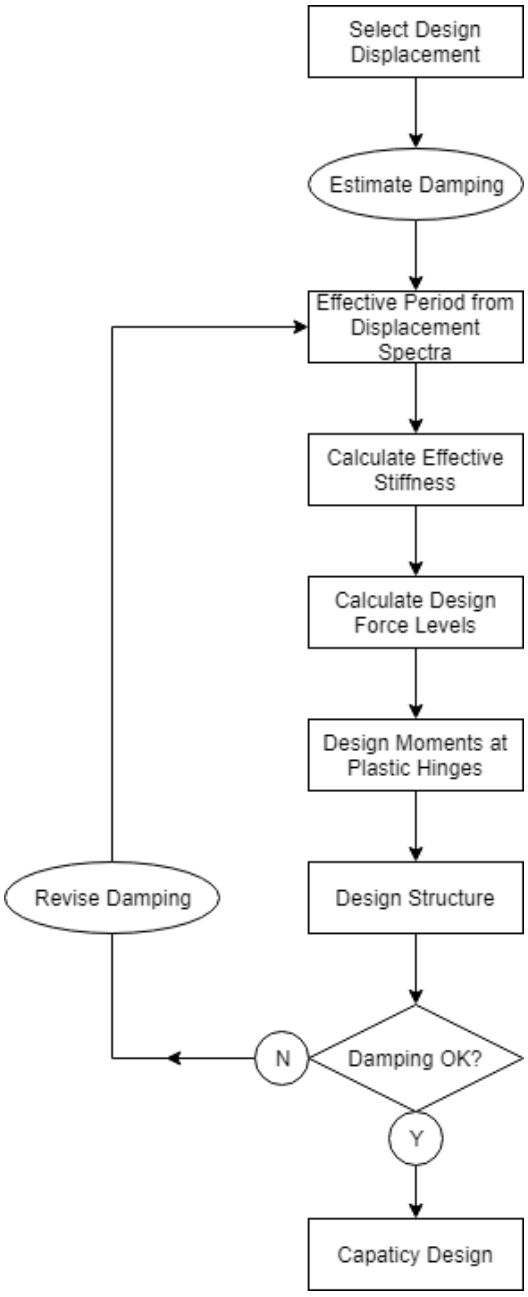

Figure 1.2. Displacement-Based Design Process (Priestley, 2002).

1.3. Introduction to Energy-Based Method

Energy-Based design method mainly focuses on the seismic behavior in terms of the input energy of the earthquake, which is absorbed and dissipated by the system. Unlike conventional methods, this method considers both peak displacement, velocity and acceleration response demands of the system, as well as, time history response

demand. Energy-Based approach takes into account the energy dissipation capacity as plastic deformations and viscous damping, while other methods, as mentioned before, disregard.

Most commonly, only strength capacity and deformation limits are determined for seismic design. However, structures should also have enough energy dissipation capacity to endure the seismic forces in terms of viscous damping and plastic deformations. Figure 1.3 illustrates two identical structures having the same yield and displacement capacity, however, it does not always mean that they have the same energy dissipation capacity. According to Displacement-Based design, these two structures behave identical behavior since they have similar yield and deformation capacities. However, the closed area of force-deformation curves, which equals to plastic energy dissipation, may be different (Dindar, 2009). Structural damages during earthquake could be controlled greatly by the energy dissipating mechanism. Total input energy should not exceed total energy dissipating capacity so that structural endure seismic forces without failure.

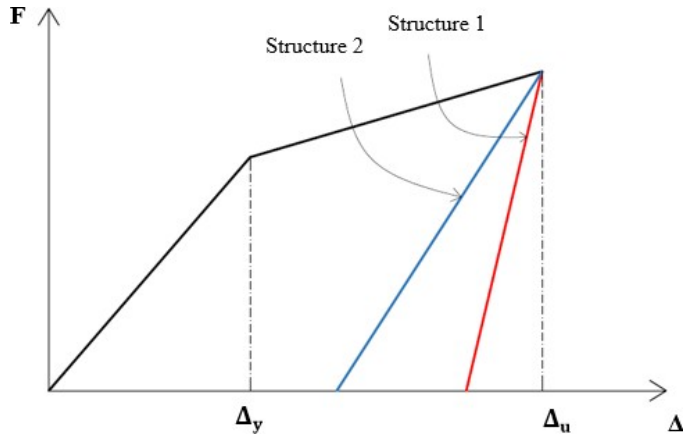

Figure 1.3. Two identical structures with different energy dissipation capacity (Dindar, 2009).

Moreover, Energy-Based design method considers duration and frequency content of the earthquake and ground motion records unlike other conventional methods, as mentioned in above sub-sections.

Framework of Energy-Based seismic design is illustrated in Figure 1.4. It describes the Displacement-Based design method in steps 1-3-4-5-9, while Energy-Based design method is described in steps 1-2-6-7-8-9 (Ye, 2000). In addition to these, visualizing physical meaning of the energy could be difficult and it is hard to accept as a design parameter. Structural members should be investigated thoroughly to overcome this problem (Dindar, 2009).

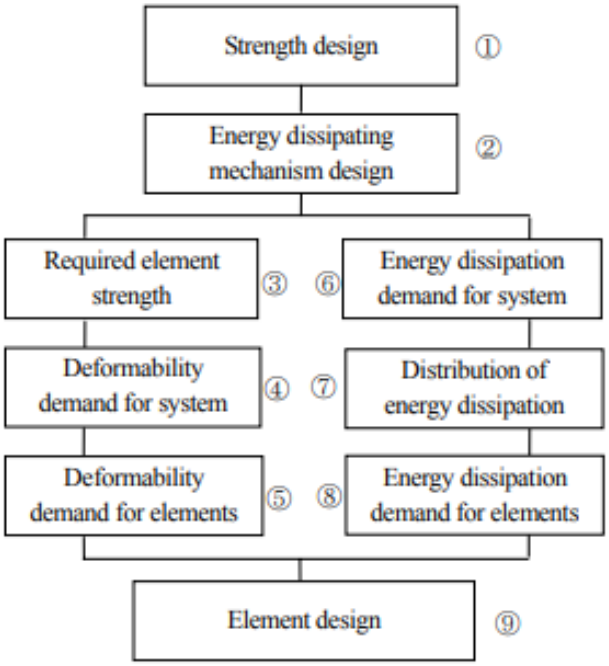

Figure 1.4. Framework of energy-based seismic design (Ye, 2009).

1.4. Literature Review

Over the past 50 years, many researches have investigated the Energy-Based approach. In 1956, Housner proposed a seismic design approach based on energy demand. In his proposal, Housner considered a seismic design method for a water tank and investigated its ability to absorb energy. Since the first proposal by G. Housner (1956), Energy-Based design method was developed significantly.

From the 1980's, this approach has attracted many researchers' attention. Zahrah (1984) studied the nonlinear response of SDOF structures and the damage potential

of earthquake excitation. Kuwamura and Galambos (1989) investigated Energy-Based velocity spectrum and developed an ultimate limit-state criterion for seismic reliability assessment of SDOF structures. Fajfar (1989) employed numerous earthquake records to investigate the elastic and inelastic responses of SDOF structures. In 1990, Uang and Bertero analyzed the physical meaning of absolute energy and relative energy formulations and then discussed the differences between them. Fajfar and Vidic (1994) proposed a procedure for the determination of inelastic spectra (for strength, displacement, hysteretic and input energy) which considers prescribed ductility factor. Decanini and Mollaioli (1998) studied a procedure for the determination of elastic design earthquake input energy spectra which considers the influence of magnitude, soil type and distance from the surface projection of the fault. Dindar (2009) developed two algorithms which aims to determinate the energy dissipation capacities of the RC columns and energy-based seismic analysis of the structures. In 2019, Güllü compared previously developed spectral input energy equations and proposed a new energy demand spectrum.

There is no study found in the literature in relation to the verification of existing energy demand spectrum. Also, experimental investigation of SDOF structures with varying damping ratios using energy-based principals is not studied before.

1.5. Objective and Scope of the Study

In this study, extensive experimental work was conducted using Energy-Based principals by considering varying damping ratios that were obtained for each experiment by using logarithmic decrement method and Chopra's (Chopra, 1996) method.

This study aims to validate (Güllü, 2019) proposed energy spectra with mass-normalized energy versus natural period of the SDOF structure with respect to varying damping ratios. Twenty-eight experiments were conducted on three identical 0.75-meter-long hollow cross section steel column specimens. Energy terms were calculated analytically and experimentally, and then, results were compared with existing the energy spectrum.

The scope of this study is to test SDOF specimens of hollow section steel columns in two-dimensional motion plane on a shake table. Three different periods were used during experimental study. Energy values of the all elements were computed analytically using SAP2000 software and developed MATLAB code. Energy terms of all the elements are calculated for elastic and inelastic cases. SAP2000 software are used to calculate input energy (EI) based on three different periods.

1.6. Research Rational

Shake table experimental research with varying damping ratios in linear and nonlinear range of SDOF systems is missing in the literature. Furthermore, developed energy demand spectra by other researchers need to be verified experimentally, especially with varying damping ratios.

Although there were many valuable researches conducted on Energy-Based design concept, the subject is still open for further development.

1.7. Organization of the Thesis

This thesis consists of five chapters. First chapter includes introduction, literature review, and objective and scope of the research, as well as research rational.

Chapter 2 consists of Energy-Based approach and formulation of the energy balance equation, and methodology of the research as part of the analytical study.

Chapter 3 discusses experimental part of the study including test set-up and experimental results.

Chapter 4 describes the analyses of test results and comparisons between experimental and analytical results. Also, energy spectra (Güllü, 2019) was taken into account and experimental results were verified with this spectrum.

Chapter 5 consists of summary, conclusions and recommendation for future investigations.

2. ENERGY-BASED APPROACH AND ANALYTIC ANALYSIS OF THE RESEARCH

This chapter introduces the energy responses of SDOF systems that are subjected to the ground motion acceleration. It features the definition and derivation of energy terms using energy balance equation of SDOF systems.

2.1. Energy Balance Equation

There is an important concern for formulating the effects of the ground motion on the structures since the equation of motion defining SDOF systems could be expressed in two ways. First one is the displacement of the system with respect to the resting point on the ground (absolute motion terms) and second way is from the point of initial position at rest (relative motion terms). The only difference between these two approaches could be observed at the terms that include mass of the system.

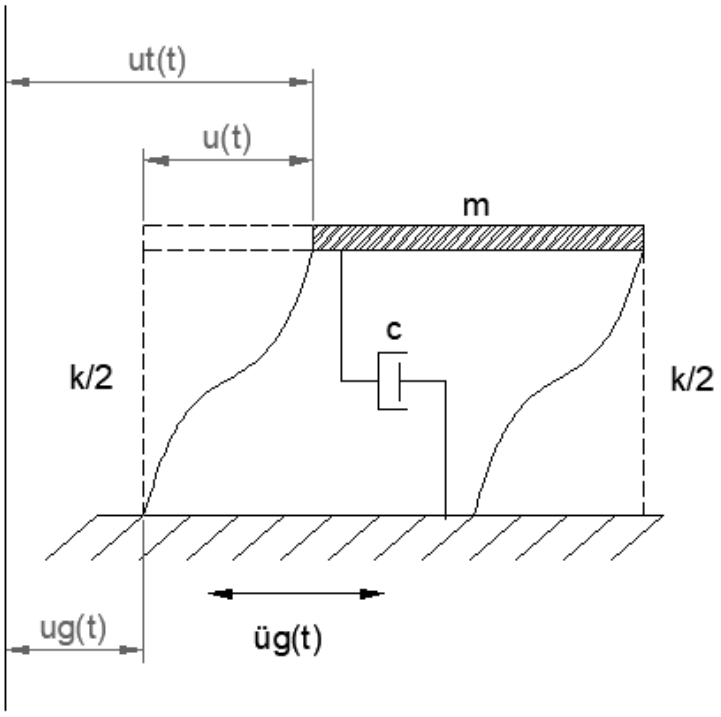

Figure 2.1. SDOF System subjected to Ground Motion.

It is assumed that the structure could be described by the SDOF equation of motion (Chopra, 1995):

$$m\ddot{u}_t(t) + c\dot{u}(t) + f_s(u(t), \dot{u}(t)) = 0 \tag{2.1}$$

where m, c, f_s are the mass, damping coefficient of the system and the spring force, respectively. The terms $\ddot{u}_t(t)$, $\dot{u}(t)$ and $u(t)$ are the time-histories of total acceleration, relative velocity and relative displacement of the system, respectively. Also, $\ddot{u}_t(t)$ is the total acceleration, as expressed by Equation 2.2, consists of $\ddot{u}_g(t)$ (ground acceleration) and $\ddot{u}(t)$ (relative acceleration) of the SDOF systems.

$$\ddot{u}_t(t) = \ddot{u}_g(t) + \ddot{u}(t) \tag{2.2}$$

Thus, using Equation 2.2, Equation 2.1 could be rewritten as;

$$m\ddot{u}(t) + c\dot{u}(t) + f_s(u(t), \dot{u}(t)) = -m\ddot{u}_g(t) \tag{2.3}$$

where $\ddot{u_g}(t)$ indicates the static equivalent lateral force. where $m\ddot{u}(t)$ is the inertia force due to the mass, $c\dot{u}(t)$ is damping force due to the internal friction, $f_s(u(t), \dot{u}(t))$ is the restoring force of the system. Also, $f_s(u(t), \dot{u}(t))$ may be expressed as for a linear elastic system where k is the stiffness. Therefore, Equation 2.3 becomes;

$$m\ddot{u}(t) + c\dot{u}(t) + ku(t) = -m\ddot{u}_g(t) \tag{2.4}$$

During ground motion excitation, the equation of motion of SDOF system represents the response of the structure in terms of displacement, velocity and acceleration. The external and internal forces subjected to ground motion are in balance at any time instance of its duration, so the work done by internal and external forces should also stay in balance during ground motion duration (Akiyama, 1985).

2.1.1. Derivation of Absolute and Relative Energy Equations

There are two types of energy equations to study SDOF systems excited by earthquake ground motions according to Uang and Bertero (1988); absolute and relative energy equations. The formulation of these approaches result the same except from the input and kinetic energy. Taking integration of Equation 2.1 with respect to the relative displacement of $u(t)$ of the system, energy balance equations could be determined as;

$$\int m\ddot{u}(t)du + \int c\dot{u}(t)du + \int f_s du = 0 \tag{2.5}$$

If the Equation 2.5 rewritten by taking $u_t(t) = u(t) + u_g(t)$ the result becomes as follows:

$$\int m\ddot{u}_t(t)du_t + \int c\dot{u}(t)du + \int f_s du = \int m\ddot{u}_t du_g \tag{2.6}$$

The Equation 2.6 is named the Absolute Energy Equation where the terms, from left to right of the equation, are Absolute Kinetic Energy, Damping Energy, Absorbed Energy and Absolute Input Energy, respectively. Therefore, Equation 2.6 could also be rewritten as in form of;

$$E_k + E_d + E_a = E_I \tag{2.7}$$

where Absorbed Energy, E_a, contains both Elastic Strain Energy and Plastic Strain Energy, E_p, which is dissipated during inelastic deformation of the system. Thus,

$$E_a = E_s + E_p \tag{2.8}$$

where E_s is the Elastic Strain Energy and E_p is the Plastic Strain Energy.

However, the integration of Equation 2.3 instead of Equation 2.1 with respect to the relative displacement $u(t)$ of the system generates another form of energy balance

equation as the following;

$$\int m\ddot{u}(t)du + \int c\dot{u}(t)du + \int f_s du = -\int m\ddot{u}_g(t)du \tag{2.9}$$

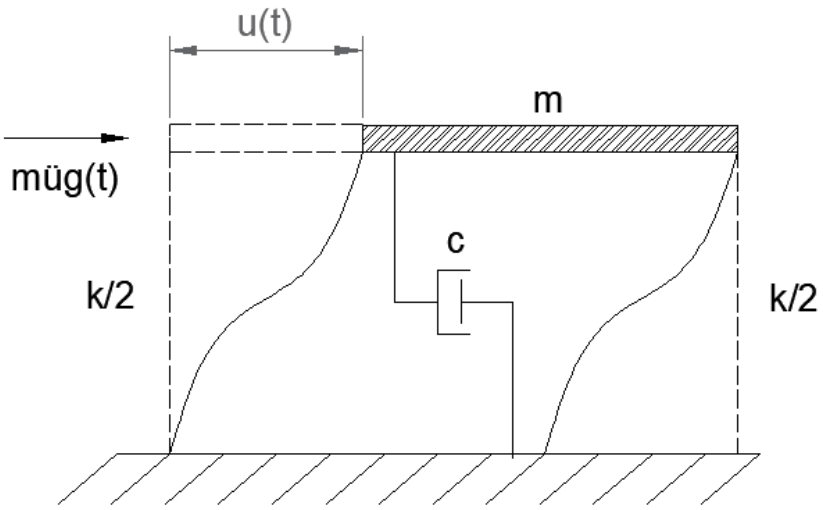

Figure 2.2. Fixed-Based SDOF System.

The equation 2.9 is defined as Relative Energy Equation, where $\int m\ddot{u}(t)du$ represents the Relative Kinetic Energy term, $\int c\dot{u}(t)du$ represents the Damping Energy term, $\int f_s du$ represents Absorbed Energy term, and $\int m\ddot{u}_g(t)du$ represents Relative Input Energy term, which is the work done by the equivalent lateral force of $-m\ddot{u}_g$ as shown in Figure 2.1.

Thus, Relative Energy Equation could be re-expressed as;

$$E'_k + E_d + (E_s + E_p) = E'_I \tag{2.10}$$

where E'_k is the Relative Kinetic Energy, E_d is the Damping Energy, E_s is the Elastic Strain Energy, E_p is the Plastic Strain Energy and E'_I is the Relative Input Energy, respectively.

In this research, the relative energy terms will be used. Thus, relative energy terms will be shown as E'_k, E'_I, instead of E_k, E_I.

2.2. Concept and Formulation of Energy Components

Energy terms represent a certain physical characteristics of a structure. The Input Energy consists of two terms; recoverable and irrecoverable energies which are imparted into the structure, as in Figure 2.3.

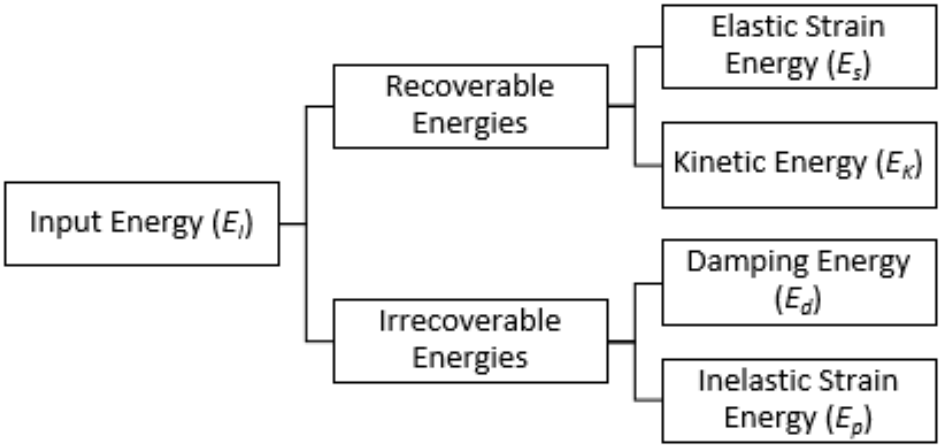

Figure 2.3. Energy Components (Dindar, 2009).

The Elastic Strain Energy and Kinetic Energy occur during the main excitation and then come to zero at the end of the duration. On the other hand, the Damping Energy and Inelastic Strain Energy increase during vibration of the ground. Thus, the Elastic Strain Energy and Kinetic Energy are recoverable while Damping Energy and Inelastic Strain Energy are irrecoverable.

A brief definition of each energy terms in Equation 2.9 and their derivations explained separately in the following subsections.

2.2.1. Input Energy

The physical meaning of relative Input Energy is the work done by the equivalent lateral force $-m\ddot{u}_g$ on the system. It could be derived from the right hand side of the relative energy equation.

$$E_I = -\int m\ddot{u}_g(t)du = -\int m\ddot{u}_g(t)du \times \frac{dt}{dt} = -m\int \ddot{u}_g(t)\dot{u}dt \tag{2.11}$$

2.2.2. Kinetic Energy

Kinetic Energy is defined as energy of motion. The related formulation could be derived from the first component of the left hand side of the Equation 2.9.

$$E_k = \int m\ddot{u}du = \int m\ddot{u}\frac{dt}{dt}du = \int m\ddot{u}\dot{u}dt = \int m\dot{u}\frac{d\dot{u}}{dt}dt = m\int \dot{u}d\dot{u} = \frac{m\dot{u}^2}{2} \tag{2.12}$$

2.2.3. Damping Energy

Energy dissipating mechanism of a structure under dynamic loading is defined as damping. It could be derived from the second component of the left side of the Relative Energy equation.

$$E_d = \int c\dot{u}du\frac{dt}{dt} = c\int \dot{u}^2dt \tag{2.13}$$

2.2.4. Absorbed Energy

Absorbed Energy consists of Elastic Strain Energy and Plastic Strain Energy, as shown in Figure 2.4. It could be derived from the third component of the left side of

the Equation 2.9.

$$E_a = \int f_s(t)du = \int f_s(t)du \times \frac{dt}{dt} = \int f_s(t)\dot{u}dt \tag{2.14}$$

The Elastic Strain Energy which is described as the total work done on the system in linear deformations can be formulated as;

$$E_s = \frac{(f_s(t))^2}{2k} \tag{2.15}$$

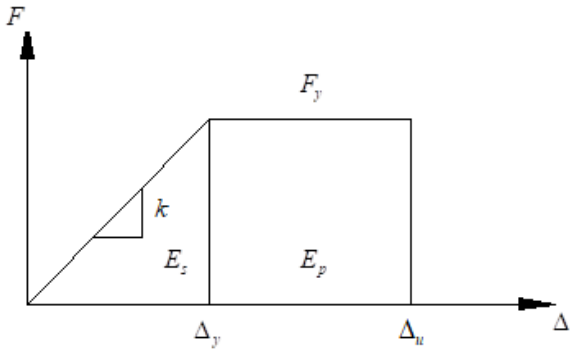

Figure 2.4. Elastic and Inelastic Strain Energies.

Up to the inelastic region, Strain Energy is equal to the area below the force-displacement relationship in Figure 2.4.

$$E_s = \frac{1}{2}F\Delta = \frac{1}{2}k\Delta^2 \tag{2.16}$$

Plastic Strain Energy is the amount of dissipated energy depending upon plastic deformations of the system. It equals to the energy balance equation when other energy components were subtracted. The general formulation for Plastic Strain Energy, as follows;

$$E_p = E_I - (E_k + E_d + E_s) \tag{2.17}$$

2.3. Analytical Study of the Research

2.3.1. Logarithmic Decrement Method

For underdamped systems, decrease in two successive peaks of free vibration defines damping ratio of the system.

$$m\ddot{u} + c\dot{u} + ku = 0 \tag{2.18}$$

The solution to Equation 2.18 is subjected to initial conditions ($u = u(0), \dot{u} = \dot{u}(0)$) for underdamped systems with or $c < c_{cr}$ is $\zeta < 1$

$$u(t) = e^{-\zeta w_n t}[u(0)\cos w_D t + (\frac{\dot{u}(0) + \zeta w_n u(0)}{w_D})\sin w_D t] \tag{2.19}$$

where

$$w_D = w_n\sqrt{1-\zeta^2} \tag{2.20}$$

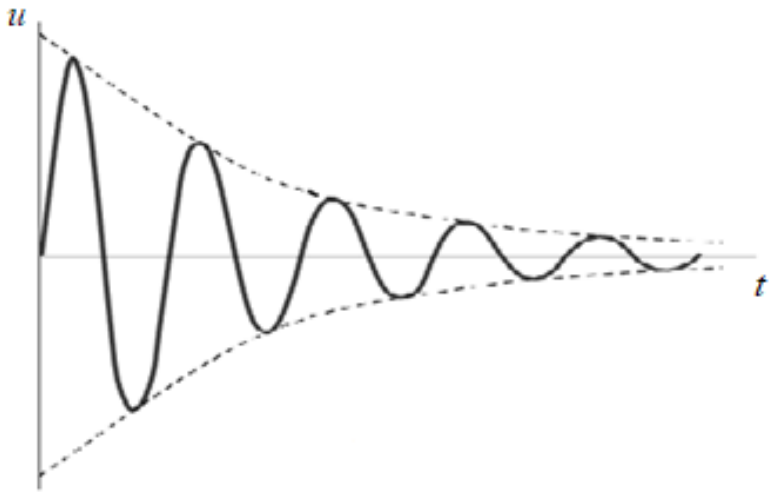

Figure 2.5. Decay of Motion.

Derivation of Equation 2.19 gives the ratio of the displacement at time t to the total time of the period t_D and t.

$$\frac{u(t)}{u(t+T_D)} = \exp(\zeta w_n T_D) = \exp(\frac{2\pi\zeta}{\sqrt{1-\zeta^2}}) \tag{2.21}$$

Equation 2.21 could be written as;

$$\frac{u_i}{u_{i+1}} = exp(\frac{2\pi\zeta}{\sqrt{1-\zeta^2}}) \tag{2.22}$$

where the natural period of the system t_n and period of the system T_D are;

$$T_n = \frac{2\pi}{w_n} \tag{2.23}$$

$$T_D = \frac{T_n}{\sqrt{1-\zeta^2}} \tag{2.24}$$

Logarithmic decrement, in other words, the natural *logarithm* of the ratio of any two successive amplitudes could be written as;

$$\delta = \ln\frac{u_i}{u_{i+1}} = \frac{2\pi\zeta}{\sqrt{1-\zeta^2}} \tag{2.25}$$

If ζ is too small $\sqrt{1-\zeta^2} \simeq 1$, Equation 2.25 could be rewritten as;

$$\delta \simeq 2\pi\zeta \tag{2.26}$$

For lightly damped systems, instead of the ratio between two successive peaks, the ratio of successive peaks of several cycles can be used to calculate damping ratio.

$$\frac{u_1}{u_{j+1}} = \frac{u_1}{u_2}\frac{u_2}{u_3}\frac{u_3}{u_4}...\frac{u_j}{u_{j+1}} = e^{j\zeta} \tag{2.27}$$

where j is the number of cycles (Chopra, 1995).

2.3.2. Chopra's Method

Viscous damping dissipates energy in one cycle of harmonic vibration. This energy (Damping Energy) could be written as;

$$E_D = \int f_D du = \int_0^{2\pi/w} (c\dot{u})\dot{u}dt = \int_0^{2\pi/w} c\dot{u}^2 dt \tag{2.28}$$

On the other hand, Potential Energy which is equal to the Strain Energy of the spring could be formulated as;

$$E_S = \int_0^{2\pi/w} k[u_o \sin(wt-\varphi)][wu_0 \cos(wt-\varphi)]dt = 0 \tag{2.29}$$

For graphical interpretation of energy dissipation in viscous damping, equation related to the damping force and the displacement are derived as;

$$f_D = cw\sqrt{u_0^2 - u_0^2 \sin^2(wt-\varphi)} = cw\sqrt{u_0^2 - [u(t)]^2} \tag{2.30}$$

This equation (shown in Figure 2.6) could be re-expressed as;

$$(\frac{u}{u_0})^2 + (\frac{f_D}{cwu_0}) = 1 \tag{2.31}$$

It is obvious that Equation 2.31 not a single-valued function but a loop. This loop known as hysteresis loop gives the dissipated energy.

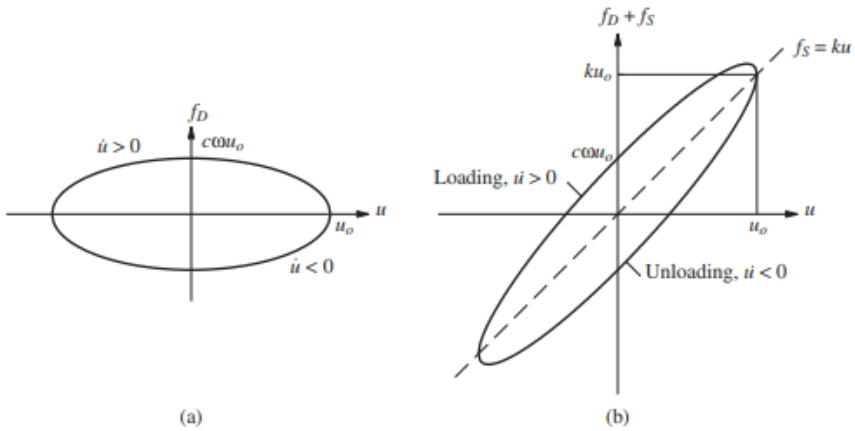

Figure 2.6. Hysteresis loops for viscous damper (Chopra, 1995).

In experiment, the total resisting force formed by elastic and damping force are considered as;

$$f_S + f_D = ku(t) + c\dot{u}(t) = ku + cw\sqrt{u_0^2 - u^2} \tag{2.32}$$

Figure 2.7 shows that $f_s + f_D$ against u, which is the rotated version of Figure 2.6.

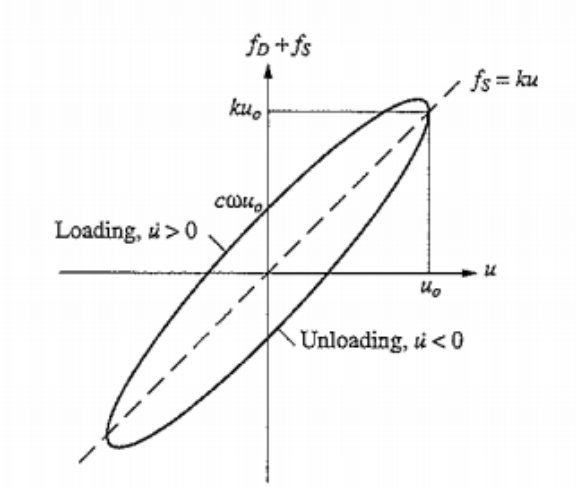

Figure 2.7. Hysteresis loop for spring and viscous damper (Chopra, 1995).

Equivalent viscous damping is generally used to represent damping in actual

structures. It could be calculated by energy dissipation of the system. Under cyclic loading, force-deformation curve acquired from an experiment is shown in Figure 2.8. E_D is the dissipated energy enclosed by a particular hysteresis loop. Equating E_D to the energy dissipated in viscous damping given by Equation 2.28 leads to;

$$4\pi\zeta_{eq}\frac{w}{w_n}E_{So} = E_D \text{or} \zeta_{eq} = \frac{1}{4\pi}\frac{1}{w/w_n}\frac{E_D}{E_{So}} \tag{2.33}$$

which is $w = w_n E_{So} = ku_0^2/2$

when $w = w_n$, Equation 2.33 becomes;

$$\zeta_{eq} = \frac{1}{4\pi}\frac{E_D}{E_{So}} \tag{2.34}$$

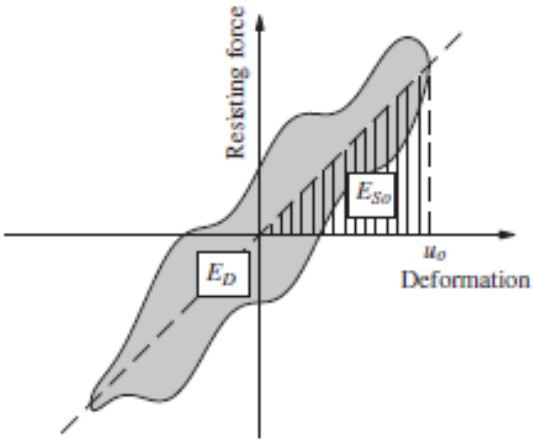

Figure 2.8. Energy dissipated E_D in a cycle of harmonic vibration determined from experiment (Chopra, 1995).

2.3.3. Material Behavior Model

There have been quite a number of research done on numerical constitutive models over the years. They define how the system responds under cyclic loading. These constitutive models split into different groups: flexure with pinching, flexure with slip, and shear models. Among all the models existed, Takeda and Clough models are the most common ones. The representation of these constitutive models are shown in

Figure 2.9. Using elastic-perfectly plastic model is the most convenient way to calculate energy components of steel structures because hysteretic behavior of the system could be described more realistically (Dindar, 2009). Elastic-perfectly plastic model is shown in Figure 2.10.

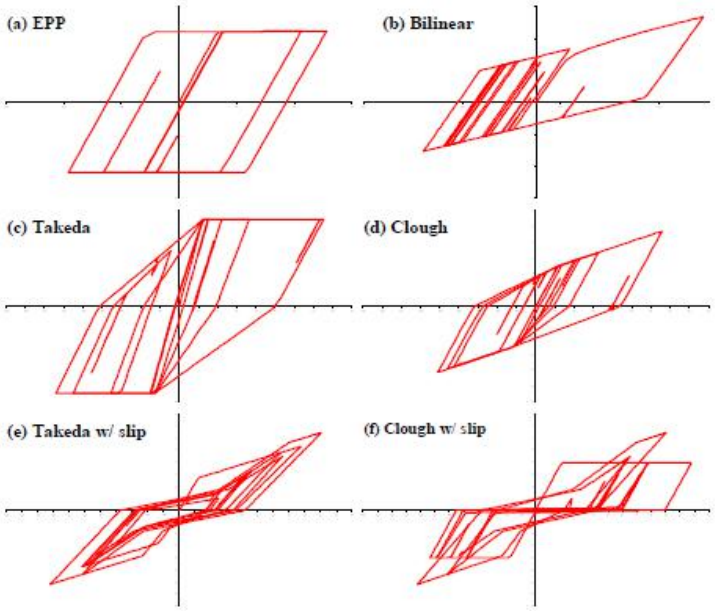

Figure 2.9. Constitutive Behavior Models (Dindar, 2009).

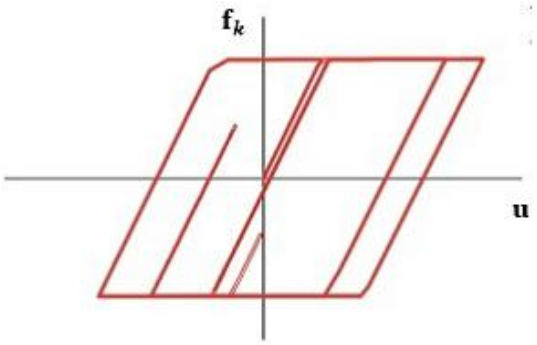

Figure 2.10. Elastic-Perfectly Plastic Constitutive Model (Dindar, 2009).

In this study, steel specimen is used to investigate numerical and experimental analysis of this research. Three identical steel specimens were used. Table 2.1 shows the dimension of these specimens.

Table 2.1. Dimensions of Three Specimens.

h (depth)	40 mm
b (width)	20 mm
t (thickness)	1.0 mm
L (length)	750 mm

Experimental tests on material were carried out to determine the yield and ultimate stresses of these specimens. Universal testing machine was used to examine coupon steel specimens. The machine and specimen are shown in Figure 2.11.

Figure 2.11. Universal Testing Machine.

Ultimate stress f_u, yield stress f_y and modulus of elasticity of material E are displayed in Table 2.2.

Table 2.2. Ultimate and Yield Stress of Coupon Specimens.

Coupon Specimen	f_u **(Mpa)**	f_y **(Mpa)**
1	446	415
2	442	410
3	441	411

These material characteristics were used in both SAP2000 model and Matlab code. Figure 2.12 shows the data obtained from experimental study.

Figure 2.12. Data obtained from Universal Testing Machine.

2.3.4. Numerical Model and Analysis

Numerical model analysis was performed in SAP2000 software. Material properties of steel specimens were determined according to the material coupon tests. Steel hollow section cantilever columns were then modelled in SAP2000 Structural Analysis software. Figure 2.13 illustrates the dimension of the specimens. Table 2.3 and Table 2.4 shows the material properties that are used in SAP2000 models.

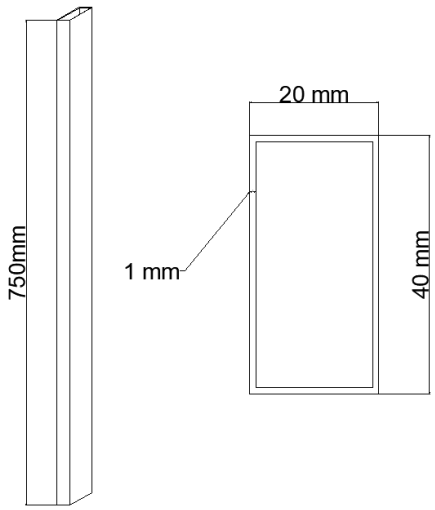

Figure 2.13. Steel hollow section specimen.

Table 2.3. Characteristics of the Specimens.

Specimen	**Height (mm)**	**Width (mm)**	**Thickness (mm)**	**Length (m)**	f_u **(Mpa)**	f_y **(Mpa)**	**E (Mpa)**
1	40	20	1	0.75	446	415	179800
2	40	20	1	0.75	442	410	190000
3	40	20	1	0.75	441	411	187000

Table 2.4. Periods and Masses of the Specimens.

Specimen	**T (s)**	**Mass (kg)**
1	0.500	62
2	0.667	87
3	1.000	186.6

San Salvador earthquake ground motion was used for all the analyses. Table 2.5 shows the properties of ground motion. Scale factors ranging from 0.20 to 1.60 were applied. All the records with varying scale factors are shown in Figure 2.14 and Figure 2.15.

Table 2.5. Earthquake Record Properties.

Earthquake	San Salvador
PGA (g)	0.148
Record Soil Type	B
Duration (s)	9.02

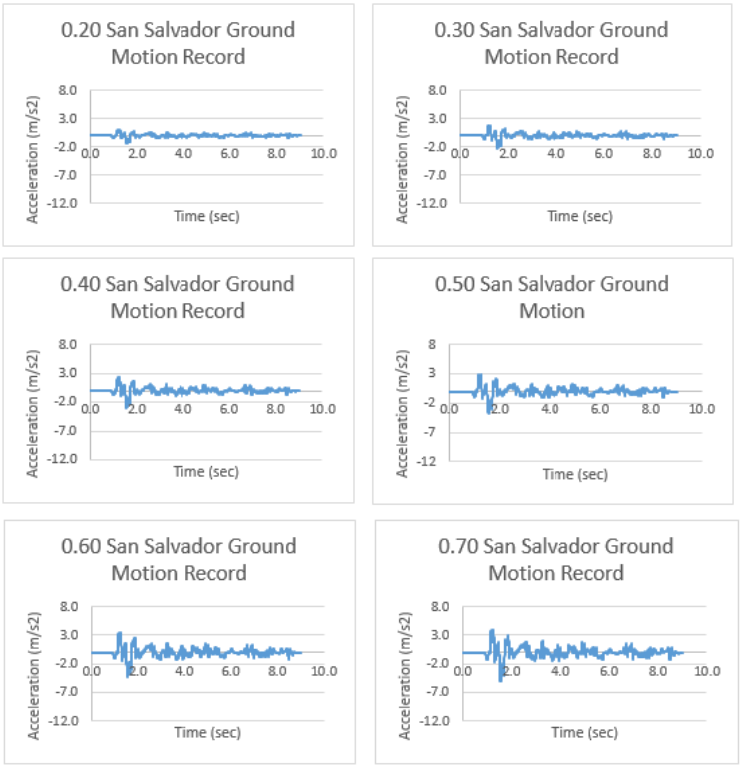

Figure 2.14. Ground Motion Records.

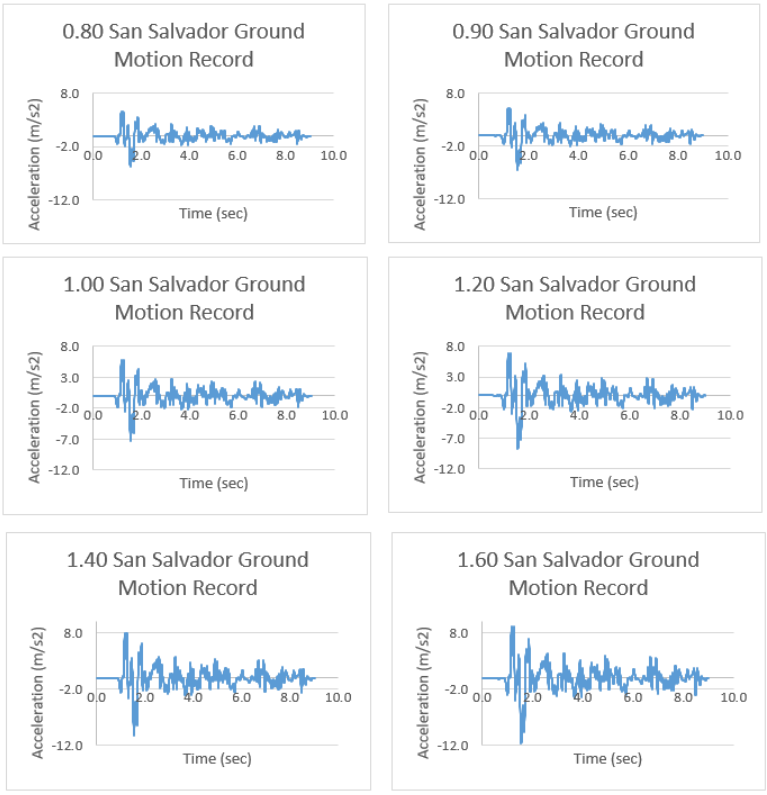

Figure 2.15. Ground Motion Records.

Input energy values calculated from SAP2000 software are shown in Figure 2.16, Figure 2.17 and Figure 2.18. This software only considers elastic behavior for energy calculations.

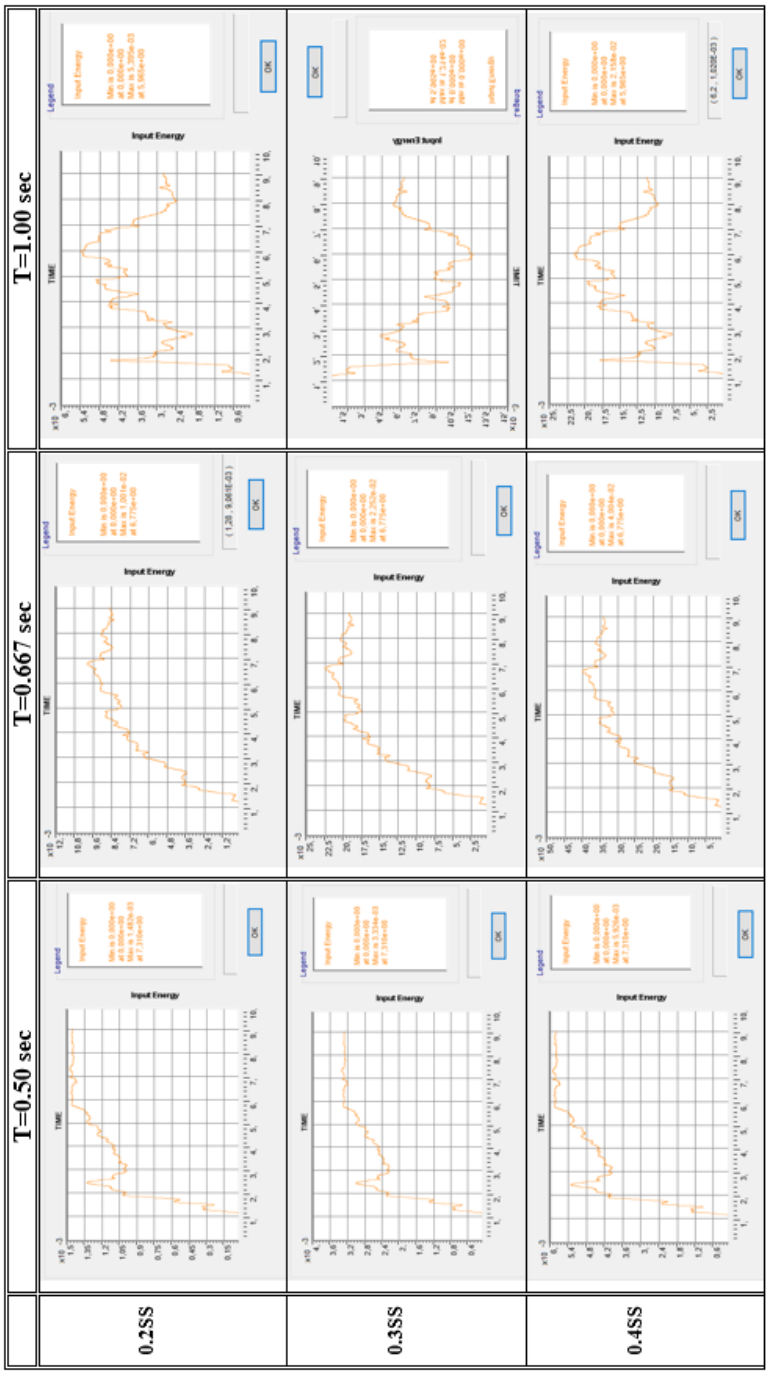

Figure 2.16. Input Energy of San Salvador Earthquake.

Figure 2.17. Input Energy of San Salvador Earthquake.

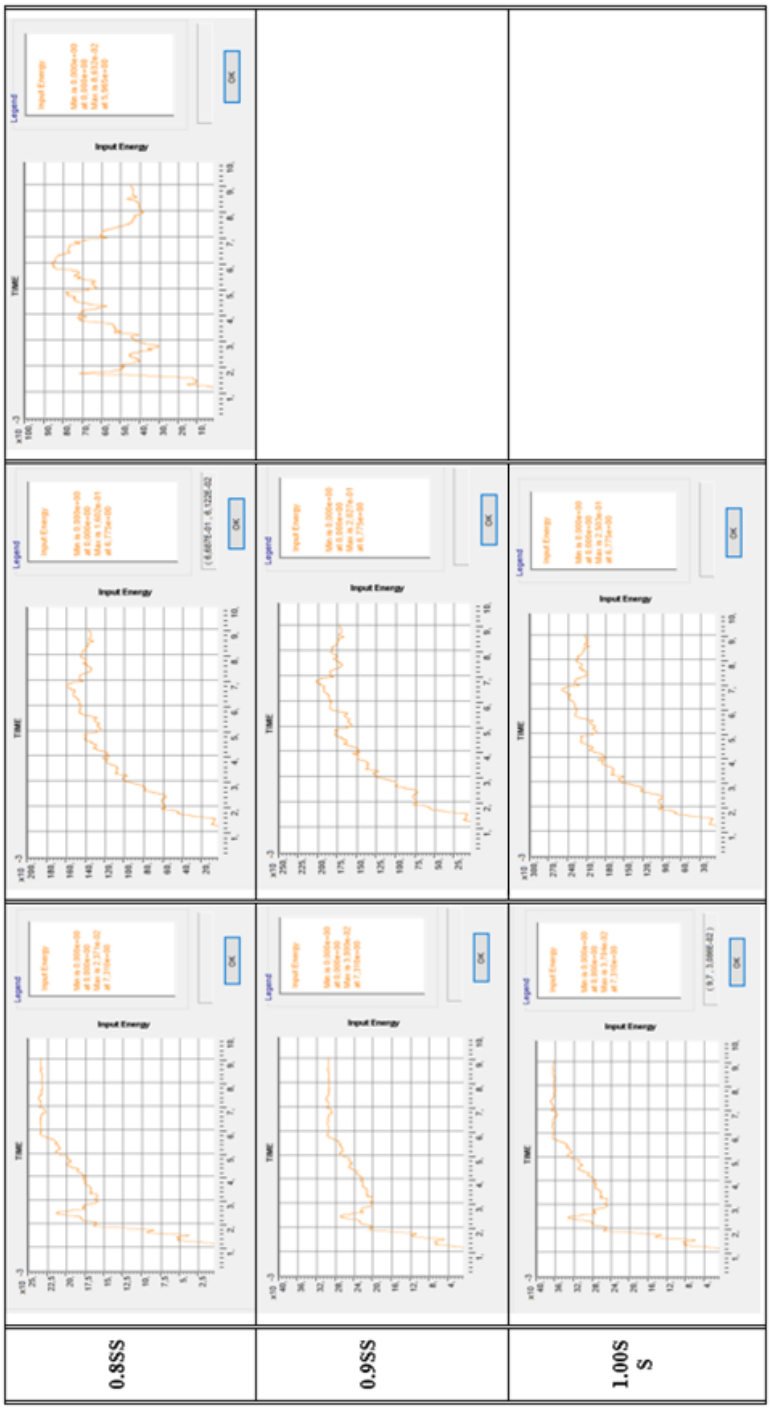

Figure 2.18. Input Energy of San Salvador Earthquake.

2.4. Güllü's Spectra

In 2019, (Güllü, 2019) proposed an improved input energy spectrum verified by the shake table tests. In (Güllü, 2019) study, experimental assessment was conducted

to the existing Dindar *et al.* (Dindar *et al.* 2015) spectra, and further improvements were achieved. This spectrum was experimentally calibrated and numerically verified for numerous near' and far-field type earthquakes. It is basically composed of three parts as illustrated in Figure 2.19. Fourier spectrum or undamped velocity spectrum is used to determine the corner period (T_c). Ordinates of the plateau (section 2) is calculated from Equation 2.35. Section 3 is the descending branch which is created by the term of $(T_c/T)^k$ in Equation 2.35.

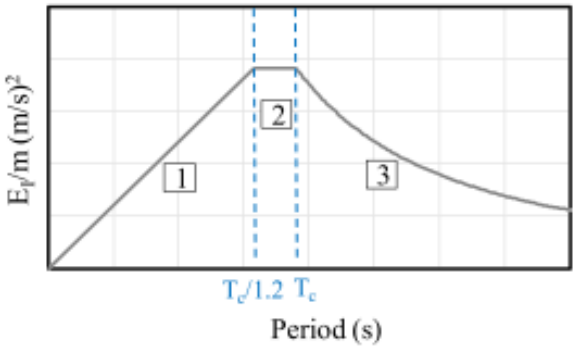

Figure 2.19. Güllü's mass-normalized input energy spectrum (Güllü, 2019).

$$\frac{E_I}{m} = B\sqrt{SV(\xi)_{\max} SA(\xi)_{@SV_{\max}} T_c I_e t_e}(T_c/T)^k \tag{2.35}$$

where $SV(\xi)_{\max} SA(\xi)_{@SV_{\max}} T_c I_e t_e$ are maximum spectral velocity in defined damping, spectral acceleration at the period that corresponds to maximum spectral velocity in defined damping, intensity and effective duration, respectively.

B and k parameters are shown in Table 2.6. These parameters were originated from Dindar *et al.* (Dindar *et al.* 2015) research. In his study, carefully-selected ground motion records were used to express the characteristics of the eartquakes. In total, 228 time histories which consisted of near field and far field type earthquake motion data that were acquired from PEER database to generate Dindar *et al.* (Dindar *et al.* 2015) spectrum and its parameters.

Table 2.6. k and B parameters (Dindar, 2009)

Parameters	**Soil A** **Rock** V_{s30} > **760 m/s**	**Soil B** **Stiff Soil** **760 m/s** > V_{s30} > **360 m/s**	**Soil C** **Soft Soil** **360 m/s** > V_{s30} > **180 m/s**	**Soil D** **Very Soft Soil** V_{s30} > **180 m/s**
B	0.065	0.0705	0.077	0.085
k	0.91	1.095	1.456	1.658

3. EXPERIMENTAL STUDY

This chapter discusses the experimental part of this study. Twenty-eight shake table experiments were completed using San Salvador ground motion data on three identical specimens of cantilever hollow section steel columns. One period was used for each specimen with seven to twelve different scale factors.

3.1. Experimental Study Set Up

Experimental tests aim to verify the inelastic input energy spectrum by finding damping ratio and then input energy of the specimen. Figure 3.1 shows the test set up sketch.

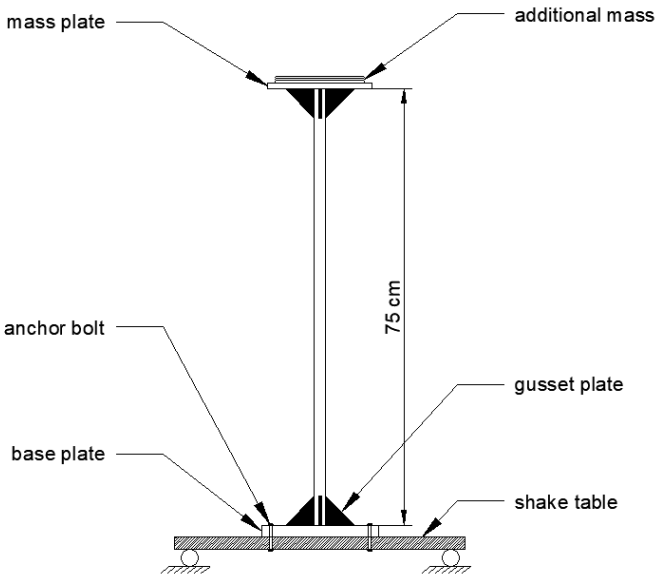

Figure 3.1. Test Set Up Sketch.

The properties of the column shown in Figure 3.2 is a 750mm height with 40/20/1 mm structural hollow section steel.

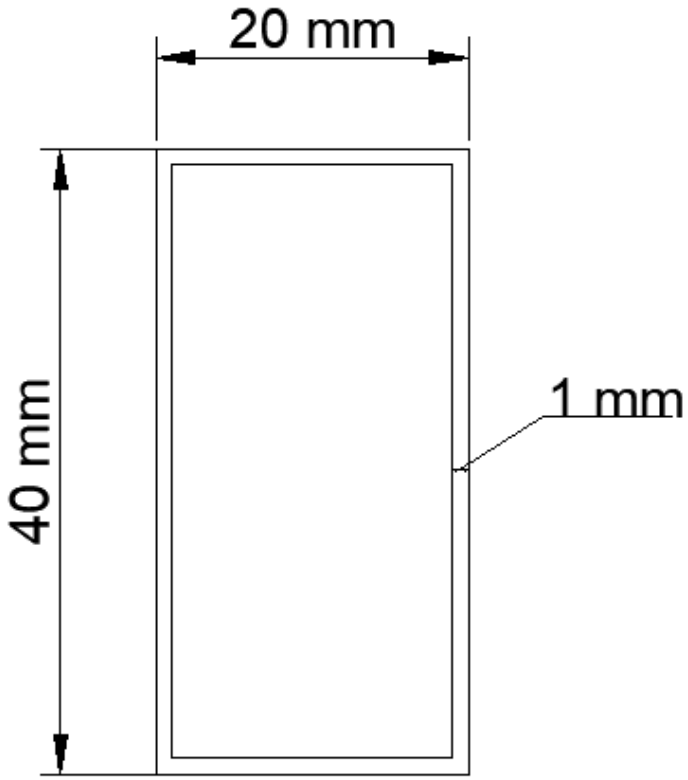

Figure 3.2. Structural Hollow Section.

Material properties of used three specimens are listed in Table 3.1 L is the length of the material, b is the width, h is the height and t is the thickness of the 40/20/1 hollow section steel specimen, and E is the modulus of elasticity of the material.

Table 3.1. Material Properties of the 40/20/1 Specimens.

Specimen	40/20/1
Material	Steel
Weight(kg)	5.0
L (m)	0.75
b (m)	0.02
h (m)	0.04
t (m)	0.001
E (MPa)	200000

Specimen properties of these three specimens are shown in Table 3.2 L is the height, I is the moment of inertia, and k is the initial stiffness of the specimen.

Table 3.2. Specimen Properties.

T (sec)	**L (m)**	**I (m^4)**	**k (N/m)**
0.500	0.75	8.1987 x 10^{-9}	10785.8
0.667	0.75	8.1987 x 10^{-9}	10785.8
1	0.75	8.1987 x 10^{-9}	10785.8

Two accelerometers and four strain gauges were used in this study. Figure 3.3 depicts the specimen with sensors. One of the accelerometer was installed on the top of the specimen, the other one on the shake table. Figure 3.4 shows the location of the accelerometers. Two of the strain gauges were placed at front of the column, two of them were placed at back of the column. Strain gauges on the specimen shown in the Figure 3.5.

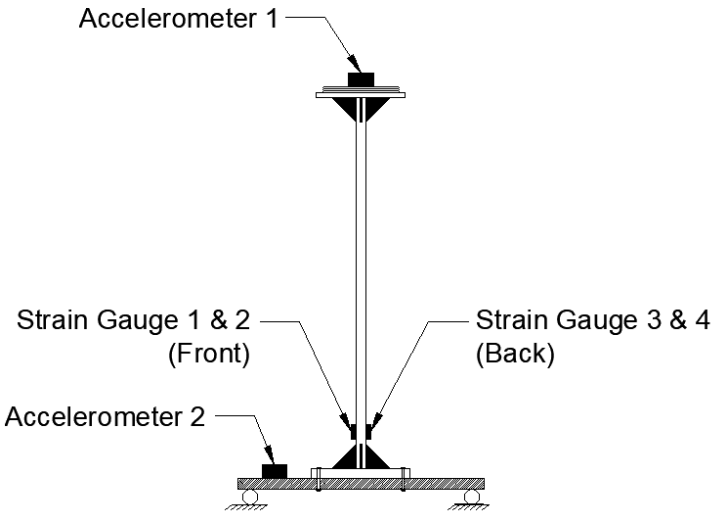

Figure 3.3. Specimen with Sensors.

Figure 3.4. Location of the accelerometers.

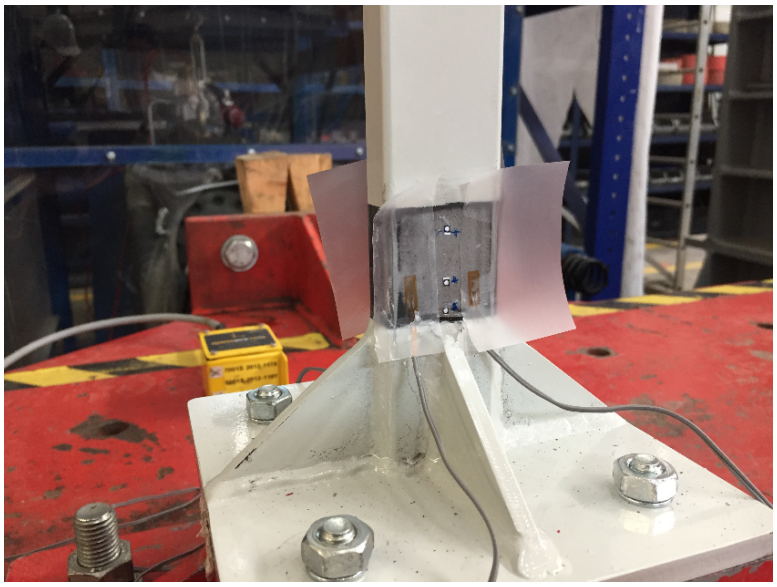

Figure 3.5. Strain Gauges on the specimen.

3.2. Experimental Study Process

Before the main tests, sensors (accelerometers and strain gauges) were checked by generating free vibration on specimens. After testing the sensors, experiments began with 40/20/1 structural hollow section steel specimen. Three identical specimens were used. Only one period was performed on each specimen. The period of test specimens were adjusted to 0.50 sec, 0.667 sec, 1.00 sec. Experimental test setups for each specimen are shown in Figure 3.6. For each period, mass of the SDOF system was calculated and mounted on top of the column. Figure 3.7 shows the frequency check for each period. Masses were adjusted gradually until the exact period was obtained.

Besides all the sensors, image processing data also obtained for these experiments.

Figure 3.6. Experimental Test Set Up.

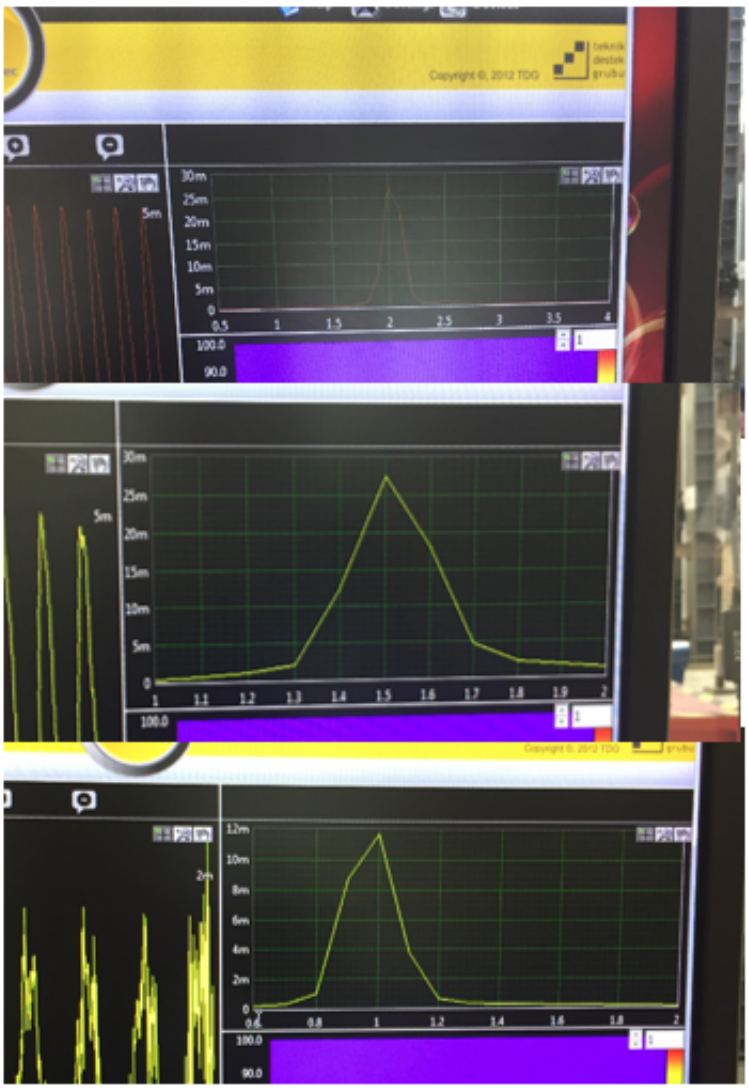

Figure 3.7. Frequency Control.

This experimental tests were performed on the shake table at Structural and Earthquake Laboratory of Istanbul Technical University. The constraints of the shake table were;

Displacement capacity: 32.5 cm.

Velocity capacity: 100 cm/s.

Acceleration capacity: 2 g.

Figure 3.8 displays the experimental test program.

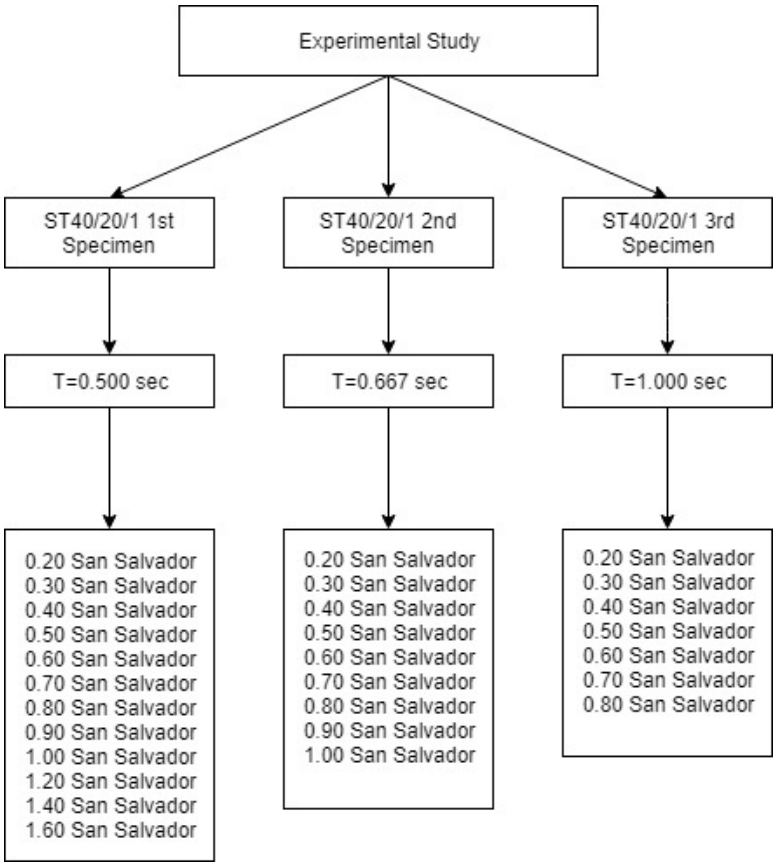

Figure 3.8. Experimental Study Program.

3.3. Data Obtained from Each Experiment

All data obtained from the experiments could be found in Appendix A.

3.4. Data Comparison

In this section, various data sources obtained from experiments were compared in order to get sensible data to be used in the analyses. Three different data sources were used to experimentally determine the responses of the specimens. The displacement response data was obtained from strain gauges that were mounted at the bottom of the column, acceleration response data was obtained from accelerometers that were placed on top of the specimen and also on the shaking table, and displacement response data was obtained from video recording to be used in image processing.

First data source was the strain gauge readings. Relative displacements were calculated using basic structural mechanics theory. After calculating the neutral axis from strain readings, forces perpendicular to the cross section were calculated, and then the moments were determined. Knowing the cantilever length of the column, lateral forces on top of the specimen that cause these moments were calculated. Taking into account of the axial load applied on the specimen, displacements were calculated including the $P-\Delta$ effect. Using mathematical derivation process, relative velocity and relative acceleration were calculated. A source code was developed for that purpose. Calculation procedure is described below.

Primarily, displacement should be obtained from strain data. Figure 3.5 shows the basic principle of the approach (Güllü, 2019).

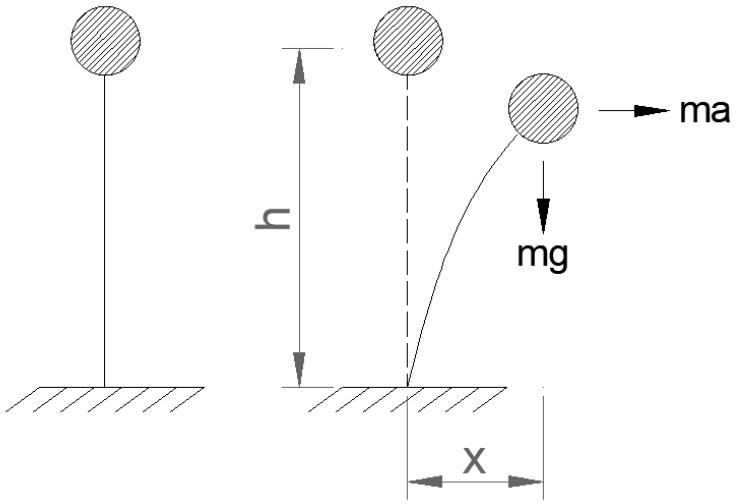

Figure 3.9. Fixed-Based SDOF System.

$$\sigma = \frac{My}{I} \tag{3.1}$$

If the Equation 3.1 rewritten by taking $I0Ay^2$, the result becomes as;

$$\sigma = \frac{M}{Ay} \tag{3.2}$$

So, moment can be re-expressed as;

$$M = \sigma A y \tag{3.3}$$

$P - \Delta$ effect, also known as second order effect, was taken into account to calculate the displacement.

$$M = kx + mgx \tag{3.4}$$

Equation 3.4 can also be rewritten by taking $k = \frac{3EI}{h^3}$ as;

$$u = -\frac{Mh^2}{3EI + mgh^2} \tag{3.5}$$

Then, displacement data were derived to obtain velocity and acceleration with using Savitzy-Golay filter which smooth noisy data. Matlab code were utilized to use this digital filter.

Secondly, accelerometers were used to measure table acceleration and specimen's top acceleration. Here, using mathematical integral operations and difference between specimen and table accelerations, relative velocity and relative displacements were calculated.

Firstly, to obtain relative acceleration, table acceleration data is subtracted from top acceleration data shown in Equation 3.6.

$$\ddot{u}_{rel} = \ddot{u}_{top} - \ddot{u}_{ground} \tag{3.6}$$

After that, since acceleration is first derivative of velocity, the integral of the

acceleration over time gives the velocity as;

$$\dot{u}_{rel} = \int \ddot{u}_{rel} dt \tag{3.7}$$

Likewise, since velocity is first derivative of displacement, the integral of the acceleration over time gives the displacement as;

$$u_{rel} = \int \dot{u}_{rel} dt \tag{3.8}$$

Displacement data obtained by taking an integral twice was not used in this study because it was noisy.

As a third data source, image processing method was used to collect relative and table displacement data. Image processing software, developed by (Yardimci, 2018), relative displacement, relative velocity and relative acceleration responses were determined. Image processing data was only available for 16 out of 28 experiments. Section 3.4.1 through Section 3.4.28 represent the data compared from experiments.

3.4.1. T=0.5 sec, 0.20 San Salvador

Comparison of relative displacements and relative accelerations are shown in Figure 3.10 and Figure 3.11, respectively.

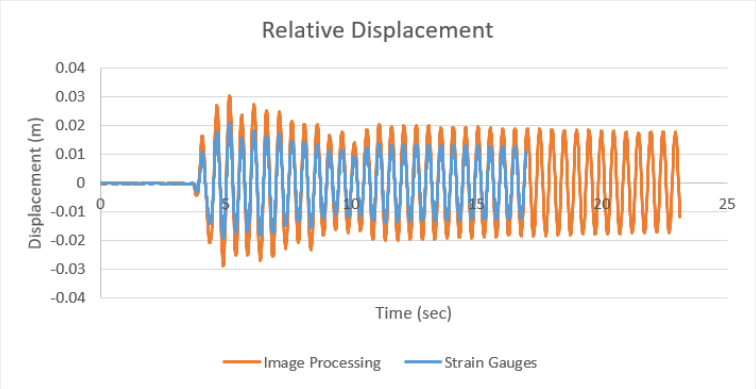

Figure 3.10. Relative Displacement Comparison.

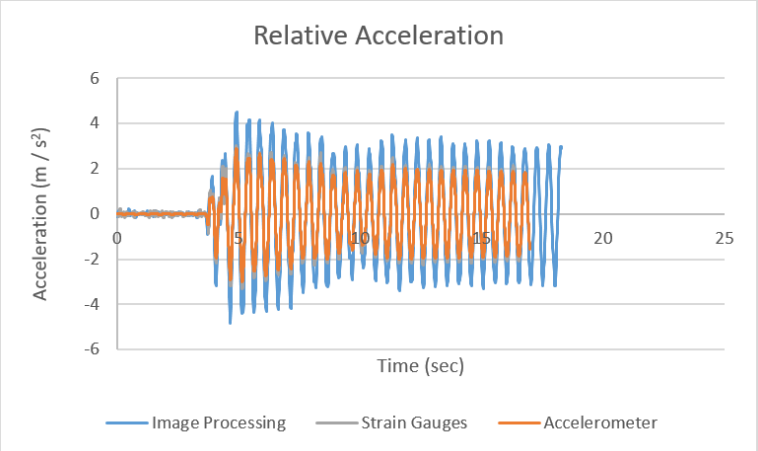

Figure 3.11. Relative Acceleration Comparison.

3.4.2. T=0.5 sec, 0.30 San Salvador

Comparison of relative displacement and relative acceleration are shown in Figure 3.12 and Figure 3.13, respectively.

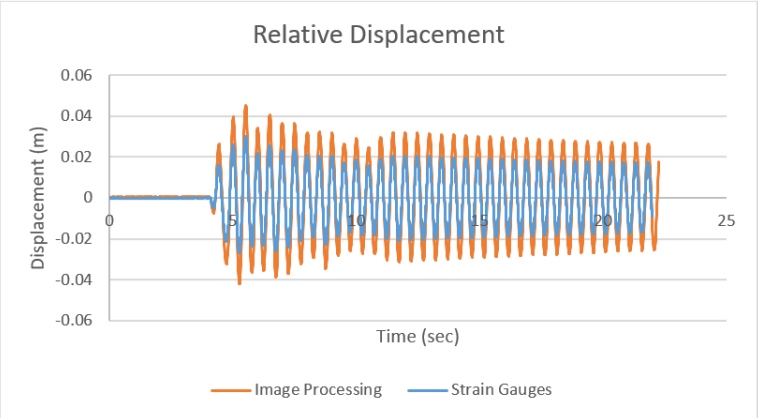

Figure 3.12. Relative Displacement Comparison.

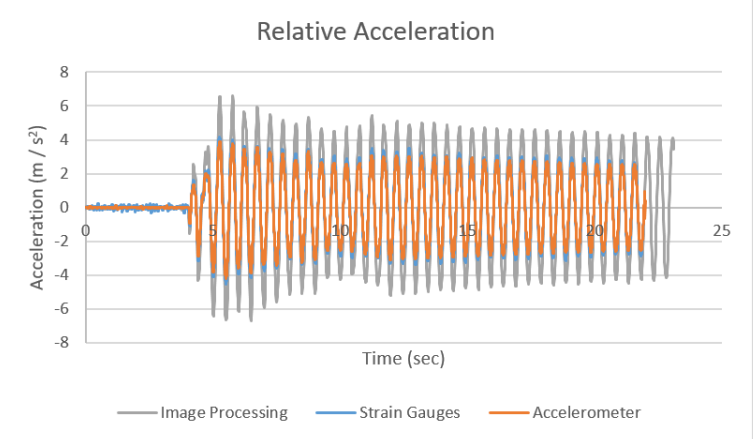

Figure 3.13. Relative Acceleration Comparison.

3.4.3. T=0.5 sec, 0.40 San Salvador

Comparison of relative displacement and comparison of relative acceleration is shown in Figure 3.14 and Figure 3.15, respectively.

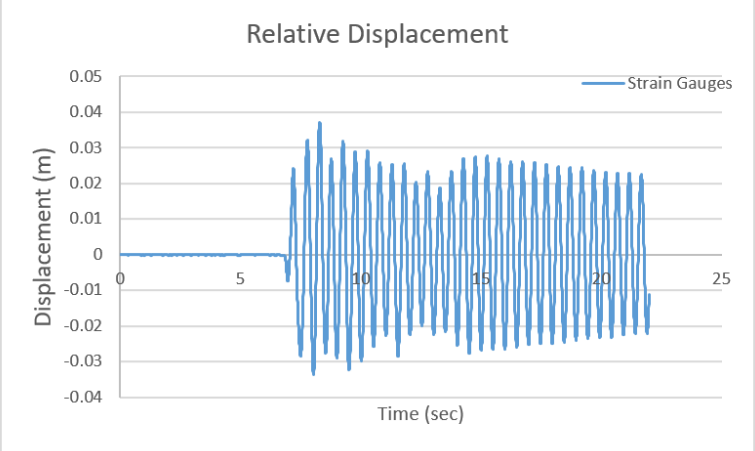

Figure 3.14. Relative Displacement Comparison.

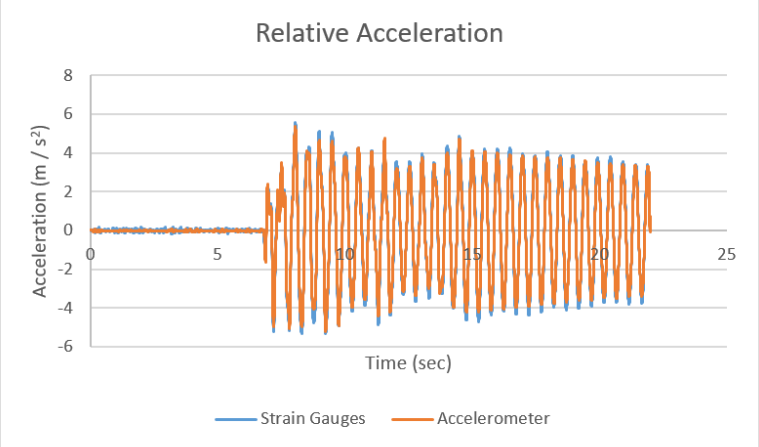

Figure 3.15. Relative Acceleration Comparison.

3.4.4. T=0.5 sec, 0.50 San Salvador

Comparison of relative displacement and comparison of relative acceleration is shown in Figure 3.16 and Figure 3.17, respectively.

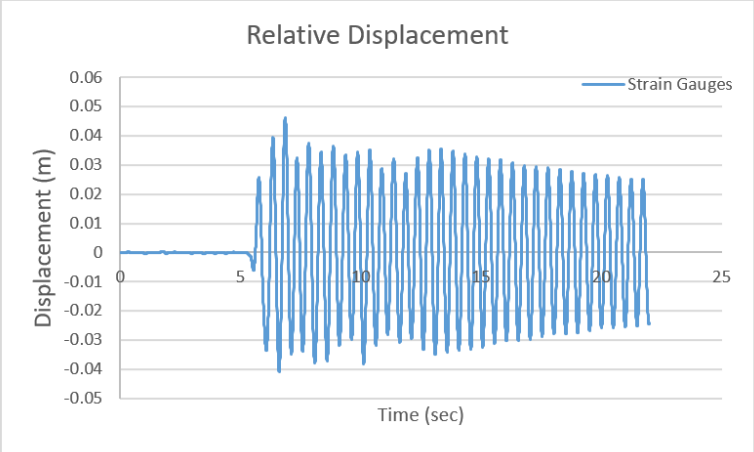

Figure 3.16. Relative Displacement Comparison.

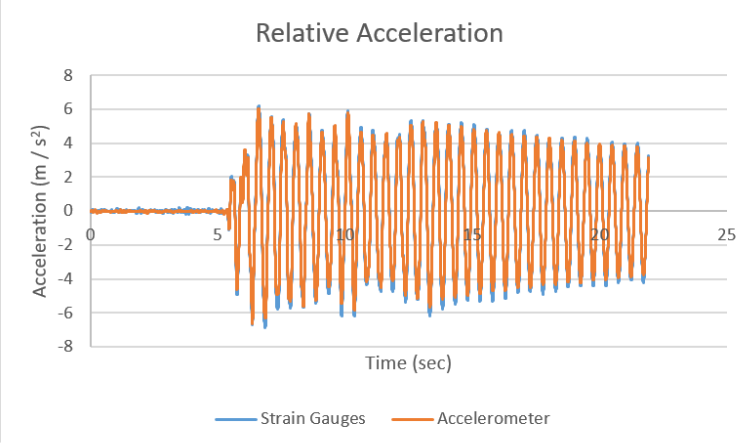

Figure 3.17. Relative Acceleration Comparison.

3.4.5. T=0.5 sec, 0.60 San Salvador

Comparison of relative displacement and comparison of relative acceleration is shown in Figure 3.18 and Figure 3.19, respectively.

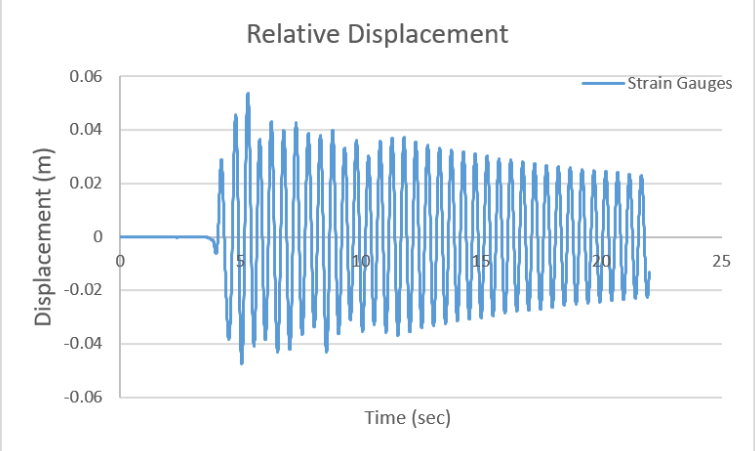

Figure 3.18. Relative Displacement Comparison.

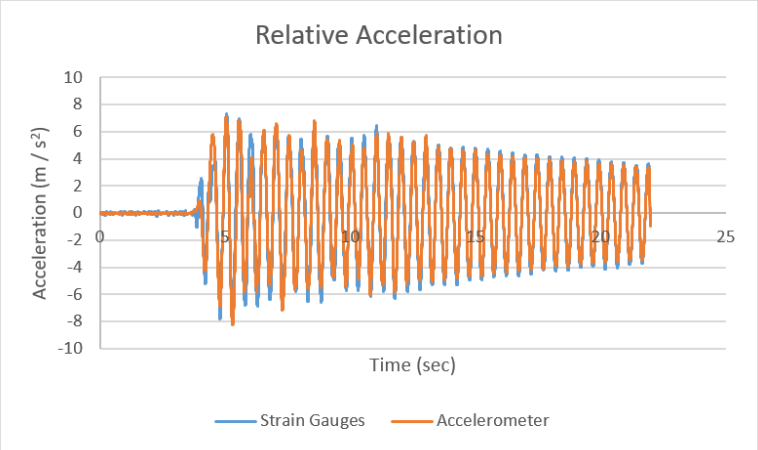

Figure 3.19. Relative Acceleration Comparison.

3.4.6. T=0.5 sec, 0.70 San Salvador

Comparison of relative displacement and comparison of relative acceleration is shown in Figure 3.20 and Figure 3.21, respectively.

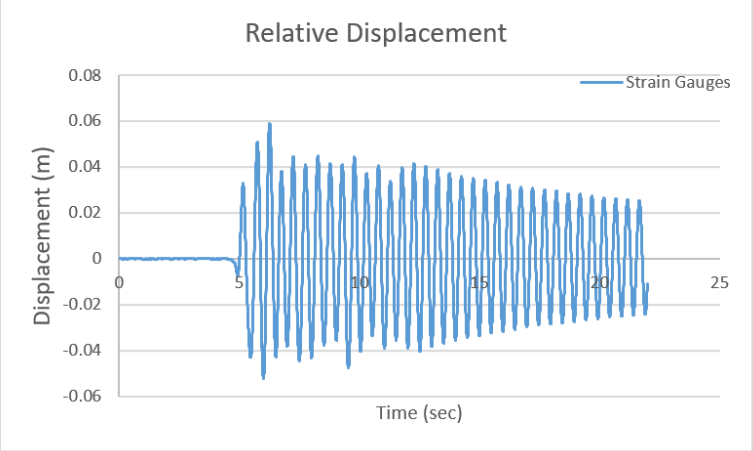

Figure 3.20. Relative Displacement Comparison.

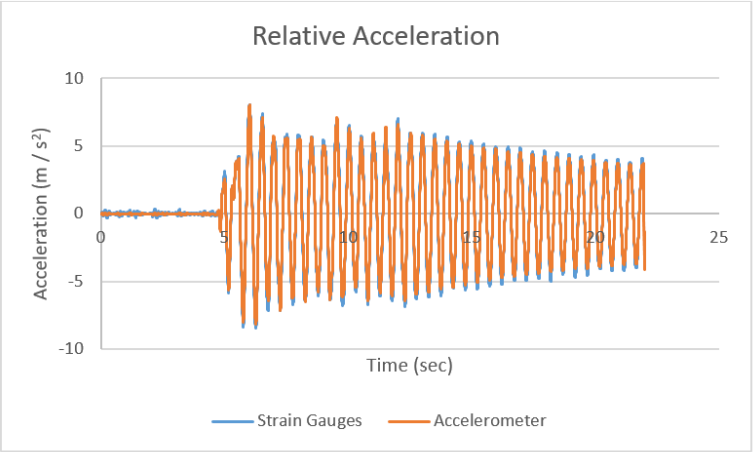

Figure 3.21. Relative Acceleration Comparison.

3.4.7. T=0.5 sec, 0.80 San Salvador

Comparison of relative displacement and comparison of relative acceleration is shown in Figure 3.22 and Figure 3.23 respectively.

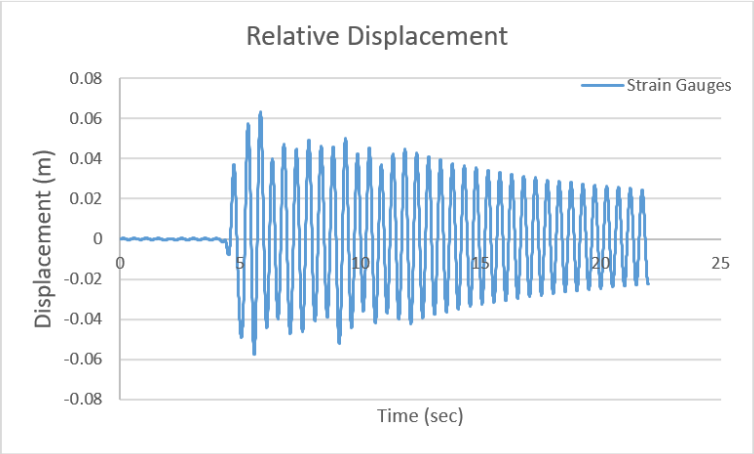

Figure 3.22. Relative Displacement Comparison.

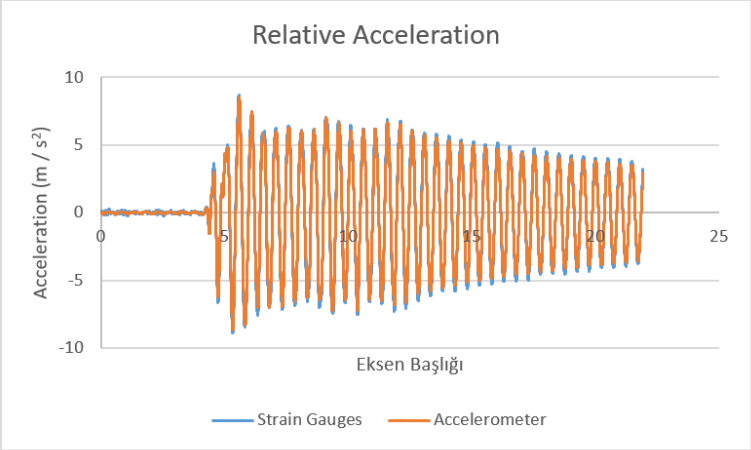

Figure 3.23. Relative Acceleration Comparison.

3.4.8. T=0.5 sec, 0.90 San Salvador

Comparison of relative displacement and comparison of relative acceleration is shown in Figure 3.24 and Figure 3.25, respectively.

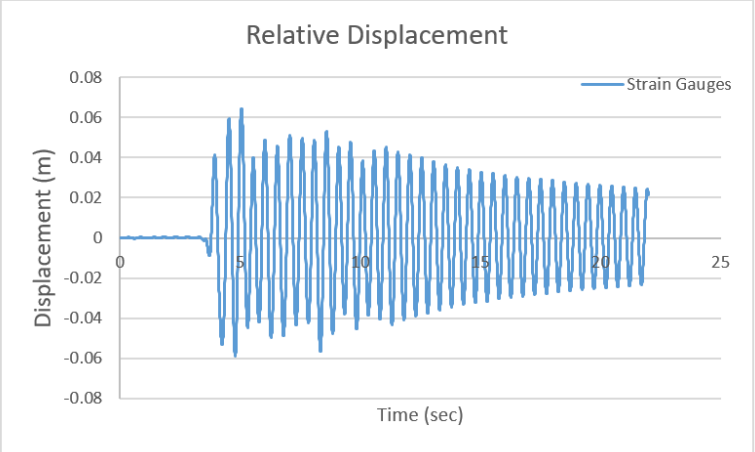

Figure 3.24. Relative Displacement Comparison.

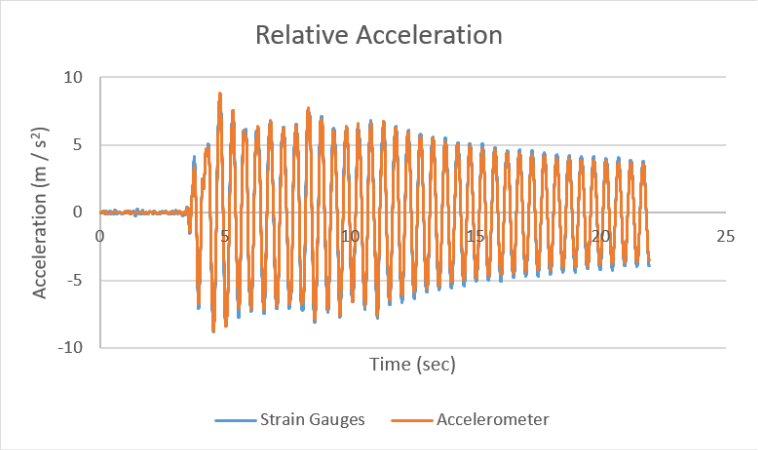

Figure 3.25. Relative Acceleration Comparison.

3.4.9. T=0.5 sec, 1.00 San Salvador

Comparison of relative displacement and comparison of relative acceleration is shown in Figure 3.26 and Figure 3.27, respectively.

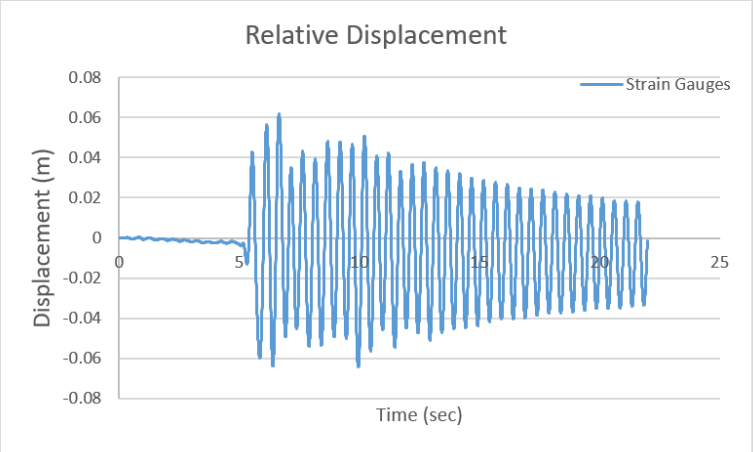

Figure 3.26. Relative Displacement Comparison.

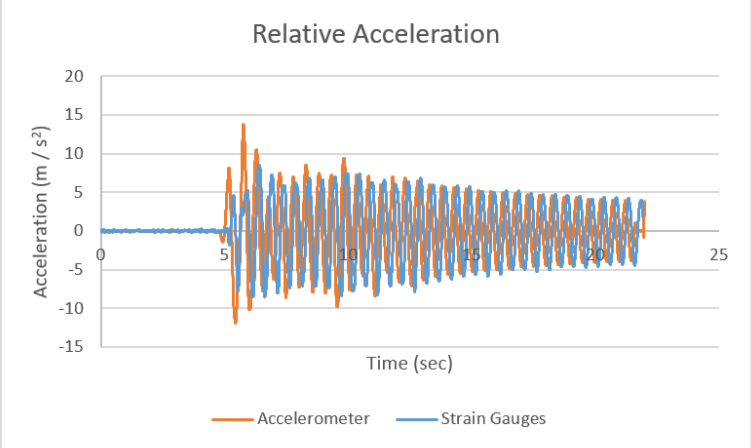

Figure 3.27. Relative Acceleration Comparison.

3.4.10. T=0.5 sec, 1.20 San Salvador

Comparison of relative displacement and comparison of relative acceleration is shown in Figure 3.28 and Figure 3.29, respectively.

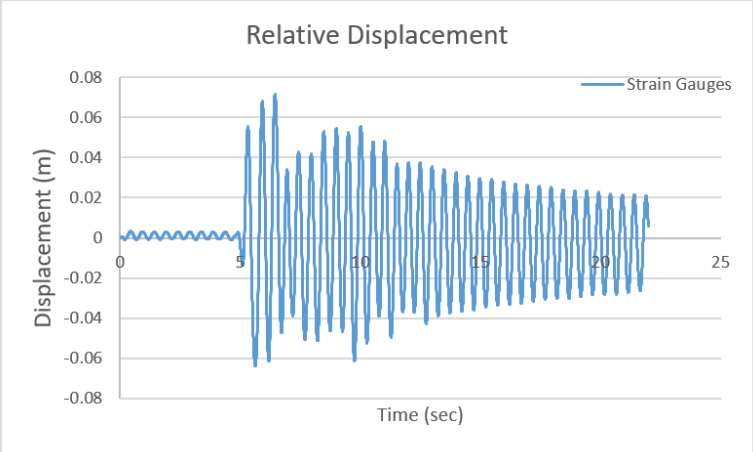

Figure 3.28. Relative Displacement Comparison.

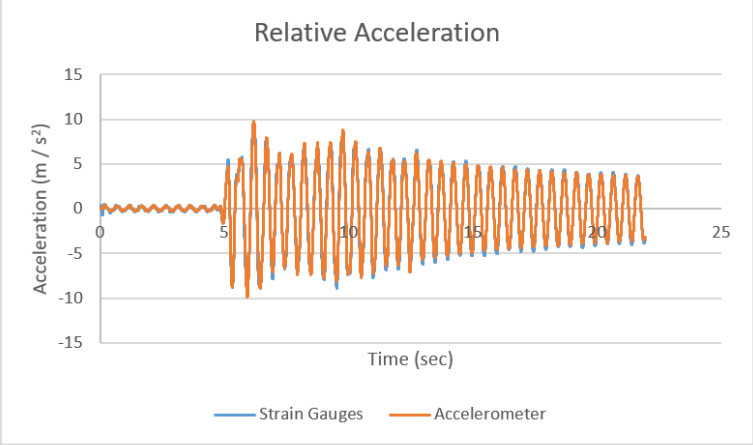

Figure 3.29. Relative Acceleration Comparison.

3.4.11. T=0.5 sec, 1.40 San Salvador

Comparison of relative displacement and comparison of relative acceleration is shown in Figure 3.30 and Figure 3.31, respectively.

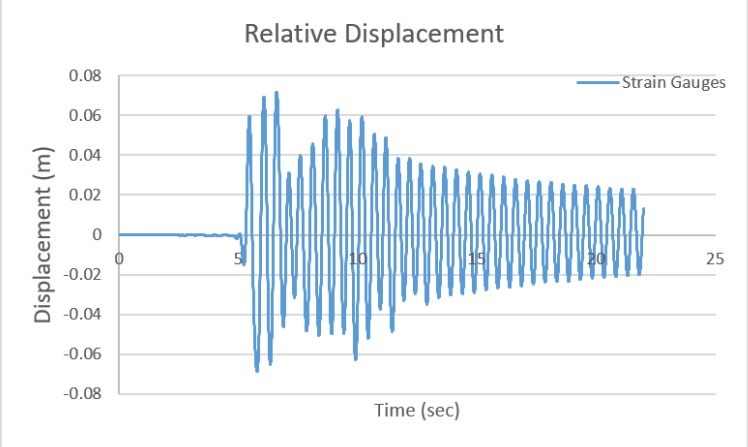

Figure 3.30. Relative Displacement Comparison.

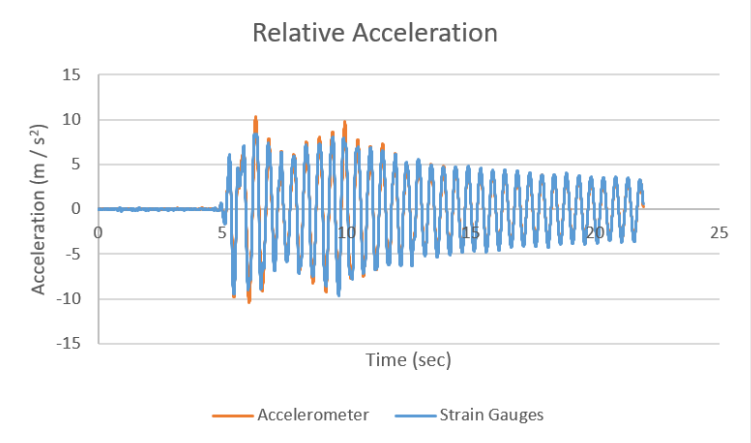

Figure 3.31. Relative Acceleration Comparison.

3.4.12. T=0.5 sec, 1.60 San Salvador

Comparison of relative displacement and comparison of relative acceleration is shown in Figure 3.32 and Figure 3.33, respectively.

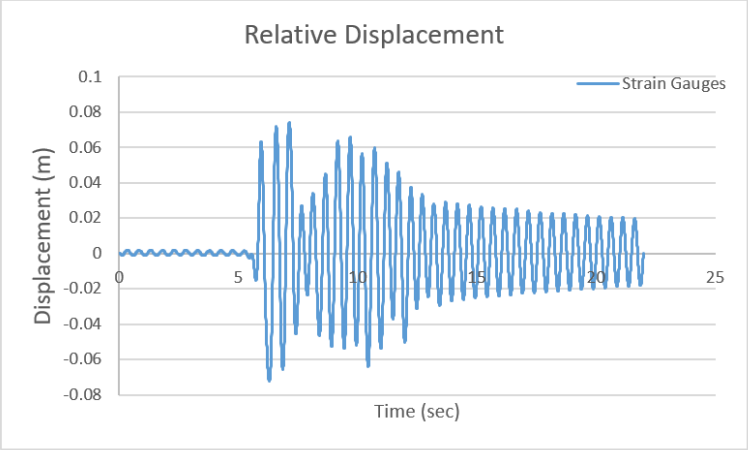

Figure 3.32. Relative Displacement Comparison.

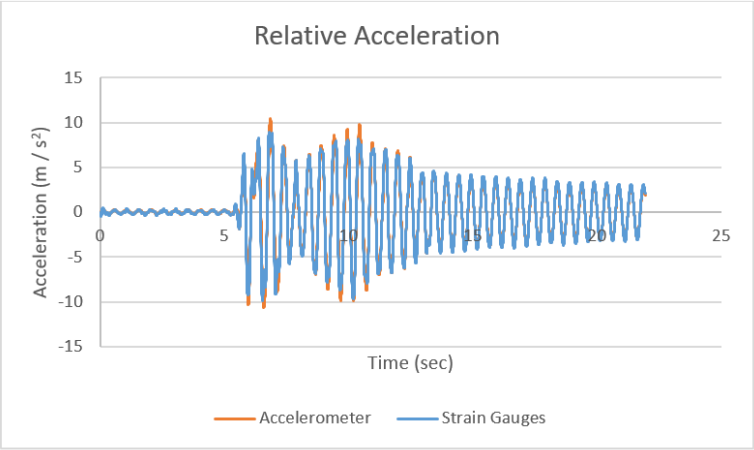

Figure 3.33. Relative Acceleration Comparison.

3.4.13. T=0.667 sec, 0.20 San Salvador

Comparison of relative displacement and comparison of relative acceleration is shown in Figure 3.34 and Figure 3.35, respectively.

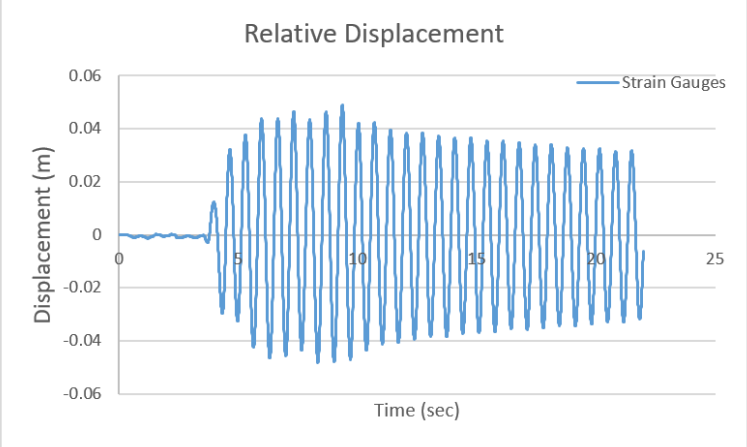

Figure 3.34. Relative Displacement Comparison.

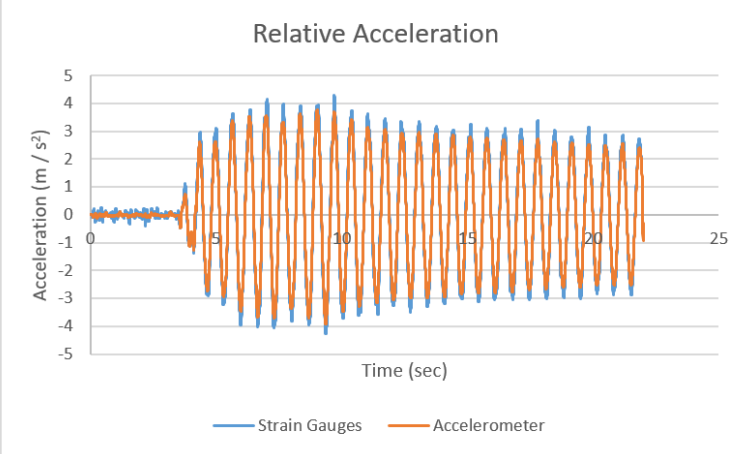

Figure 3.35. Relative Acceleration Comparison.

3.4.14. T=0.667 sec, 0.30 San Salvador

Comparison of relative displacement and comparison of relative acceleration is shown in Figure 3.36 and Figure 3.37, respectively.

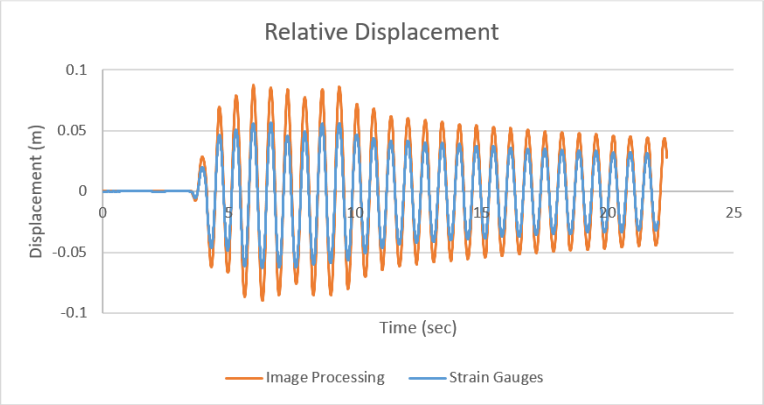

Figure 3.36. Relative Displacement Comparison.

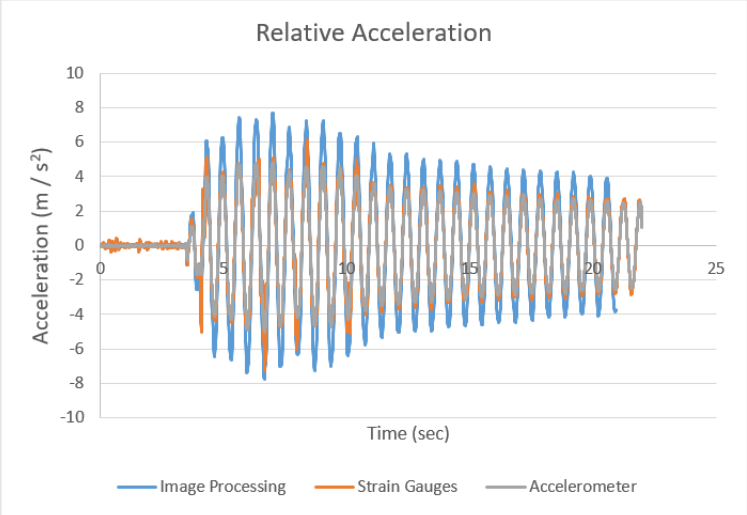

Figure 3.37. Relative Acceleration Comparison.

3.4.15. T=0.667 sec, 0.40 San Salvador

Comparison of relative displacement and comparison of relative acceleration is shown in Figure 3.38 and Figure 3.39, respectively.

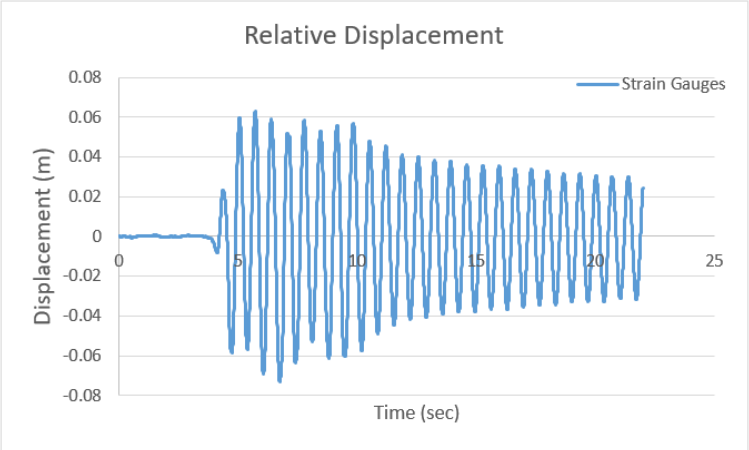

Figure 3.38. Relative Displacement Comparison.

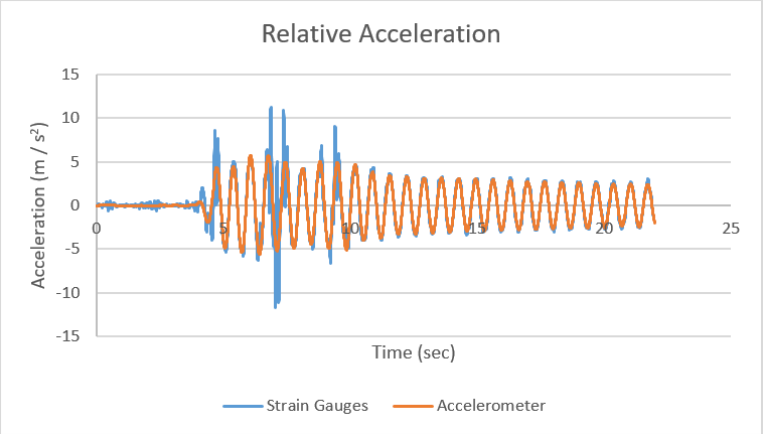

Figure 3.39. Relative Acceleration Comparison.

3.4.16. T=0.667 sec, 0.50 San Salvador

Comparison of relative displacement and comparison of relative acceleration is shown in Figure 3.40 and Figure 3.41, respectively.

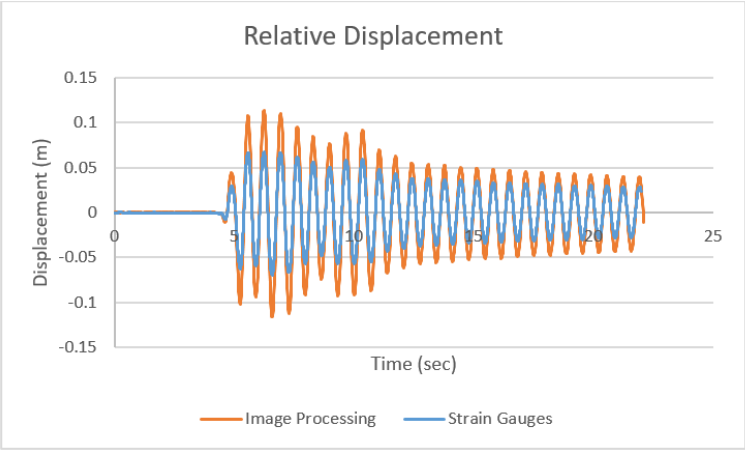

Figure 3.40. Relative Displacement Comparison.

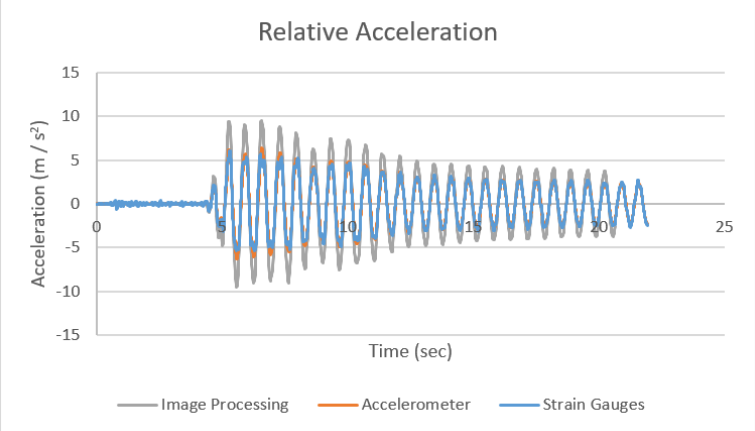

Figure 3.41. Relative Acceleration Comparison.

3.4.17. T=0.667 sec, 0.60 San Salvador

Comparison of relative displacement and comparison of relative acceleration is shown in Figure 3.42 and Figure 3.43, respectively.

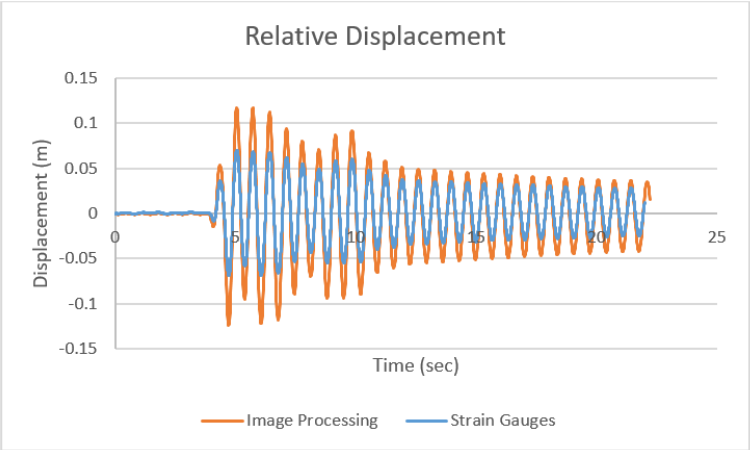

Figure 3.42. Relative Displacement Comparison.

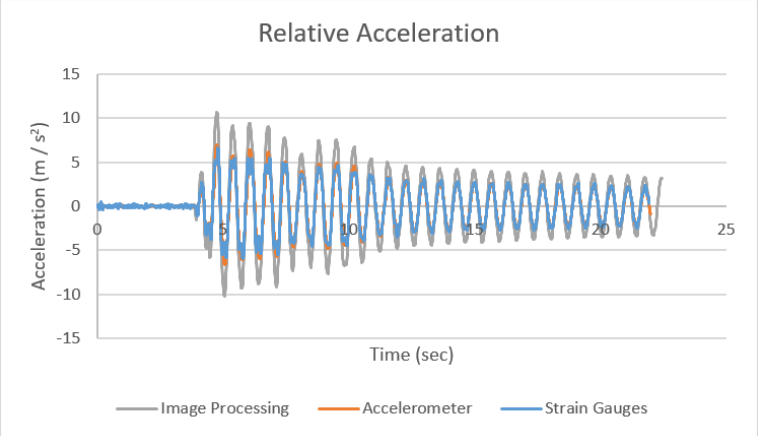

Figure 3.43. Relative Acceleration Comparison.

3.4.18. T=0.667 sec, 0.70 San Salvador

Comparison of relative displacement and comparison of relative acceleration is shown in Figure 3.44 and Figure 3.45, respectively.

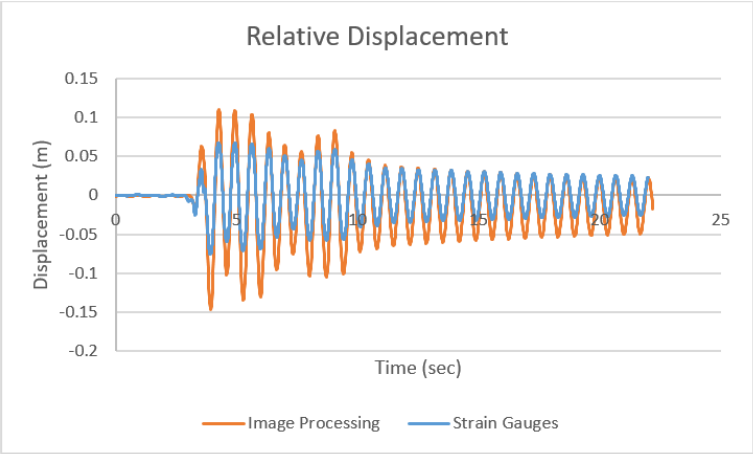

Figure 3.44. Relative Displacement Comparison.

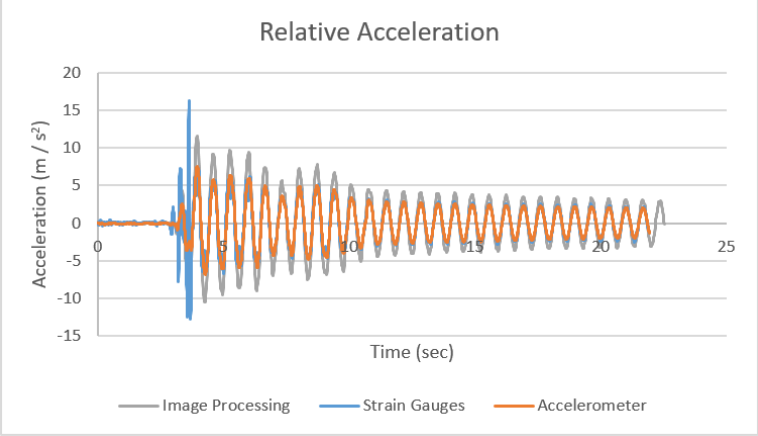

Figure 3.45. Relative Acceleration Comparison.

3.4.19. T=0.667 sec, 0.80 San Salvador

Comparison of relative displacement and comparison of relative acceleration is shown in Figure 3.46 and Figure 3.47, respectively.

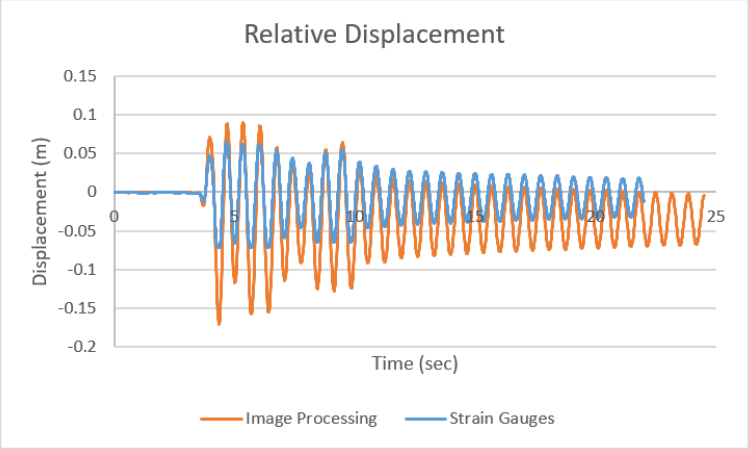

Figure 3.46. Relative Displacement Comparison.

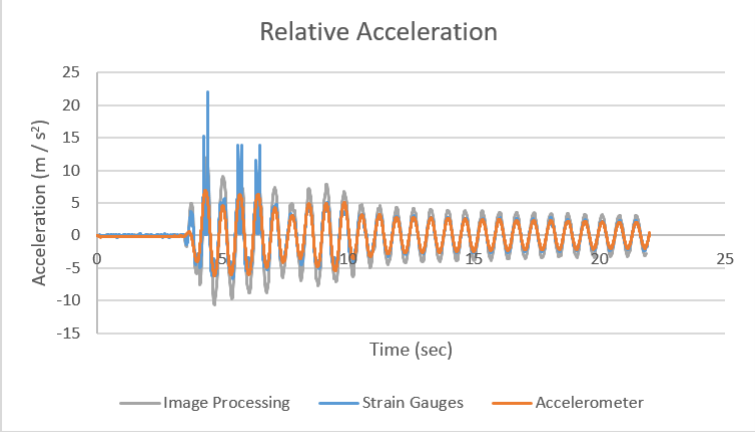

Figure 3.47. Relative Acceleration Comparison.

3.4.20. T=0.667 sec, 0.90 San Salvador

Comparison of relative displacement and comparison of relative acceleration is shown in Figure 3.48 and Figure 3.49, respectively.

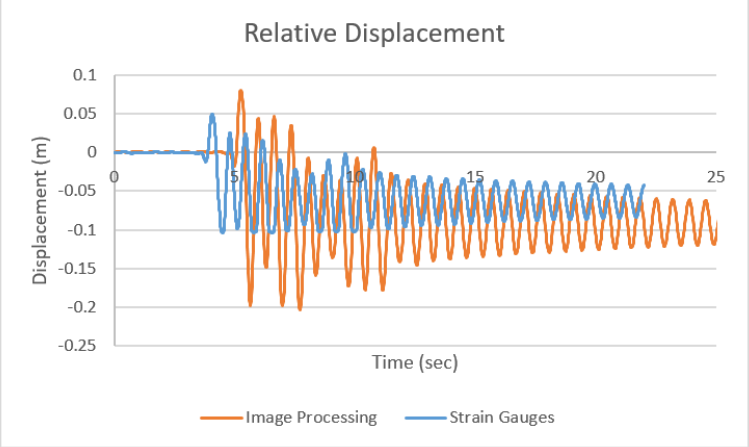

Figure 3.48. Relative Displacement Comparison.

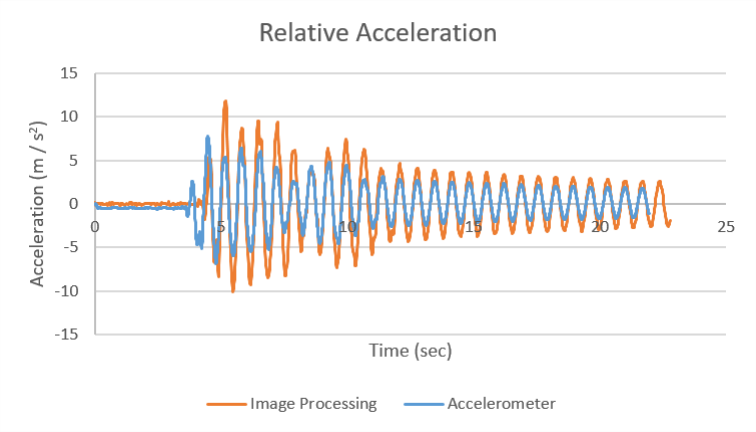

Figure 3.49. Relative Acceleration Comparison.

3.4.21. T=0.667 sec, 1.00 San Salvador

Comparison of relative displacement and comparison of relative acceleration is shown in Figure 3.50 and Figure 3.51, respectively.

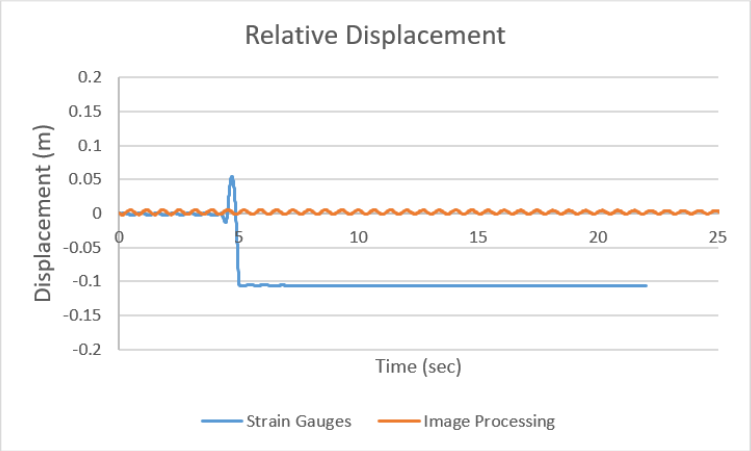

Figure 3.50. Relative Displacement Comparison.

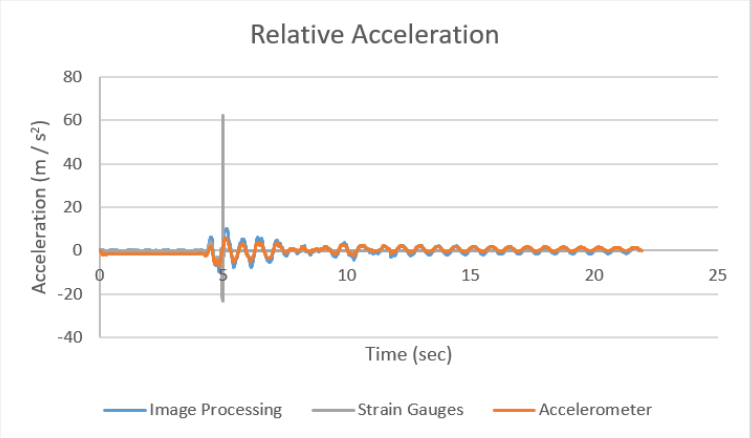

Figure 3.51. Relative Acceleration Comparison.

3.4.22. T=1.00 sec, 0.20 San Salvador

Comparison of relative displacement and comparison of relative acceleration is shown in Figure 3.52 and Figure 3.53, respectively.

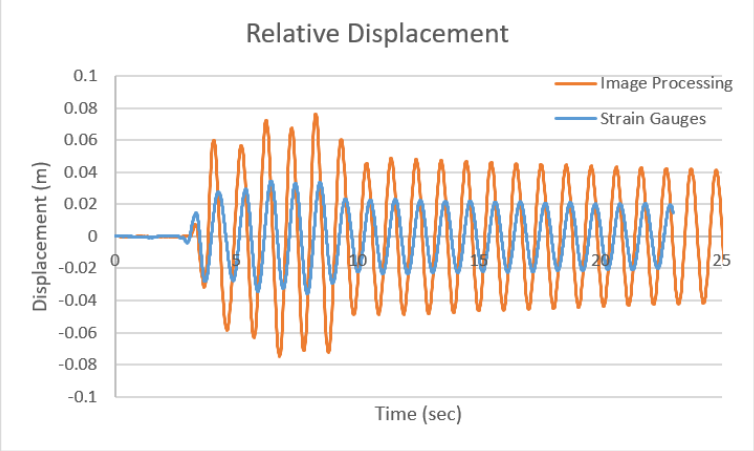

Figure 3.52. Relative Displacement Comparison.

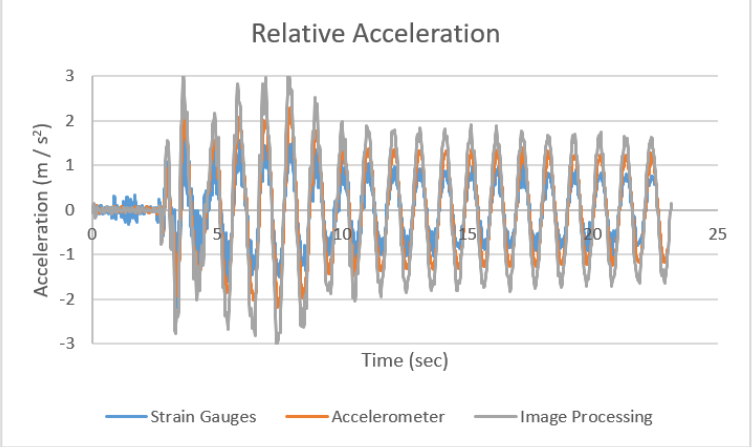

Figure 3.53. Relative Acceleration Comparison.

3.4.23. T=1.00 sec, 0.30 San Salvador

Comparison of relative displacement and comparison of relative acceleration is shown in Figure 3.54 and Figure 3.55, respectively.

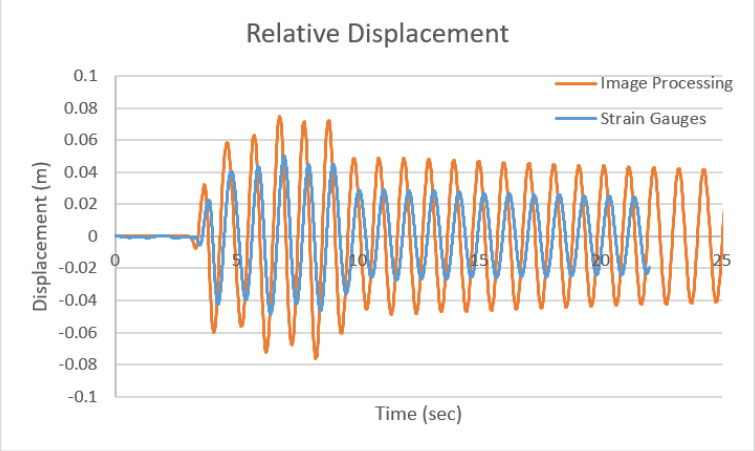

Figure 3.54. Relative Displacement Comparison.

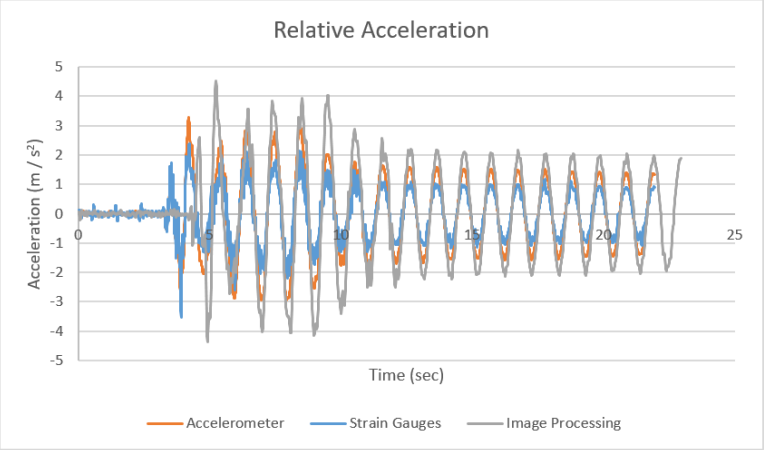

Figure 3.55. Relative Acceleration Comparison.

3.4.24. T=1.00 sec, 0.40 San Salvador

Comparison of relative displacement and comparison of relative acceleration is shown in Figure 3.56 and Figure 3.57, respectively.

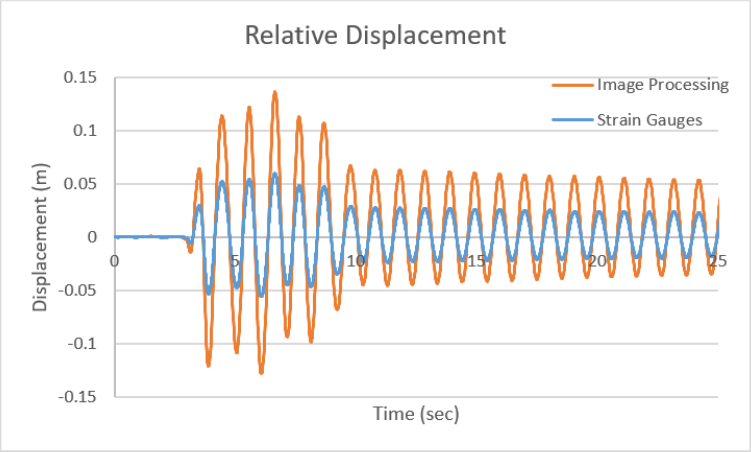

Figure 3.56. Relative Displacement Comparison.

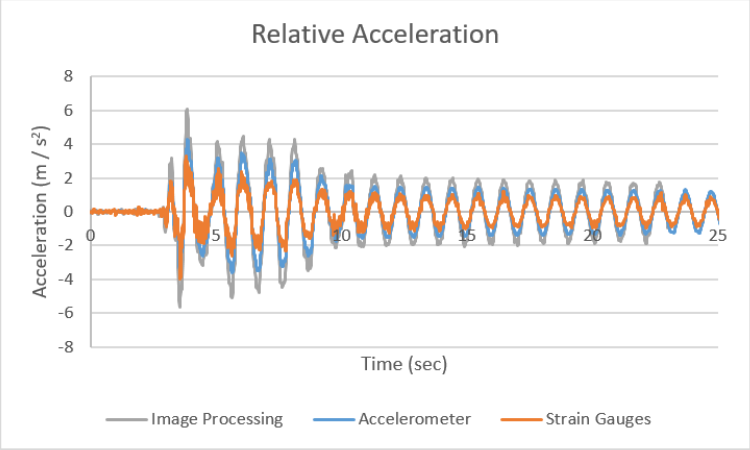

Figure 3.57. Relative Acceleration Comparison.

3.4.25. T=1.00 sec, 0.50 San Salvador

Comparison of relative displacement and comparison of relative acceleration is shown in Figure 3.58 and Figure 3.59, respectively.

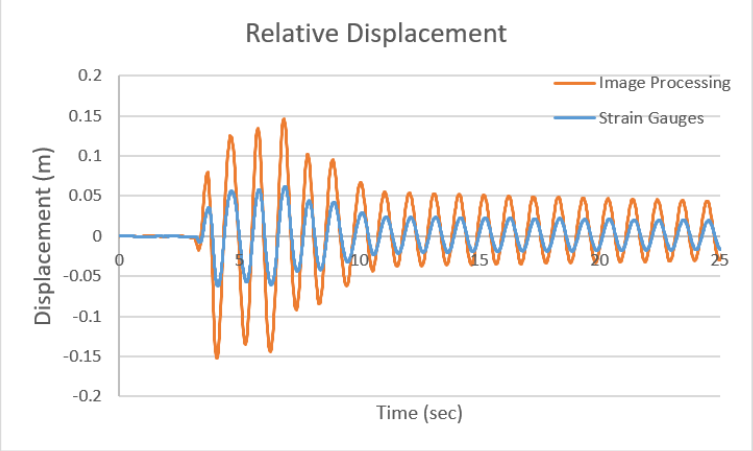

Figure 3.58. Relative Displacement Comparison.

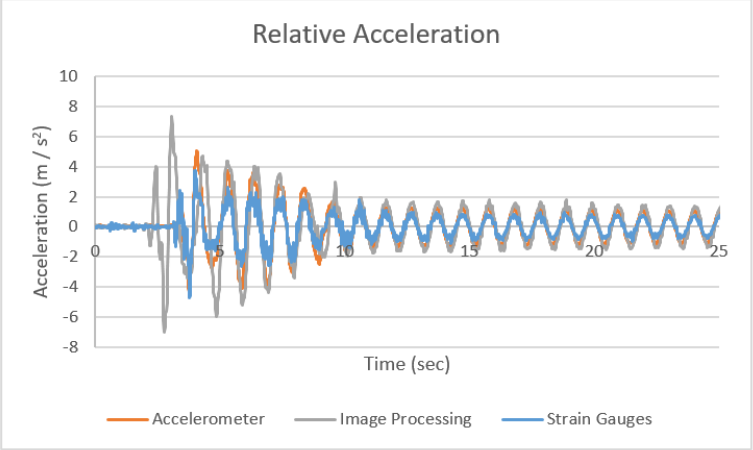

Figure 3.59. Relative Acceleration Comparison.

3.4.26. T=1.00 sec, 0.60 San Salvador

Comparison of relative displacement and comparison of relative acceleration is shown in Figure 3.60 and Figure 3.61, respectively.

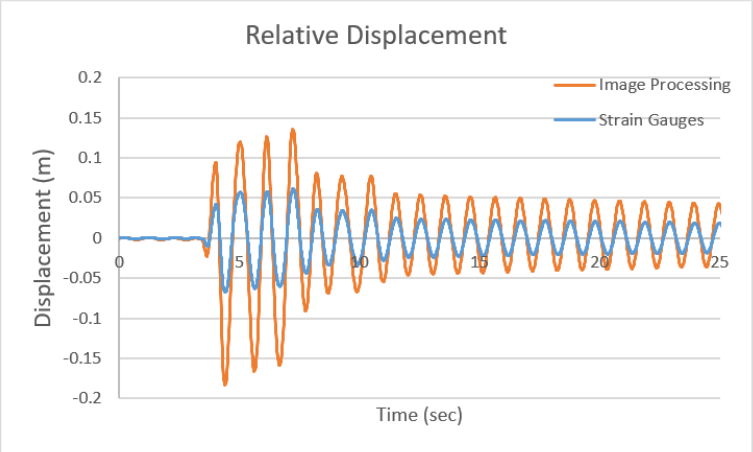

Figure 3.60. Relative Displacement Comparison.

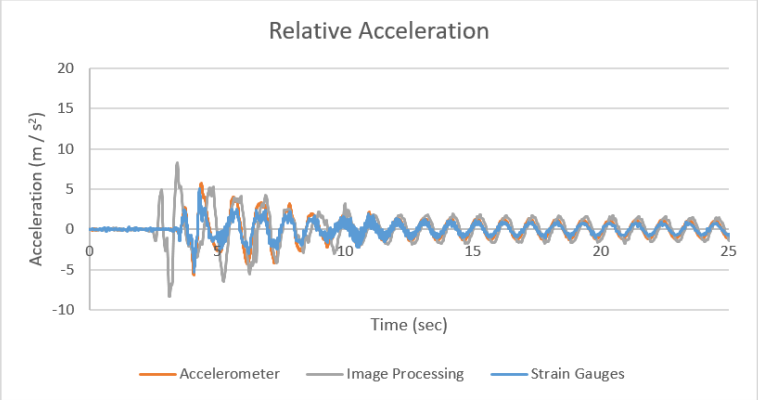

Figure 3.61. Relative Acceleration Comparison.

3.4.27. T=1.00 sec, 0.70 San Salvador

Comparison of relative displacement and comparison of relative acceleration is shown in Figure 3.62 and Figure 3.63, respectively.

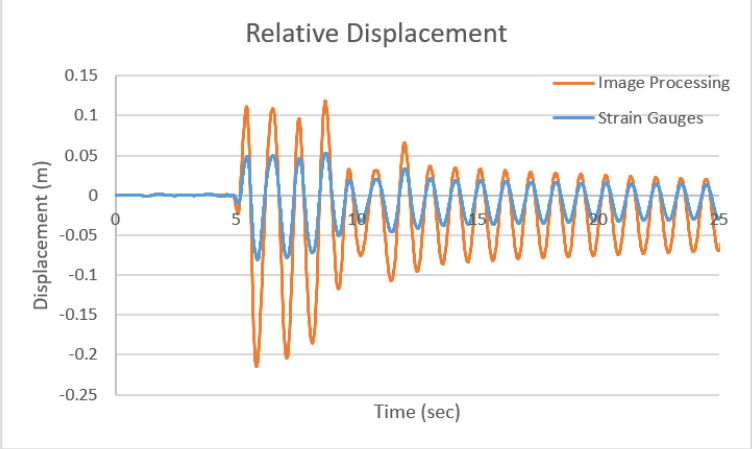

Figure 3.62. Relative Displacement Comparison.

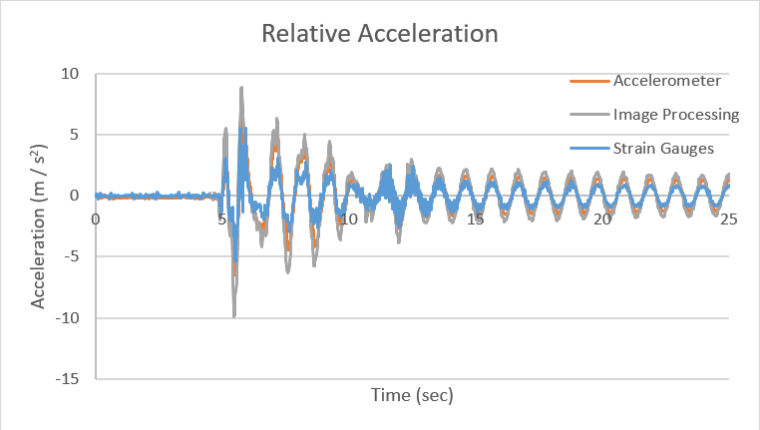

Figure 3.63. Relative Acceleration Comparison.

3.4.28. T=1.00 sec, 0.80 San Salvador

Comparison of relative displacement and comparison of relative acceleration is shown in Figure 3.64 and Figure 3.65, respectively.

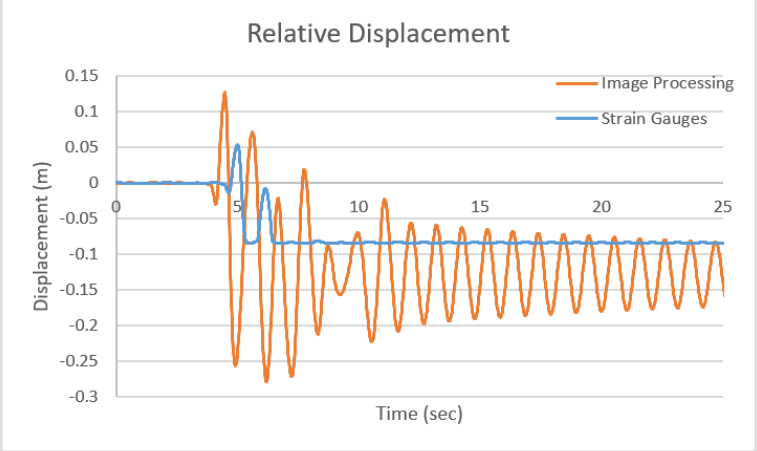

Figure 3.64. Relative Displacement Comparison.

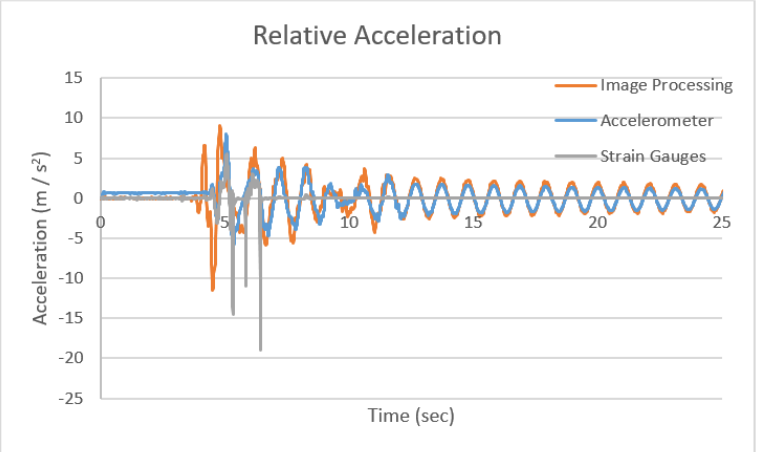

Figure 3.65. Relative Acceleration Comparison.

3.5. Comments on Data Acquisition

In preceding section 3.4 comparisons of both displacement and acceleration data from different data sources for San Salvador Earthquake were plotted. The aim of this part to obtain most reliable data for the rest of the research. The following figures are examples for each period. They show that how the data used for the rest of the study was selected. All the graphs plotted from experiments demonstrated that the data from strain gauges and accelerometer matched but the peak values of image processing were higher than these two. For this reason, accelerometers' measurements of acceleration and strain gauges' measurements of displacement will be used for the

rest of this research. In subsequent experiments, the same approach was applied to select data.

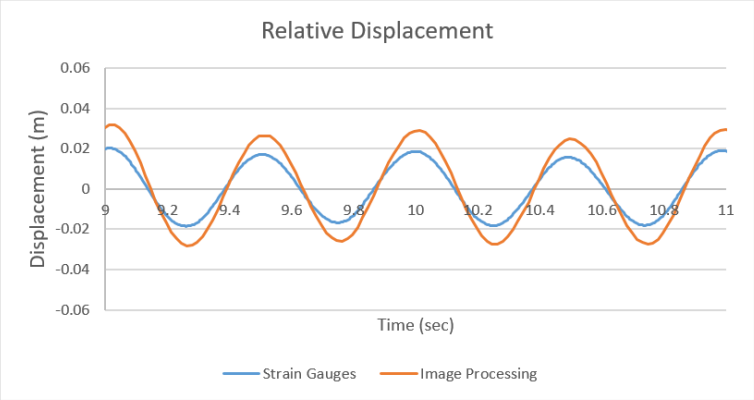

Figure 3.66. Relative Displacement Comparison from T=0.50 sec, 0.30 San Salvador.

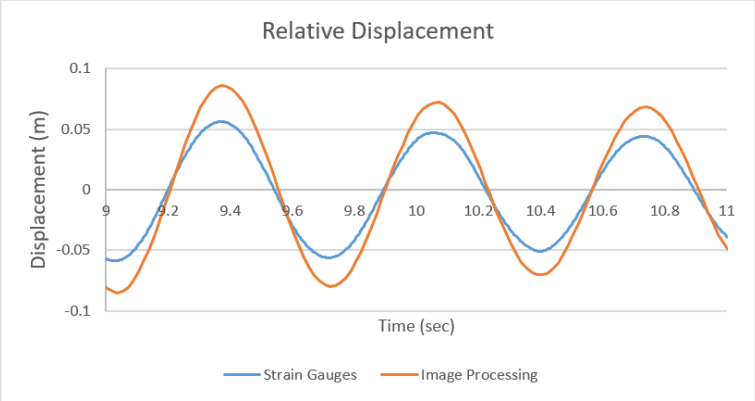

Figure 3.67. Relative Displacement Comparison from T=0.667 sec, 0.30 San Salvador.

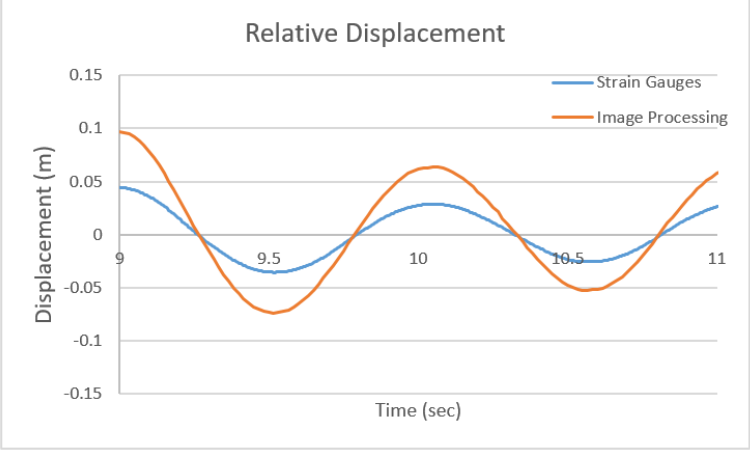

Figure 3.68. Relative Displacement Comparison from T=1.00 sec, 0.30 San Salvador.

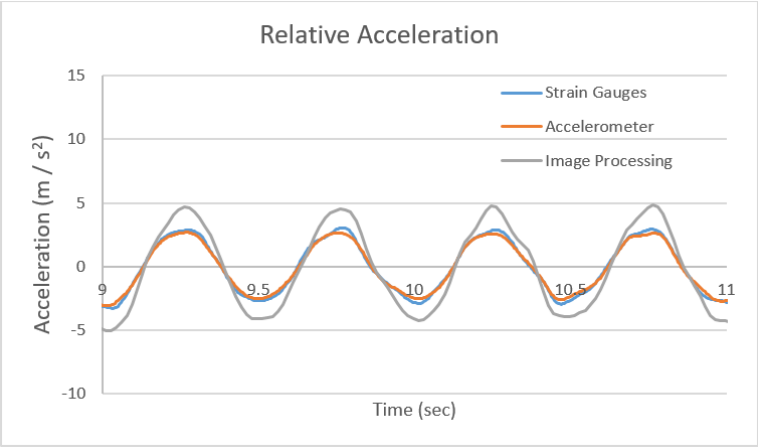

Figure 3.69. Relative Acceleration Comparison from T=0.50 sec, 0.30 San Salvador.

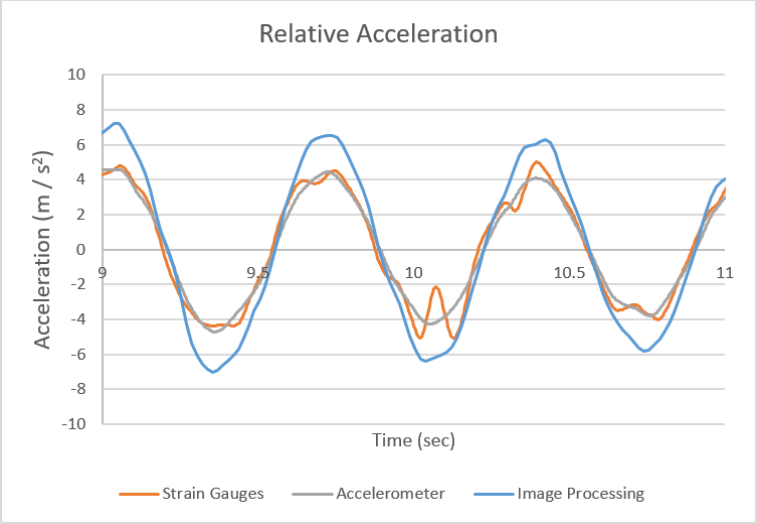

Figure 3.70. Relative Acceleration Comparison from T=0.667 sec, 0.30 San Salvador.

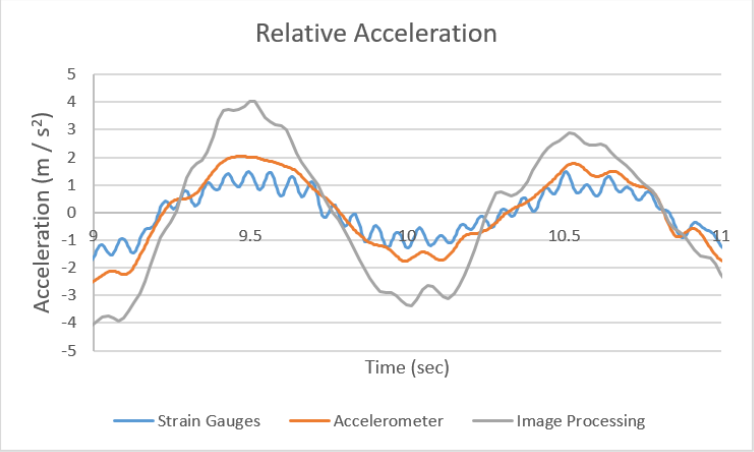

Figure 3.71. Relative Acceleration Comparison from T=1 sec, 0.30 San Salvador.

3.6. Data Selection

Data selection table was created to show which data available and which data was selected. Selected data for the analyses was marked with a check mark.

Table 3.3. Selected Data.

		Data Selection											
		Accelerometer		Strain Gauges							Image Processing		
Period	Scale Factor	Top Acceleration	Table Acceleration	SG1	SG2	SG3	SG4	Relative Displacement	Relative Velocity	Relative Acceleration	Top acceleration	Table Acceleration	Relative Displacement
0.5	0.20	√	√	X	X	X	X	√	X	X	X	X	X
	0.30	√	√	X	X	X	X	√	X	X	X	X	
	0.40	√	√		X		X	√	X	X			
	0.50	√	√	X	X		X	√	X	X			
	0.60	√	√	X			X	√	X	X			
	0.70	√	√	X			X	√	X	X			
	0.90	√	√	X			X	√	X	X			
	1.00	√	√	X	X		X	√	X	X			
	1.20	√	√	X	X		X	√	X	X			
	1.40	√	√	X	X		X	√	X	X			
	1.60	√	√	X	X		X	√	X	X			
0.66	0.20	√	√	X	X	X	X	√	X	X			
7	0.30	√	√	X	X	X	X	√	X	X	X	X	X
	0.40	√	√	X		X	X	√	X	X			
	1.00	√	√	X	X	X	X	√	X	X			
1	0.60	√	√		X	X	X	√	X	X	X	X	X
	0.70	√	√	X	X	X	X	√	X	X	X	X	X
	0.80	√	√	X	X	X	X	√	X	X	X	X	X
	0.90	√	√	X	X	X	X	√	X	X	X	X	X
	1.00	√	√	X	X	X	X	√	X	X	X	X	X
	0.2	√	√	X	X	X	X	√	X	X	X	X	X
	0.30	√	√	X	X	X	X	√	X	X	X	X	X
	0.40	√	√	X	X	X	X	√	X	X	X	X	X
	0.50	√	√	X	X	X	X	√	X	X	X	X	X
	0.60	√	√	X	X	X	X	√	X	X	X	X	X
	0.70	√	√	X	X	X	X	√	X	X	X	X	X
	0.80	√	√	X	X	X	X	√	X	X	X	X	X

4. ANALYSIS AND COMPARISON OF THE EXPERIMENTAL RESULTS

In this chapter, analytical and experimental results of this study were analyzed and comparisons were made with Güllü's mass-normalized Input Energy Spectra.

4.1. Experimental Results

For each scale factor, two methods were used to calculate damping ratio: logarithmic decrement and Chopra's method. Firstly, logarithmic decrement method was used. Experimental test results showed that it was more convenient to use the ratio between the two successive peaks of damped free vibration for lightly damped system. Also, Chopra's Method (Chopra, 1996) was used to calculate the damping ratio of the experimental results. A Matlab code was developed to compute damping ratios of the selected data and energy components of the system. Mass-normalized Input Energy *(EI/m)*, mass-normalized Damping Energy *(ED/m)*, mass normalized Strain Energy *(ES/m)* and mass normalized Kinetic Energy *(EK/m)* of the system were plotted in the following subsections.

4.1.1. T=0.50 sec, 0.20 San Salvador Experimental Results

Figure 4.1 and Figure 4.2 show the acceleration data at free vibration after the occurrence of ground motion excitation, and also, force versus relative displacement data during the earthquake excitation, respectively. Table 4.1 shows the calculated damping ratios of the system in both methods.

Table 4.1. Damping ratio calculated with different methods.

Logarithmic Decrement	0.00106
Chopra's Method	0.00380

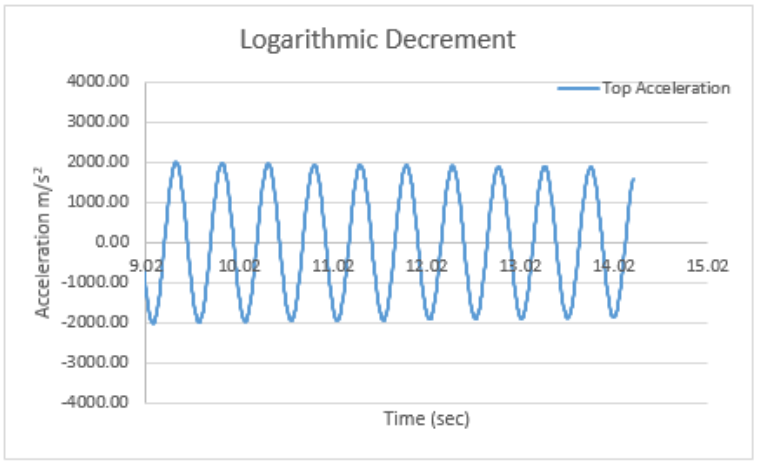

Figure 4.1. Post-Earthquake Data.

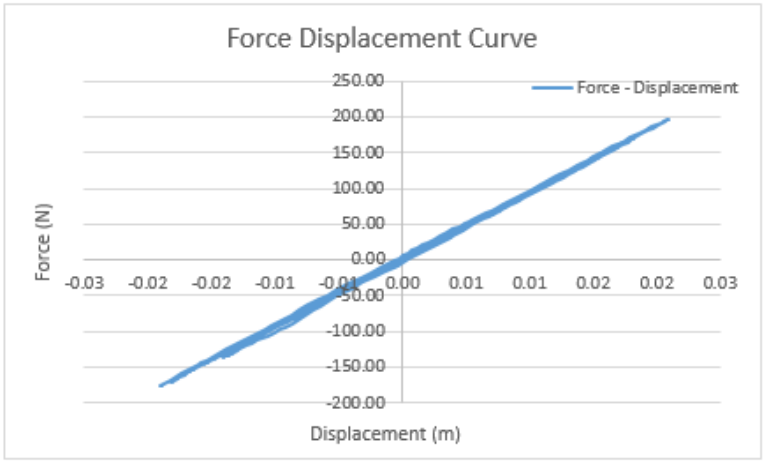

Figure 4.2. Force-Displacement Data.

4.1.2. T=0.50 sec, 0.30 San Salvador Experimental Results

Table 4.2. Damping ratio calculated with different methods.

Logarithmic Decrement	0.0015
Chopra's Method	0.00220

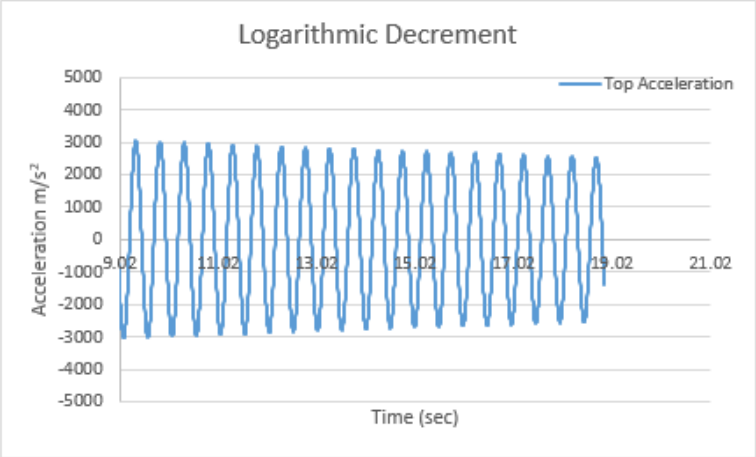

Figure 4.3. Post-earthquake Data.

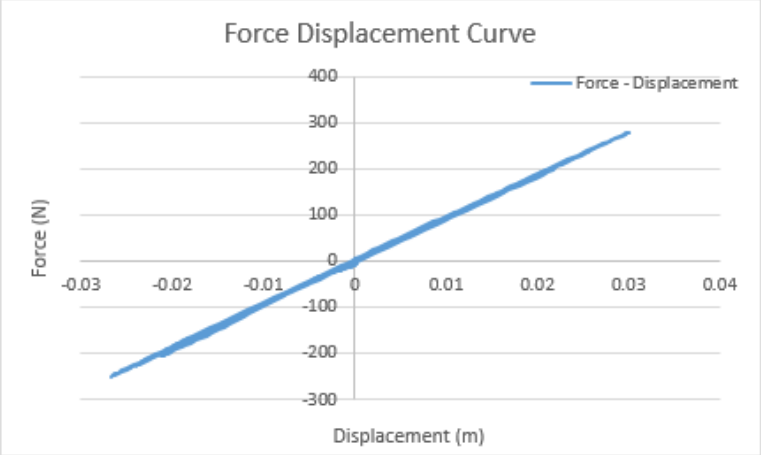

Figure 4.4. Force-Displacement Data.

4.1.3. T=0.50 sec, 0.40 San Salvador Experimental Results

Figure 4.5 and Figure 4.6 show the acceleration data at free vibration after the occurrence of ground motion excitation, and also, force versus relative displacement data during the earthquake excitation, respectively. Table 4.3 shows the calculated damping ratios of the system in both methods.

Table 4.3. Damping ratio calculated with different methods.

Logarithmic Decrement	0.00247
Chopra's Method	0.00330

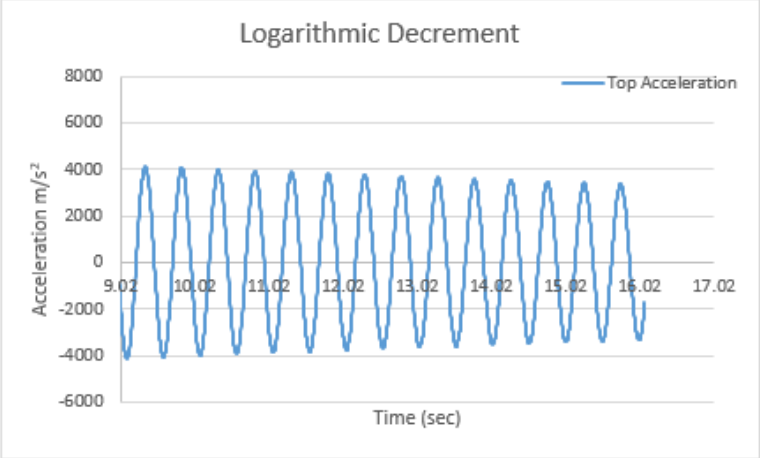

Figure 4.5. Post-earthquake Data.

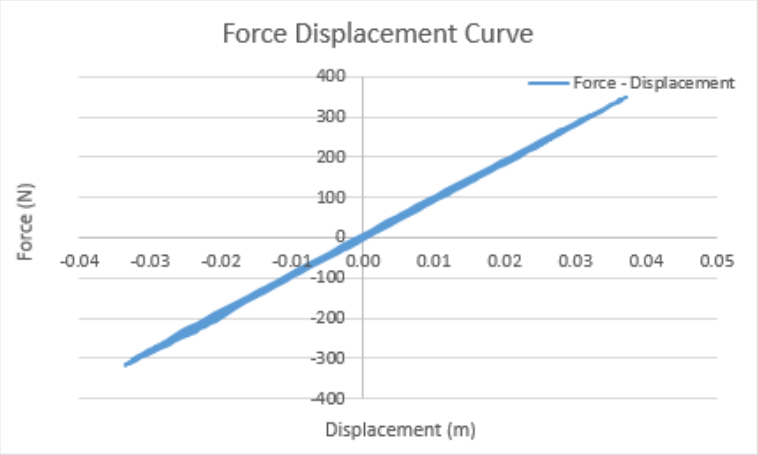

Figure 4.6. Force-Displacement Data.

4.1.4. T=0.50 sec, 0.50 San Salvador Experimental Results

Figure 4.7 and Figure 4.8 show the acceleration data at free vibration after the occurrence of ground motion excitation, and also, force versus relative displacement data during the earthquake excitation, respectively. Table 4.4 shows the calculated damping ratios of the system in both methods.

Table 4.4. Damping ratio calculated with different methods.

Logarithmic Decrement	0.00319
Chopra's Method	0.00200

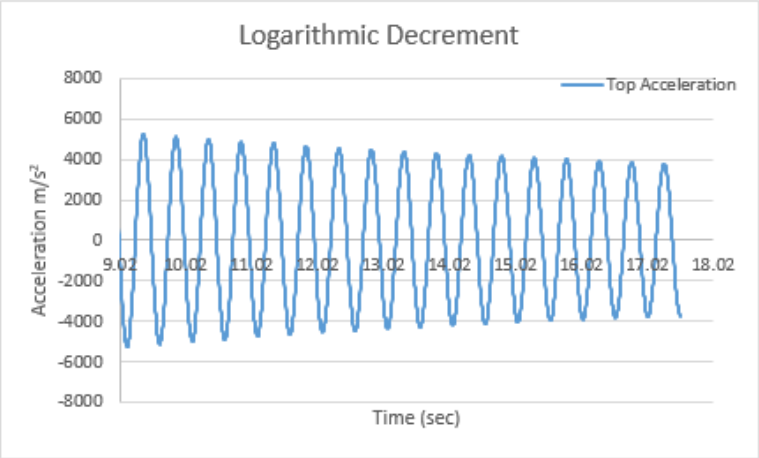

Figure 4.7. Post-earthquake Data.

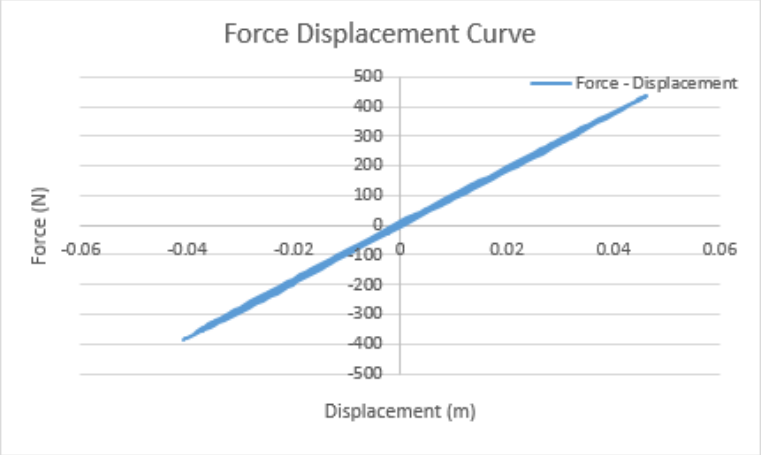

Figure 4.8. Force-Displacement Data.

4.1.5. T=0.50 sec, 0.60 San Salvador Experimental Results

Figure 4.9 and Figure 4.10 show the acceleration data at free vibration after the occurrence of ground motion excitation, and also, force versus relative displacement data during the earthquake excitation, respectively. Table 4.5 shows the calculated damping ratio of the system in both methods.

Table 4.5. Damping ratio calculated with different methods.

Logarithmic Decrement	0.00358
Chopra's Method	0.00160

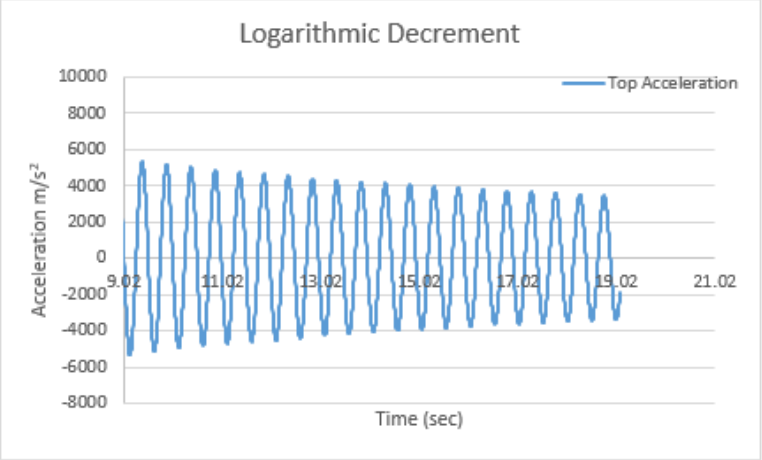

Figure 4.9. Post-earthquake Data.

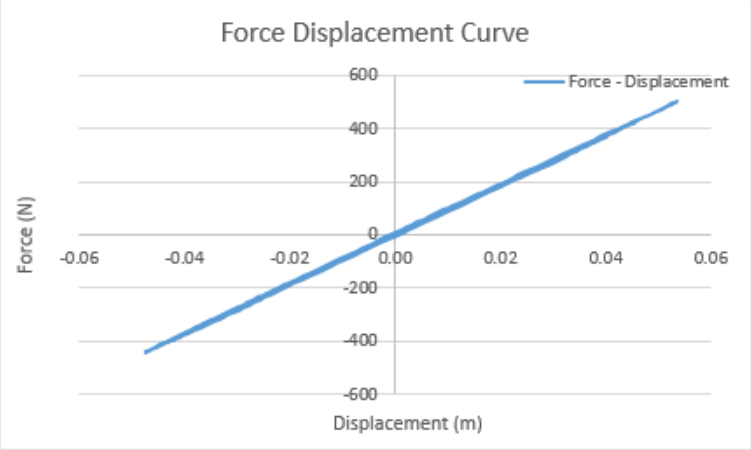

Figure 4.10. Force-Displacement Data.

4.1.6. T=0.50 sec, 0.70 San Salvador Experimental Results

Figure 4.11 and Figure 4.12 show the acceleration data at free vibration after the occurrence of ground motion excitation, and also, force versus relative displacement data during the earthquake excitation, respectively. Table 4.6 shows the calculated damping ratio of the system in both methods.

Table 4.6. Damping ratio calculated with different methods.

Logarithmic Decrement	0.00407
Chopra's Method	0.00170

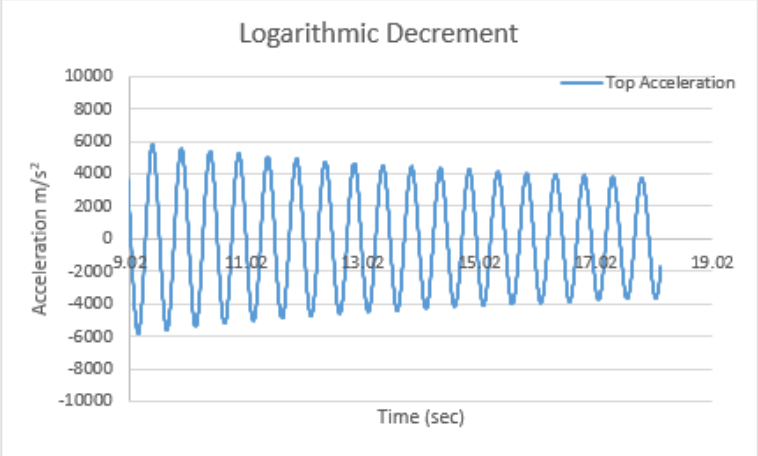

Figure 4.11. Post-earthquake Data.

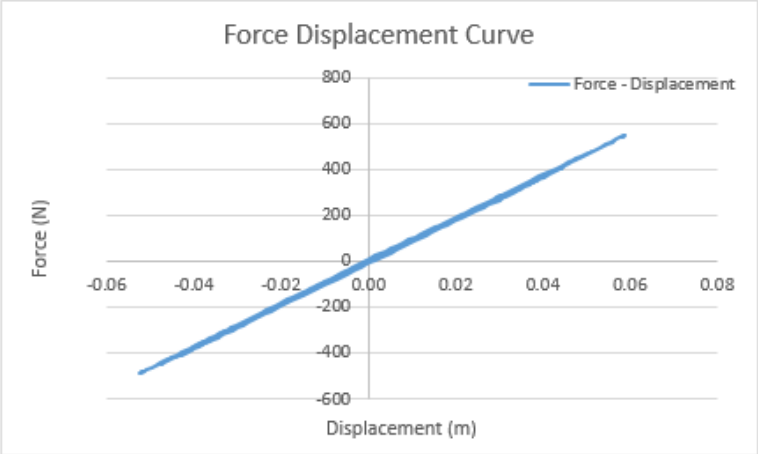

Figure 4.12. Force-Displacement Data.

4.1.7. T=0.50 sec, 0.80 San Salvador Experimental Results

Figure 4.13 and Figure 4.14 show the acceleration data at free vibration after the occurrence of ground motion excitation, and also, force versus relative displacement data during the earthquake excitation, respectively. Table 4.7 shows the calculated damping ratio of the system in both methods.

Table 4.7. Damping ratio calculated with different methods.

Logarithmic Decrement	0.00462
Chopra's Method	0.00140

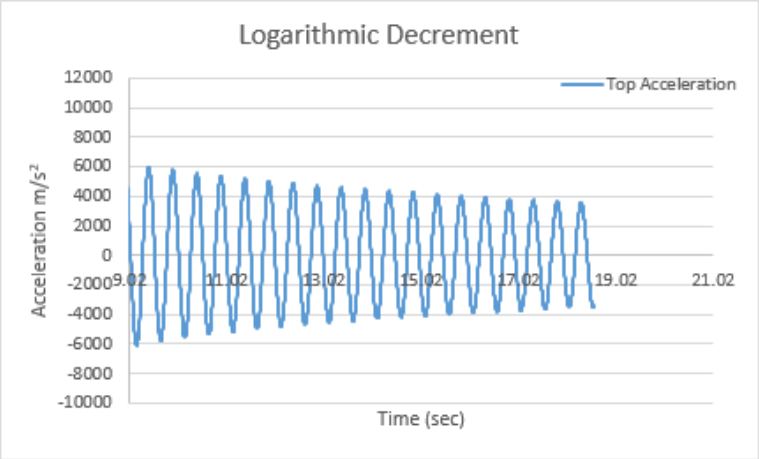

Figure 4.13. Post-earthquake Data.

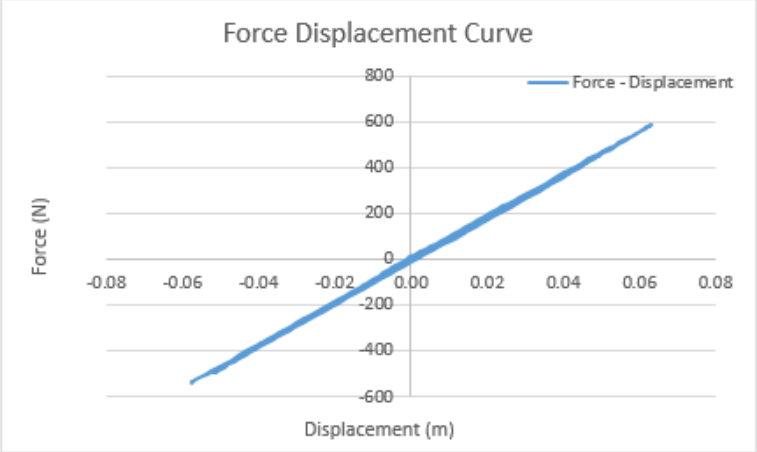

Figure 4.14. Force-Displacement Data.

4.1.8. T=0.50 sec, 0.90 San Salvador Experimental Results

Figure 4.15 and Figure 4.16 show the acceleration data at free vibration after the occurrence of ground motion excitation, and also, force versus relative displacement data during the earthquake excitation, respectively. Table 4.8 shows the calculated damping ratio of the system in both methods.

Table 4.8. Damping ratio calculated with different methods.

Logarithmic Decrement	0.00436
Chopra's Method	0.00150

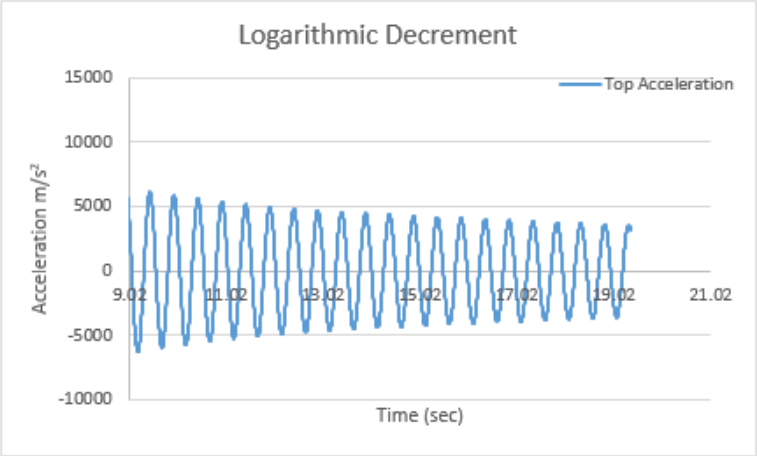

Figure 4.15. Post-earthquake Data.

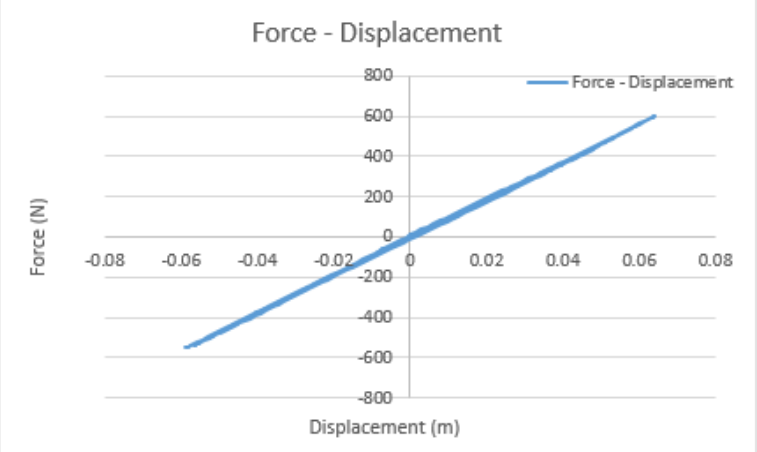

Figure 4.16. Force-Displacement Data.

4.1.9. T=0.50 sec, 1.00 San Salvador Experimental Results

Figure 4.17 and Figure 4.18 show the acceleration data at free vibration after the occurrence of ground motion excitation, and also, force versus relative displacement data during the earthquake excitation, respectively. Table 4.9 shows the calculated damping ratio of the system in both methods.

Table 4.9. Damping ratio calculated with different methods.

Logarithmic Decrement	0.00430
Chopra's Method	0.00470

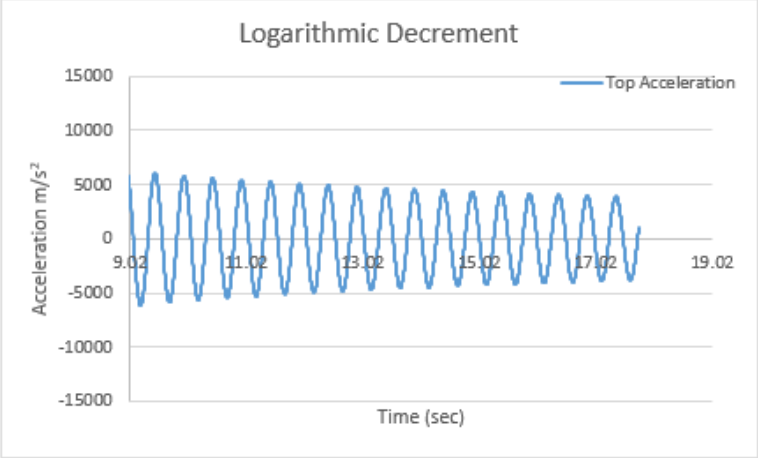

Figure 4.17. Post-earthquake Data.

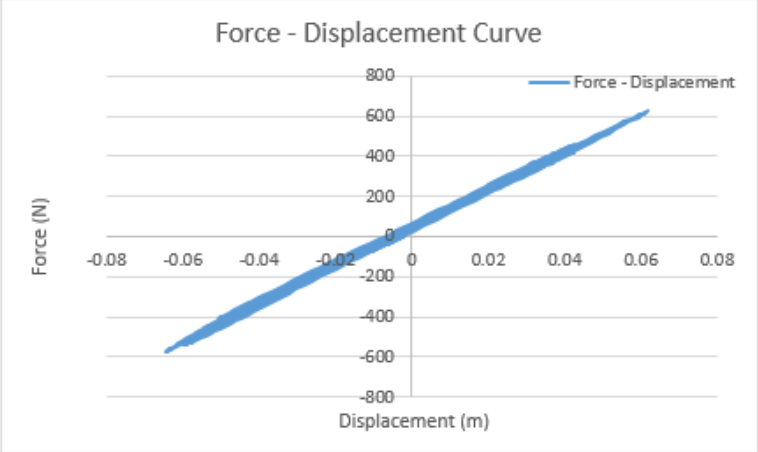

Figure 4.18. Force-Displacement Data.

4.1.10. T=0.50 sec, 1.20 San Salvador Experimental Results

Figure 4.19 and Figure 4.20 show the acceleration data at free vibration after the occurrence of ground motion excitation, and also, force versus relative displacement data during the earthquake excitation, respectively. Table 4.10 shows the calculated damping ratio of the system in both methods.

Table 4.10. Damping ratio calculated with different methods.

Logarithmic Decrement	0.00406
Chopra's Method	0.00480

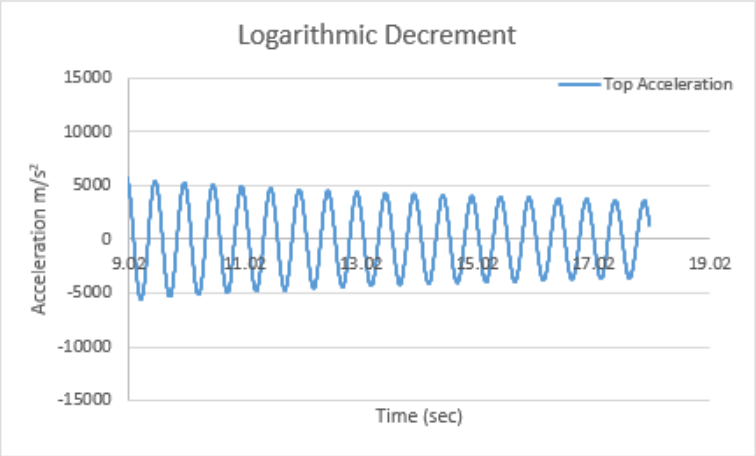

Figure 4.19. Post-earthquake Data.

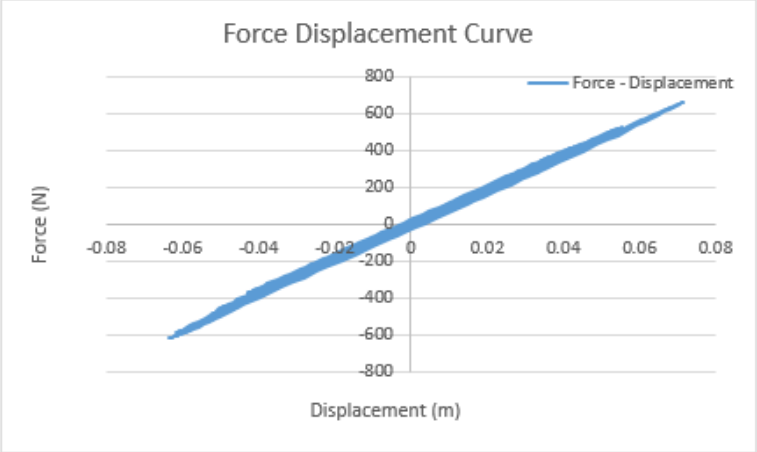

Figure 4.20. Force-Displacement Data.

4.1.11. T=0.50 sec, 1.40 San Salvador Experimental Results

Figure 4.21 and Figure 4.22 show the acceleration data at free vibration after the occurrence of ground motion excitation, and also, force versus relative displacement data during the earthquake excitation, respectively. Table 4.11 shows the calculated damping ratio of the system in both methods.

Table 4.11. Damping ratio calculated with different methods.

Logarithmic Decrement	0.0041
Chopra's Method	0.00230

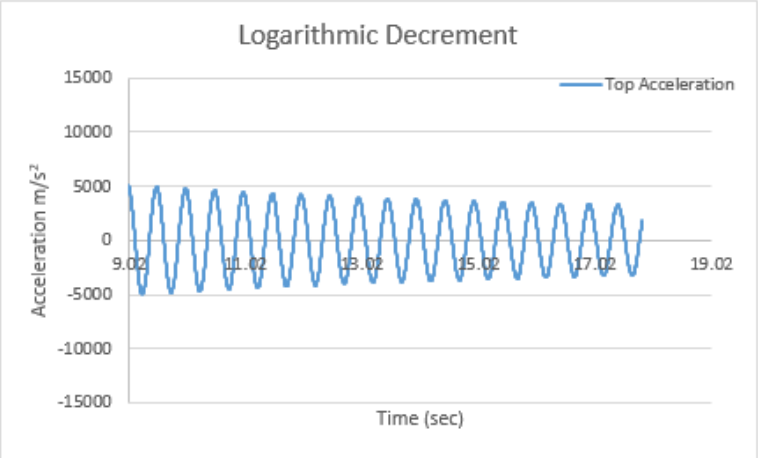

Figure 4.21. Post-earthquake Data.

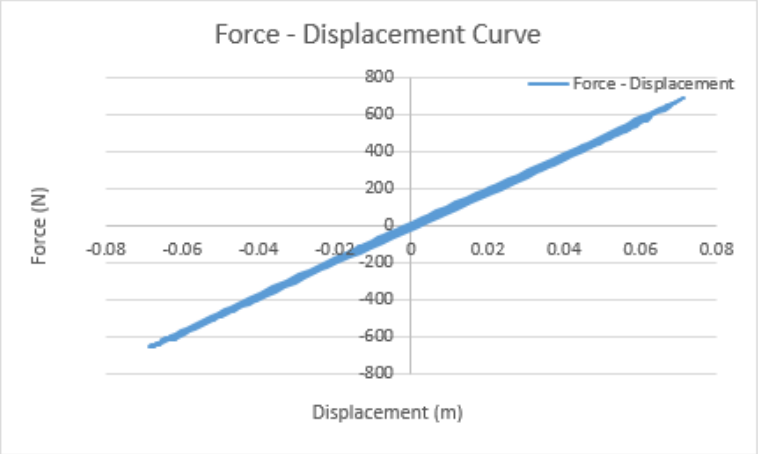

Figure 4.22. Force-Displacement Data.

4.1.12. T=0.50 sec, 1.60 San Salvador Experimental Results

Figure 4.23 and Figure 4.24 show the acceleration data at free vibration after the occurrence of ground motion excitation, and also, force versus relative displacement data during the earthquake excitation, respectively. Table 4.12 shows the calculated damping ratio of the system in both methods.

Table 4.12. Damping ratio calculated with different methods.

Logarithmic Decrement	0.00218
Chopra's Method	0.00240

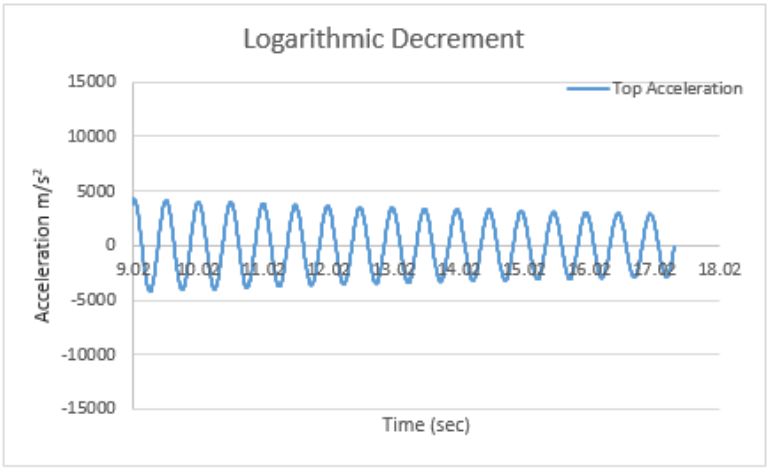

Figure 4.23. Post-earthquake Data.

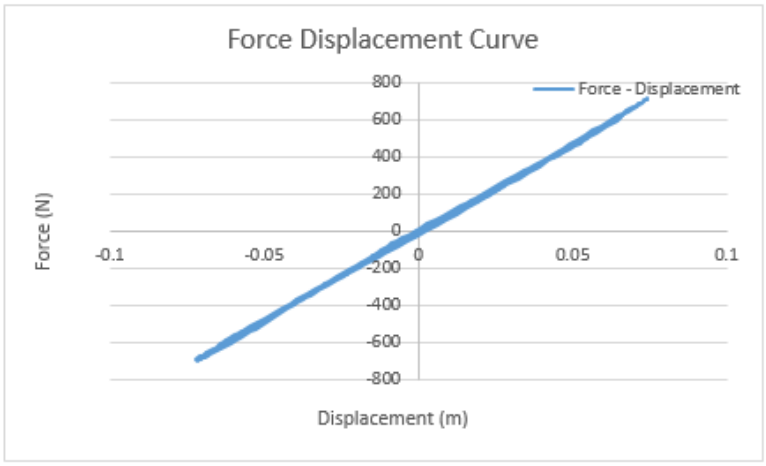

Figure 4.24. Force-Displacement Data.

4.1.13. T=0.667 sec, 0.20 San Salvador Experimental Results

Figure 4.25 and Figure 4.26 show the acceleration data at free vibration after the occurrence of ground motion excitation, and also, force versus relative displacement data during the earthquake excitation, respectively. Table 4.13 shows the calculated damping ratio of the system in both methods.

Table 4.13. Damping ratio calculated with different methods.

Logarithmic Decrement	0.00230
Chopra's Method	0.01140

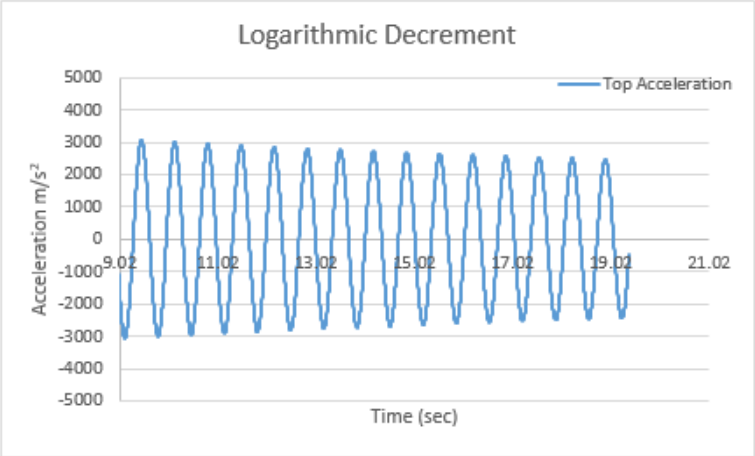

Figure 4.25. Post-earthquake Data.

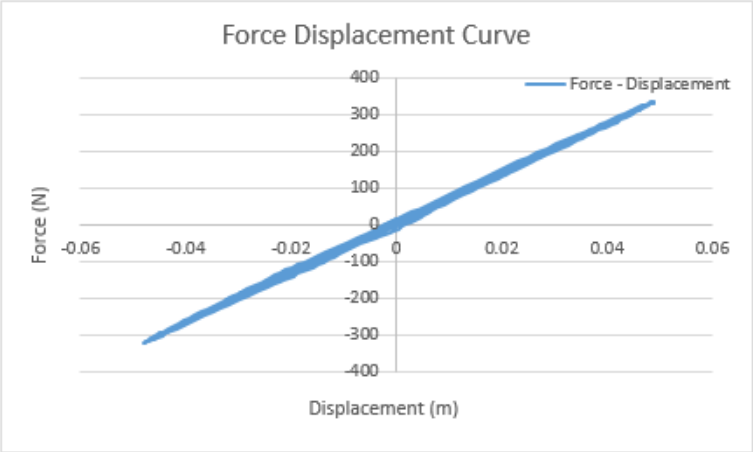

Figure 4.26. Force-Displacement Data.

4.1.14. T=0.667 sec, 0.30 San Salvador Experimental Results

Figure 4.27 and Figure 4.28 show the acceleration data at free vibration after the occurrence of ground motion excitation, and also, force versus relative displacement data during the earthquake excitation, respectively. Table 4.14 shows the calculated damping ratio of the system in both methods.

Table 4.14. Damping ratio calculated with different methods.

Logarithmic Decrement	0.00341
Chopra's Method	0.02080

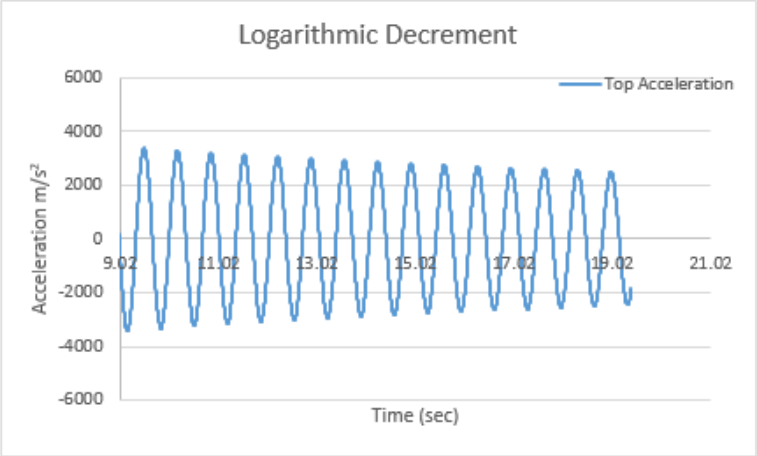

Figure 4.27. Post-earthquake Data.

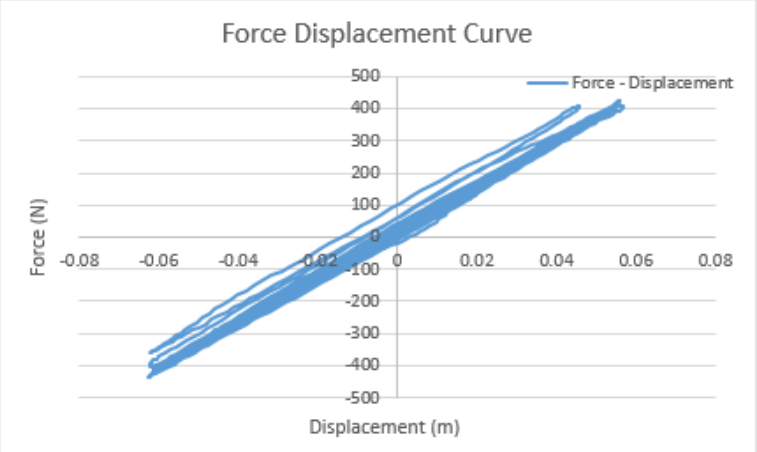

Figure 4.28. Force-Displacement Data.

4.1.15. T=0.667 sec, 0.40 San Salvador Experimental Results

Figure 4.29 and Figure 4.30 show the acceleration data at free vibration after the occurrence of ground motion excitation, and also, force versus relative displacement data during the earthquake excitation, respectively. Table 4.15 shows the calculated damping ratio of the system in both methods.

Table 4.15. Damping ratio calculated with different methods.

Logarithmic Decrement	0.00354
Chopra's Method	0.03820

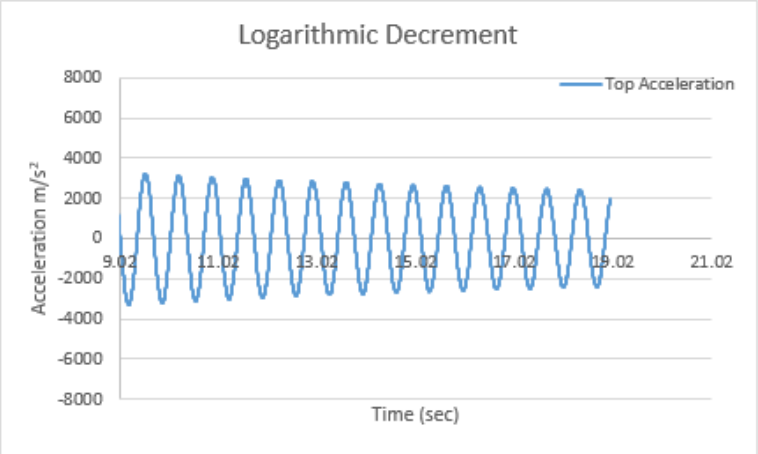

Figure 4.29. Post-earthquake Data.

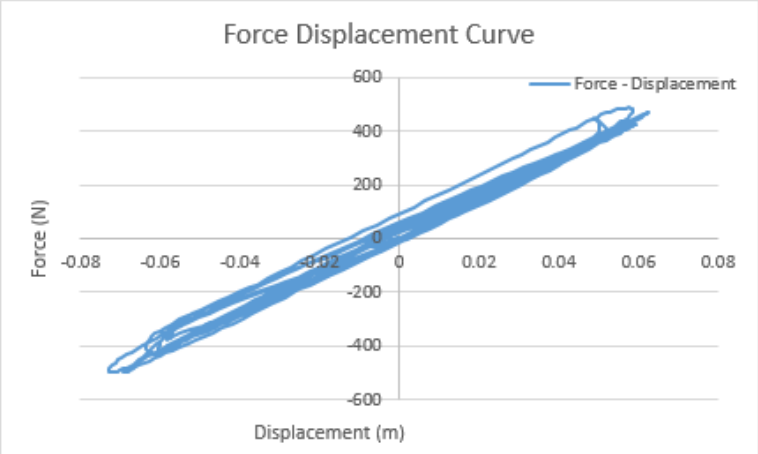

Figure 4.30. Force-Displacement Data.

4.1.16. T=0.667 sec, 0.50 San Salvador Experimental Results

Figure 4.31 and Figure 4.32 show the acceleration data at free vibration after the occurrence of ground motion excitation, and also, force versus relative displacement data during the earthquake excitation, respectively. Table 4.16 shows the calculated damping ratio of the system in both methods.

Table 4.16. Damping ratio calculated with different methods.

Logarithmic Decrement	0.00355
Chopra's Method	0.02690

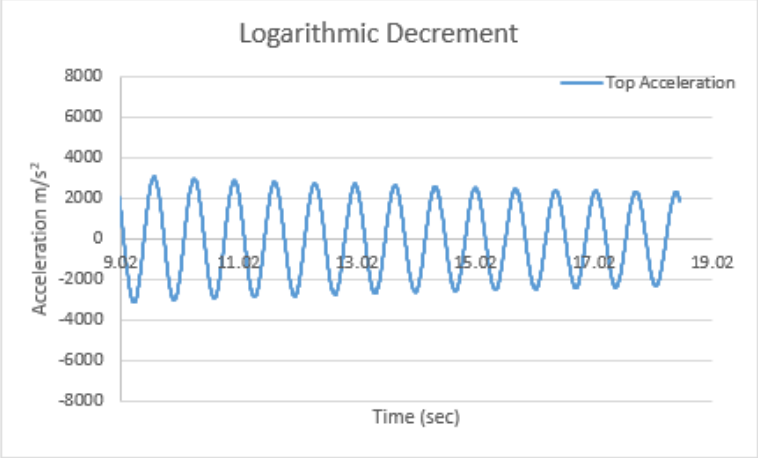

Figure 4.31. Post-earthquake Data.

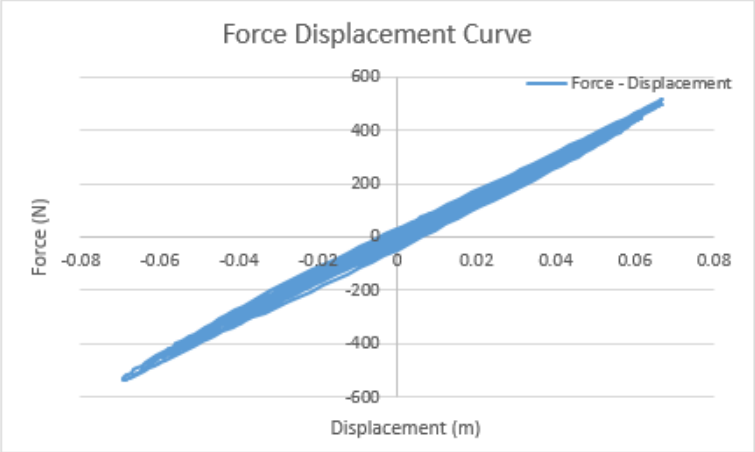

Figure 4.32. Force-Displacement Data.

4.1.17. T=0.667 sec, 0.60 San Salvador Experimental Results

Figure 4.33 and Figure 4.34 show the acceleration data at free vibration after the occurrence of ground motion excitation, and also, force versus relative displacement data during the earthquake excitation, respectively. Table 4.17 shows the calculated damping ratio of the system in both methods.

Table 4.17. Damping ratio calculated with different methods.

Logarithmic Decrement	0.00374
Chopra's Method	0.03180

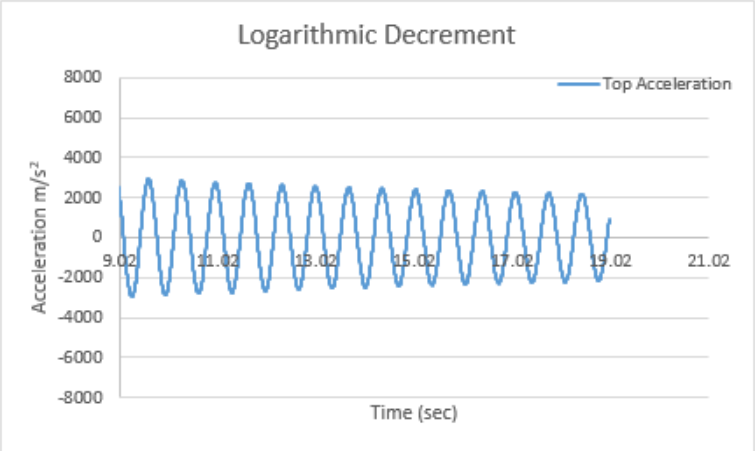

Figure 4.33. Post-earthquake Data.

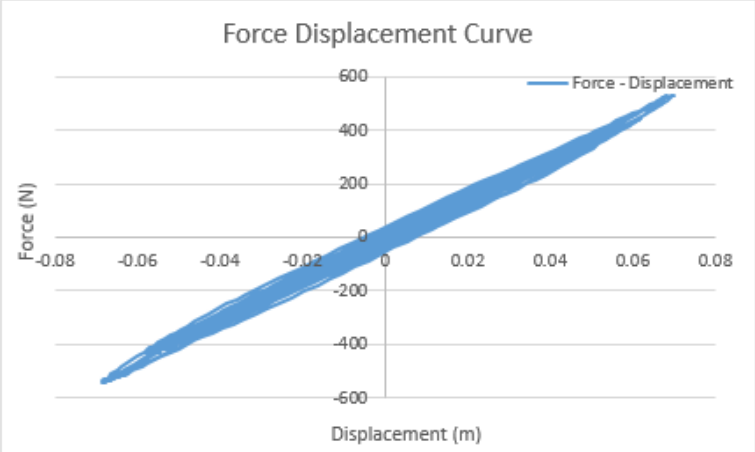

Figure 4.34. Force-Displacement Data.

4.1.18. T=0.667 sec, 0.70 San Salvador Experimental Results

Figure 4.35 and Figure 4.36 show the acceleration data at free vibration after the occurrence of ground motion excitation, and also, force versus relative displacement data during the earthquake excitation, respectively. Table 4.18 shows the calculated damping ratio of the system in both methods.

Table 4.18. Damping ratio calculated with different methods.

Logarithmic Decrement	0.00373
Chopra's Method	0.03570

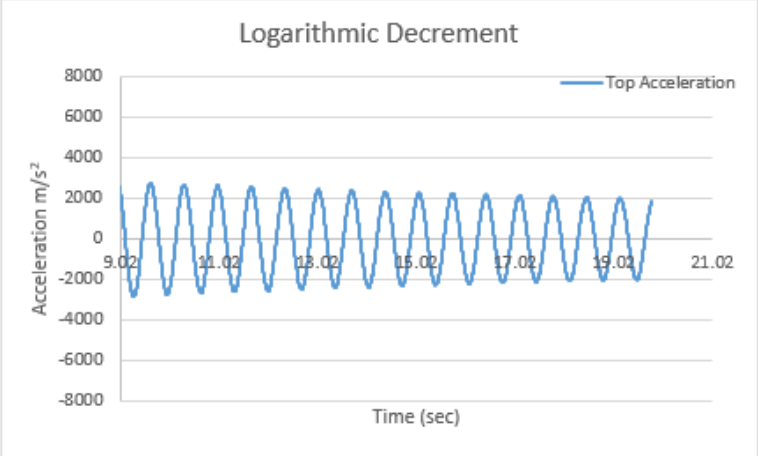

Figure 4.35. Post-earthquake Data.

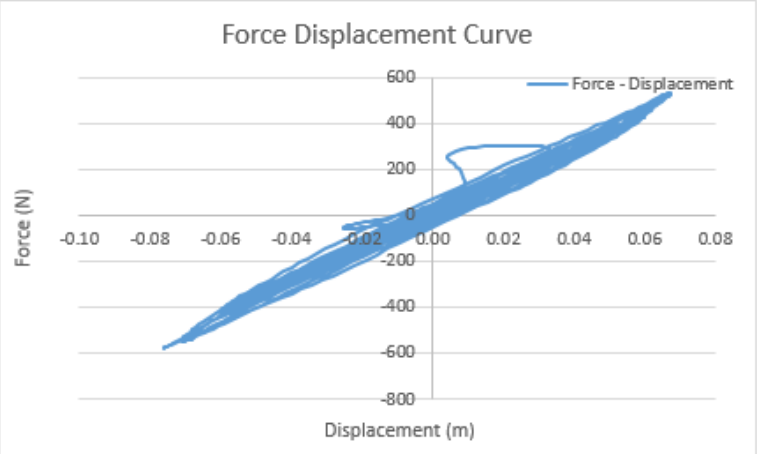

Figure 4.36. Force-Displacement Data.

4.1.19. T=0.667 sec, 0.80 San Salvador Experimental Results

Figure 4.37 and Figure 4.38 show the acceleration data at free vibration after the occurrence of ground motion excitation, and also, force versus relative displacement data during the earthquake excitation, respectively. Table 4.19 shows the calculated damping ratio of the system in both methods.

Table 4.19. Damping ratio calculated with different methods.

Logarithmic Decrement	0.00388
Chopra's Method	0.02980

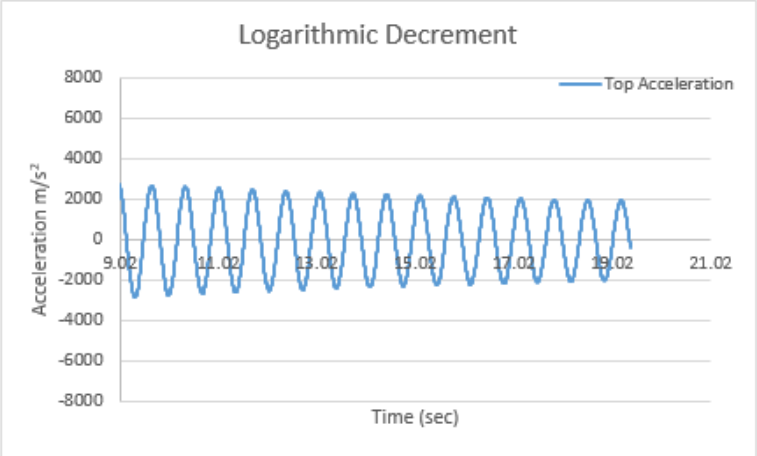

Figure 4.37. Post-earthquake Data.

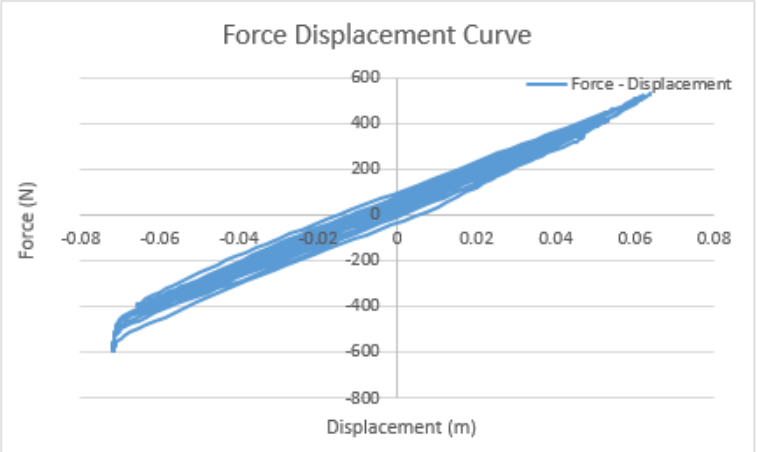

Figure 4.38. Force-Displacement Data.

4.1.20. T=0.667 sec, 0.90 San Salvador Experimental Results

Figure 4.39 and Figure 4.40 show the acceleration data at free vibration after the occurrence of ground motion excitation, and also, force versus relative displacement data during the earthquake excitation, respectively. Table 4.20 shows the calculated damping ratio of the system in both methods.

Table 4.20. Damping ratio calculated with different methods.

Logarithmic Decrement	0.00610
Chopra's Method	0.09000

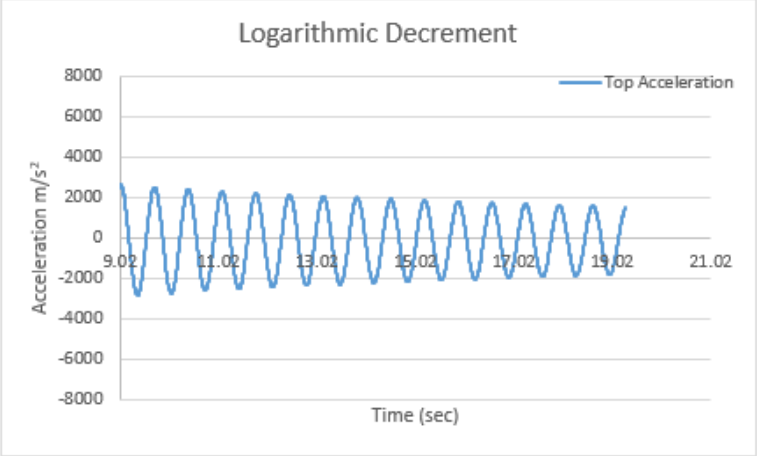

Figure 4.39. Post-earthquake Data.

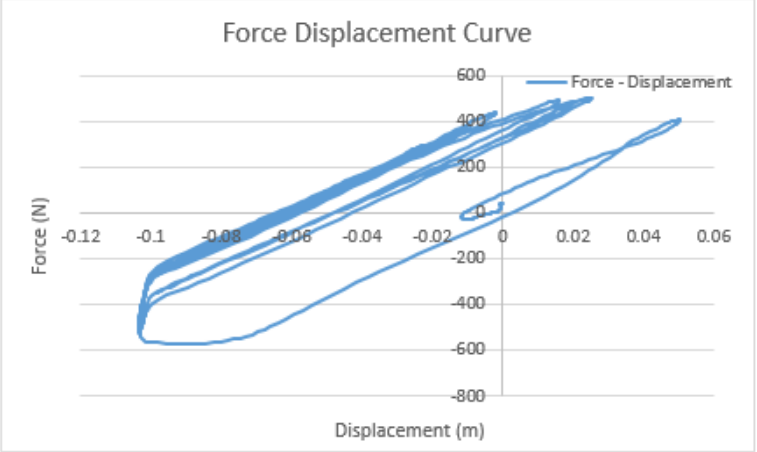

Figure 4.40. Force-Displacement Data.

4.1.21. T=0.667 sec, 1.00 San Salvador Experimental Results

Figure 4.41 and Figure 4.42 show the acceleration data at free vibration after the occurrence of ground motion excitation, and also, force versus relative displacement data during the earthquake excitation, respectively. Table 4.21 shows the calculated damping ratio of the system in both methods.

Table 4.21. Damping ratio calculated with different methods.

Logarithmic Decrement	0.00480
Chopra's Method	0.10910

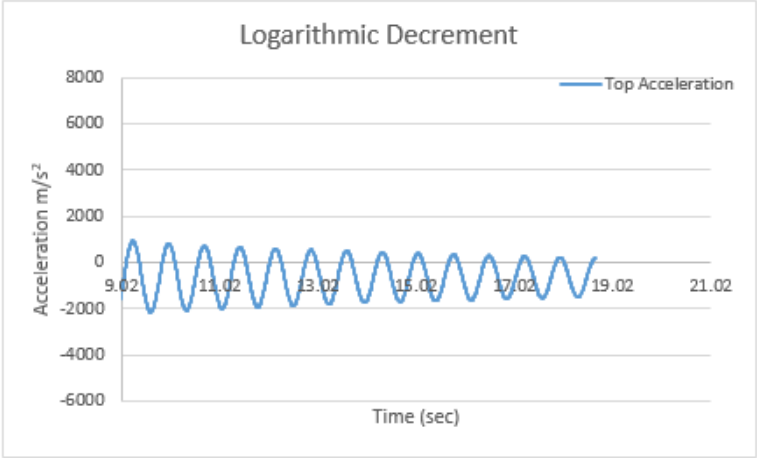

Figure 4.41. Post-earthquake Data.

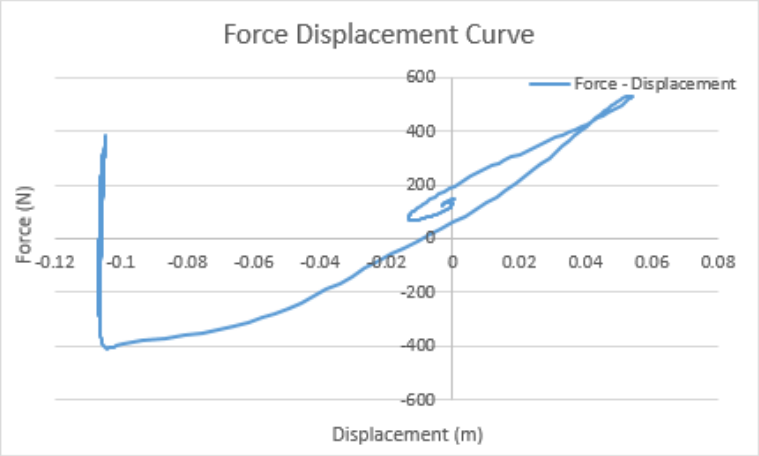

Figure 4.42. Force-Displacement Data.

4.1.22. T=1.00 sec, 0.20 San Salvador Experimental Results

Figure 4.43 and Figure 4.44 show the acceleration data at free vibration after the occurrence of ground motion excitation, and also, force versus relative displacement data during the earthquake excitation, respectively. Table 4.22 shows the calculated damping ratio of the system in both methods.

Table 4.22. Damping ratio calculated with different methods.

Logarithmic Decrement	0.00200
Chopra's Method	0.00650

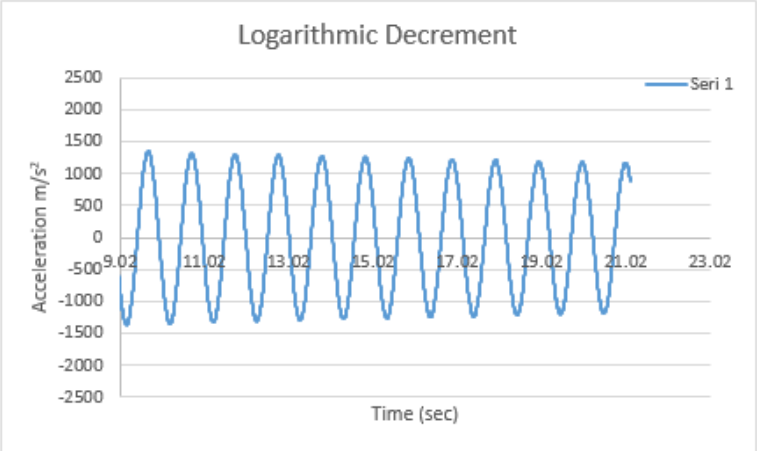

Figure 4.43. Post-earthquake Data.

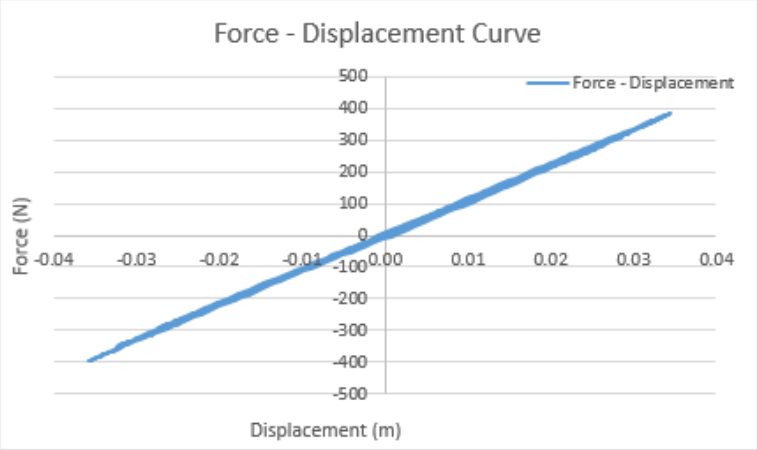

Figure 4.44. Force-Displacement Data.

4.1.23. T=1.00 sec, 0.30 San Salvador Experimental Results

Figure 4.45 and Figure 4.46 show the acceleration data at free vibration after the occurrence of ground motion excitation, and also, force versus relative displacement data during the earthquake excitation, respectively. Table 4.23 shows the calculated damping ratio of the system in both methods.

Table 4.23. Damping ratio calculated with different methods.

Logarithmic Decrement	0.00300
Chopra's Method	0.01060

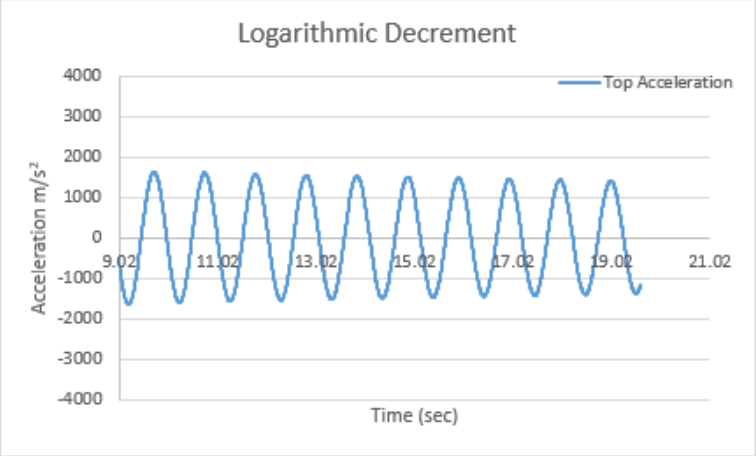

Figure 4.45. Post-earthquake Data.

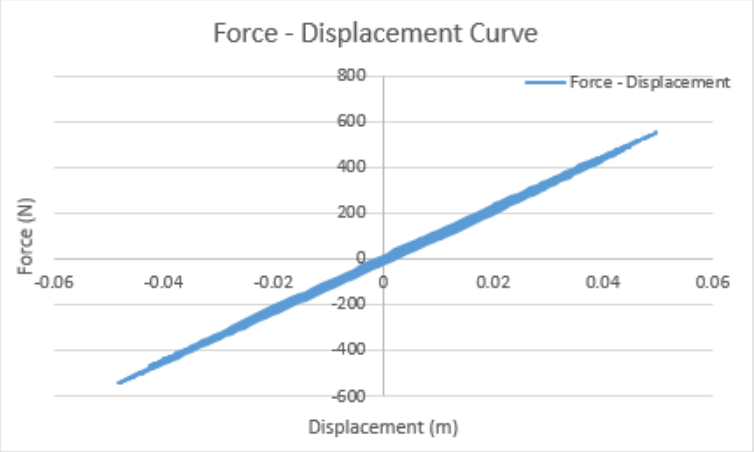

Figure 4.46. Force-Displacement Data.

4.1.24. T=1.00 sec, 0.40 San Salvador Experimental Results

Figure 4.47 and Figure 4.48 show the acceleration data at free vibration after the occurrence of ground motion excitation, and also, force versus relative displacement data during the earthquake excitation, respectively. Table 4.24 shows the calculated damping ratio of the system in both methods.

Table 4.24. Damping ratio calculated with different methods.

Logarithmic Decrement	0.00300
Chopra's Method	0.01530

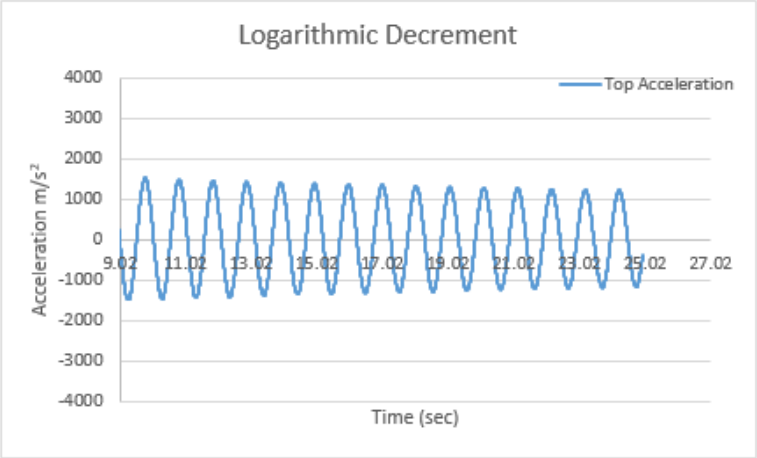

Figure 4.47. Post-earthquake Data.

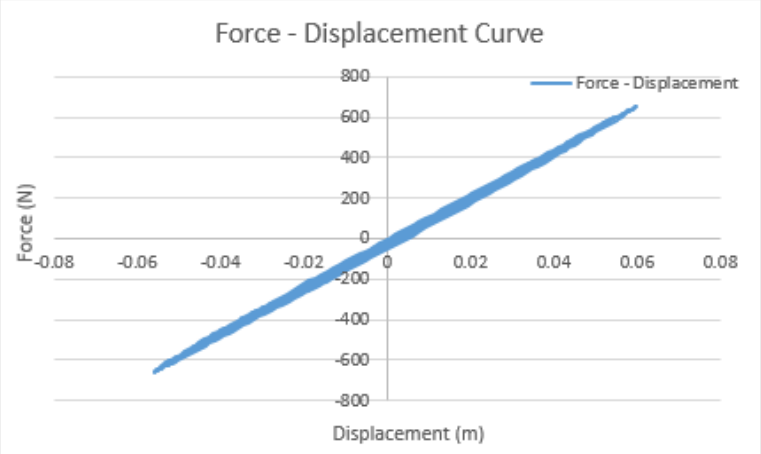

Figure 4.48. Force-Displacement Data.

4.1.25. T=1.00 sec, 0.50 San Salvador Experimental Results

Figure 4.49 and Figure 4.50 show the acceleration data at free vibration after the occurrence of ground motion excitation, and also, force versus relative displacement data during the earthquake excitation, respectively. Table 4.25 shows the calculated damping ratio of the system in both methods.

Table 4.25. Damping ratio calculated with different methods.

Logarithmic Decrement	0.00357
Chopra's Method	0.01650

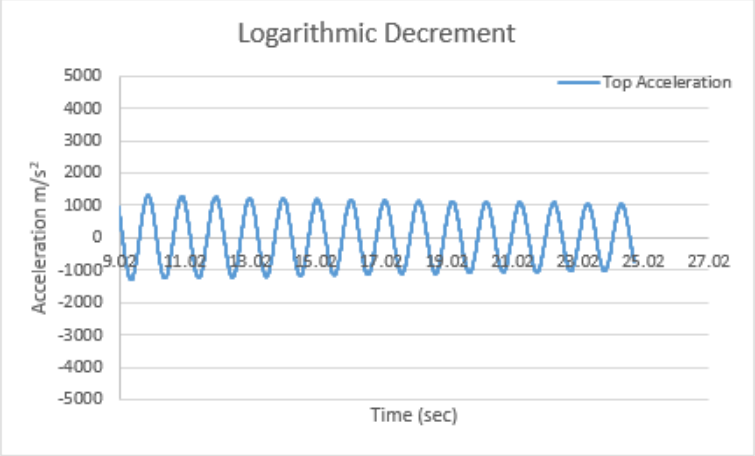

Figure 4.49. Post-earthquake Data.

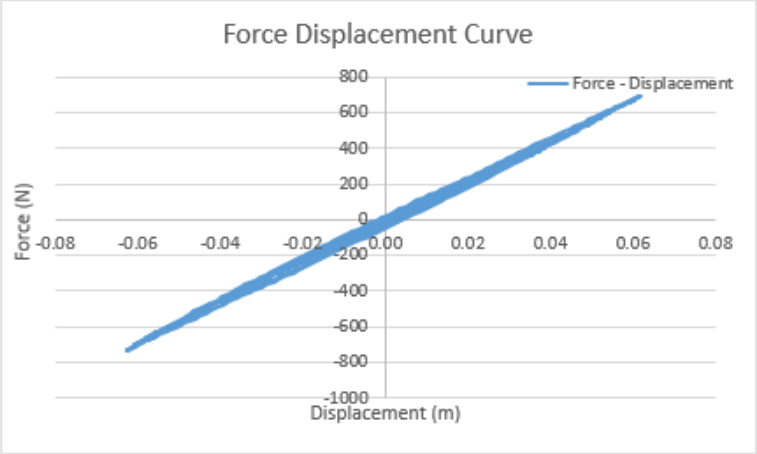

Figure 4.50. Force-Displacement Data.

4.1.26. T=1.00 sec, 0.60 San Salvador Experimental Results

Figure 4.51 and Figure 4.52 show the acceleration data at free vibration after the occurrence of ground motion excitation, and also, force versus relative displacement data during the earthquake excitation, respectively. Table 4.26 shows the calculated damping ratio of the system in both methods.

Table 4.26. Damping ratio calculated with different methods.

Logarithmic Decrement	0.00294
Chopra's Method	0.01960

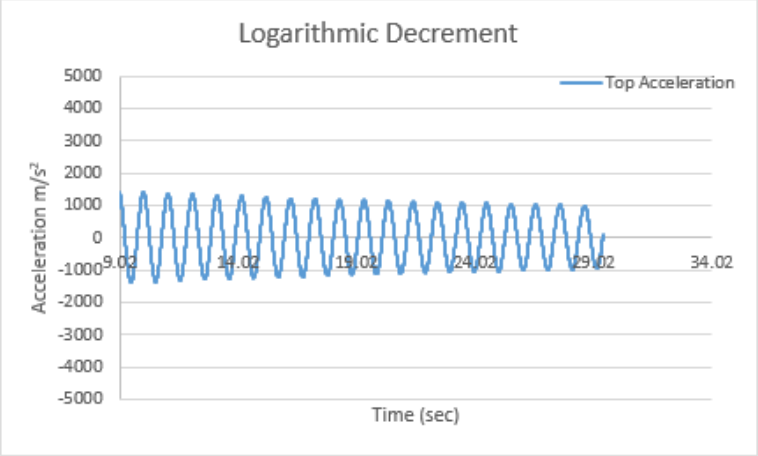

Figure 4.51. Post-earthquake Data.

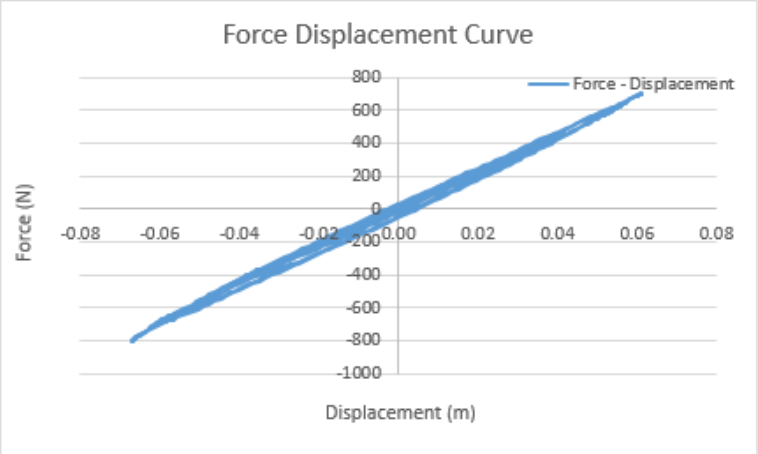

Figure 4.52. Force-Displacement Data.

4.1.27. T=1.00 sec, 0.70 San Salvador Experimental Results

Figure 4.53 and Figure 4.54 show the acceleration data at free vibration after the occurrence of ground motion excitation, and also, force versus relative displacement data during the earthquake excitation, respectively. Table 4.27 shows the calculated damping ratio of the system in both methods.

Table 4.27. Damping ratio calculated with different methods.

Logarithmic Decrement	0.00415
Chopra's Method	0.01940

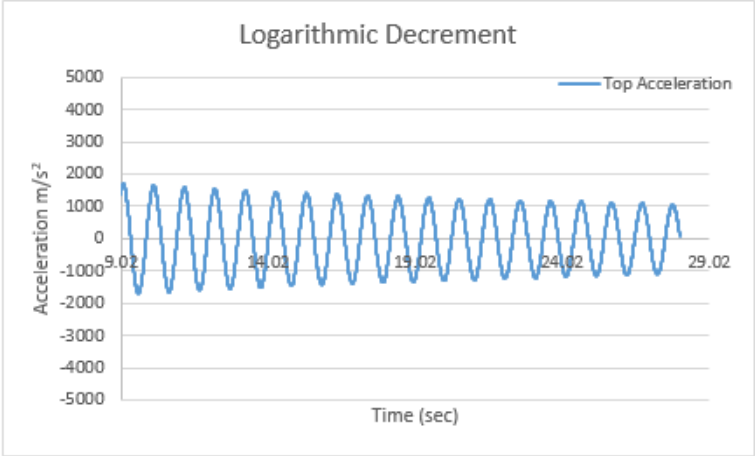

Figure 4.53. Post-earthquake Data.

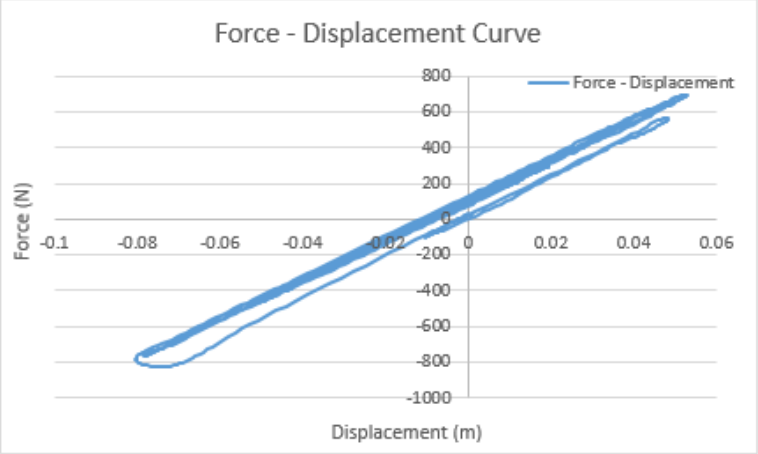

Figure 4.54. Force-Displacement Data.

4.1.28. T=1.00 sec, 0.80 San Salvador Experimental Results

Figure 4.55 and Figure 4.56 show the acceleration data at free vibration after the occurrence of ground motion excitation, and also, force versus relative displacement data during the earthquake excitation, respectively. Table 4.28 shows the calculated damping ratio of the system in both methods.

Table 4.28. Damping ratio calculated with different methods.

Logarithmic Decrement	0.00648
Chopra's Method	0.07450

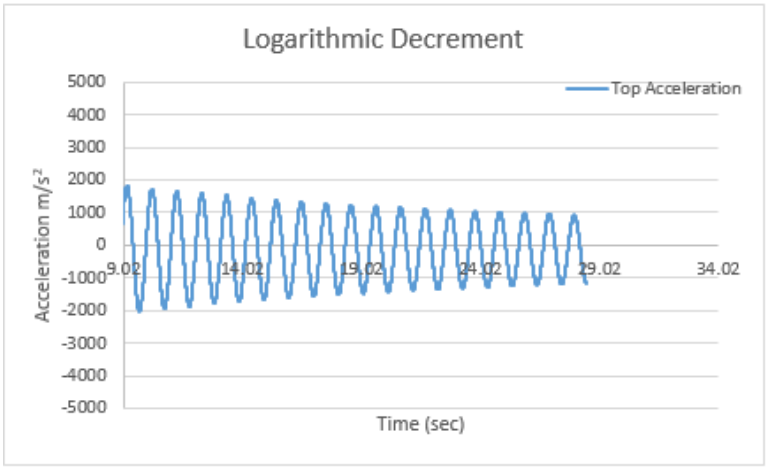

Figure 4.55. Post-earthquake Data.

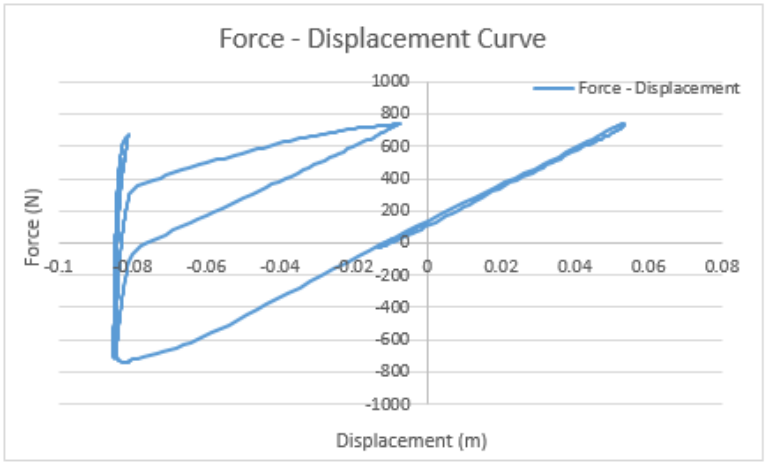

Figure 4.56. Force-Displacement Energy Comparisons of All Experiments.

Force-deformation curves verify that all three specimens exceeded their elastic displacement limits. According to experimental data shown above, there are some major differences between logarithmic decrement and Chopra's methods in the determination of damping ratios. As the hysteretic behavior became closer to linear range, logarithmic decrement somewhat gave better energy results.

4.2. Energy Components

Figure 4.5 shows the mass-normalized Input Energy (E_I/m), mass-normalized Damping Energy (E_D/m), mass-normalized Strain Energy (E_S/m) and mass-normalized

Kinetic Energy (E_K/m) of the system according to both damping ratios. Energy graphs were produced using code developed with Matlab software.

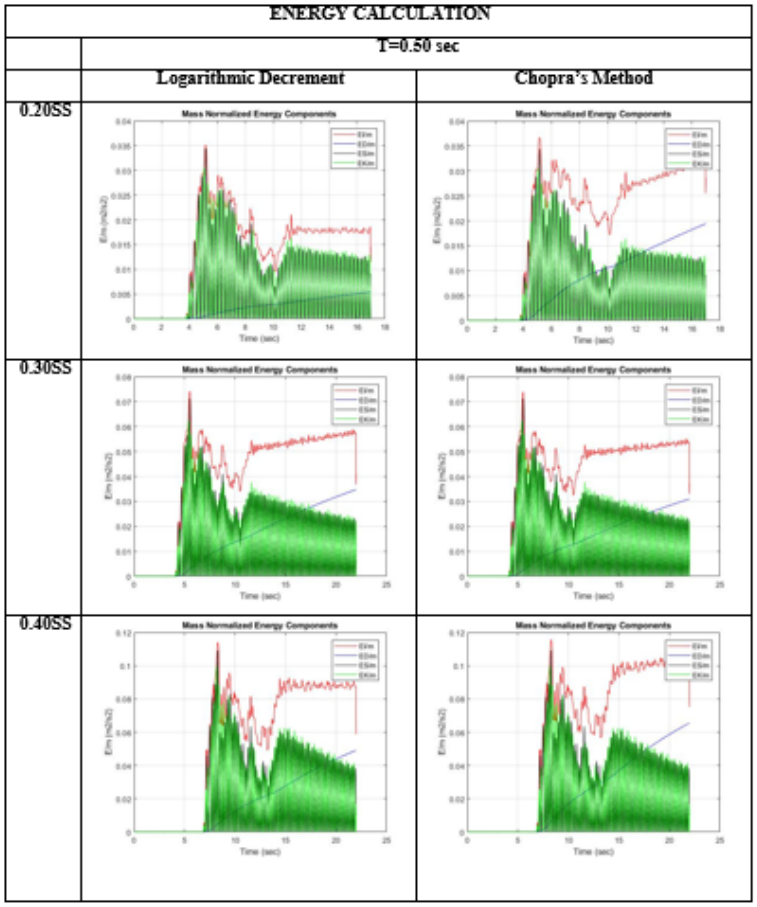

Figure 4.57. Energy Comparisons of All Experiments (T=0.50 sec).

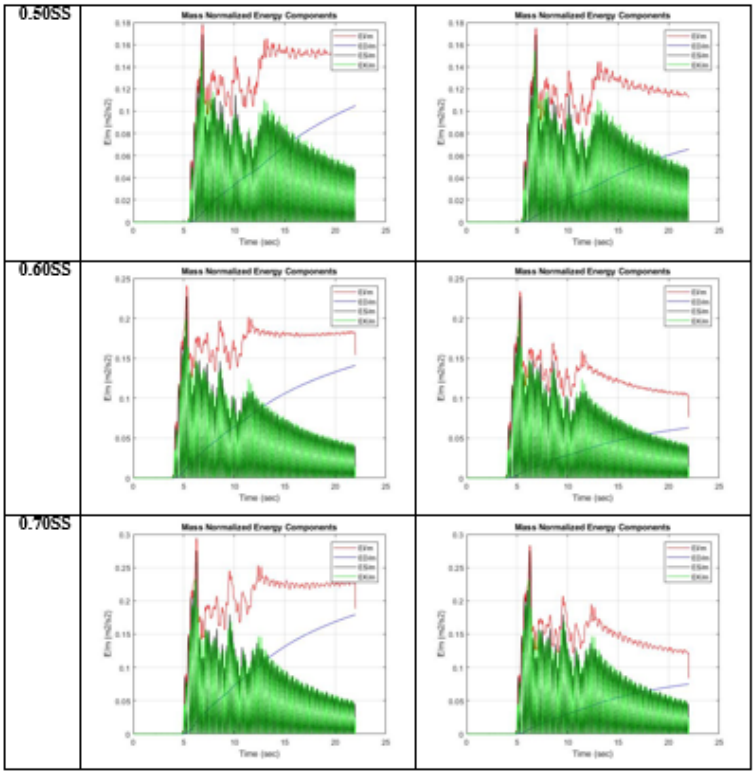

Figure 4.58. Energy Comparisons of All Experiments (T=0.50 sec)(Cont.).

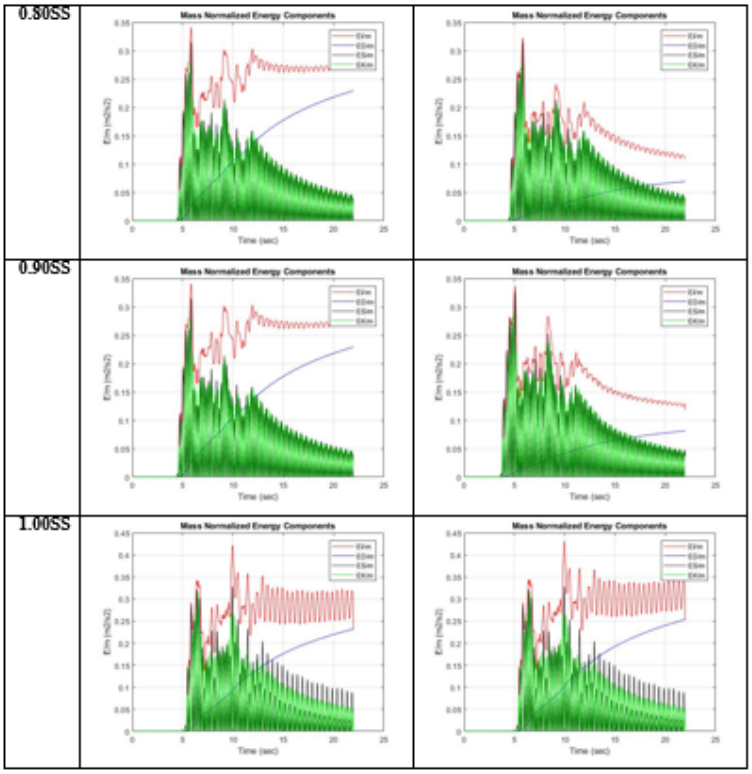

Figure 4.59. Energy Comparisons of All Experiments (T=0.50 sec)(Cont.).

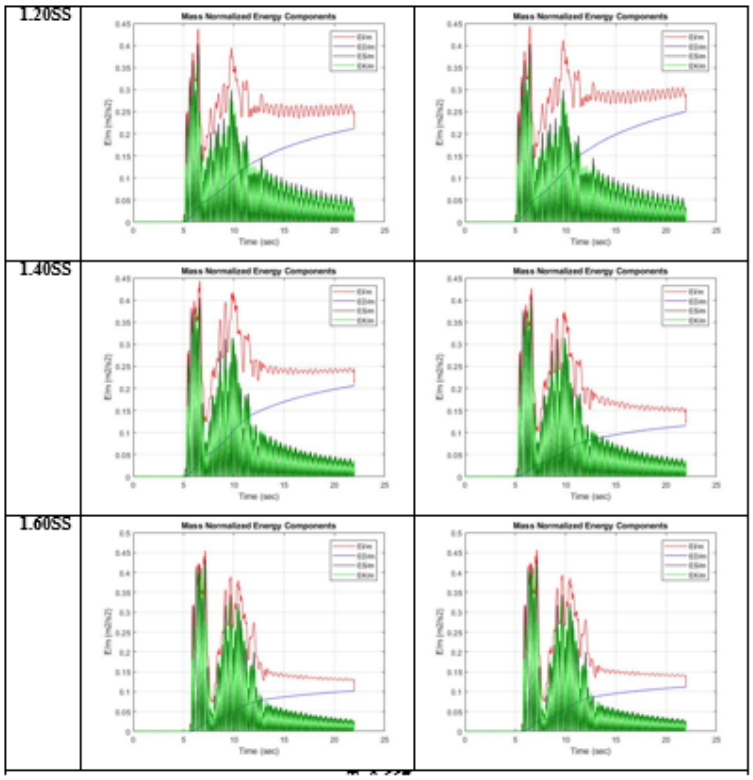

Figure 4.60. Energy Comparisons of All Experiments (T=0.50 sec)(Cont.).

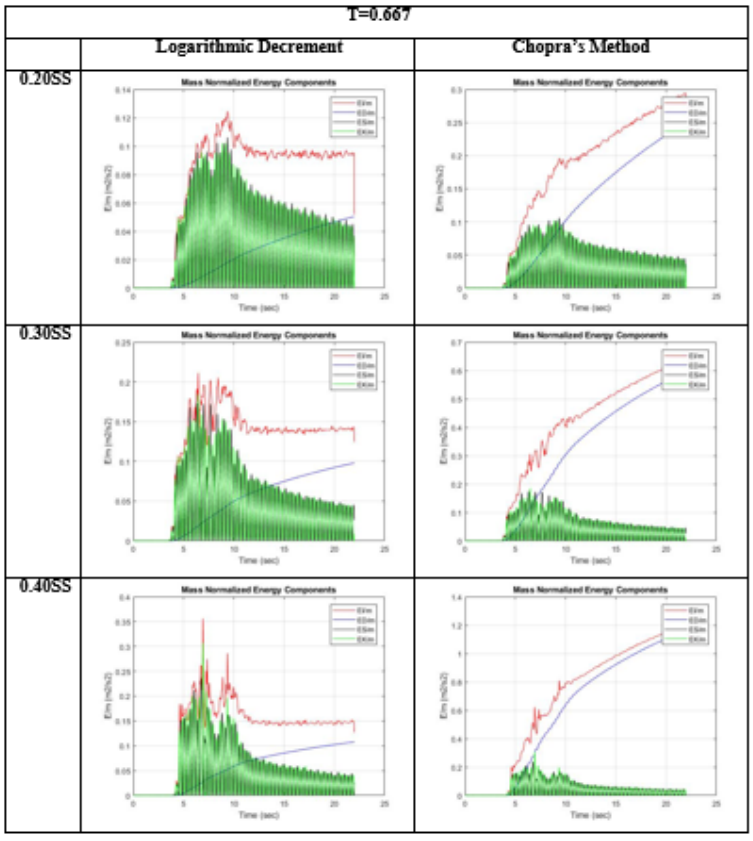

Figure 4.61. Energy Comparisons of All Experiments (T=0.667).

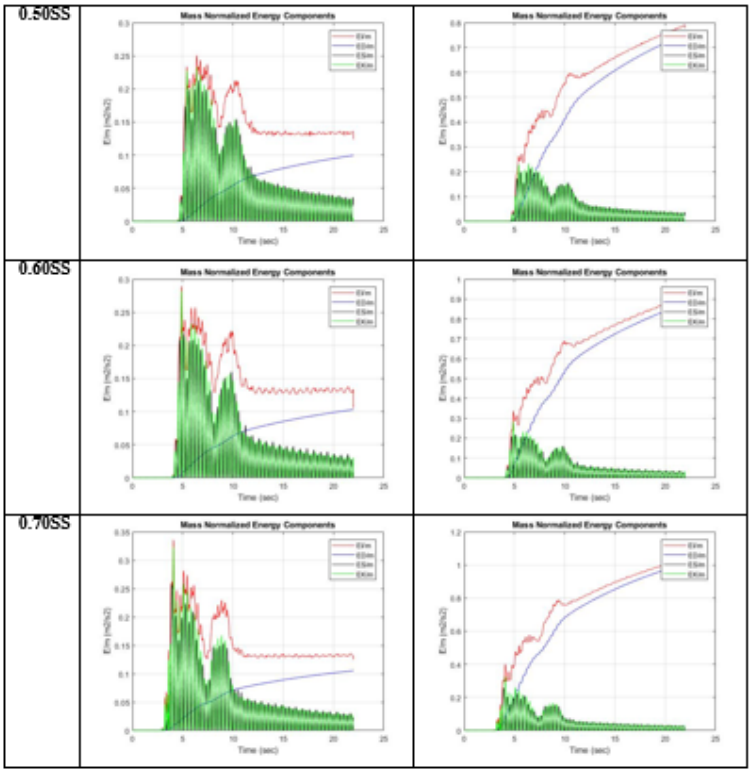

Figure 4.62. Energy Comparisons of All Experiments (T=0.667)(Cont.).

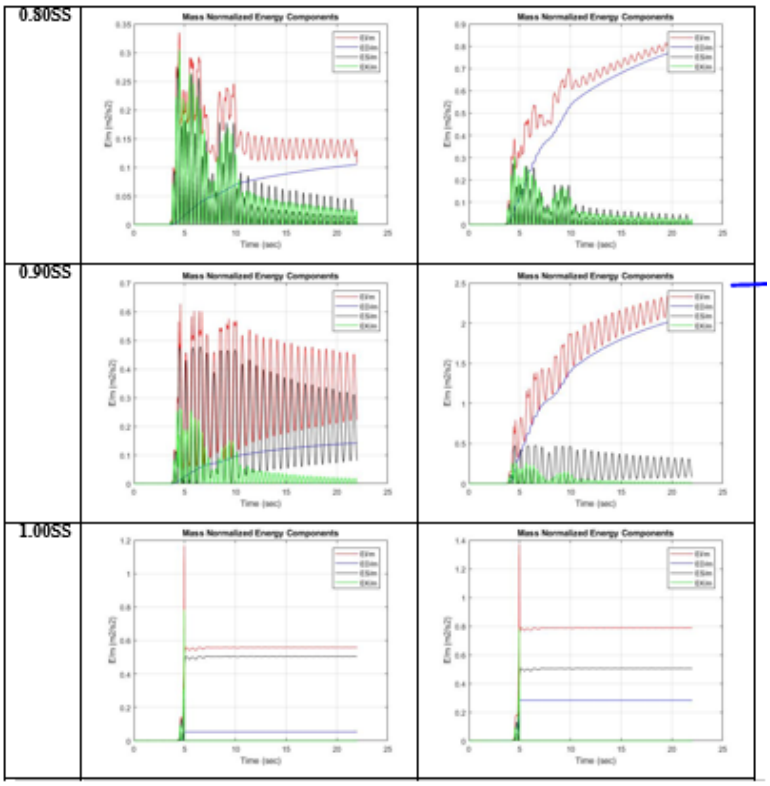

Figure 4.63. Energy Comparisons of All Experiments (T=0.50 sec)(Cont.).

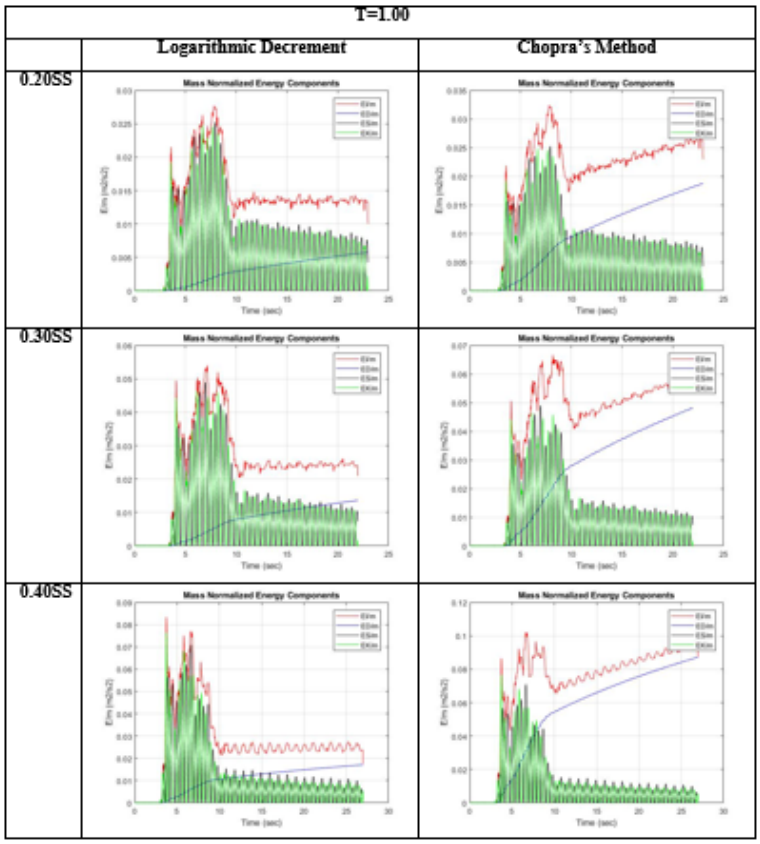

Figure 4.64. Energy Comparisons of All Experiments (T=1.00).

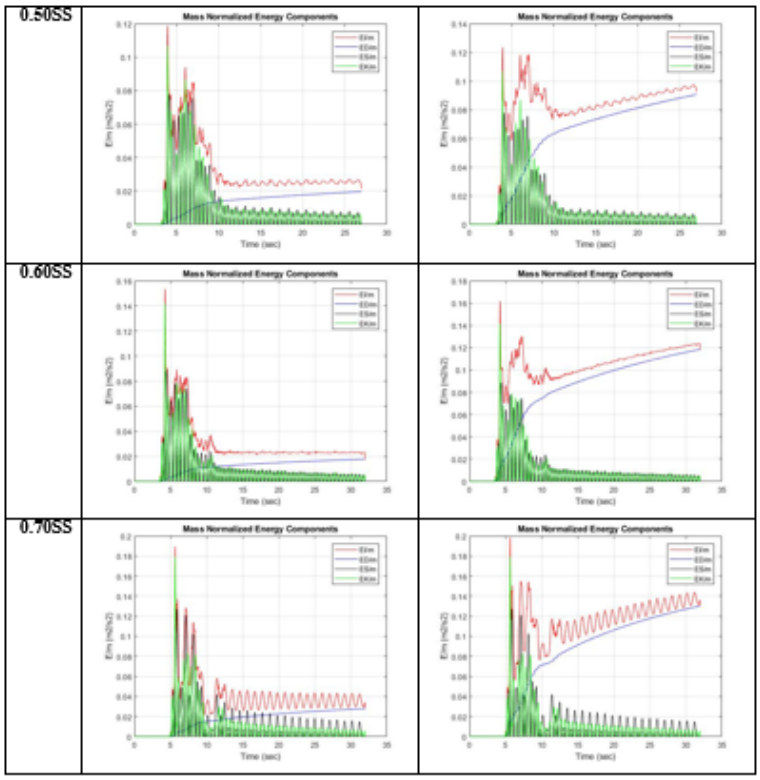

Figure 4.65. Energy Comparisons of All Experiments (T=1.00)(Cont.).

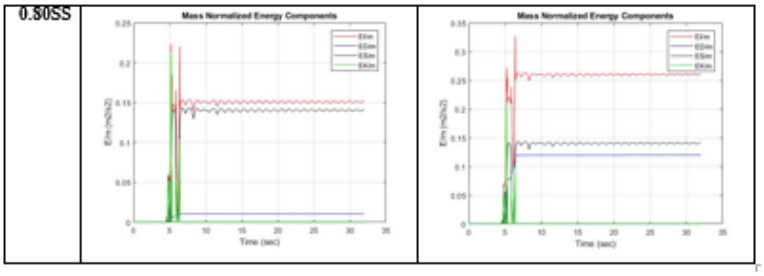

Figure 4.66. Energy Comparisons of All Experiments (T=1.00)(Cont.).

As seen in the graphs above, there are certain differences between some of the mass-normalized Input Energy values when the same scale factors were evaluated. The difference between 12 out of 28 experiments in terms of mass-normalized Input Energy values were noticeable. When two energies with same scale factor and same period were compared, the only variable was damping ratio.

4.3. Damping Ratio and Input Energy Relation

Figure 4.67 and Figure 4.69 show the damping ratio of the system with varying scale factors using logarithmic decrement and Chopra's methods. Also, Figure 4.688 and Figure 4.70 demonstrate mass-normalized Input Energy of the system with varying scale factors with both methods.

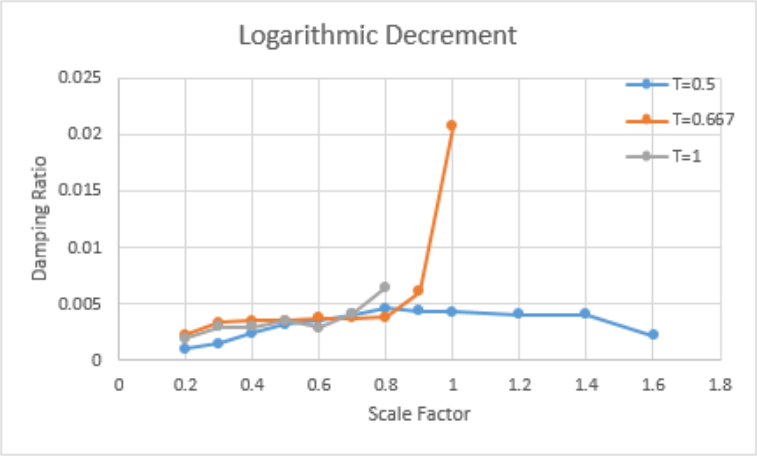

Figure 4.67. Damping Ratio with varying Scale Factors.

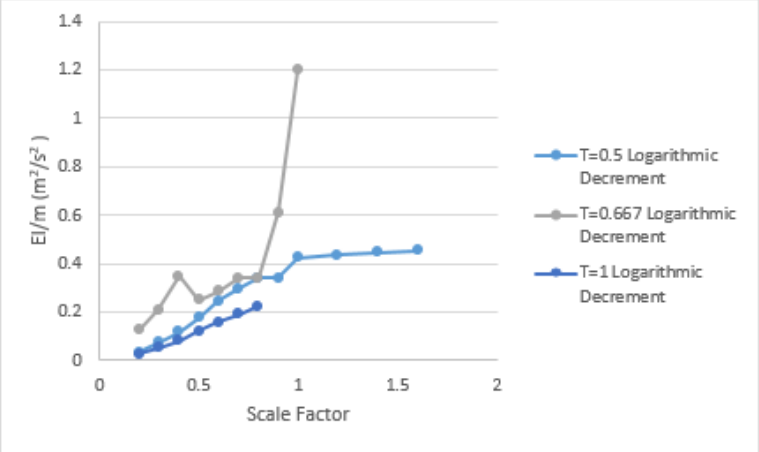

Figure 4.68. Mass-Normalized Input Energy with varying Scale Factors.

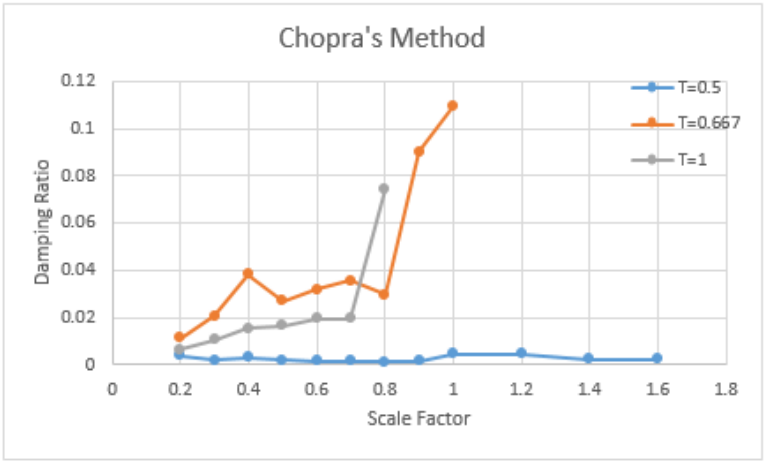

Figure 4.69. Damping Ratio with varying Scale Factors.

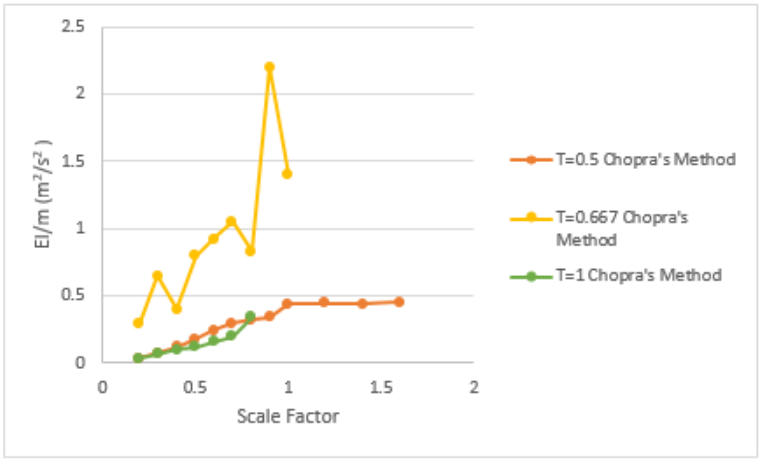

Figure 4.70. Mass-Normalized Input Energy with varying Scale Factors.

The graphs above show that there is a definite relationship between damping ratio and mass-normalized Input Energy. The similar trend between damping ratio versus scale factor graphs and mass-normalized Input Energy versus scale factor graphs is apparent. Inconsistency in Input Energy of experiment 21 (1.00 scale factor, T=0.667 period) in Chopra's Method could be explained with irregularity in Figure 4.42.

4.4. Verification of Güllü's Input Energy Spectrum

As mentioned in the Section 2.4., Input Energy spectra were plotted for all experiments using different calculated damping ratios. Mass-normalized Input Energies

from Section 4.2. were compared with these spectral values. Figure 4.71 to Figure 4.82 show the Input Energy spectra and mass-normalized Input Energies from experiments.

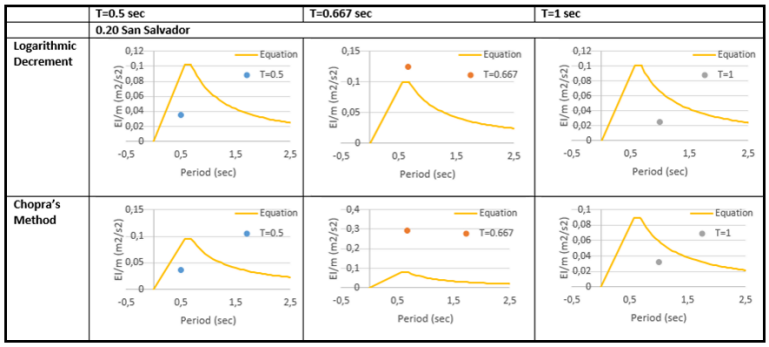

Figure 4.71. 0.20 Scale Factor San Salvador Input Energy Spectrum.

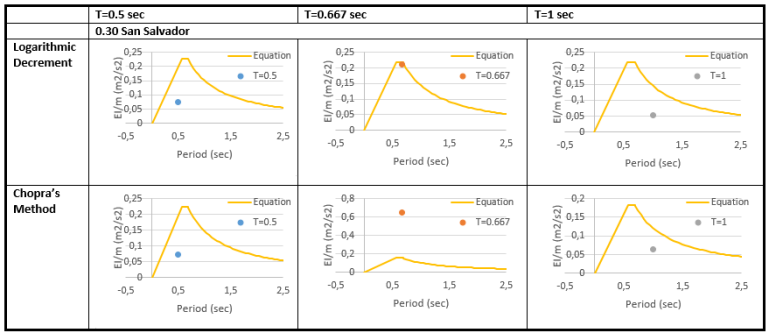

Figure 4.72. 0.30 Scale Factor San Salvador Input Energy Spectrum.

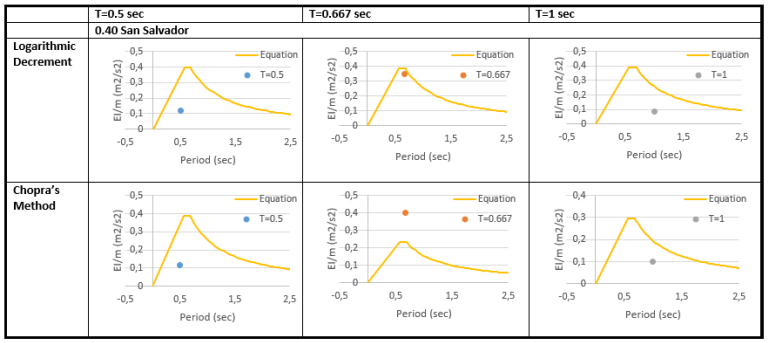

Figure 4.73. 0.40 Scale Factor San Salvador Input Energy Spectrum.

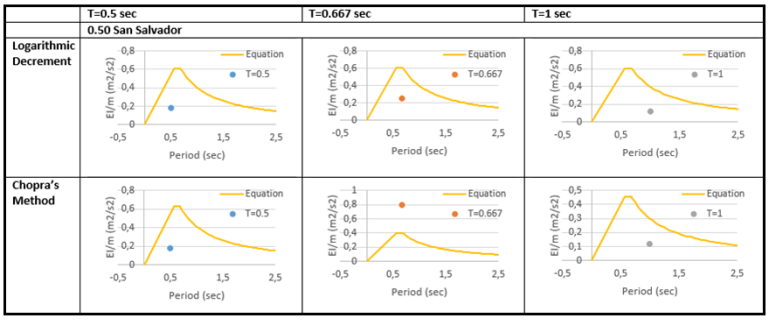

Figure 4.74. 0.50 Scale Factor San Salvador Input Energy Spectrum.

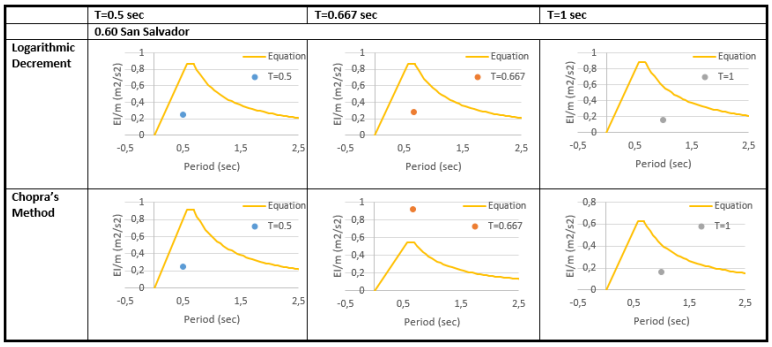

Figure 4.75. 0.60 Scale Factor San Salvador Input Energy Spectrum.

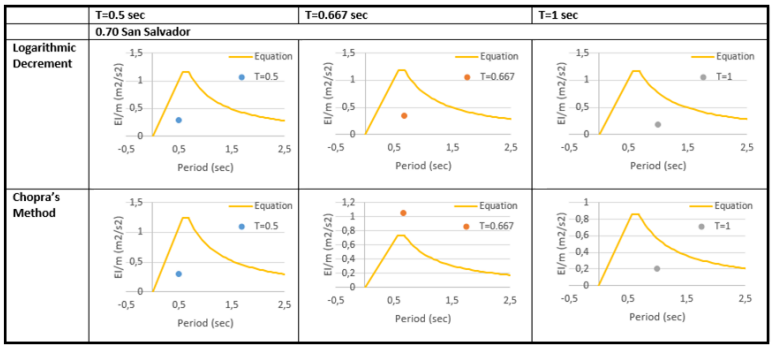

Figure 4.76. 0.70 Scale Factor San Salvador Input Energy Spectrum.

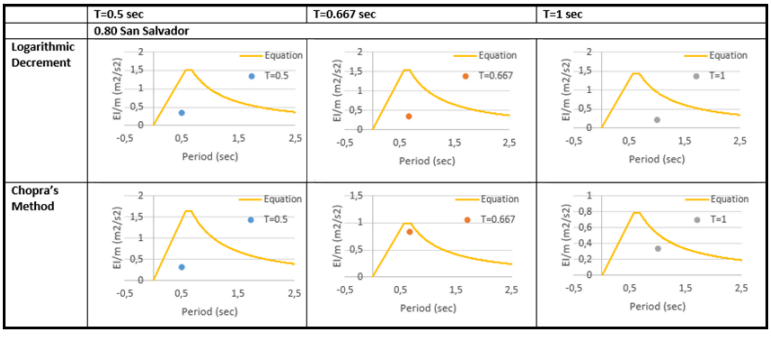

Figure 4.77. 0.80 Scale Factor San Salvador Input Energy Spectrum.

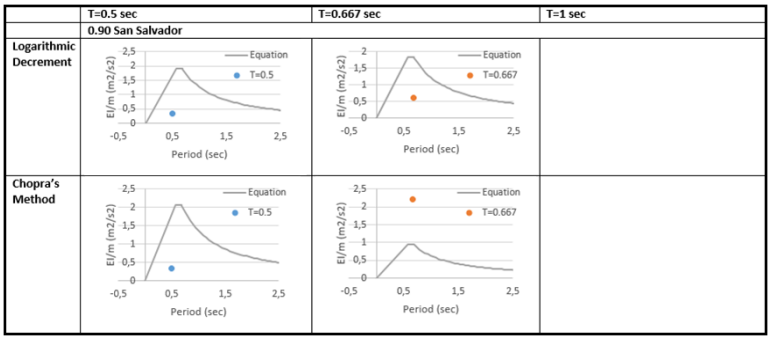

Figure 4.78. 0.90 Scale Factor San Salvador Input Energy Spectrum.

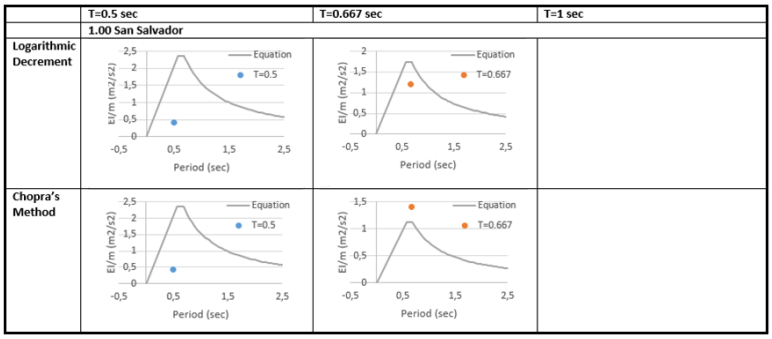

Figure 4.79. 1.00 Scale Factor San Salvador Input Energy Spectrum.

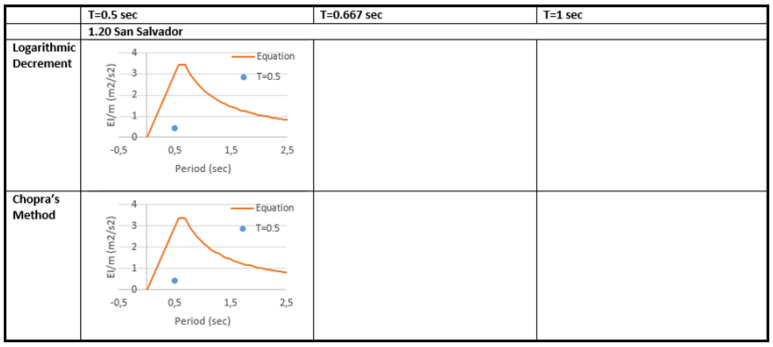

Figure 4.80. 1.20 Scale Factor San Salvador Input Energy Spectrum.

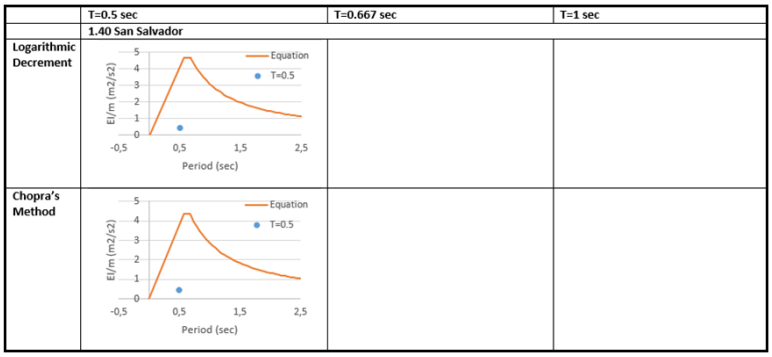

Figure 4.81. 1.40 Scale Factor San Salvador Input Energy Spectrum.

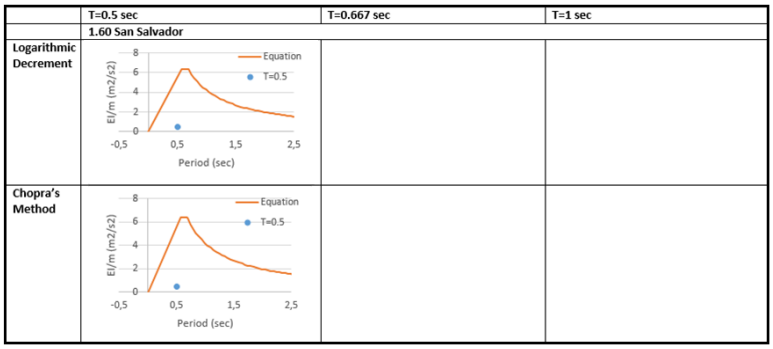

Figure 4.82. 1.60 Scale Factor San Salvador Input Energy Spectrum.

As shown in the previous sections, the damping ratios calculated from Chopra's method are much greater than those damping ratios calculated from logarithmic decrement method. The increase in damping ratio boosts the input energies. Besides, in (Güllü, 2019) Spectra, increase in damping ratio lowers the input energy limits because it lowers the maximum spectral velocity and spectral acceleration. Therefore, input energy corresponds to corner period decreased. Mass-normalized input energy of 27 experiments stays below the limits for logarithmic decrement method. On the other hand, input energy of 20 experiments stays below the limits for Chopra's method. Also, trends in all graphs obtained from experimental data was consistent for different intensities. For periods 0.5 sec. and 1.0 sec., mass-normalized input energies from experimental data were below the limits as shown in the Figure 4.83. Yet, for period 0.667 sec, mass-normalized input energies from experimental data reached the peaks successfully and in some cases it exceeded the peaks far too much. High damping ratios obtained from Chopra's method can be shown as the reason for this. The aim of this design spectra is to reach peak for resonance period which is 0.667 sec for this system.

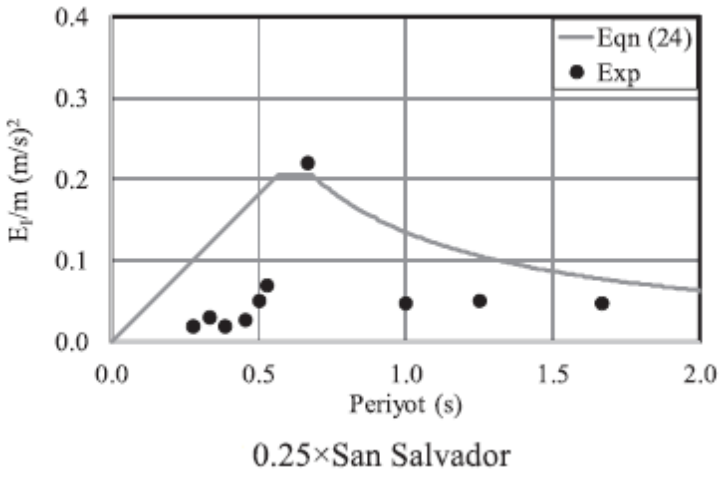

Figure 4.83. The proposed record-specific input energy spectrum vs the experimental results (Güllü, 2019).

According to close form method developed by (Güllü, 2018), mass-normalized input energies for original record were obtained. Elastic and inelastic cases were compared. Trends were re-aligned again. Figure 4.84 and Figure 4.85 shows the spectra and mass-normalized input energies. As damping ratio were increased, the compliance with trend decreased.

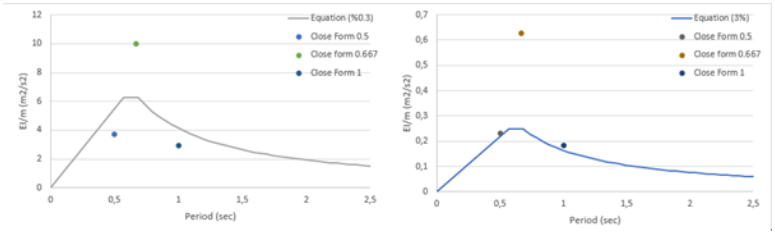

Figure 4.84. 0.4 Scale Factor San Salvador (ζ=0.3 and ζ=3).

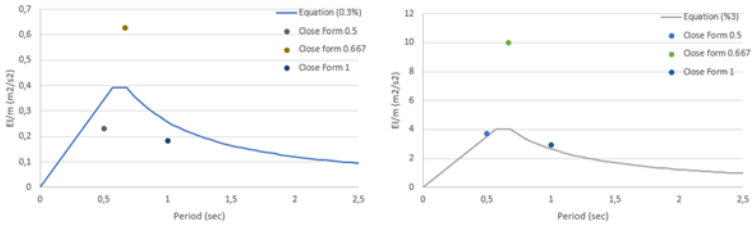

Figure 4.85. 1.6 Scale Factor San Salvador (ζ=0.3 and ζ=3).

5. SUMMARY AND CONCLUSIONS

In this study, Energy-Based approach was used to analyze extensive experimental work. 0.75-meter high 3 identical SDOF specimens were utilized to verify the existing input energy spectra. Twenty-eight experiments were conducted with three different data source. SAP2000 software was used in analytical part of the study. Responses from experimental part were used to calculate energy components of the SDOF and elasto-plastic material behavior was considered during the entire study. The damping ratios of the specimens were determined through logarithmic decrement and Chopra's Methods (Chopra, 1995).

Results of this research could be expressed as;

- Experimental results show that all three specimens exceed their elastic displacement limits.
- There are significant differences between the results of logarithmic decrement and Chopra's methods in terms of damping ratios. As the hysteretic behavior became closer to linear range, logarithmic decrement somewhat gave better energy results.
- Increase in damping ratio increased the Input Energy for each experiment. Also, increase in damping ratio lowered the maximum spectral velocity and spectral acceleration values. Therefore, Input Energy corresponding to corner period is decreased.
- Trends in all graphs obtained from experimental data was consistent for different intensities according to (Güllü, 2019) spectrum.
- Most of the data from experiments showed that mass-normalized Input Energy spectrum with varying damping ratios verified the (Güllü, 2019) spectrum.

REFERENCES

Akiyama, H., *Earthquake-Resistant Limit-State Design for Buildings*, University of Tokyo Press, Japan, 1985.

Bertero, V.V. and C.M. Uanga, *Implications of Recorded Earthquake Ground Motions on Seismic Design of Building Structures*, Research Report, UCB/EERC- 88/13, University of California at Berkeley, United States of Americ, 1988.

Uang, C.M. and V.V. Bertero, "Evaluation of Seismic Energy in Structures1, *Earthquake Engineering and Structural Dynamics*, Vol. 19, No. 1, pp. 77-90, 1990.

Chopra, A.K., *Dynamics of Structures: Theory and Applications to Earthquake Engineering*, Prentice Hall, Englewood Cliffs, New Jersey, 1995.

Decanini, L.D. and F. Mollaioli, 1998, "Formulation of Elastic Earthquake Input Energy Spectra", *Earthquake Engineering and Structural Dynamic*s, Vol. 27, pp. 1503-1522.

Dindar, A.A., *Energy-Based Earthquake Response Analysis and Design of Reinforced Concrete SDOF Columns*, Ph.D. Thesis, Department of Civil Engineering, Bogazici University, Istanbul, Turkey, 2009.

Dindar, A.A, C. Yalçın, E. Yüksel, H. Özkaynak, O. Büyüköztürk, "Development of earthquake energy demand spectra", *Earthquake Spectra*, Vol. 31, No. 3, pp. 1667-1689, 2015.

Fajfar, P., T. Vidic and M. Fischinger, "Seismic Demand in Medium-and Long period Structures", *Earthquake Engineering and Structural Dynamics*, Vol. 18, pp. 1133-1144, 1989.

Gioncu, V. and M. Federico, *Earthquake Engineering For Structural Design*, CRC

Press, 2010.

Güllü, A., *Determination of the inelastic displacement demand and response control of steel frame type structures by seismic energy equations*, PhD Thesis, Department of Civil Engineering, Istanbul Technical University, Istanbul, Turkey, 2018.

Güllü, A, E. Yüksel, C. Yalçın, A:A. Dindar, H. Özkaynak, O. Büyüköztürk, "An Improved Input Energy Spectrum Verified By The Shake Table Tests", *Earthquake Engineering Structural Dynamic*, pp. 1-19, 2018.

Housner, G.W., "Limit Design of Structures to Resist Earthquakes", *Proceedings of First World Conference on Earthquake Engineering*, pp.5-1, 1956.

Kuwamura, H., and T.V. Galambos, "Earthquake Load for Structural Reliability", *Structural Engineering*, Vol. 115, No. 6. pp. 1446-1462, 1989.

Priestley, M.J.N., "Performance Based Seismic Design", *Proceedings of 12th World Conference on Earthquake Engineering*, pp. 28-31, 2000.

Priestley, M.J.N., "Performance Based Seismic Design", *Bulletin of the New Zealand Society for Earthquake Engineering*, Vol. 33, No. 3, pp. 325-346, 2002.

Vidic, T., P. Fajfar and M. Fischinger, "Consistent Inelastic Design Spectra: Strength and Displacement", *Earthquake Engineering and Structural Dynamics*, Vol. 23, No. 5, pp. 507-521, 1994.

Yardimci, F., *Application of image-based sensing methods in shake table experiments*, M Sc Thesis, Department of Civil Engineering, Bogazici University, Istanbul, Turkey, 2018.

Ye, L., "Study on Energy-Based Seismic Design Method and Application on Steel Braced Frame Structures1", *Jianzhu Jiegou Xuebao Journal of Building Structures*, Vol. 33, No. 11, pp. 36-45, 2012.

Zahrah, T.F. and W.J. Hall, "Earthquake Energy Absorption in SDOF Structures", *Journal of Structural Engineering*, Vol. 110, No. 8, pp.1757-1773, 1984.

APPENDIX A: STRAIN GAUGES READINGS

A.1. T=0.500 sec, 0.20 San Salvador

Figure A.8 to Figure A.6 represent the data obtained from the first experimental test.

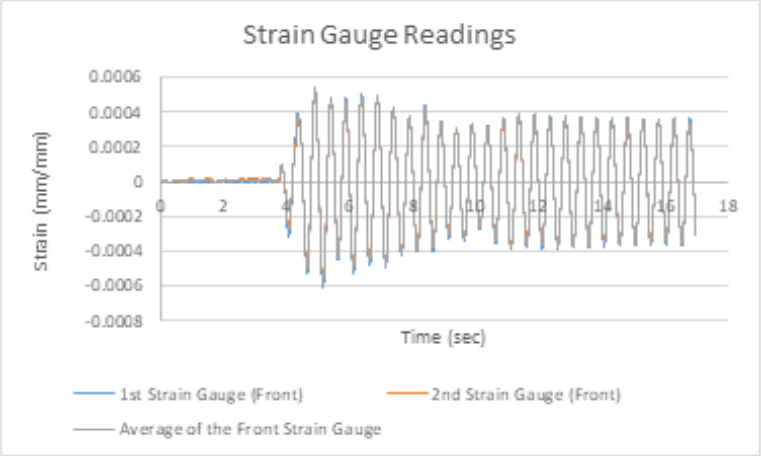

Figure A.1. Strain Data from Front Strain Gauges.

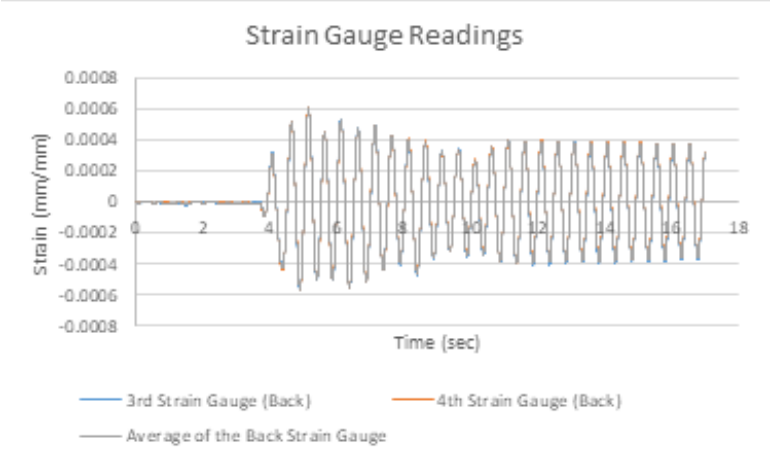

Figure A.2. Strain Data from Back Strain Gauges.

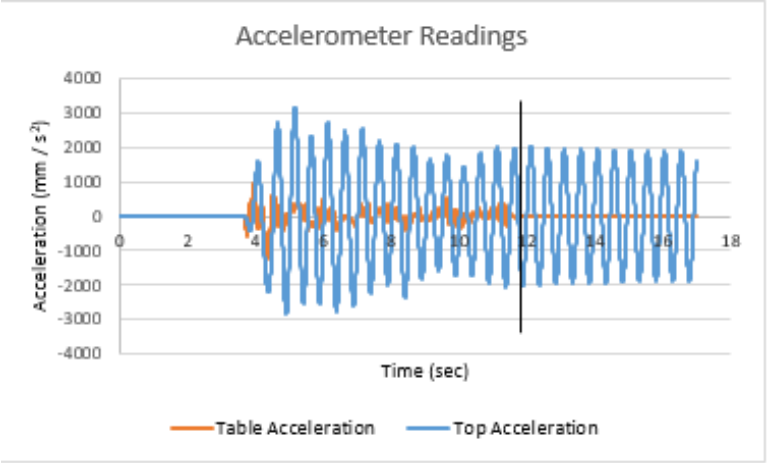

Figure A.3. Table and Top Acceleration Data.

The black vertical line shown in Figure A.3 indicates post earthquake excitation starts.

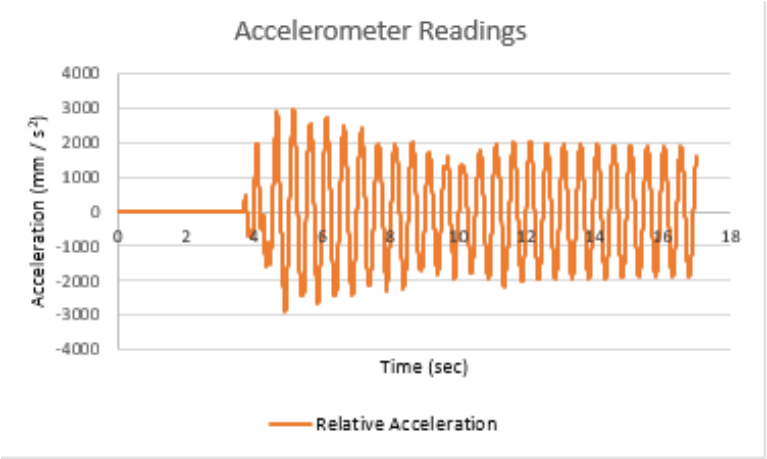

Figure A.4. Relative Acceleration Data.

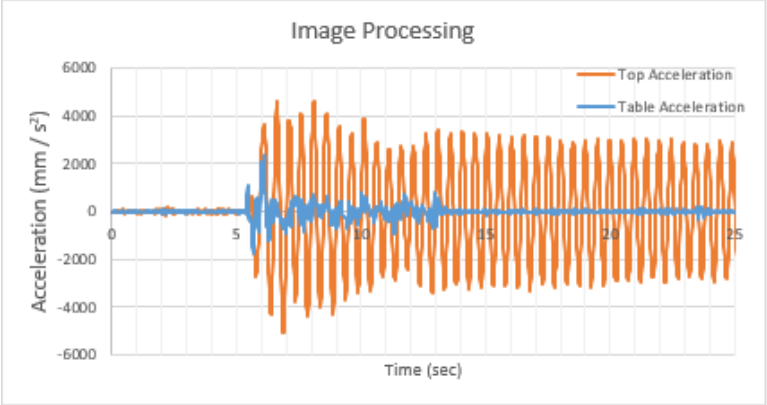

Figure A.5. Top Acceleration and Table Acceleration from Image Processing Data.

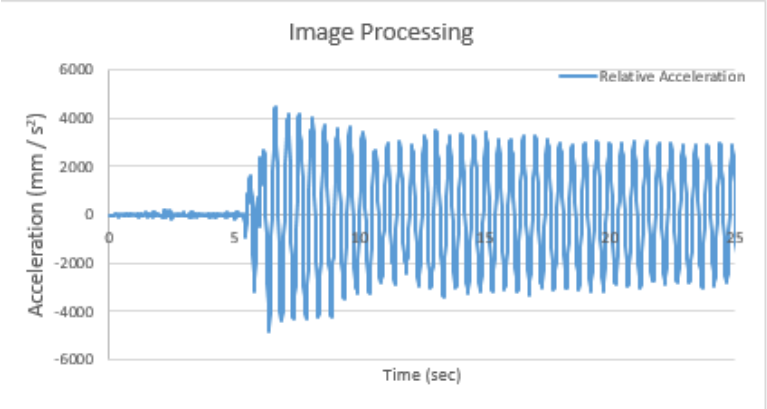

Figure A.6. Relative Acceleration from Image Processing Data.

A.2. T=0.500 sec, 0.30 San Salvador

Figure A.7 to Figure A.13 represent the data obtained from the second experimental test.

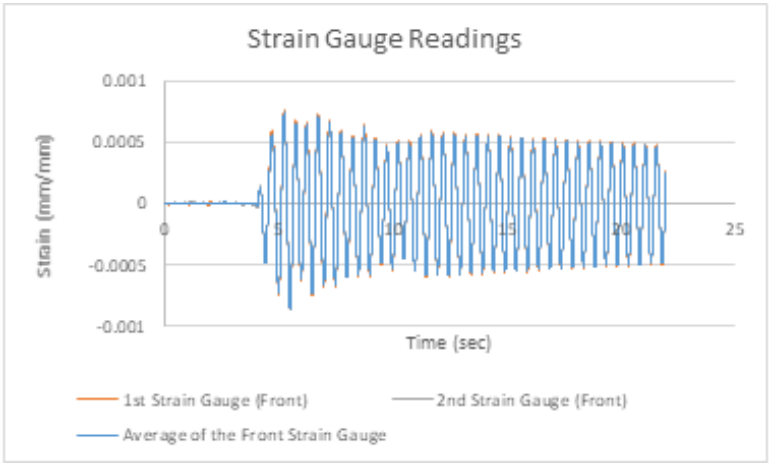

Figure A.7. Strain Data from Front Strain Gauges.

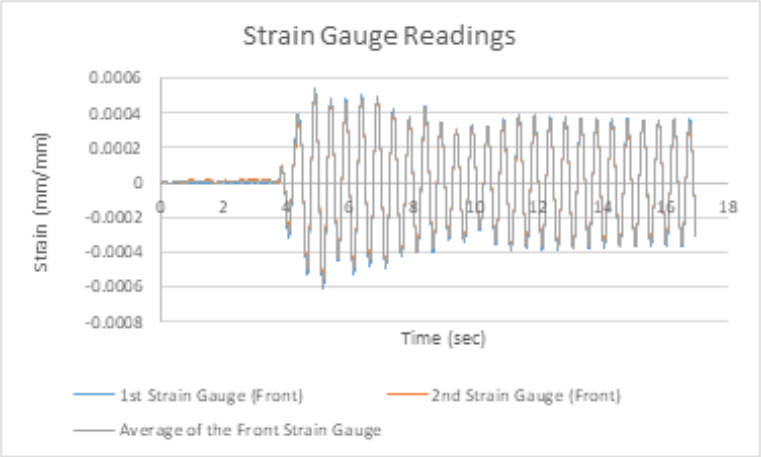

Figure A.8. Strain Data from Front Strain Gauges.

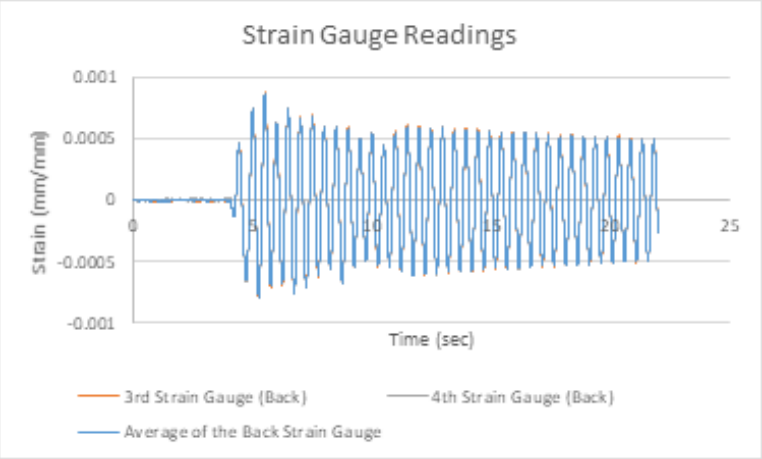

Figure A.9. Strain Data from Back Strain Gauges.

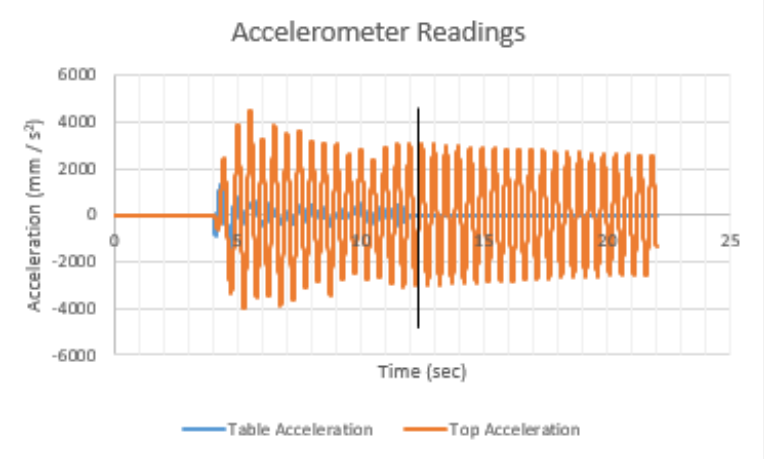

Figure A.10. Table and Top Acceleration Data.

The black vertical line shown in Figure A.10 indicates post-earthquake excitation starts.

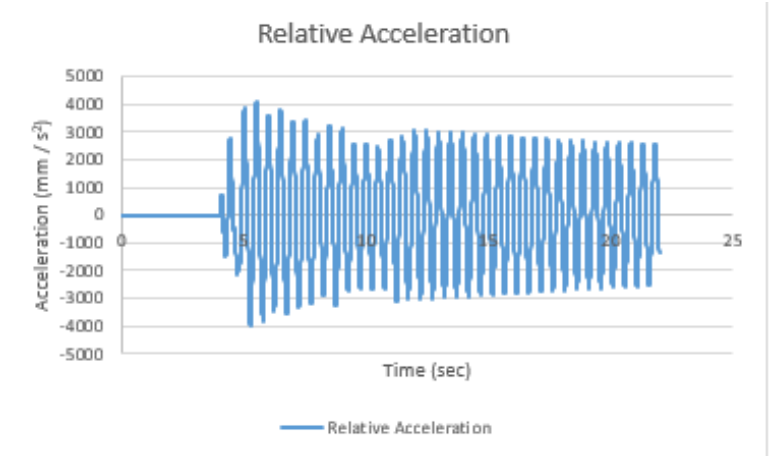

Figure A.11. Relative Acceleration Data.

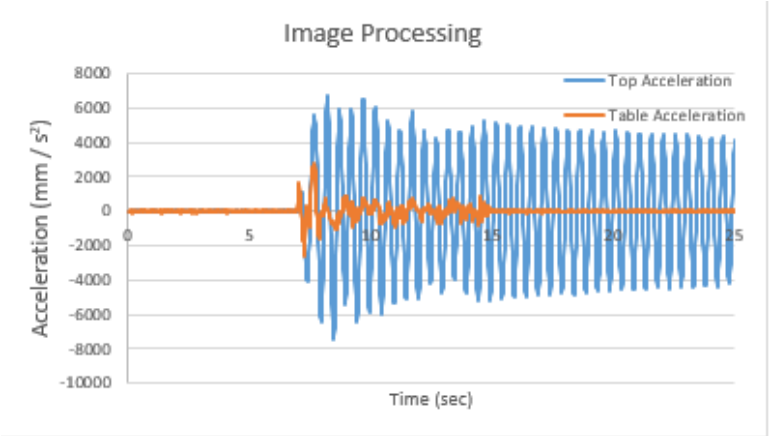

Figure A.12. Top Acceleration and Table Acceleration from Image Processing Data.

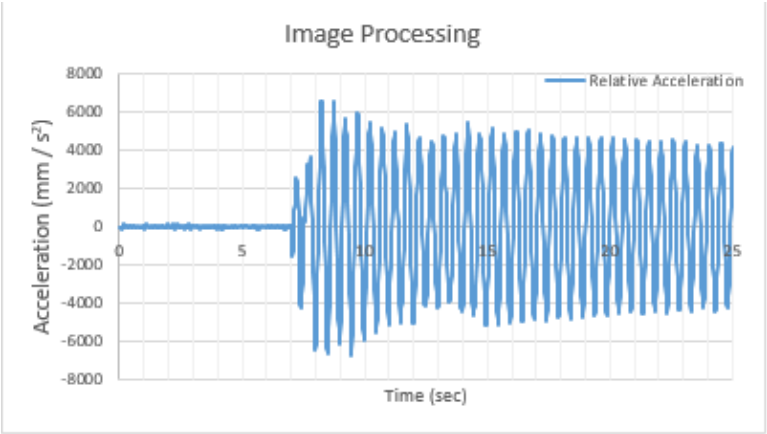

Figure A.13. Relative Acceleration from Image Processing Data.

A.3. T=0.500 sec, 0.40 San Salvador

Figure A.14 to Figure A.17 represent the data obtained from the third experimental test.

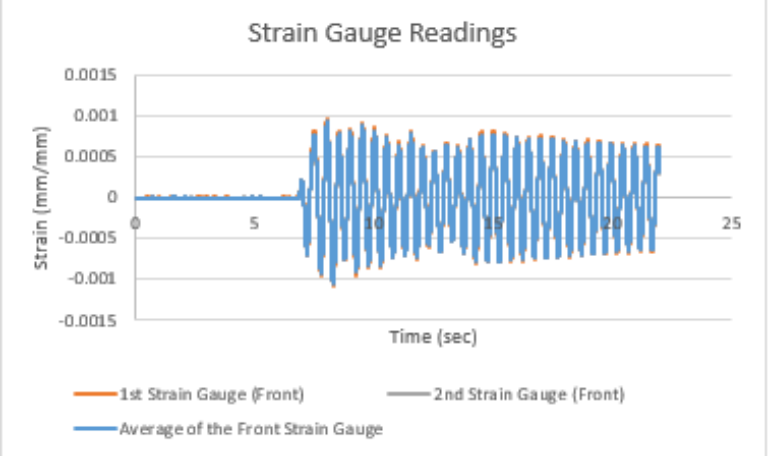

Figure A.14. Strain Data from Front Strain Gauges.

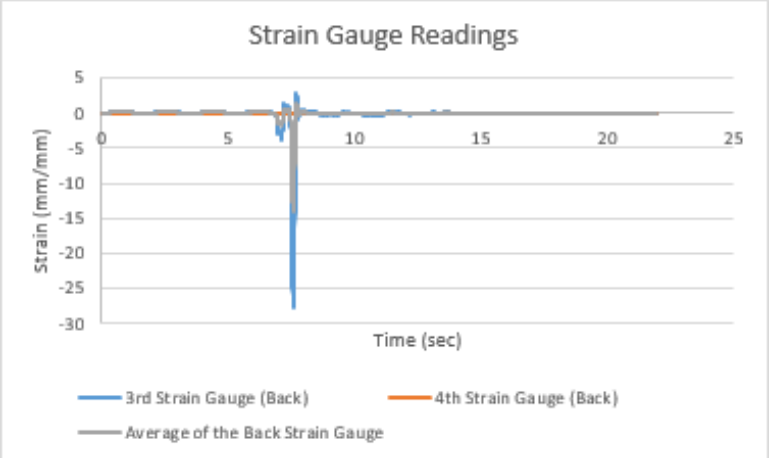

Figure A.15. Strain Data from Back Strain Gauges.

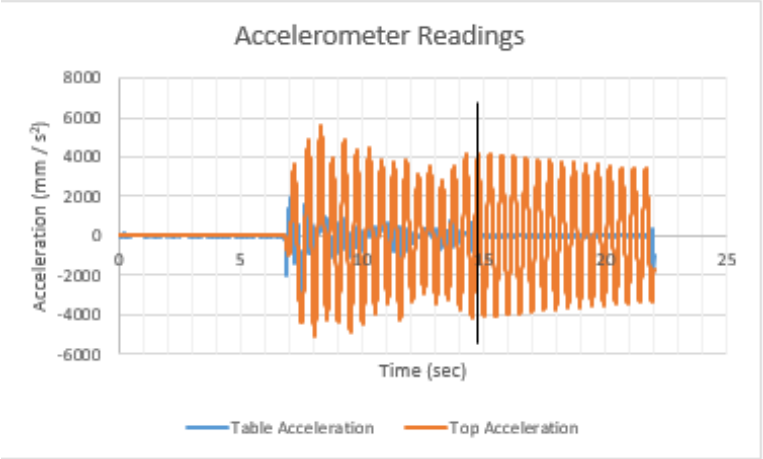

Figure A.16. Table and Top Acceleration Data.

The black vertical line shown in Figure A.16 indicates post earthquake excitation starts.

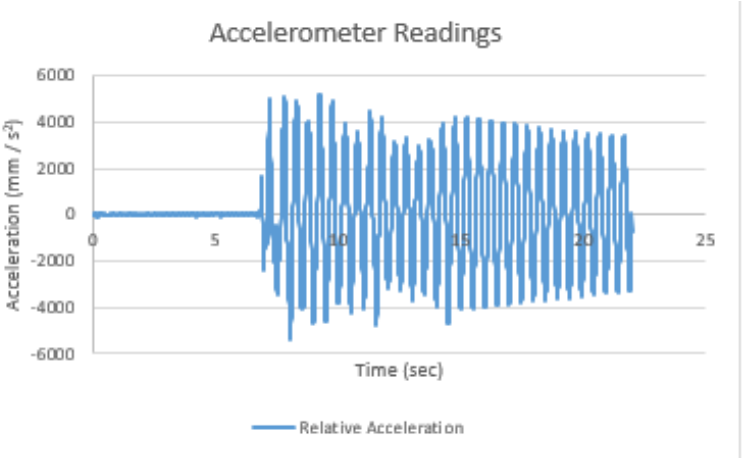

Figure A.17. Relative Acceleration Data.

A.4. T=0.500 sec, 0.50 San Salvador

Figure A.18 to Figure A.21 represent the data obtained from the fourth experimental test.

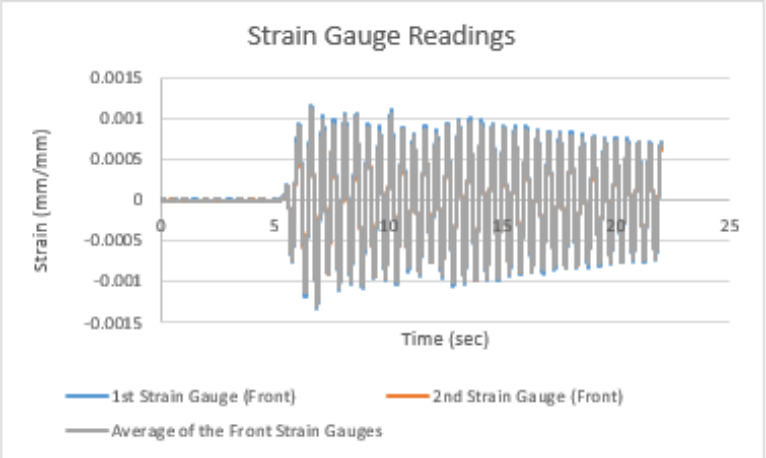

Figure A.18. Strain Data from Front Strain Gauges.

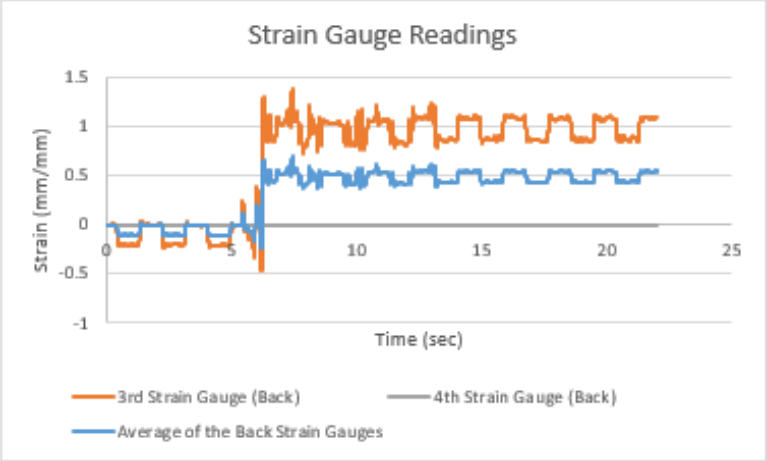

Figure A.19. Strain Data from Back Strain Gauges.

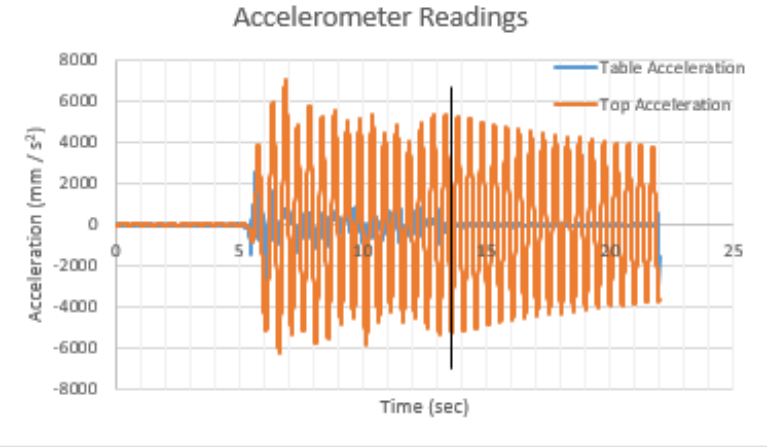

Figure A.20. Table and Top Acceleration Data.

The black vertical line shown in Figure A.20 indicates post earthquake excitation

starts.

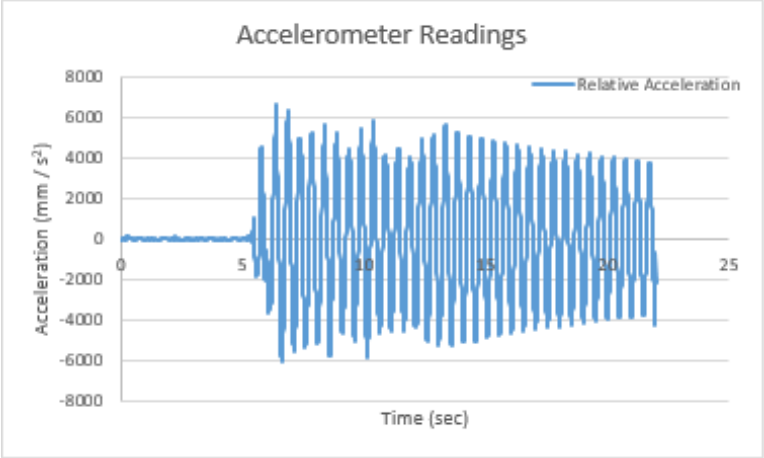

Figure A.21. Relative Acceleration Data.

A.5. T=0.500 sec, 0.60 San Salvador

Figure A.22 to Figure A.25 represent the data obtained from the fifth experimental test.

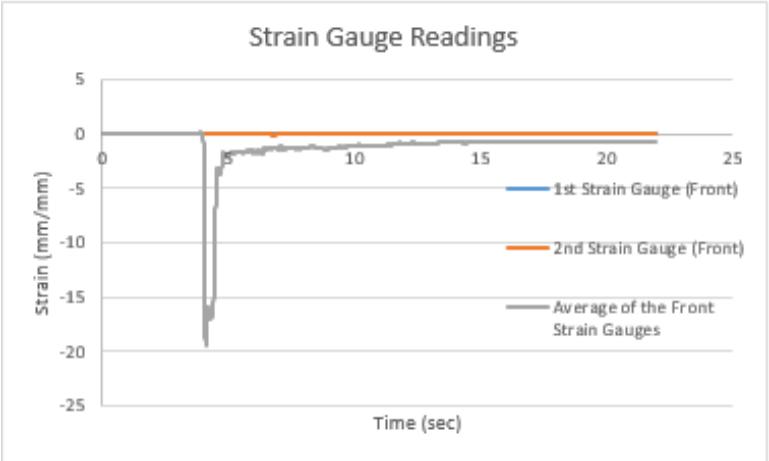

Figure A.22. Strain Data from Front Strain Gauges.

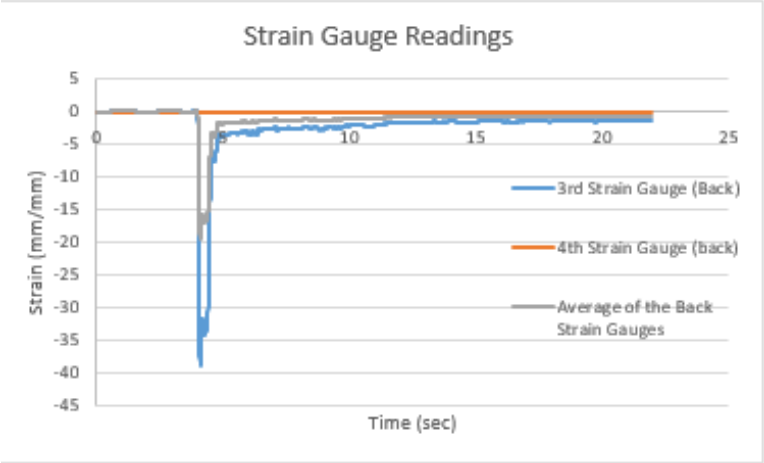

Figure A.23. Strain Data from Back Strain Gauges.

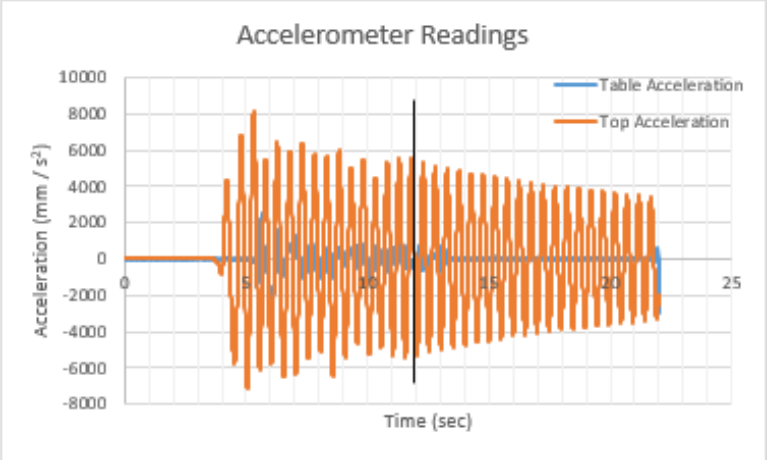

Figure A.24. Table and Top Acceleration Data.

The black vertical line shown in Figure A.24 indicates post earthquake excitation starts.

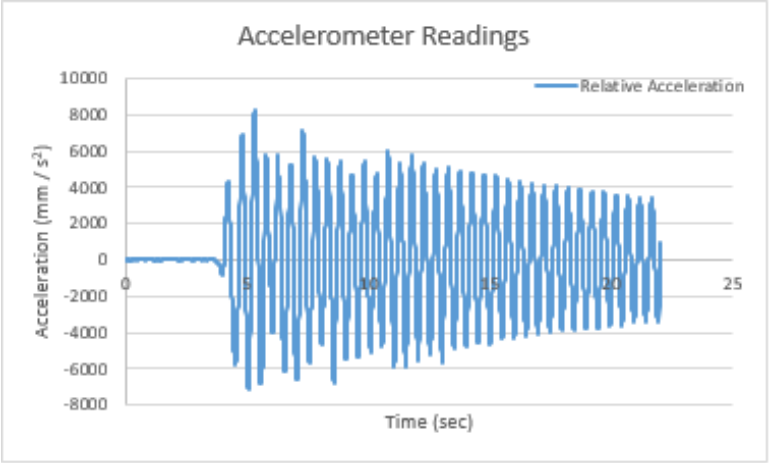

Figure A.25. Relative Acceleration Data.

A.6. T=0.500 sec, 0.70 San Salvador

Figure A.26 to Figure A.29 represent the data obtained from the sixth experimental test.

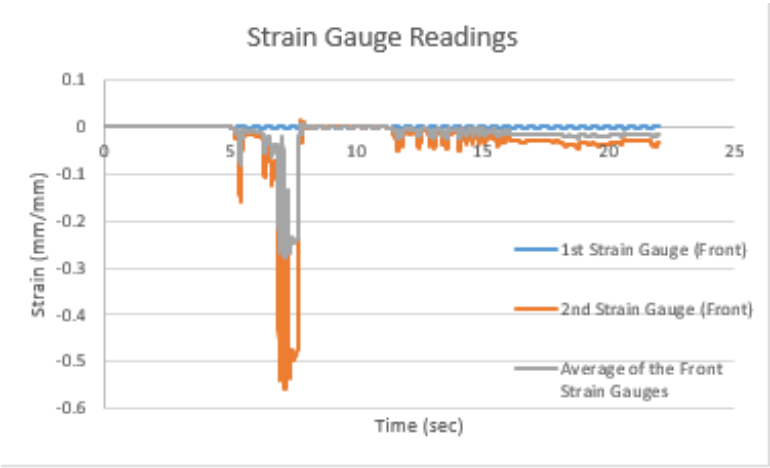

Figure A.26. Strain Data from Front Strain Gauges.

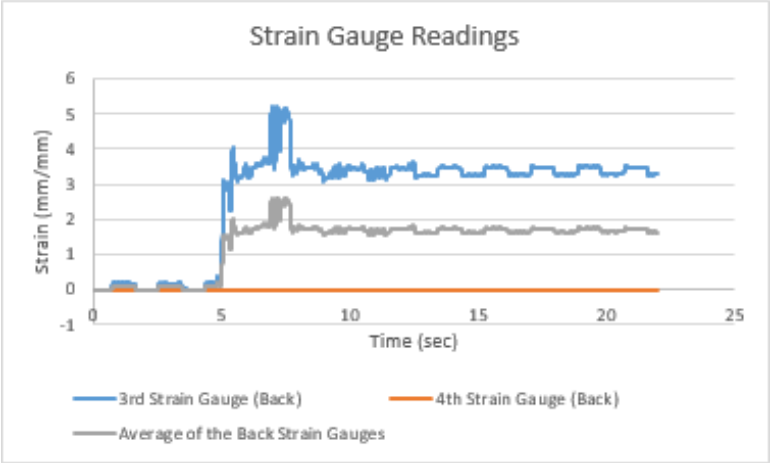

Figure A.27. Strain Data from Back Strain Gauges.

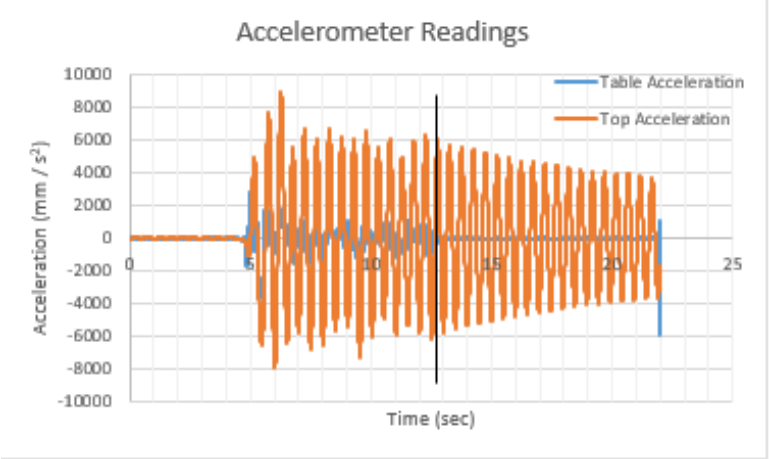

Figure A.28. Table and Top Acceleration Data.

The black vertical line shown in Figure A.28 indicates post earthquake excitation starts.

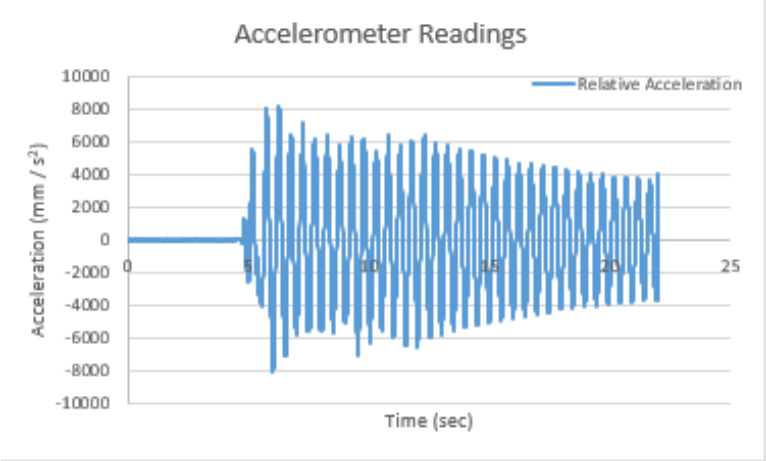

Figure A.29. Relative Acceleration Data.

A.7. T=0.500 sec, 0.80 San Salvador

Figure A.30 to Figure A.33 represent the data obtained from the seventh experimental test.

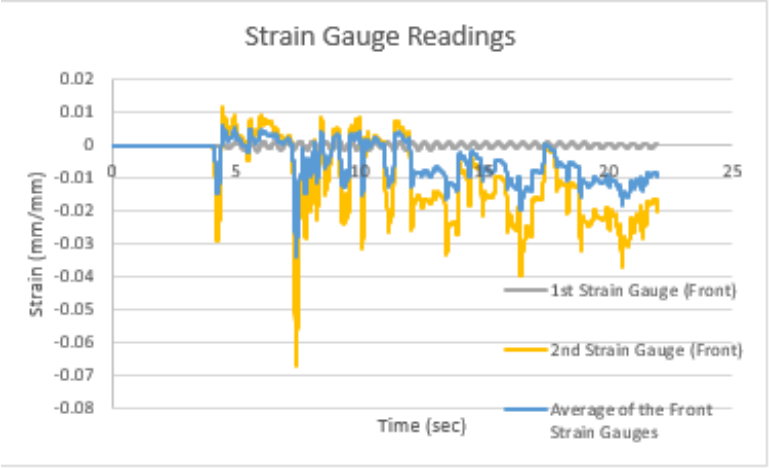

Figure A.30. Strain Data from Front Strain Gauges.

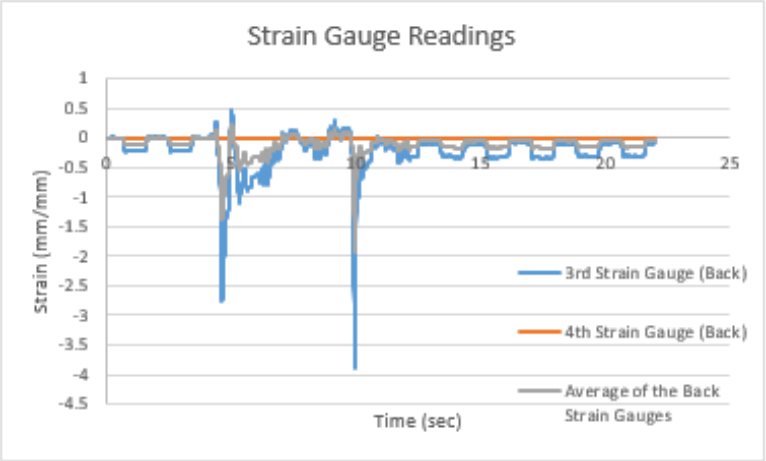

Figure A.31. Strain Data from Back Strain Gauges.

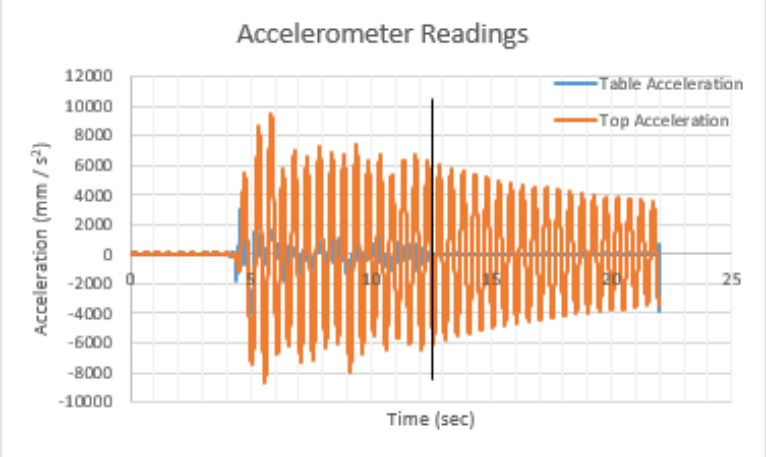

Figure A.32. Table and Top Acceleration Data.

The black vertical line shown in Figure A.32 indicates post earthquake excitation starts.

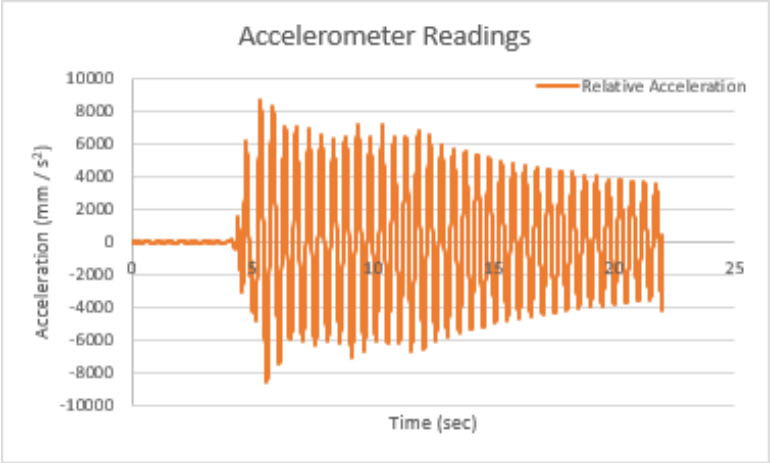

Figure A.33. Relative Acceleration Data.

A.8. T=0.500 sec, 0.90 San Salvador

Figure A.34 to Figur6e represent the data obtained from the eighth experimental test.

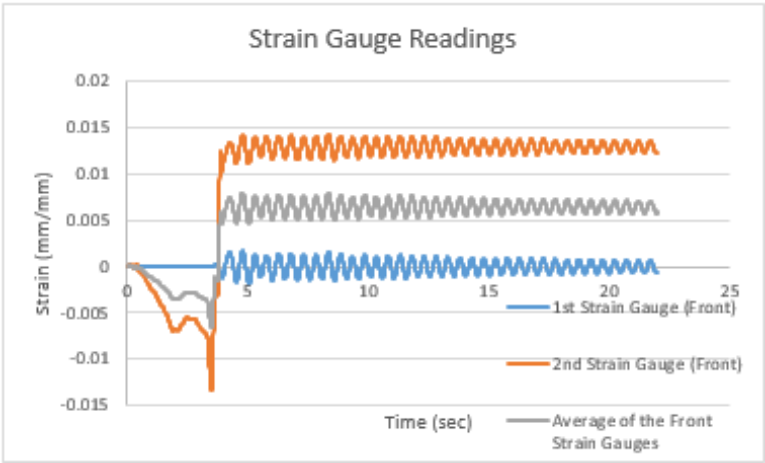

Figure A.34. Strain Data from Front Strain Gauges.

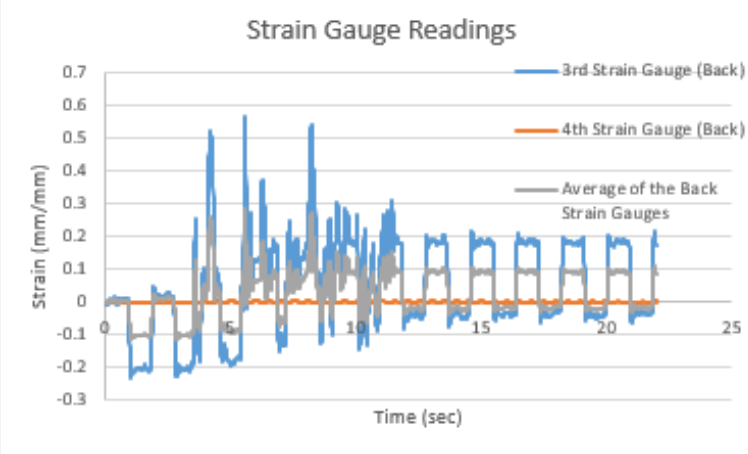

Figure A.35. Strain Data from Back Strain Gauges.

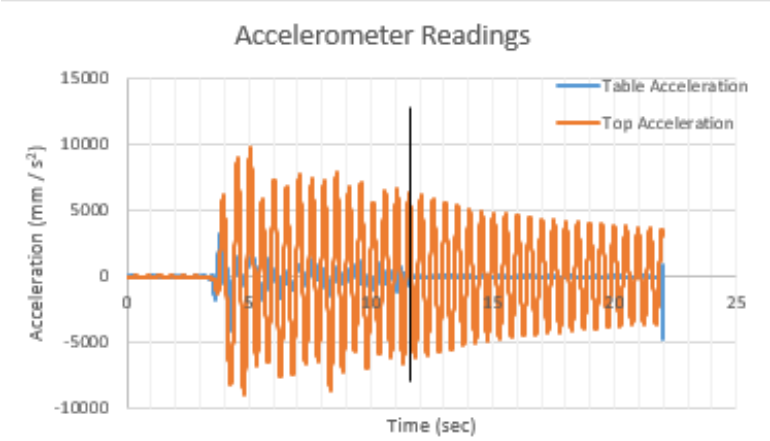

Figure A.36. Table and Top Acceleration Data.

The black vertical line shown in Figure A.36 indicates post earthquake excitation starts.

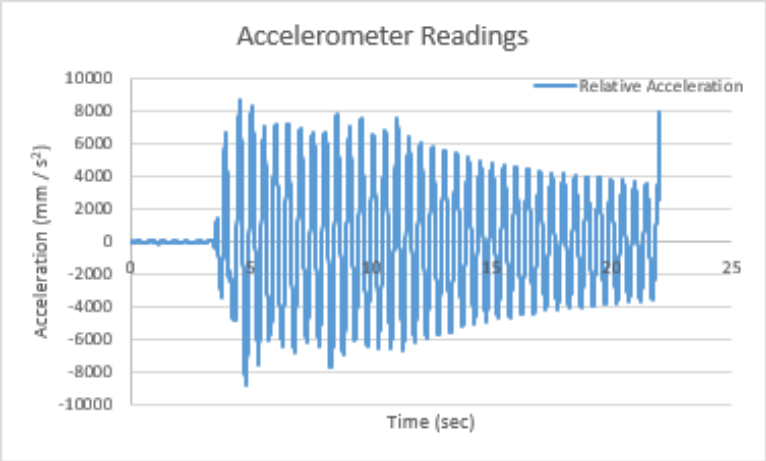

Figure A.37. Relative Acceleration Data.

A.9. T=0.500 sec, 1.00 San Salvador

Figure A.38 to Figure A.41 represent the data obtained from the ninth experimental test.

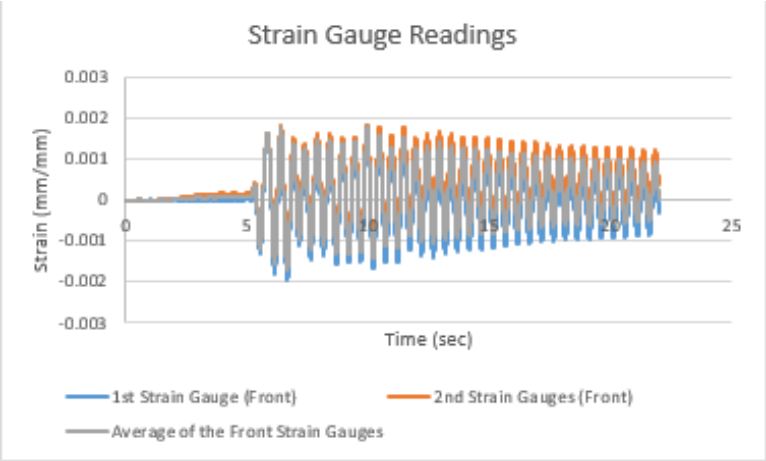

Figure A.38. Strain Data from Front Strain Gauges.

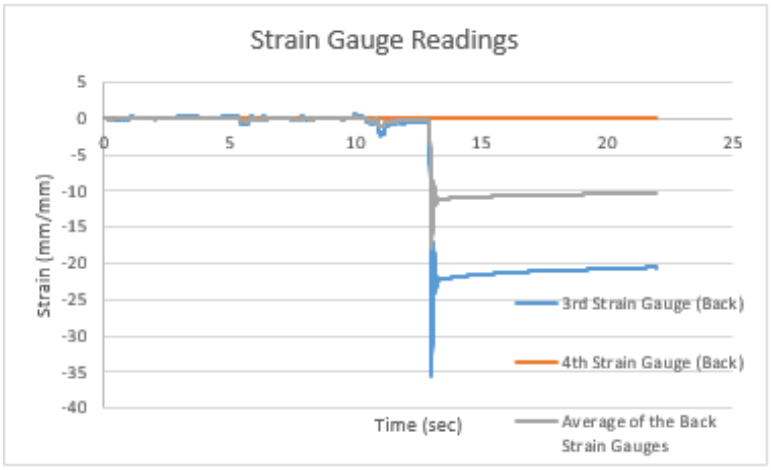

Figure A.39. Strain Data from Back Strain Gauges.

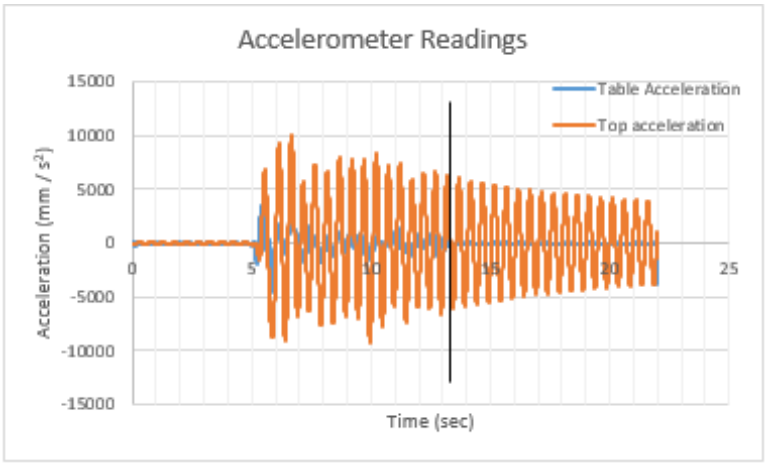

Figure A.40. Table and Top Acceleration Data.

The black vertical line shown in Figure A.40 indicates post earthquake excitation starts.

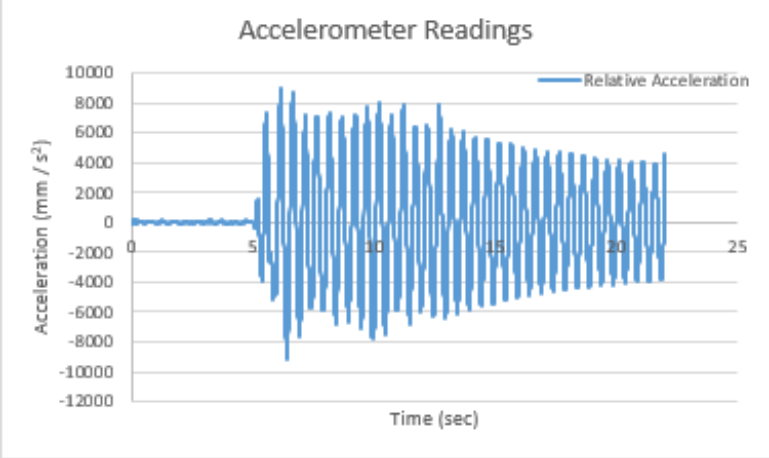

Figure A.41. Relative Acceleration Data.

A.10. T=0.500 sec, 1.20 San Salvador

Figure A.42 to Figure A.45 represent the data obtained from the tenth experimental test.

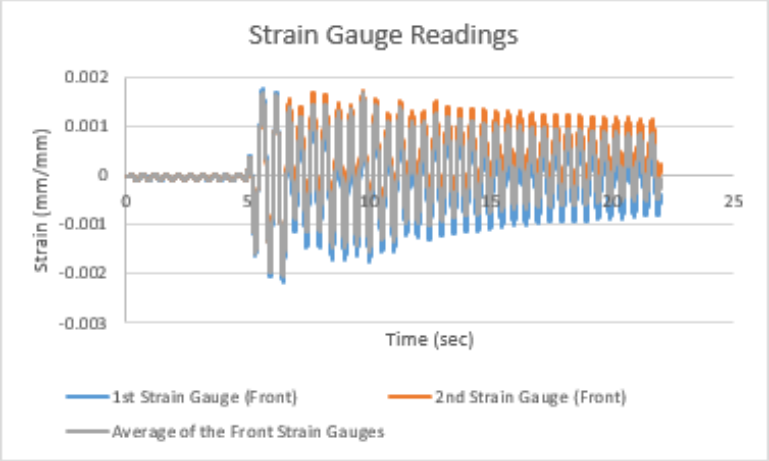

Figure A.42. Strain Data from Front Strain Gauges.

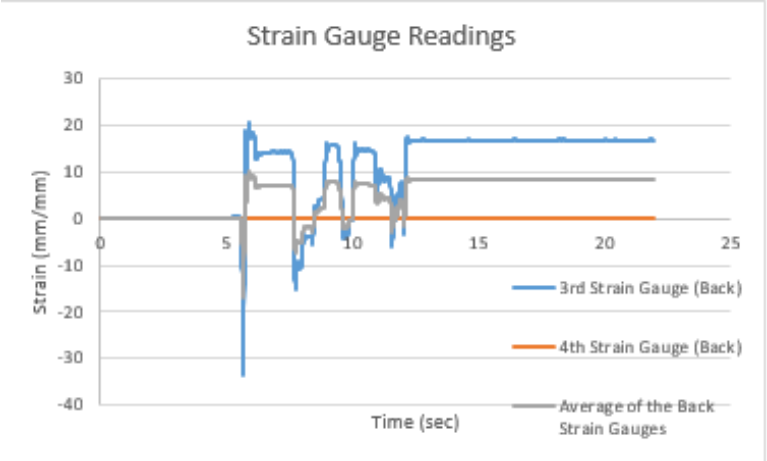

Figure A.43. Strain Data from Back Strain Gauges.

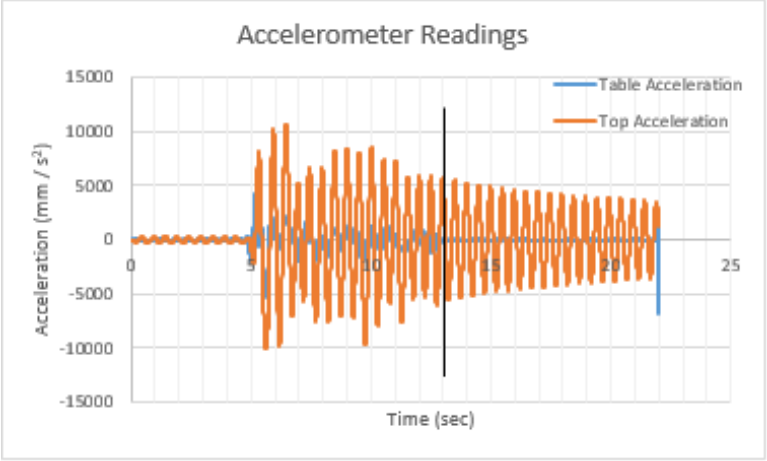

Figure A.44. Table and Top Acceleration Data.

The black vertical line shown in Figure A.44 indicates post earthquake excitation starts.

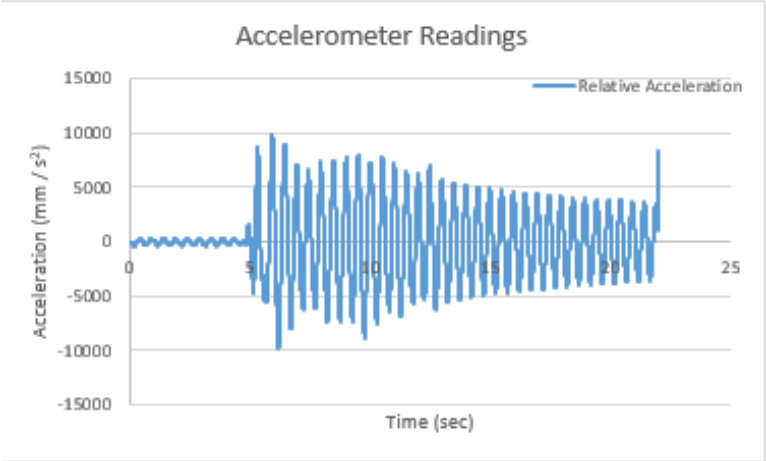

Figure A.45. Relative Acceleration Data.

A.11. T=0.500 sec, 1.40 San Salvador

Figure A.46 to Figure A.49 represent the data obtained from the eleventh experimental test.

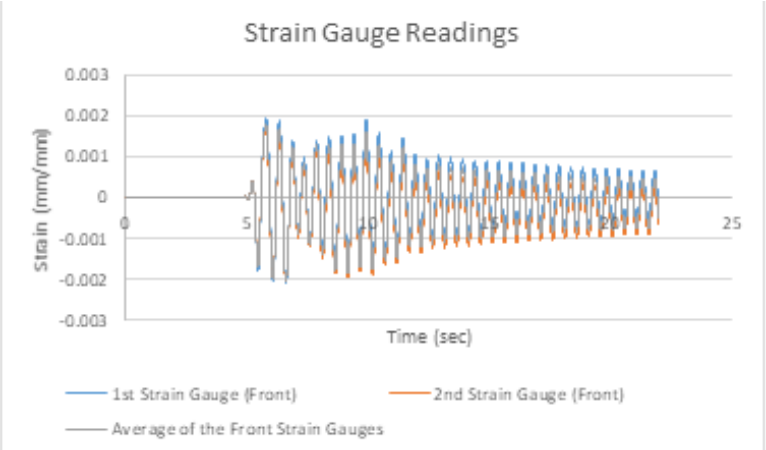

Figure A.46. Strain Data from Front Strain Gauges.

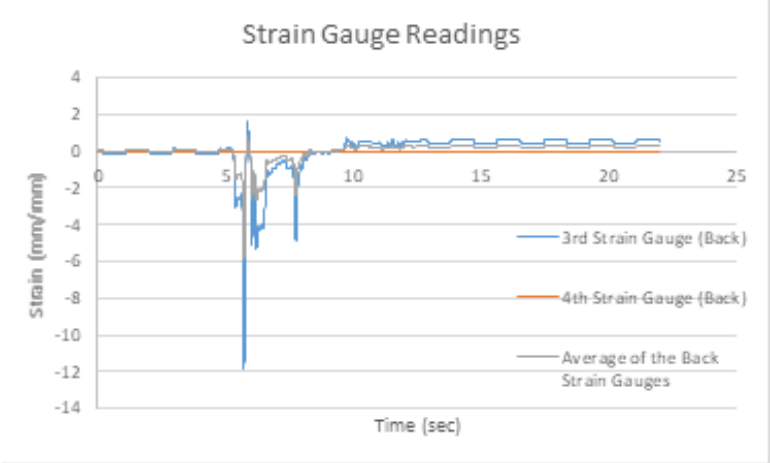

Figure A.47. Strain Data from Back Strain Gauges.

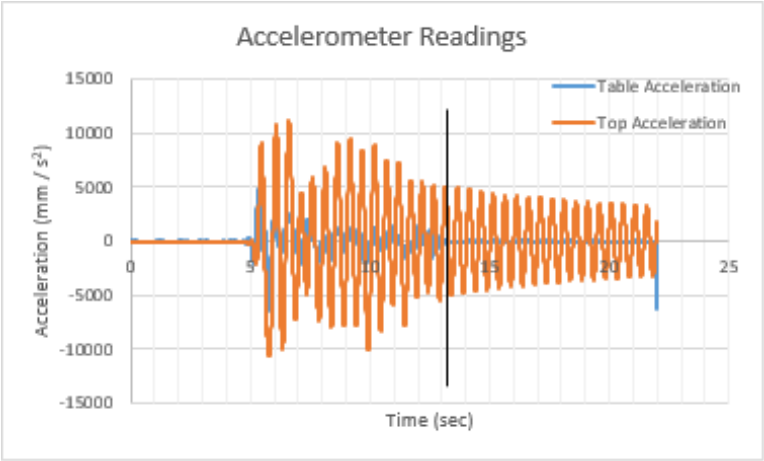

Figure A.48. Table and Top Acceleration Data.

The black vertical line shown in Figure A.48 indicates post earthquake excitation starts.

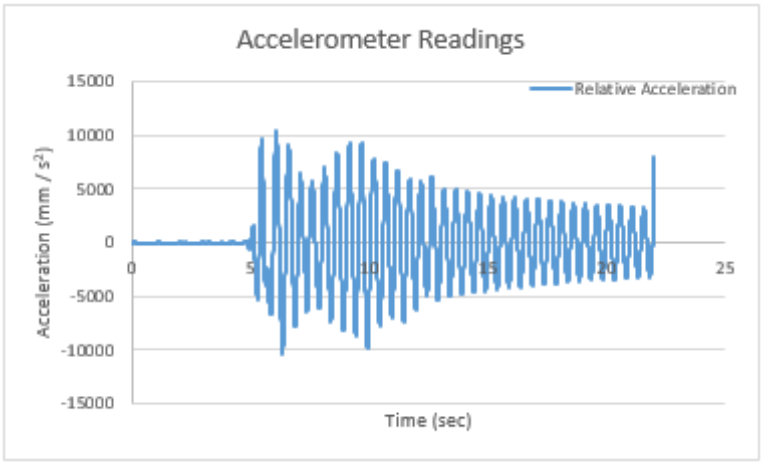

Figure A.49. Relative Acceleration Data.

A.12. T=0.500 sec, 1.60 San Salvador

Figure A.50 to Figure A.53 represent the data obtained from the twelfth experimental test.

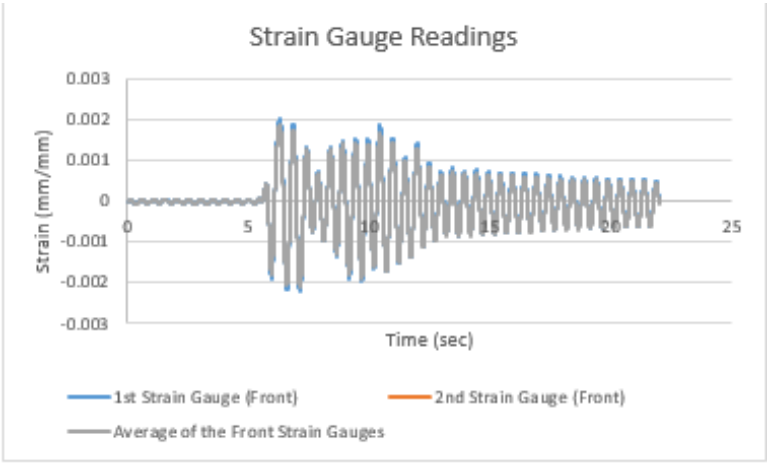

Figure A.50. Strain Data from Front Strain Gauges.

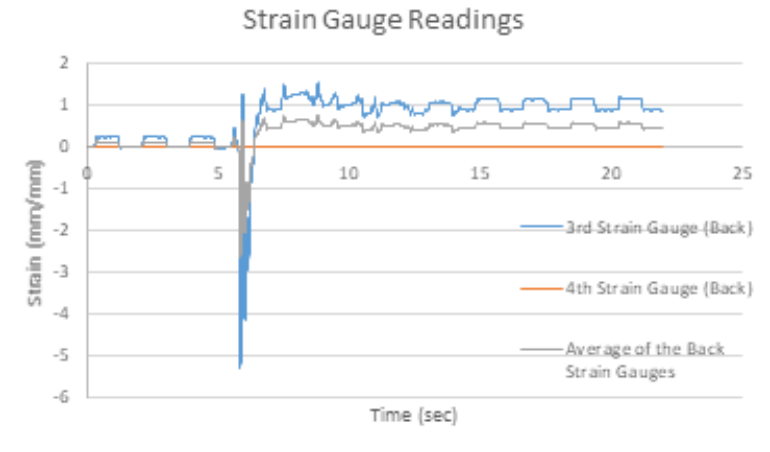

Figure A.51. Strain Data from Back Strain Gauges.

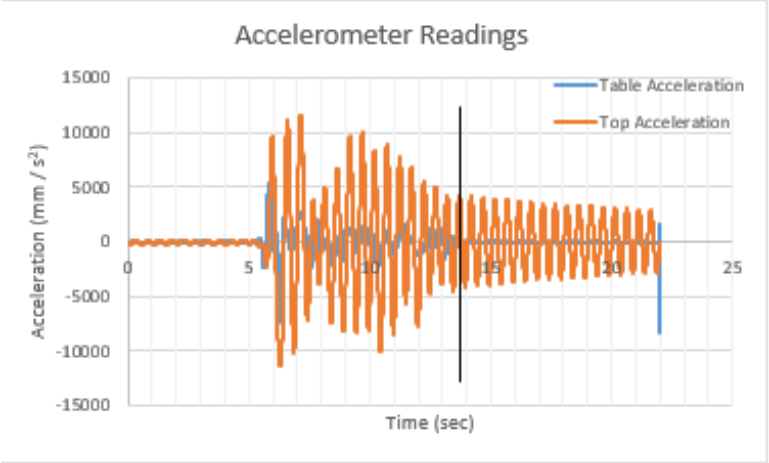

Figure A.52. Table and Top Acceleration Data.

The black vertical line shown in Figure A.52 indicates post earthquake excitation starts.

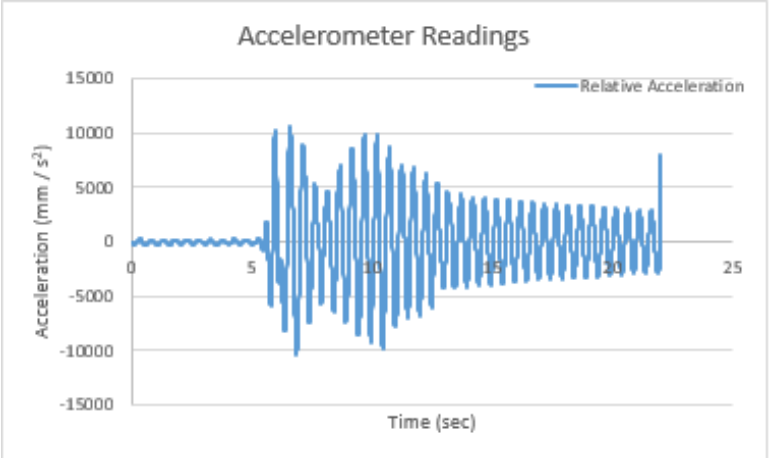

Figure A.53. Relative Acceleration Data.

A.13. T=0.667 sec, 0.20 San Salvador

Figure A.54 to Figure A.57 represent the data obtained from the thirteenth experimental test.

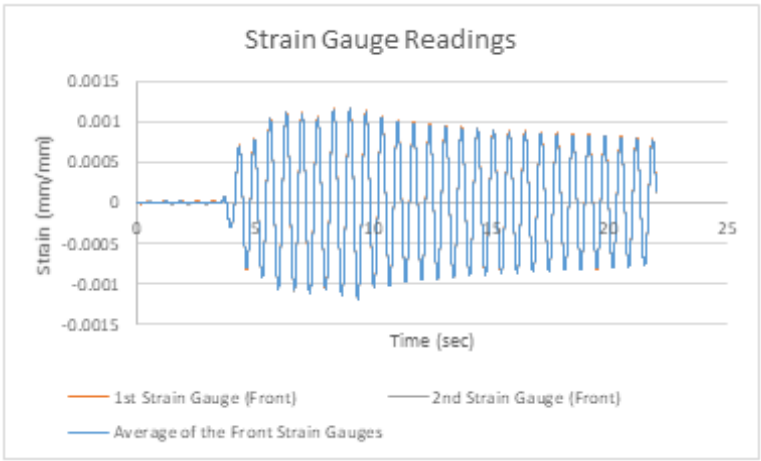

Figure A.54. Strain Data from Front Strain Gauges.

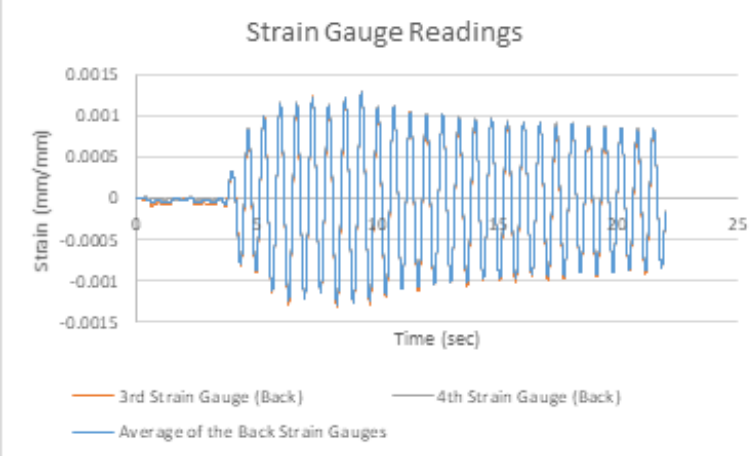

Figure A.55. Strain Data from Back Strain Gauges.

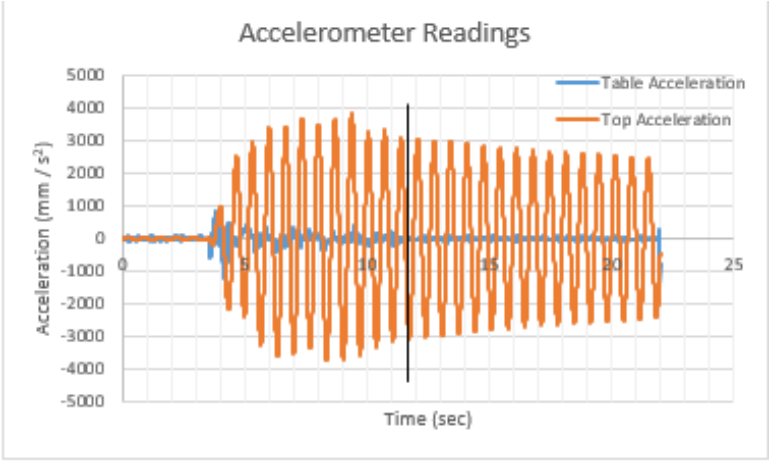

Figure A.56. Table and Top Acceleration Data.

The black vertical line shown in Figure A.56 indicates post earthquake excitation starts.

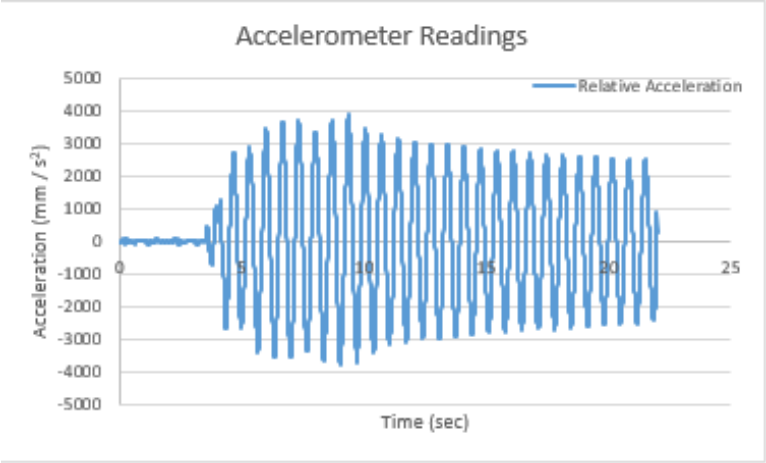

Figure A.57. Relative Acceleration Data.

A.14. T=0.667 sec, 0.30 San Salvador

Figure A.58 to Figure A.63 represent the data obtained from the fourteenth experimental test.

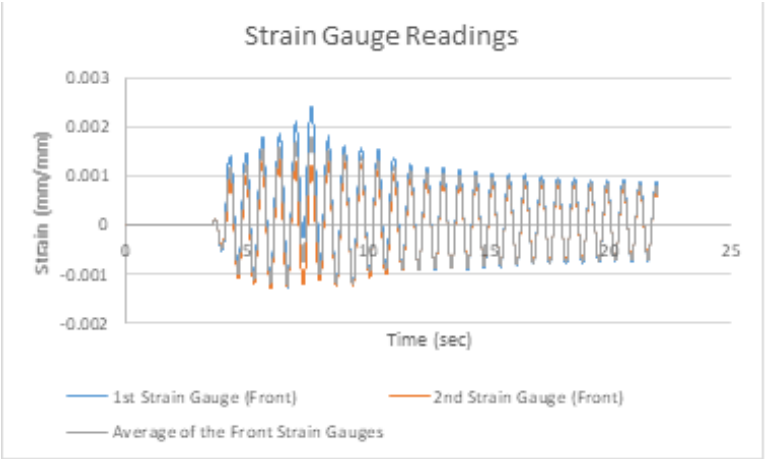

Figure A.58. Strain Data from Front Strain Gauges.

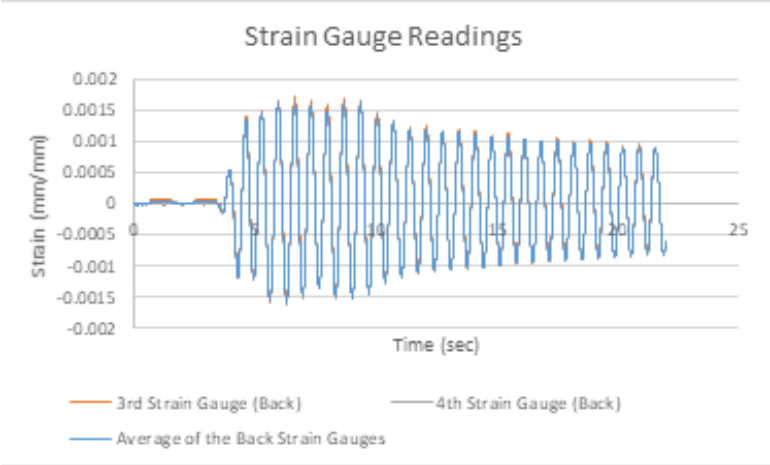

Figure A.59. Strain Data from Back Strain Gauges.

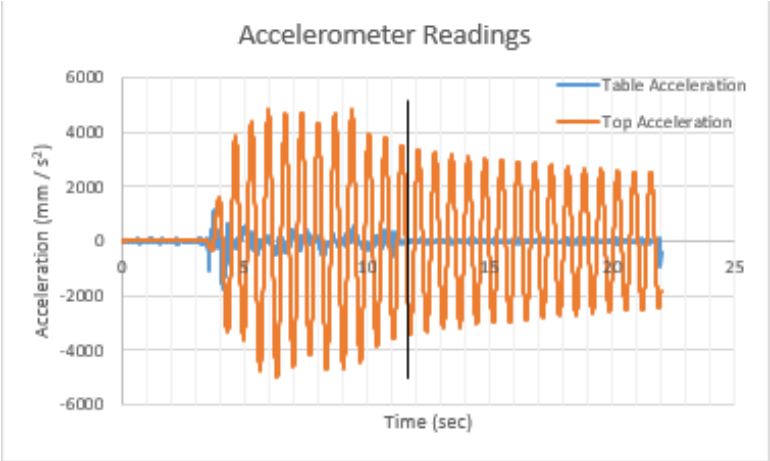

Figure A.60. Strain Data from Front Strain Gauges.

The black vertical line shown in Figure A.60 indicates post earthquake excitation starts.

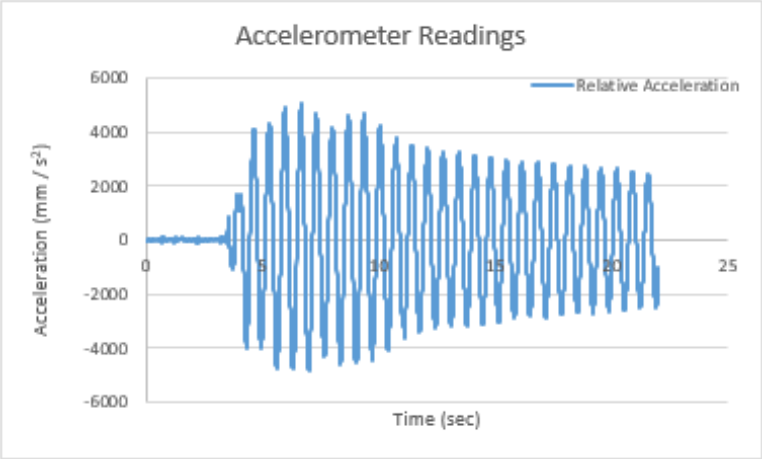

Figure A.61. Relative Acceleration Data.

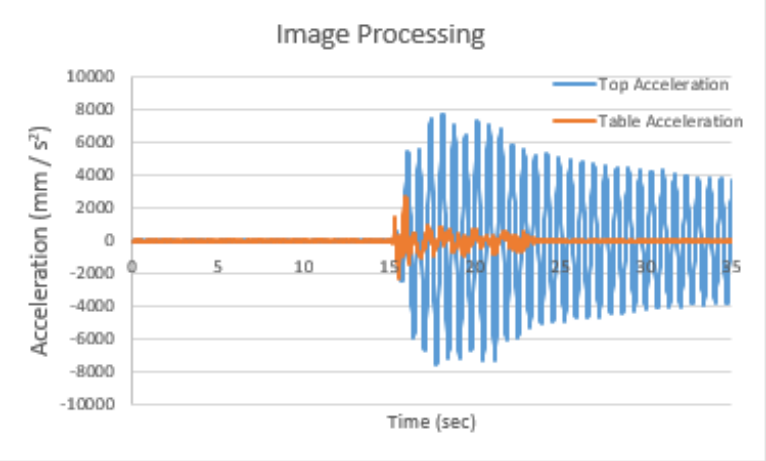

Figure A.62. Top Acceleration and Table Acceleration from Image Processing Data.

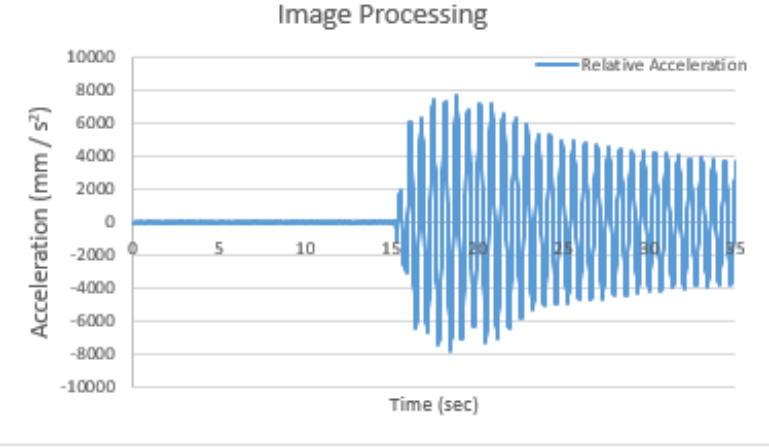

Figure A.63. Relative Acceleration from Image Processing Data.

A.15. T=0.667 sec, 0.40 San Salvador

Figure A.64 to Figure A.67 represent the data obtained from the fifteenth experimental test.

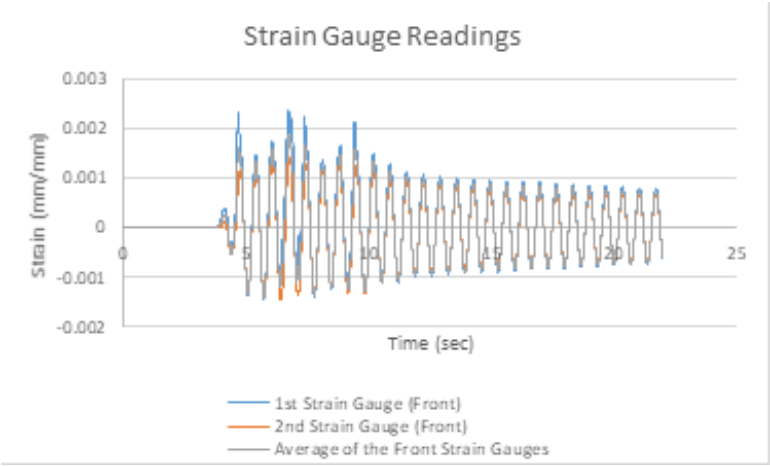

Figure A.64. Strain Data from Front Strain Gauges.

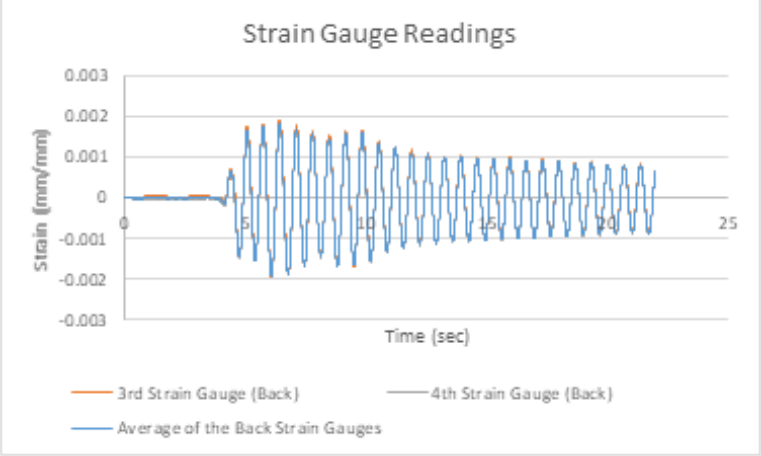

Figure A.65. Strain Data from Back Strain Gauges.

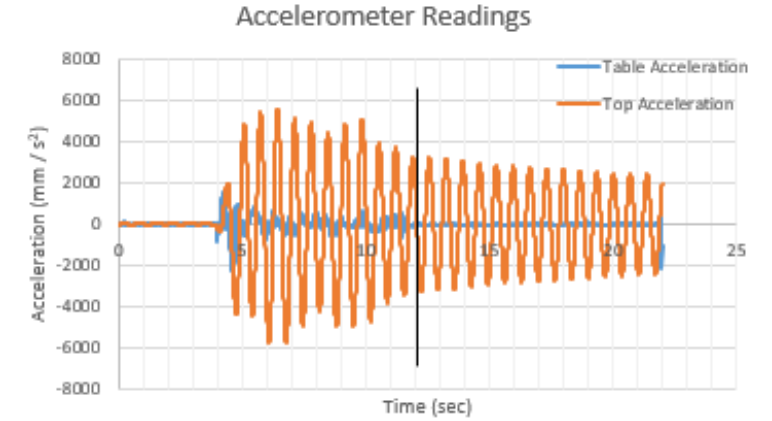

Figure A.66. Table and Top Acceleration Data.

The black vertical line shown in Figure A.66 indicates post earthquake excitation starts.

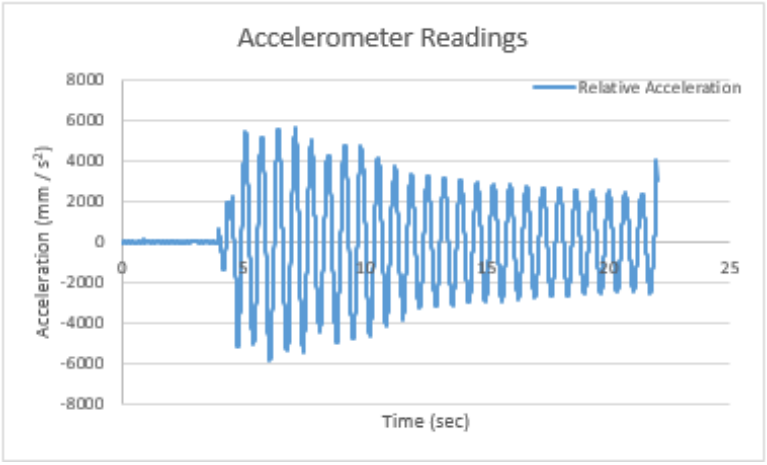

Figure A.67. Relative Acceleration Data.

A.16. T=0.667 sec, 0.50 San Salvador

Figure A.68 to Figure A.73 represent the data obtained from the sixteenth experimental test.

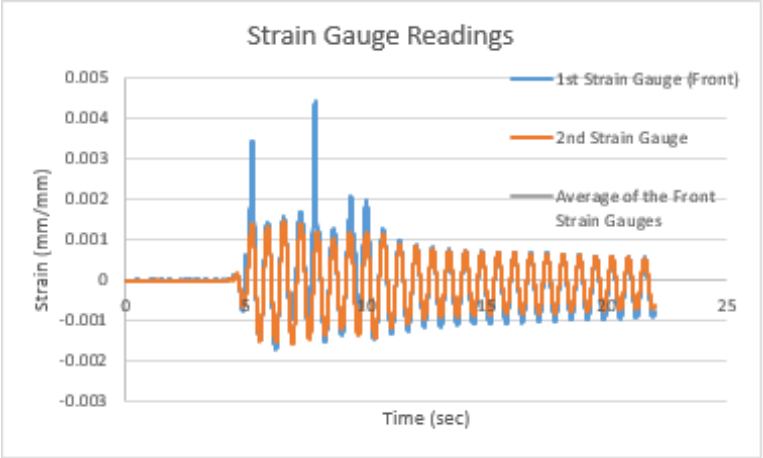

Figure A.68. Strain Data from Front Strain Gauges.

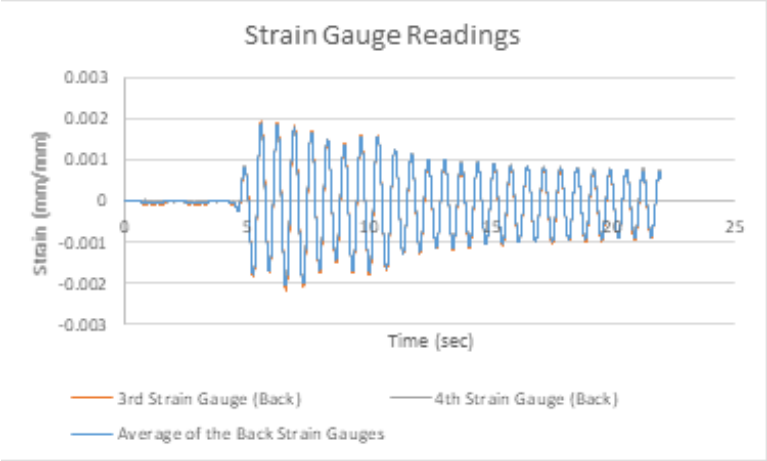

Figure A.69. Strain Data from Back Strain Gauges.

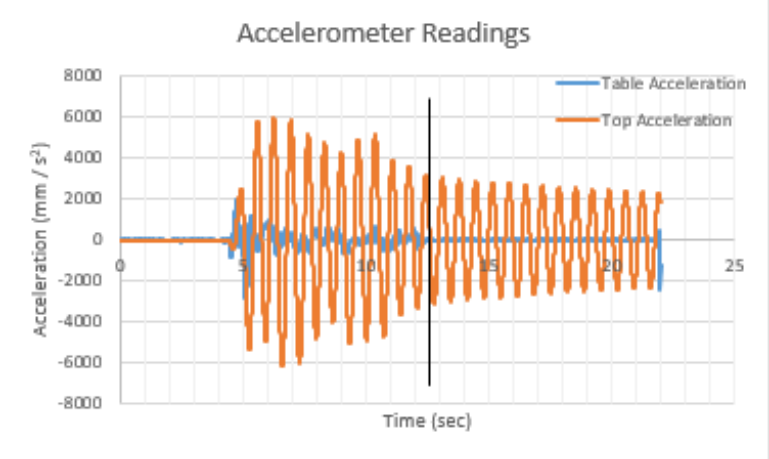

Figure A.70. Table and Top Acceleration Data.

The black vertical line shown in Figure A.70 indicates post earthquake excitation starts.

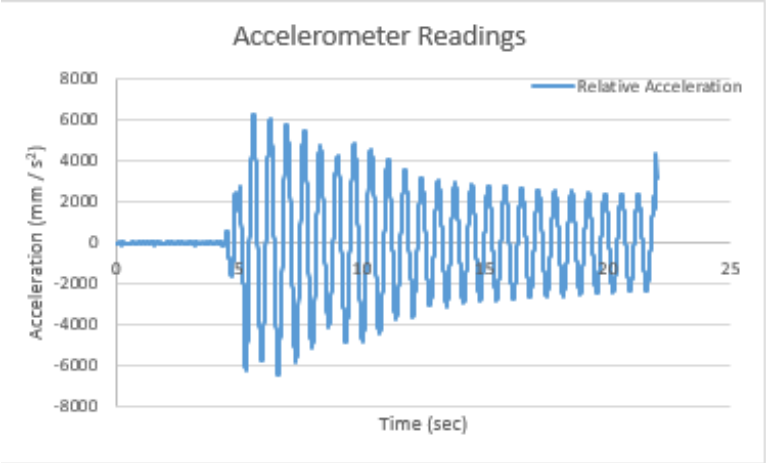

Figure A.71. Relative Acceleration Data.

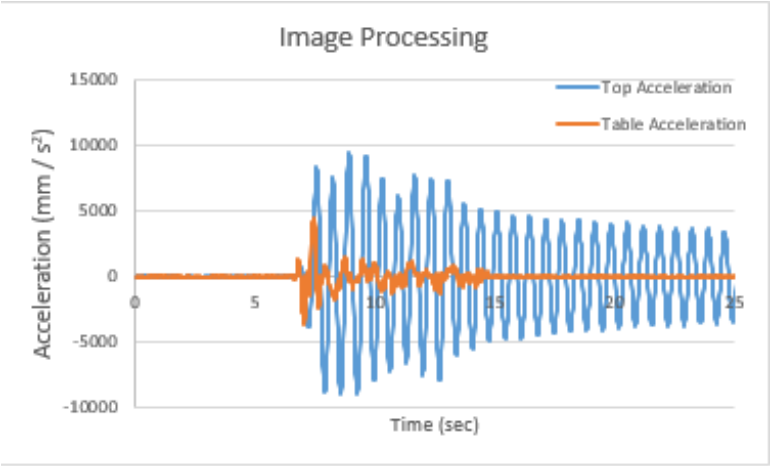

Figure A.72. Top Acceleration and Table Acceleration from Image Processing Data.

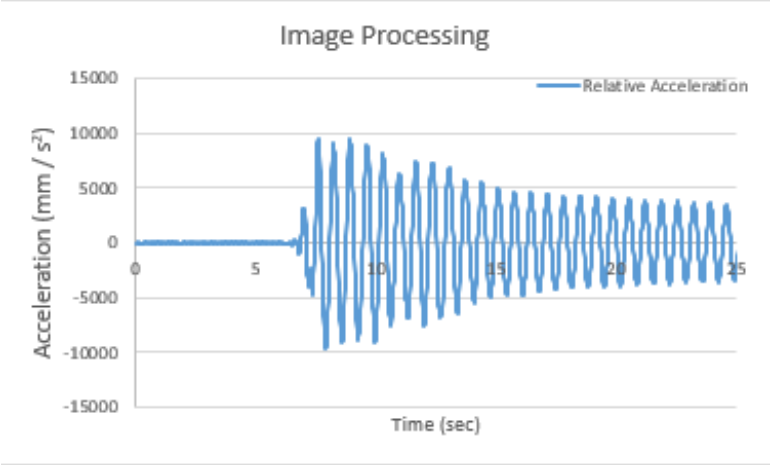

Figure A.73. Relative Acceleration from Image Processing Data.

A.17. T=0.667 sec, 0.60 San Salvador

Figure A.74 to A.79 represent the data obtained from the seventeenth experimental test.

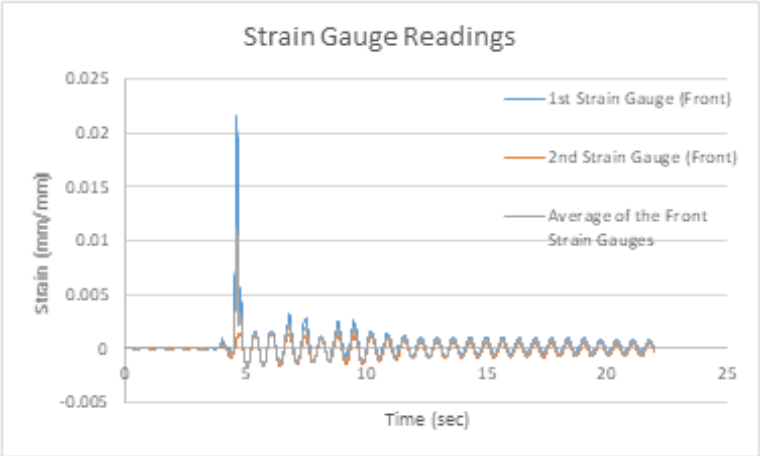

Figure A.74. Strain Data from Front Strain Gauges.

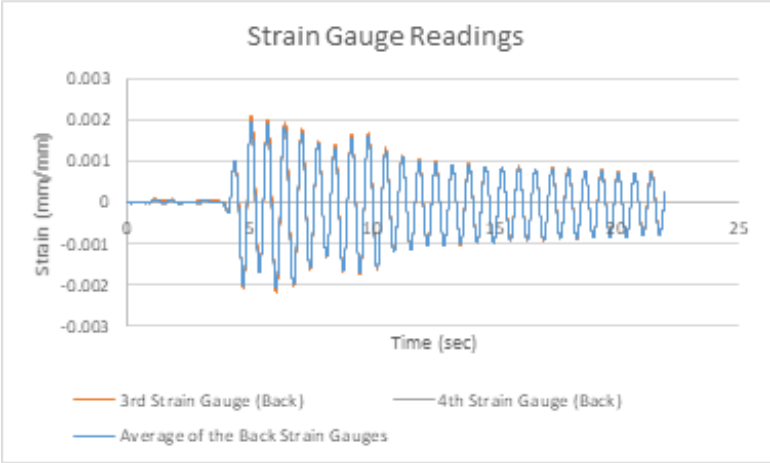

Figure A.75. Strain Data from Back Strain Gauges.

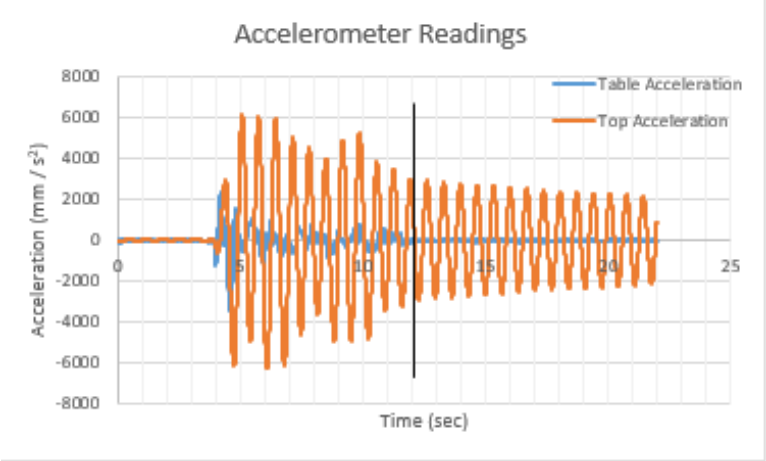

Figure A.76. Table and Top Acceleration Data.

The black vertical line shown in Figure A.76 indicates post earthquake excitation starts.

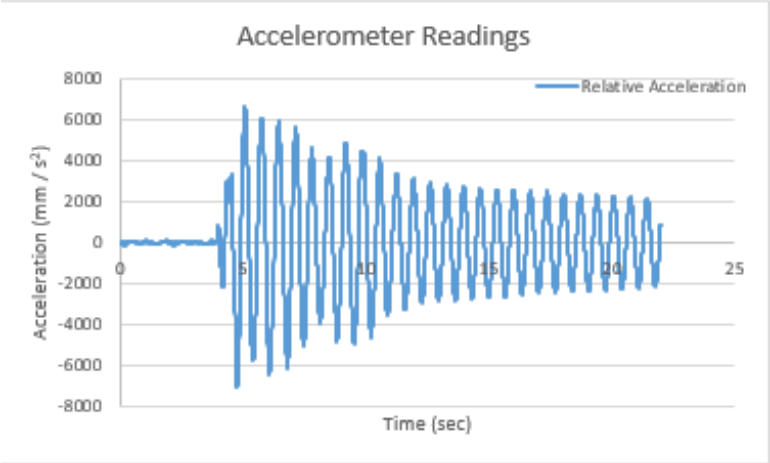

Figure A.77. Relative Acceleration Data.

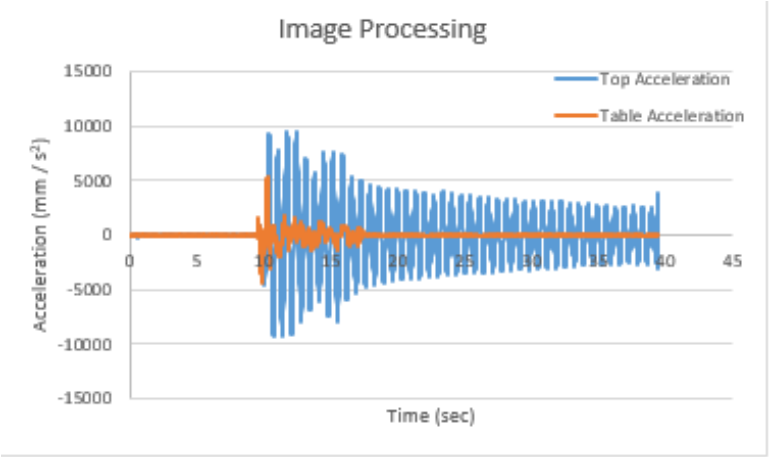

Figure A.78. Top Acceleration and Table Acceleration from Image Processing Data.

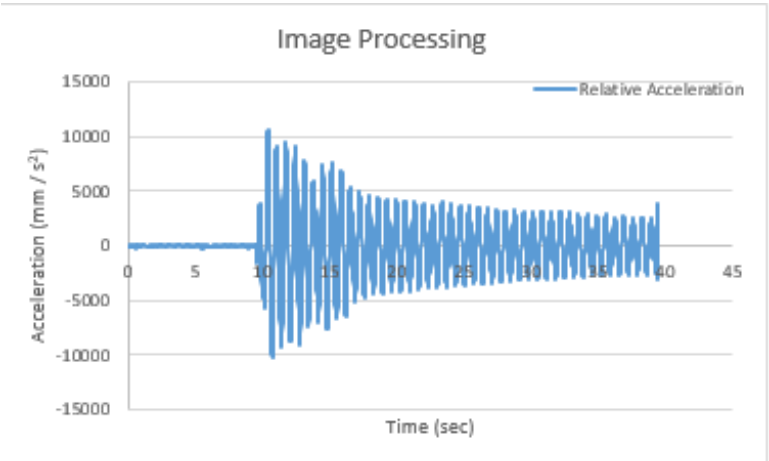

Figure A.79. Relative Acceleration from Image Processing Data.

A.18. T=0.667 sec, 0.70 San Salvador

Figure A.80 to Figure A.85 represent the data obtained from the eighteenth experimental test.

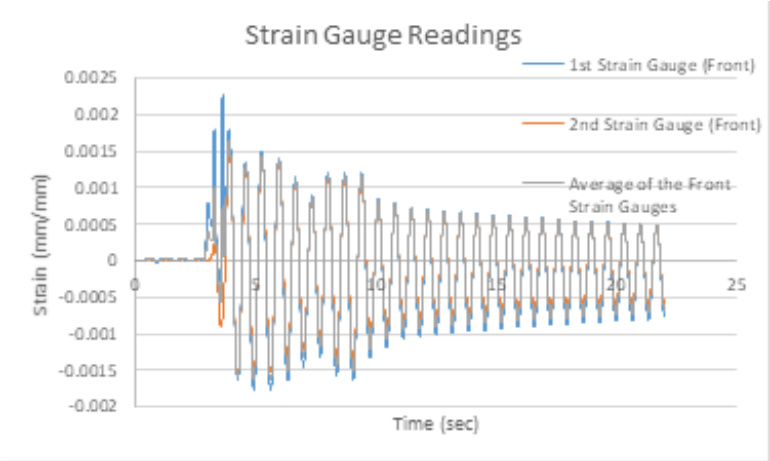

Figure A.80. Strain Data from Front Strain Gauges.

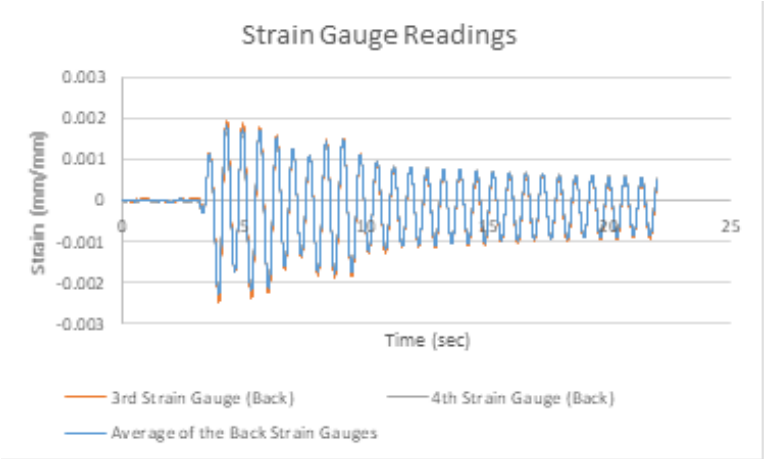

Figure A.81. Strain Data from Back Strain Gauges.

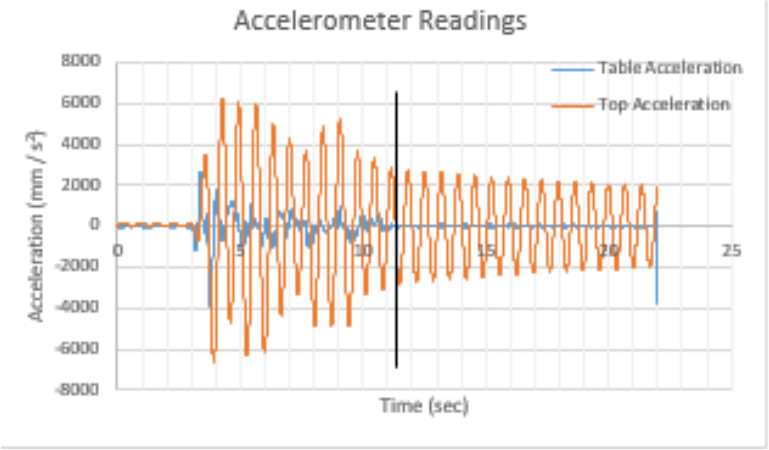

Figure A.82. Table and Top Acceleration Data.

The black vertical line shown in Figure A.82 indicates post earthquake excitation starts.

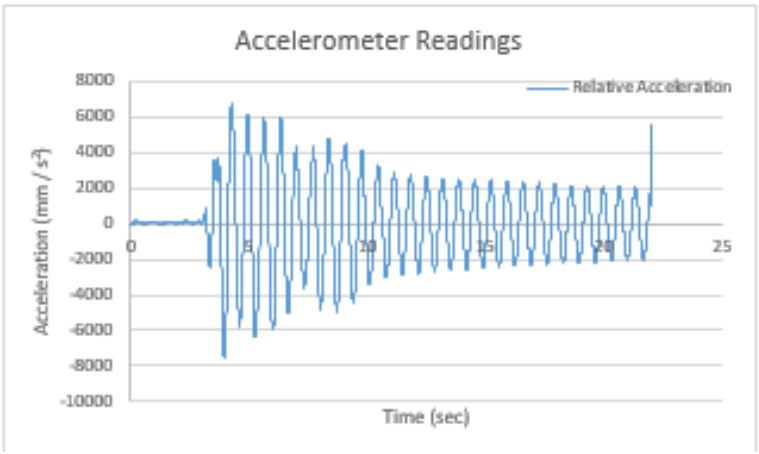

Figure A.83. Relative Acceleration Data.

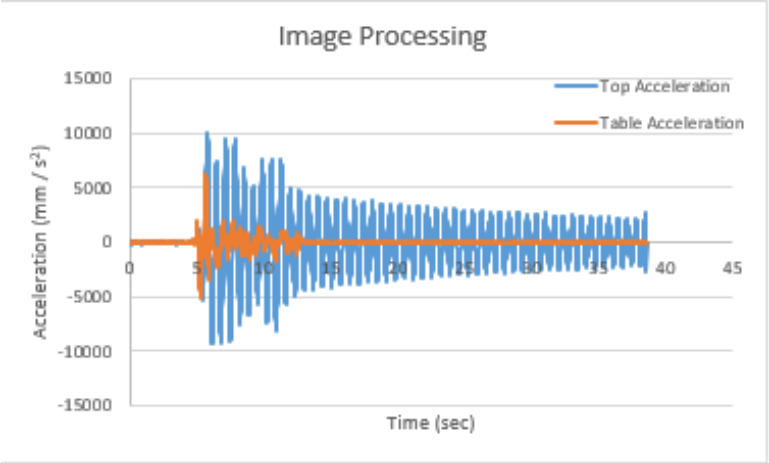

Figure A.84. Top Acceleration and Table Acceleration from Image Processing Data.

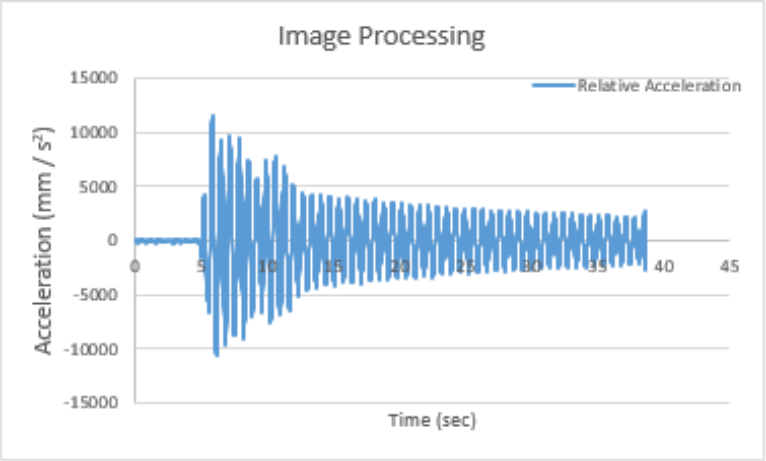

Figure A.85. Relative Acceleration from Image Processing Data.

A.19. T=0.667 sec, 0.80 San Salvador

Figure A.86 to Figure A.91 represent the data obtained from the nineteenth experimental test.

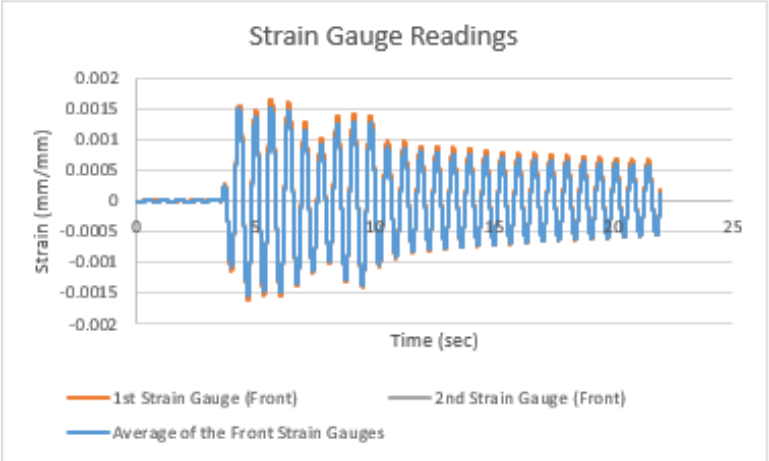

Figure A.86. Strain Data from Front Strain Gauges.

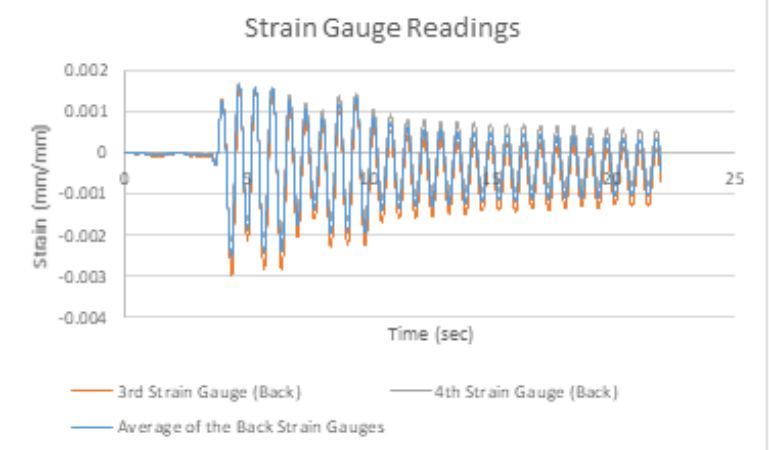

Figure A.87. Strain Data from Back Strain Gauges.

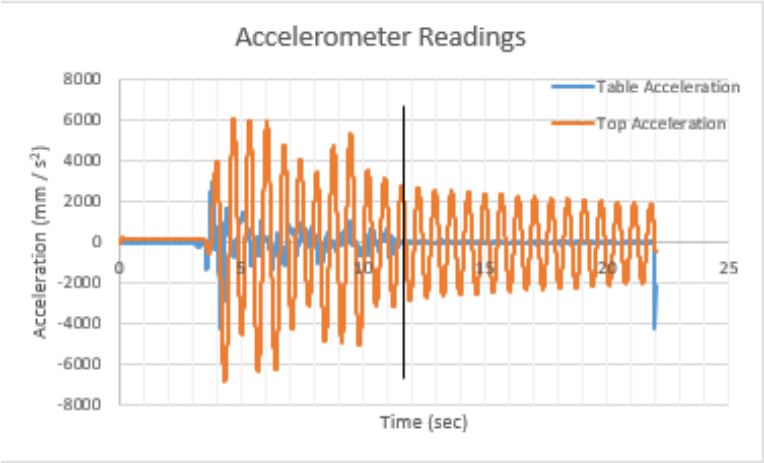

Figure A.88. Table and Top Acceleration Data.

The black vertical line shown in Figure A.88 indicates post earthquake excitation

starts.

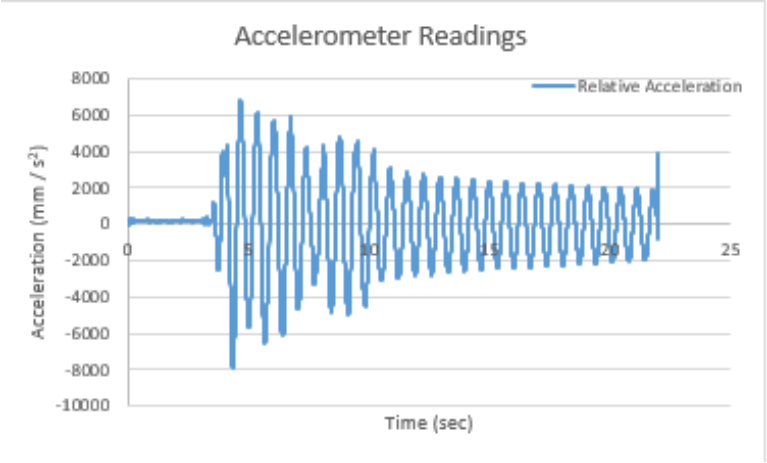

Figure A.89. Relative Acceleration Data.

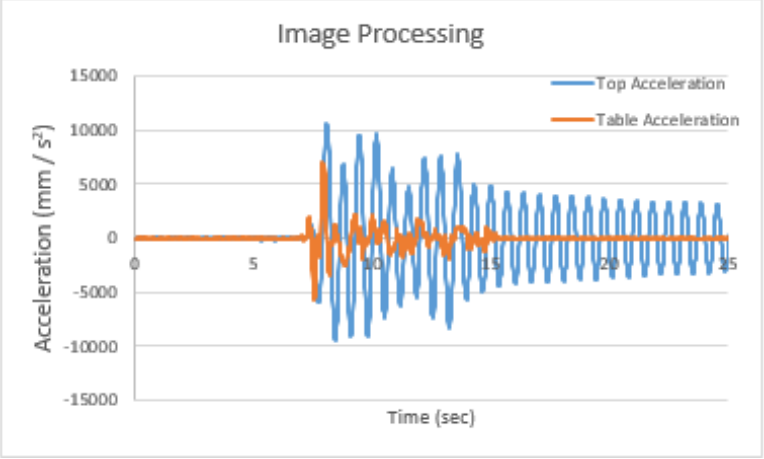

Figure A.90. Top Acceleration and Table Acceleration from Image Processing Data.

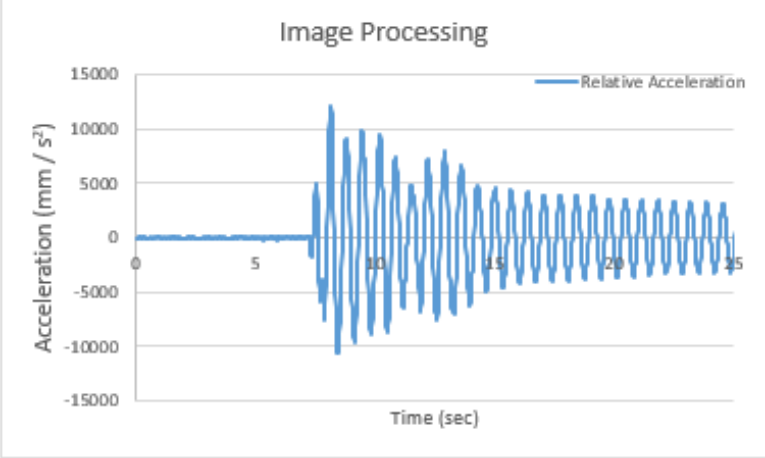

Figure A.91. Relative Acceleration from Image Processing Data.

A.20. T=0.667 sec, 0.90 San Salvador

Figure A.92 to Figure A.97 represent the data obtained from the twentieth experimental test.

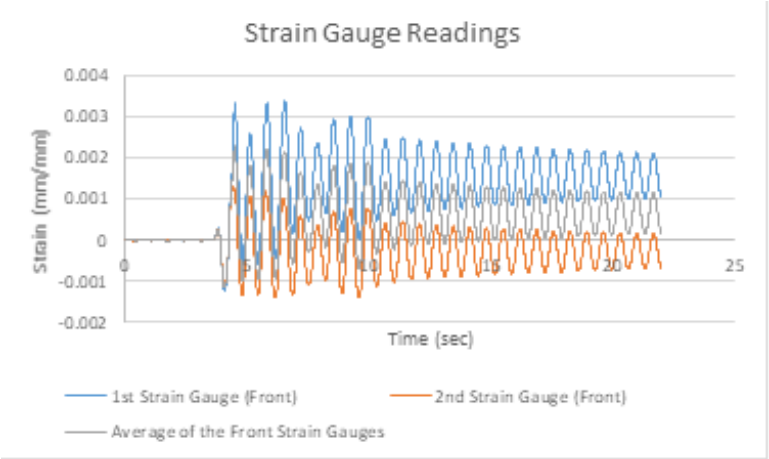

Figure A.92. Strain Data from Front Strain Gauges.

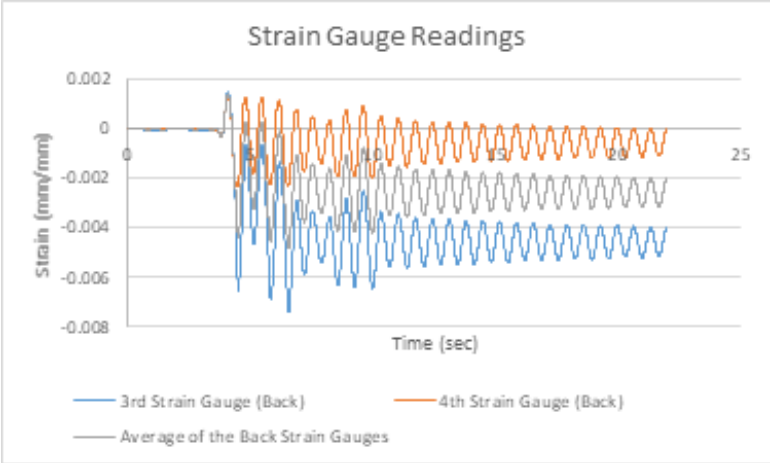

Figure A.93. Strain Data from Back Strain Gauges.

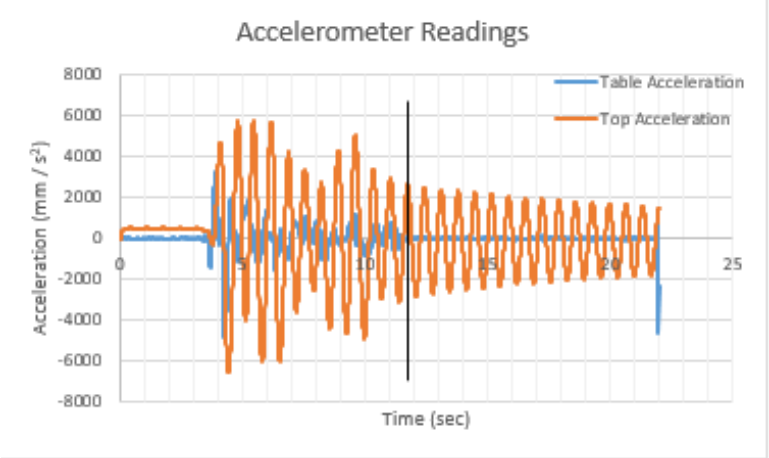

Figure A.94. Table and Top Acceleration Data.

The black vertical line shown in Figure A.94 indicates post earthquake excitation starts.

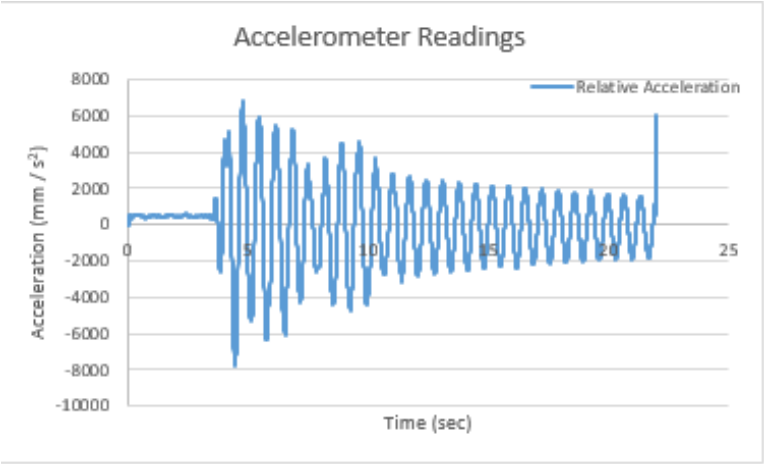

Figure A.95. Relative Acceleration Data.

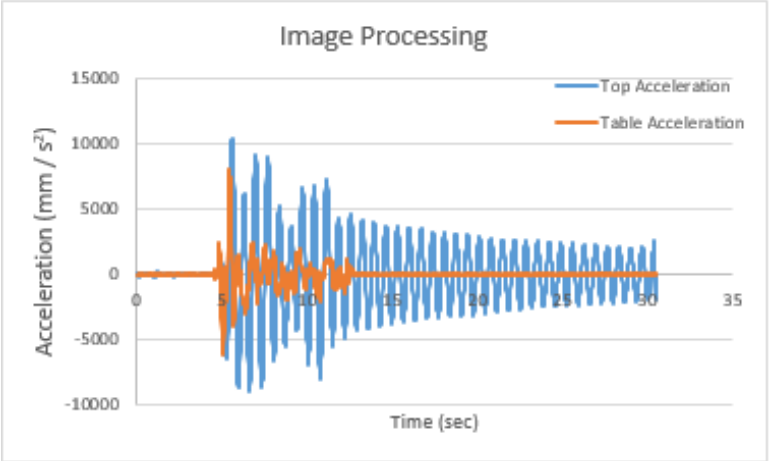

Figure A.96. Top Acceleration and Table Acceleration from Image Processing Data.

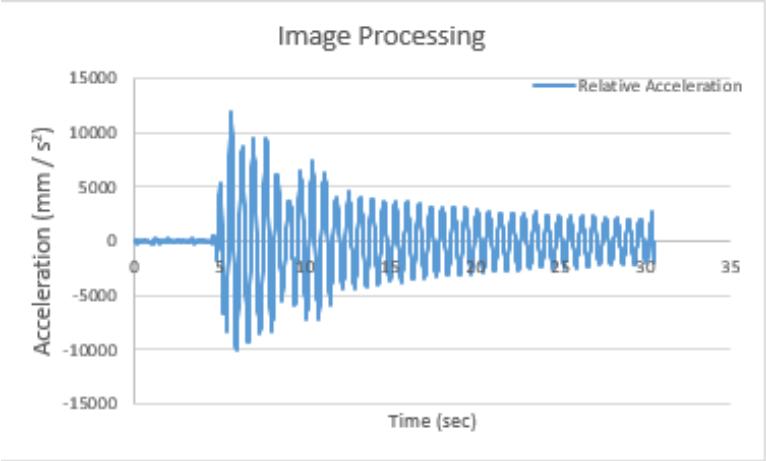

Figure A.97. Relative Acceleration from Image Processing Data.

A.21. T=0.667 sec, 1.00 San Salvador

Figure A.98 to Figure A.103 represent the data obtained from the twenty first experimental test.

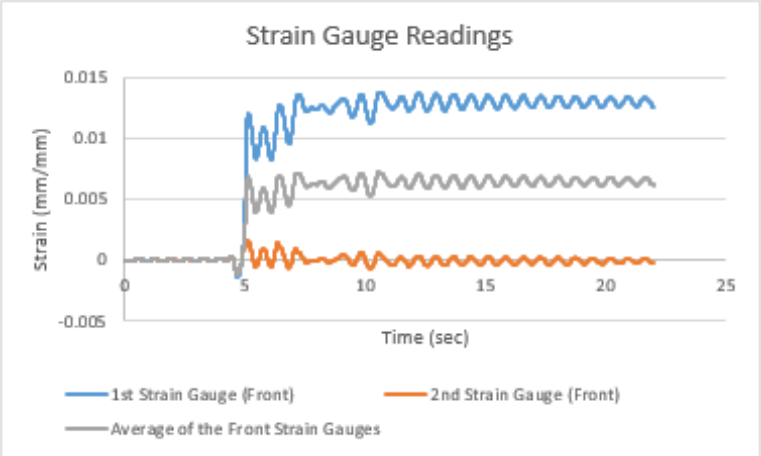

Figure A.98. Strain Data from Front Strain Gauges.

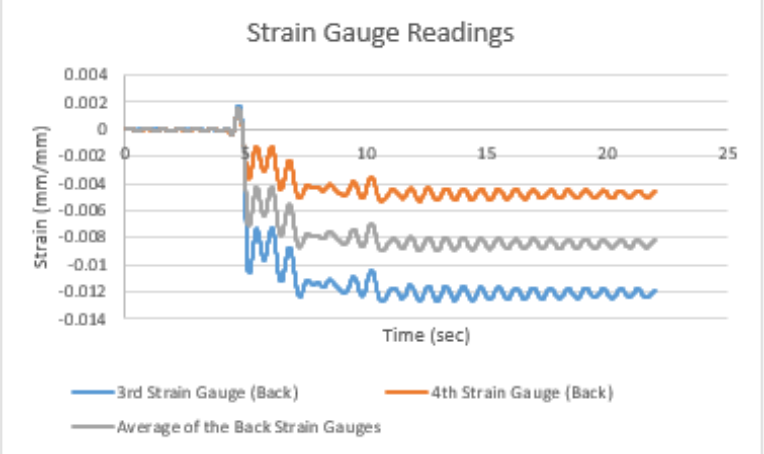

Figure A.99. Strain Data from Back Strain Gauges.

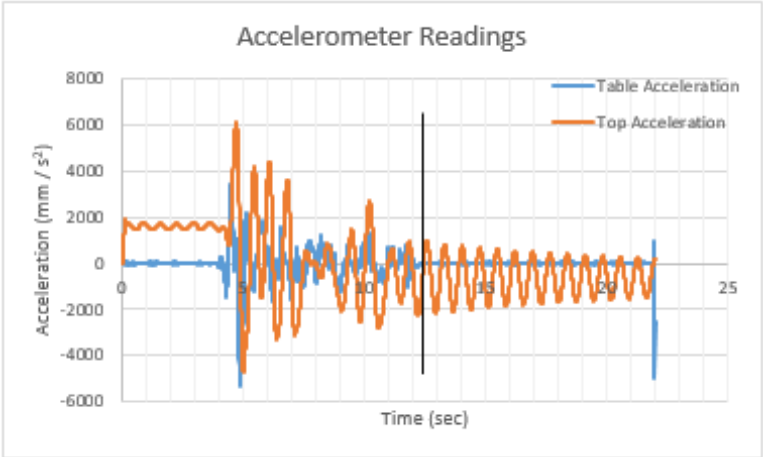

Figure A.100. Table and Top Acceleration Data.

The black vertical line shown in Figure A.100 indicates post earthquake excitation

starts.

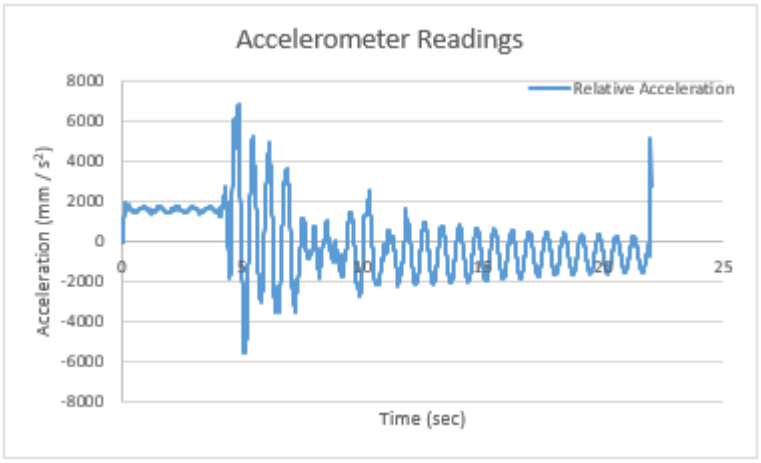

Figure A.101. Relative Acceleration Data.

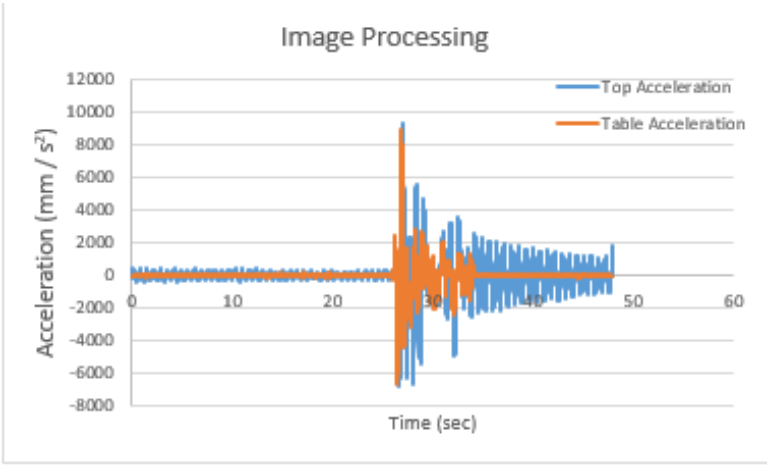

Figure A.102. Top Acceleration and Table Acceleration from Image Processing Data.

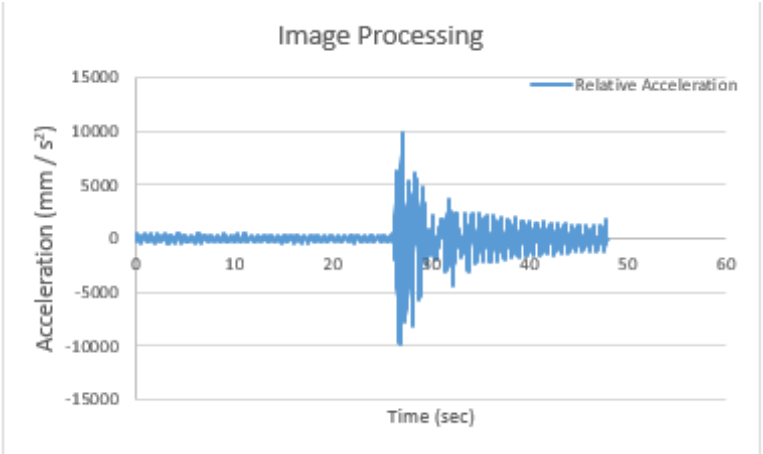

Figure A.103. Relative Acceleration from Image Processing Data.

A.22. T=1 sec, 0.20 San Salvador

Figure A.104 to Figure A.109 represent the data obtained from the twenty-second experimental test.

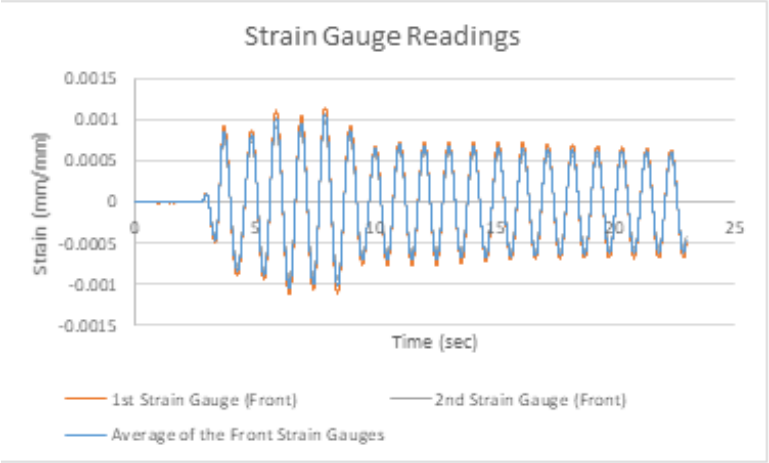

Figure A.104. Strain Data from Front Strain Gauges.

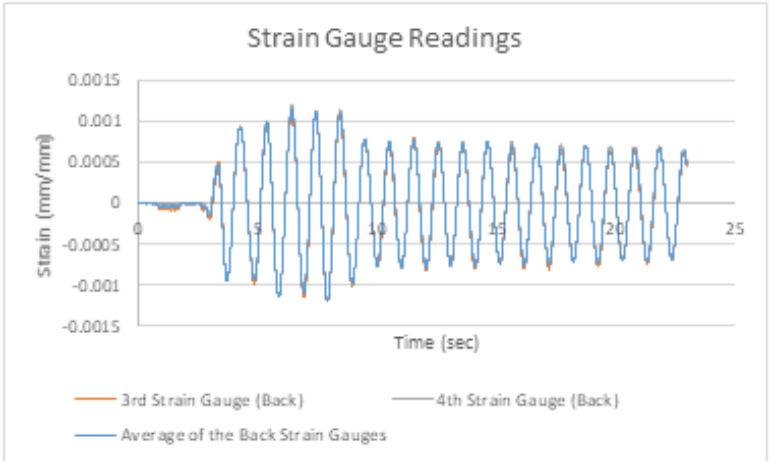

Figure A.105. Strain Data from Back Strain Gauges.

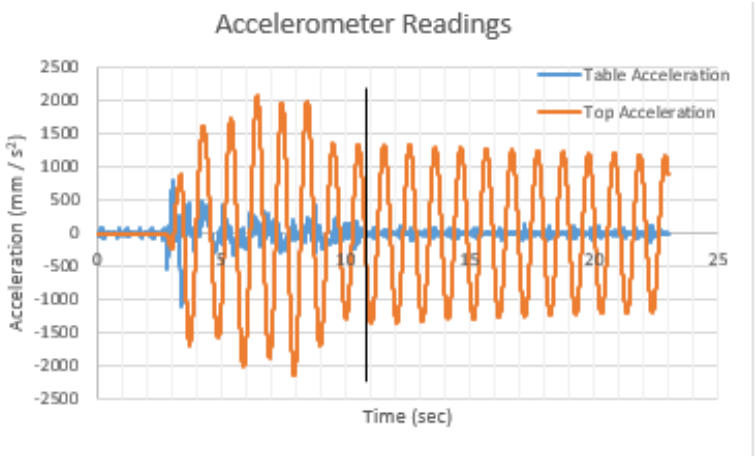

Figure A.106. Table and Top Acceleration Data.

The black vertical line shown in Figure A.106 indicates post earthquake excitation starts.

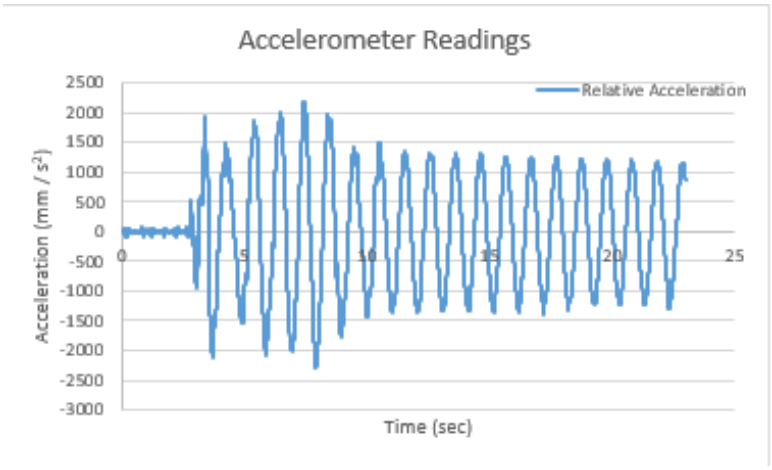

Figure A.107. Relative Acceleration Data.

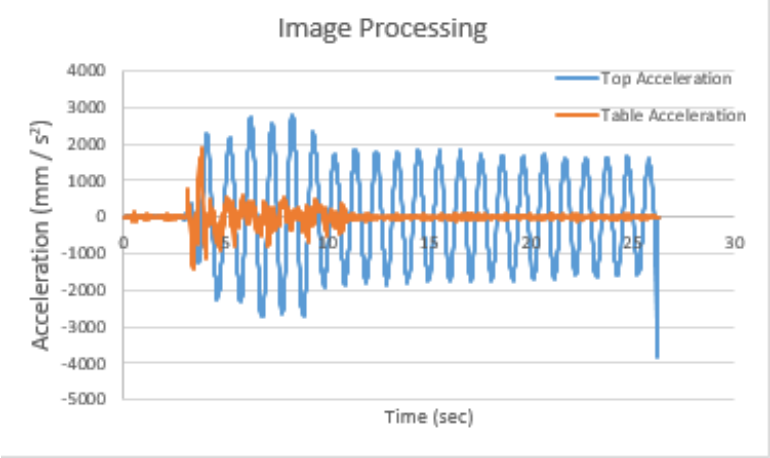

Figure A.108. Top Acceleration and Table Acceleration from Image Processing Data.

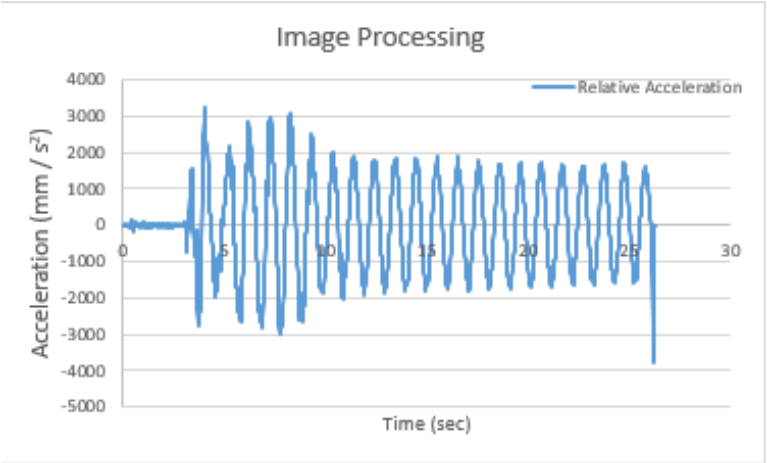

Figure A.109. Relative Acceleration from Image Processing Data.

A.23. T=1 sec, 0.30 San Salvador

Figure A.110 to Figure A.115 represent the data obtained from the twenty-third experimental test.

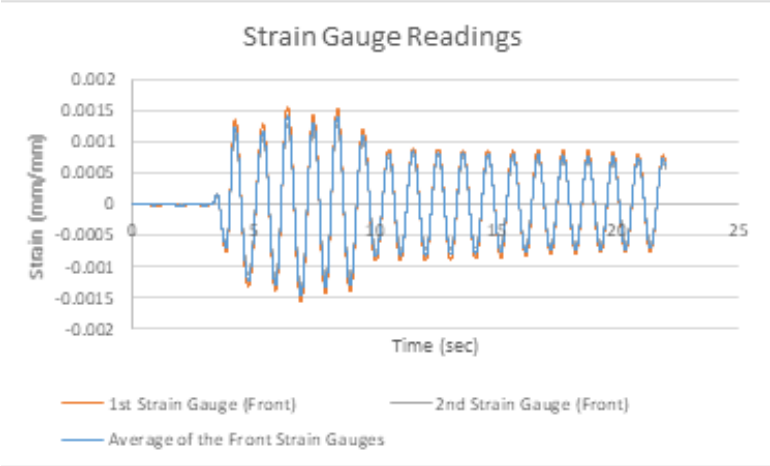

Figure A.110. Strain Data from Front Strain Gauges.

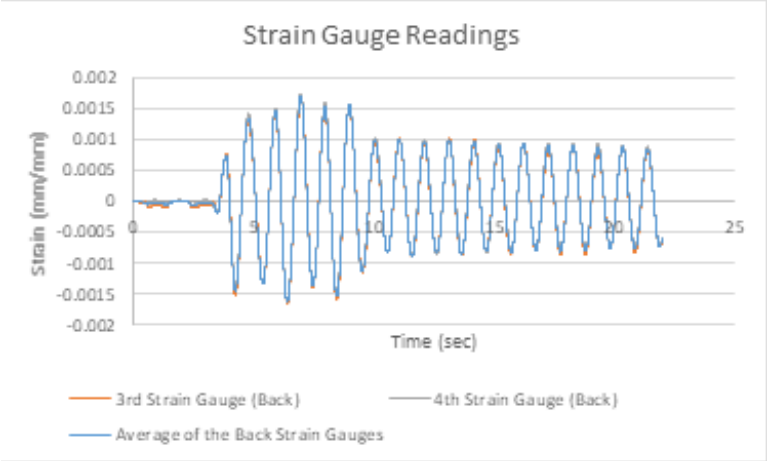

Figure A.111. Strain Data from Back Strain Gauges.

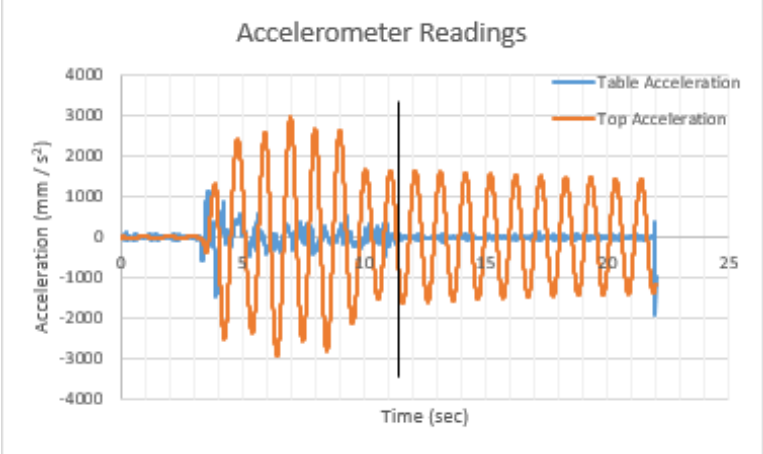

Figure A.112. Table and Top Acceleration Data.

The black vertical line shown in Figure A.112 indicates post earthquake excitation starts.

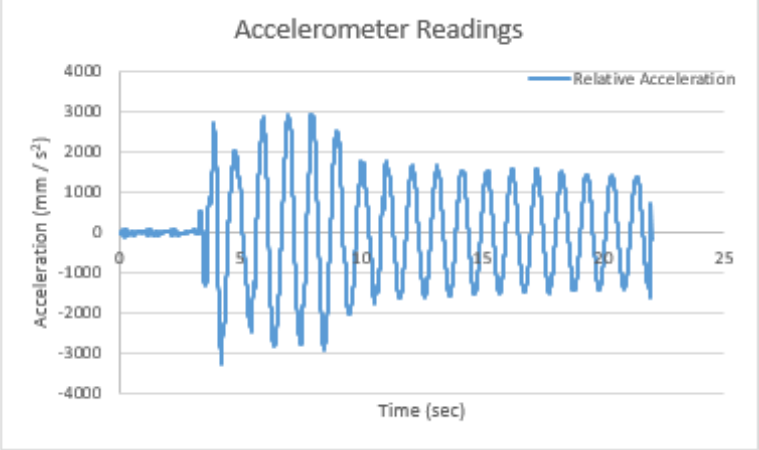

Figure A.113. Strain Data from Back Strain Gauges.

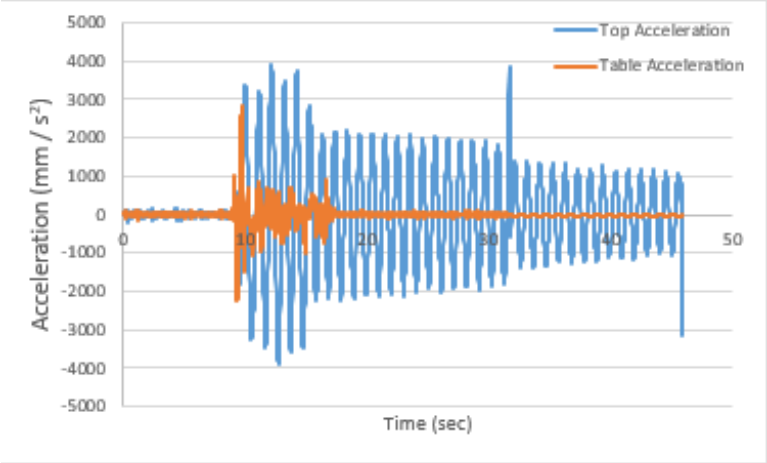

Figure A.114. Top Acceleration and Table Acceleration from Image Processing Data.

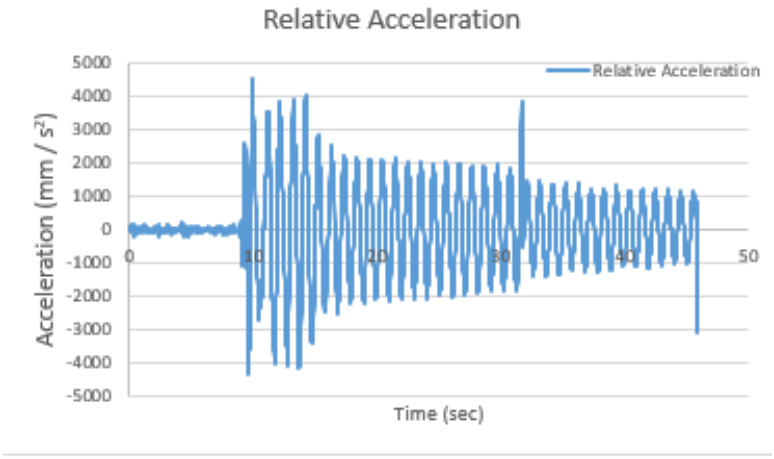

Figure A.115. Relative Acceleration from Image Processing Data.

A.24. T=1 sec, 0.40 San Salvador

Figure A.116 to Figure A.121 represent the data obtained from the twenty-fourth experimental test.

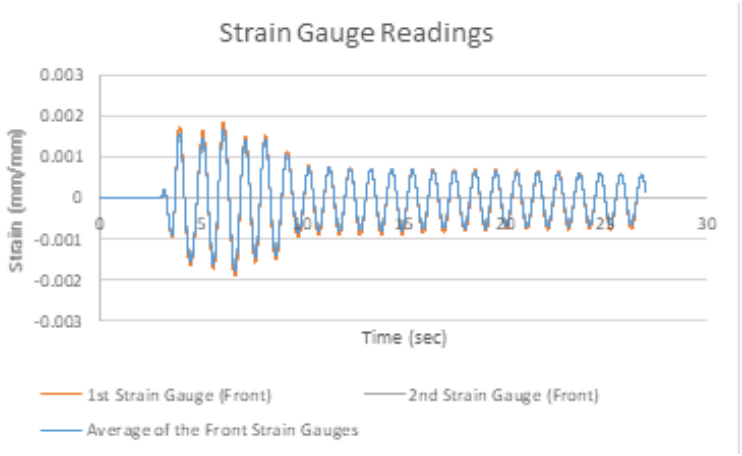

Figure A.116. Strain Data from Front Strain Gauges.

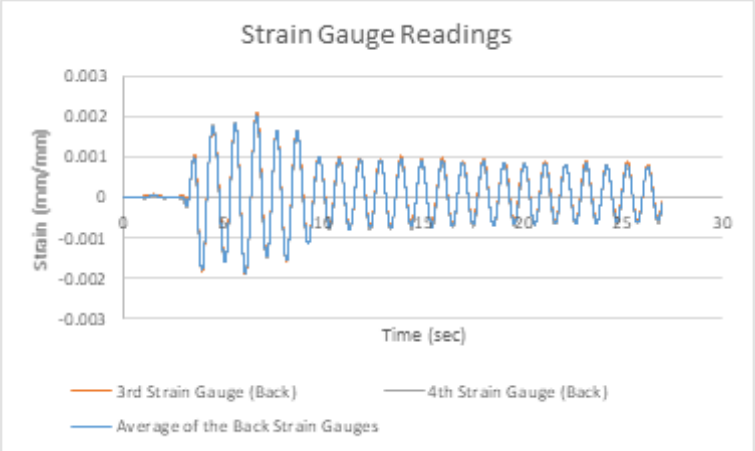

Figure A.117. Strain Data from Back Strain Gauges.

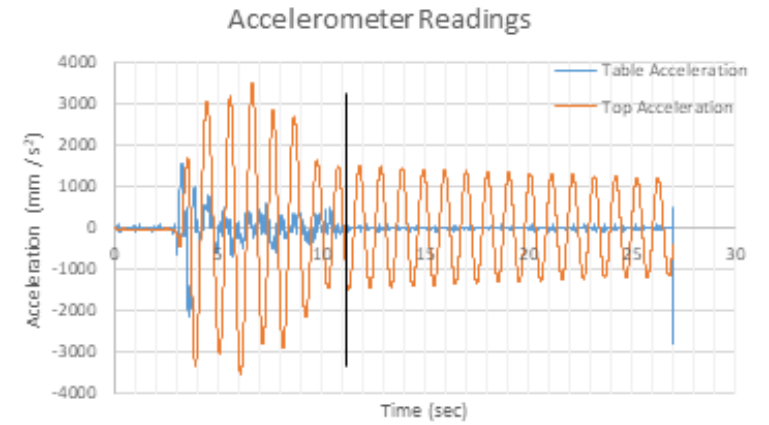

Figure A.118. Table and Top Acceleration Data.

The black vertical line shown in Figure A.118 indicates post earthquake excitation starts.

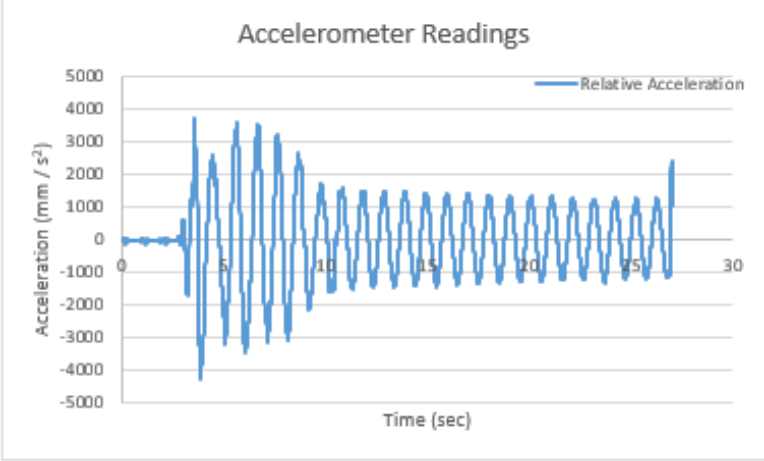

Figure A.119. Relative Acceleration Data.

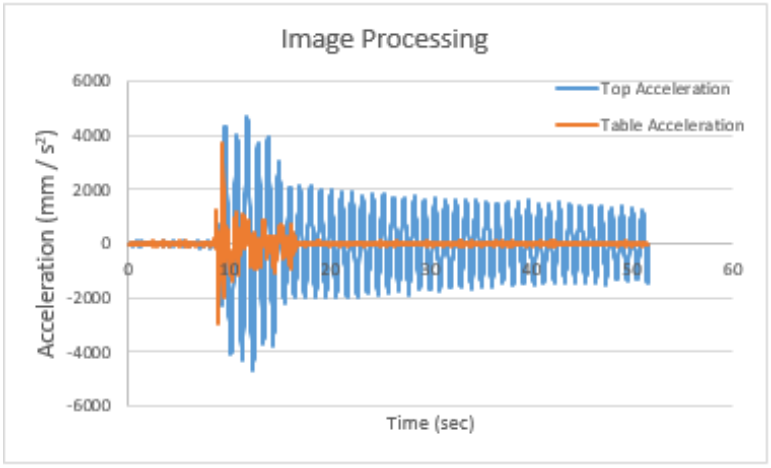

Figure A.120. Top Acceleration and Table Acceleration from Image Processing Data.

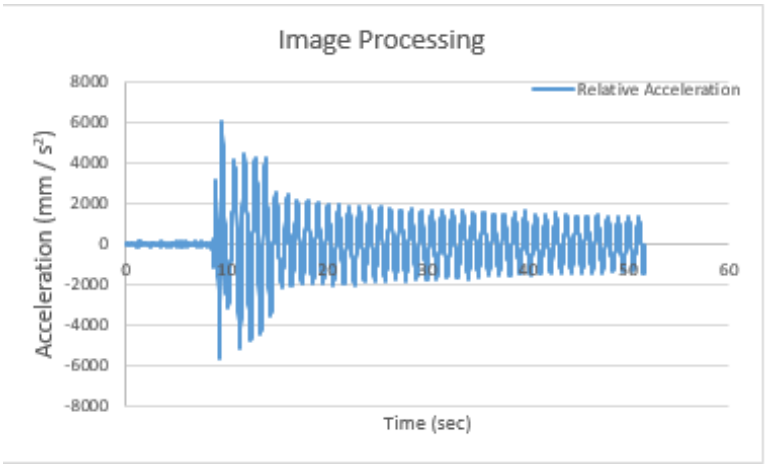

Figure A.121. Relative Acceleration from Image Processing Data.

A.25. T=1 sec, 0.50 San Salvador

Figure A.122 to Figure A.128 represent the data obtained from the twenty-fifth experimental test.

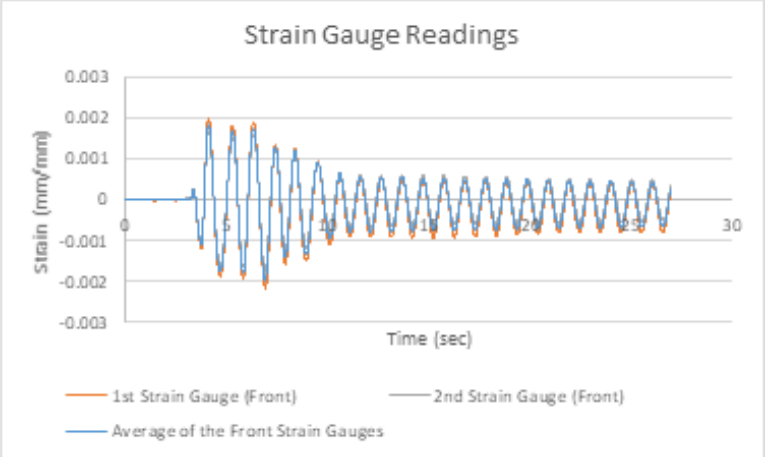

Figure A.122. Strain Data from Front Strain Gauges.

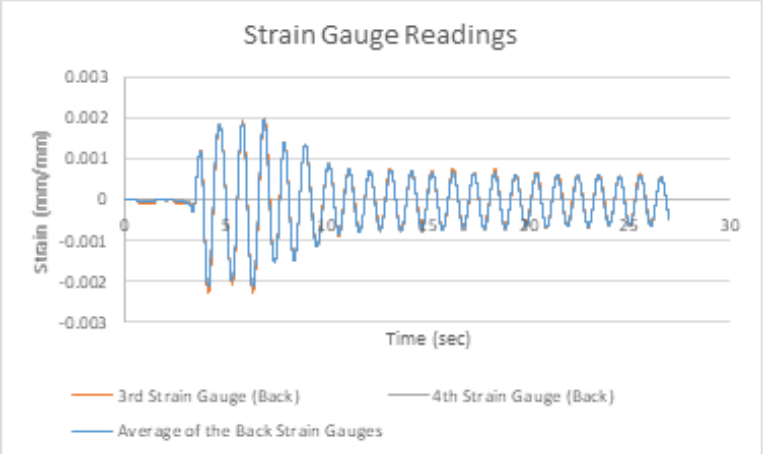

Figure A.123. Strain Data from Back Strain Gauges.

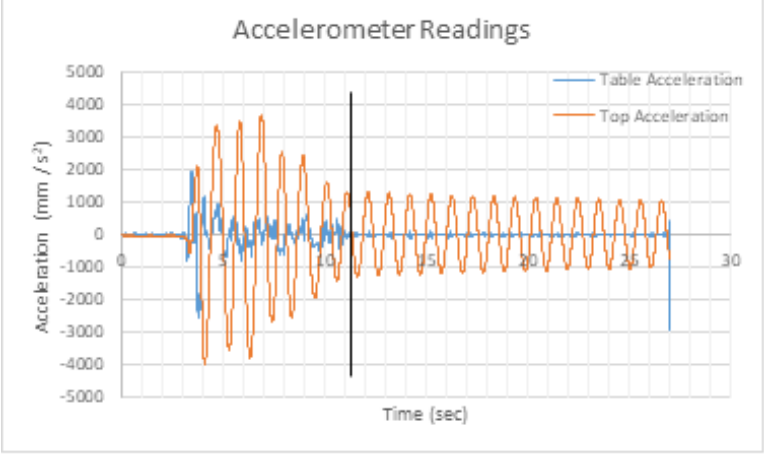

Figure A.124. Table and Top Acceleration Data.

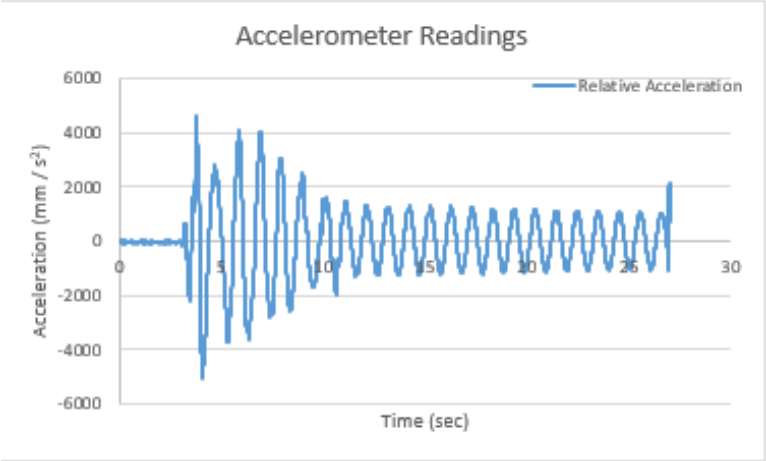

Figure A.125. Strain Data from Back Strain Gauges.

The black vertical line shown in Figure A.124 indicates post earthquake excitation starts.

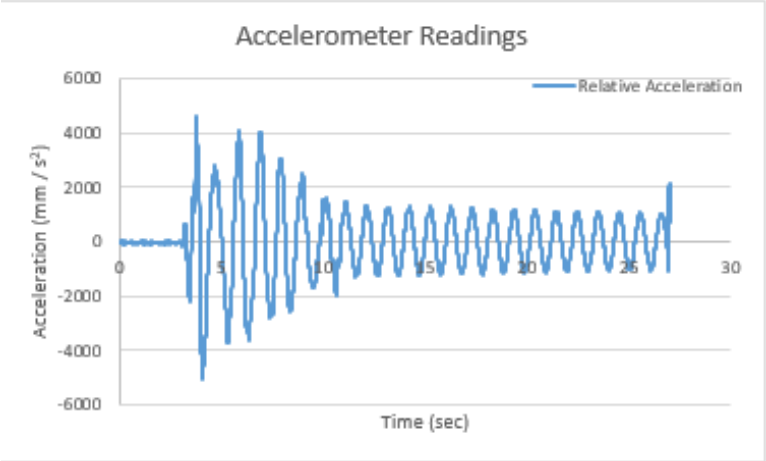

Figure A.126. Relative Acceleration Data.

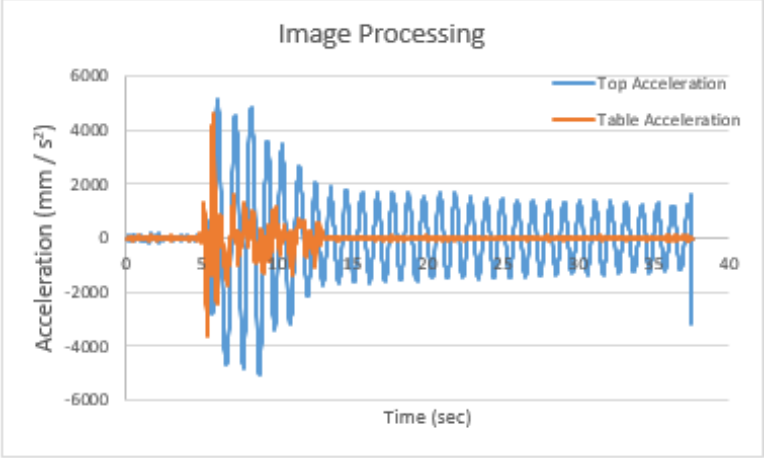

Figure A.127. Top Acceleration and Table Acceleration from Image Processing Data.

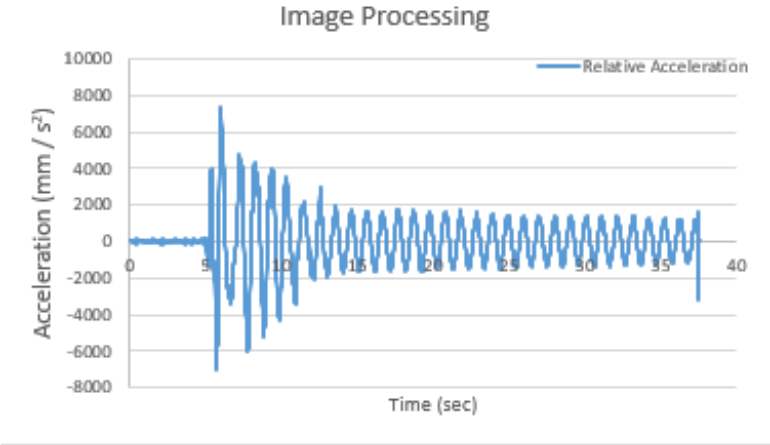

Figure A.128. Relative Acceleration from Image Processing Data.

A.26. T=1 sec, 0.60 San Salvador

Figure A.129 to Figure A.134 represent the data obtained from the twenty-sixth experimental test.

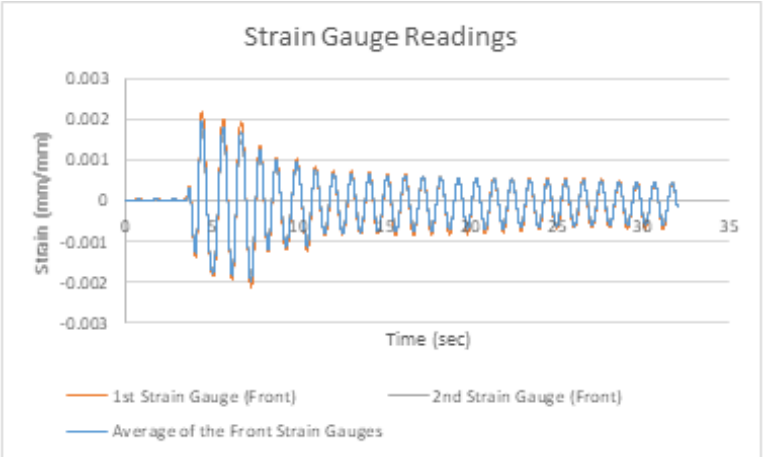

Figure A.129. Strain Data from Front Strain Gauges.

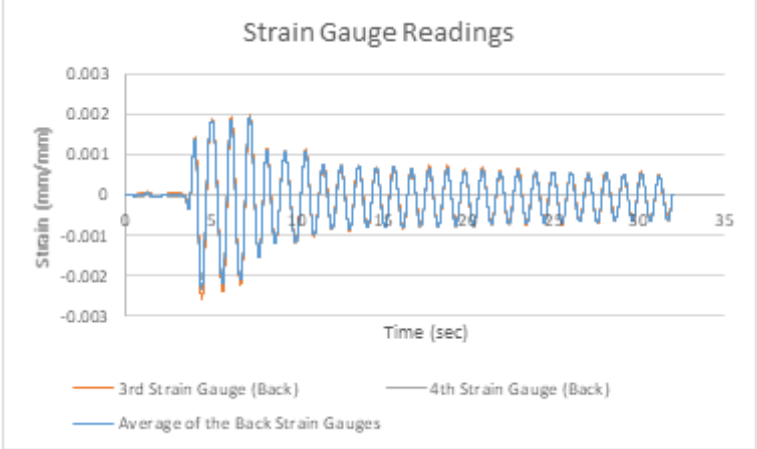

Figure A.130. Strain Data from Back Strain Gauges.

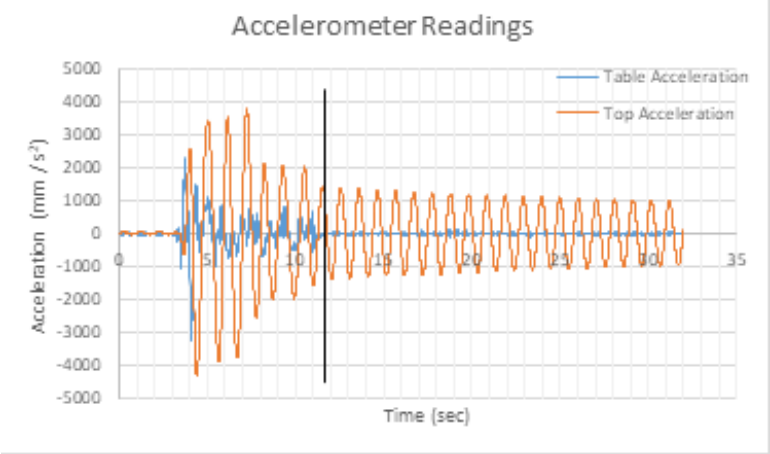

Figure A.131. Table and Top Acceleration Data.

The black vertical line shown in Figure A.131 indicates post earthquake excitation starts.

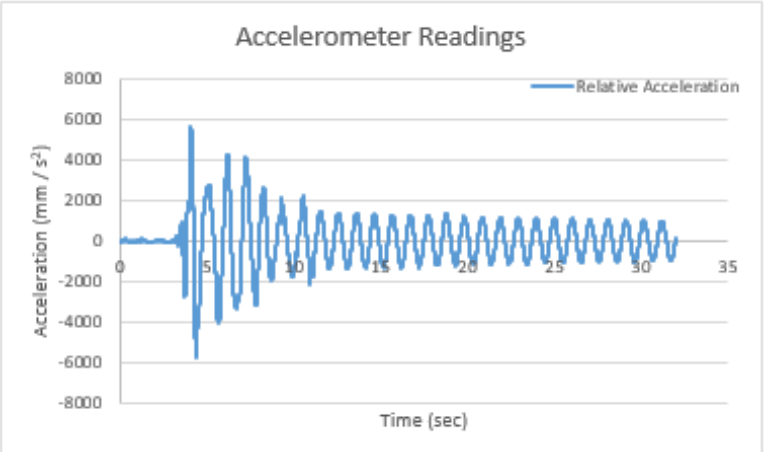

Figure A.132. Relative Acceleration Data.

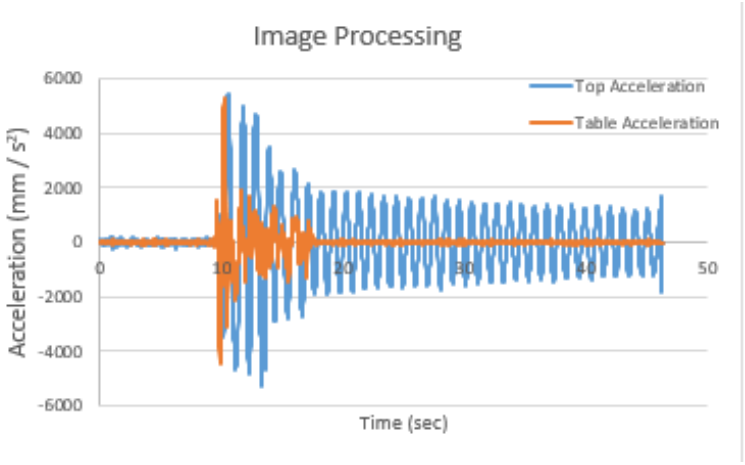

Figure A.133. Top Acceleration and Table Acceleration from Image Processing Data.

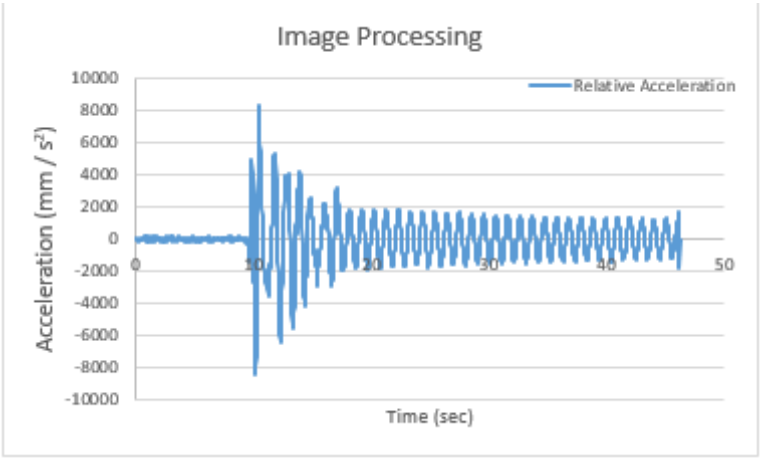

Figure A.134. Relative Acceleration from Image Processing Data.

A.27. T=1 sec, 0.70 San Salvador

Figure A.135 to Figure A.140 represent the data obtained from the twenty-seventh experimental test.

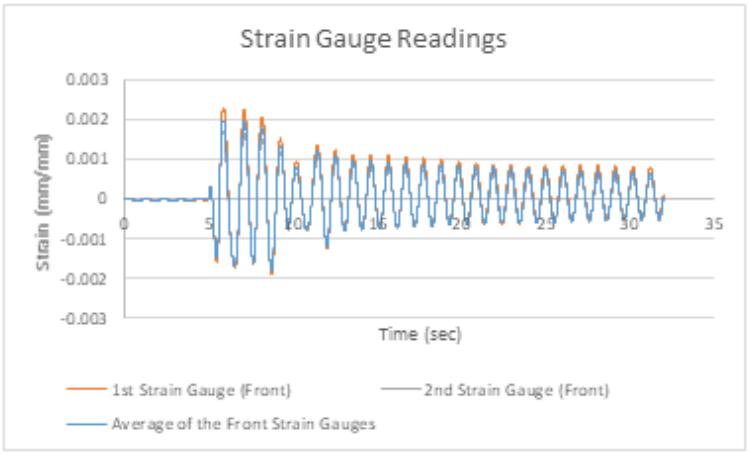

Figure A.135. Strain Data from Front Strain Gauges.

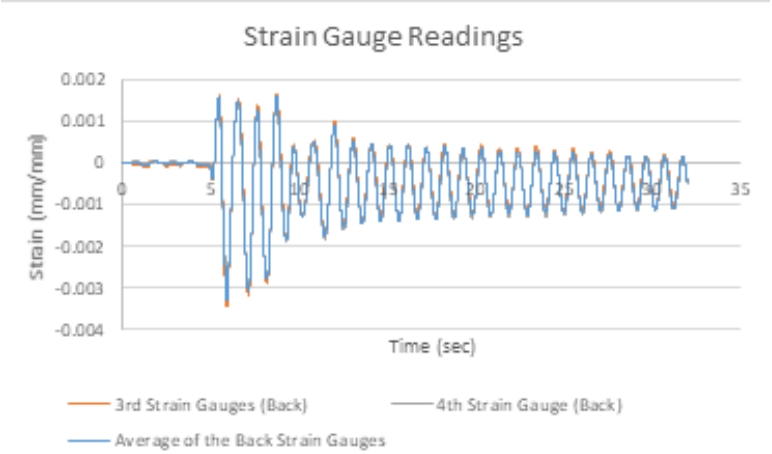

Figure A.136. Strain Data from Back Strain Gauges.

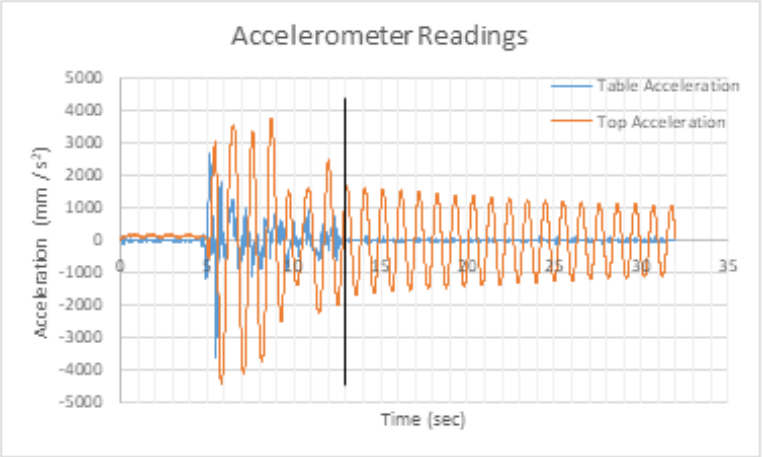

Figure A.137. Table and Top Acceleration Data.

The black vertical line shown in Figure A.137 indicates post earthquake excitation starts.

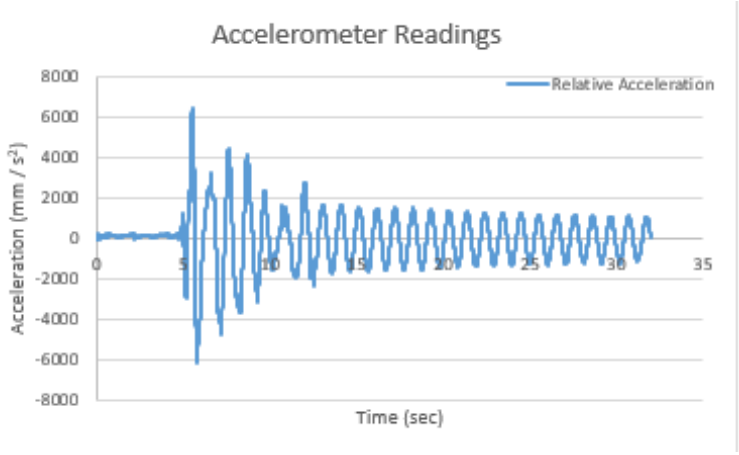

Figure A.138. Relative Acceleration Data.

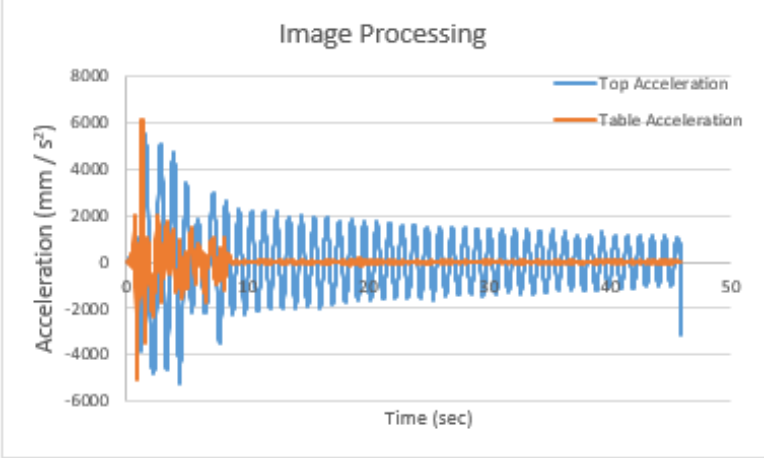

Figure A.139. Top Acceleration and Table Acceleration from Image Processing Data.

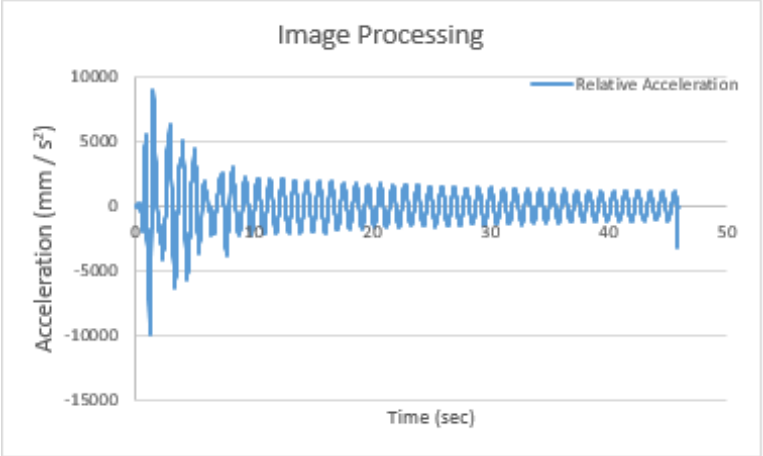

Figure A.140. Relative Acceleration from Image Processing Data.

A.28. T=1 sec, 0.80 San Salvador

Figure A.141 to Figure A.146 represent the data obtained from the twenth-eighth experimental test.

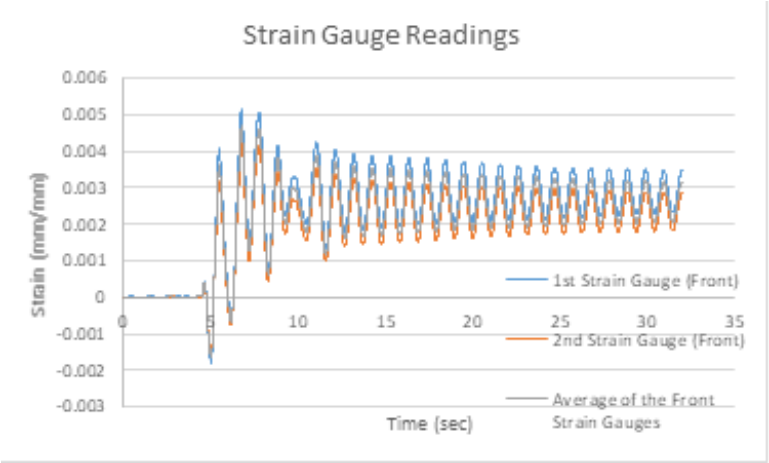

Figure A.141. Strain Data from Front Strain Gauges.

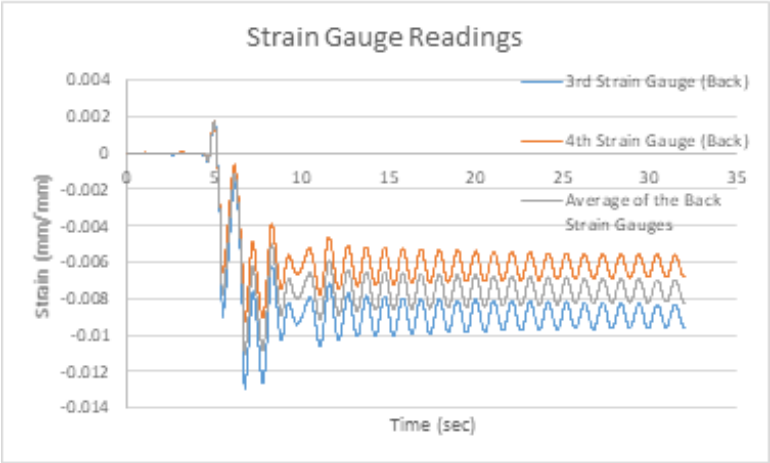

Figure A.142. Strain Data from Back Strain Gauges.

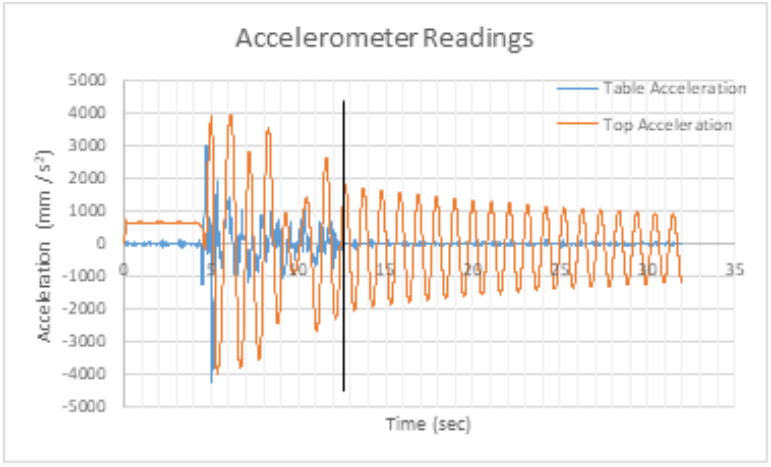

Figure A.143. Table and Top Acceleration Data.

The black vertical line shown in Figure A.143 indicates post earthquake excitation starts.

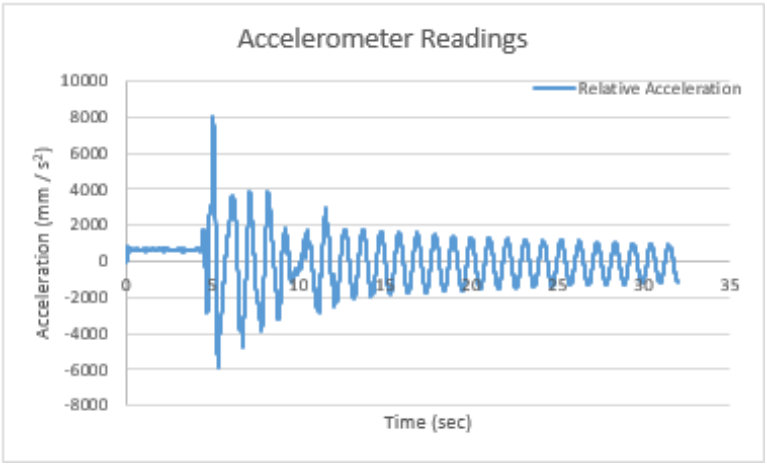

Figure A.144. Relative Acceleration Data.

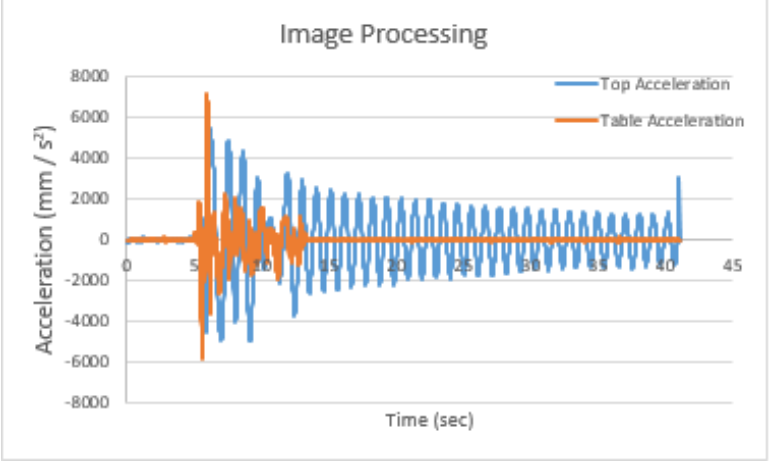

Figure A.145. Top Acceleration and Table Acceleration from Image Processing Data.

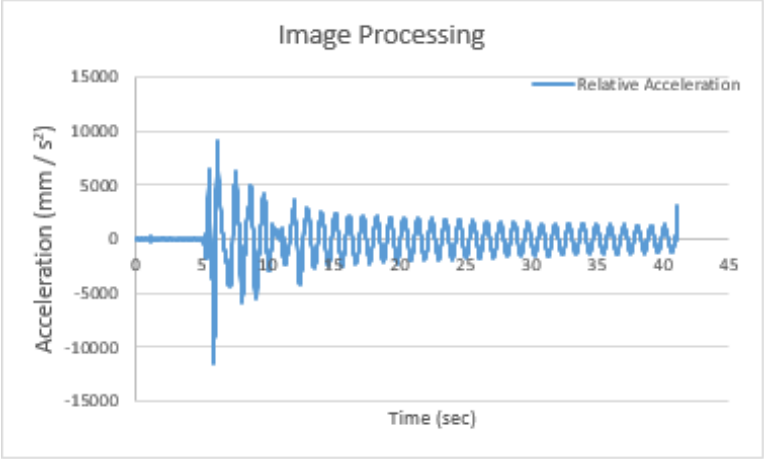

Figure A.146. Relative Acceleration from Image Processing Data.